Transient Boiling Heat Transfer in Saturated Liquid Nitrogen and F113 at Standard and Zero Gravity

EMIN OKER

HEŔMAN MERTE, JR.

October 1973

Department of Mechanical Engineering
Heat Transfer Laboratory

074610-5?-F

THE UNIVERSITY OF MICHIGAN

COLLEGE OF ENGINEERING
Department of Mechanical Engineering
Heat Transfer Laboratory

Final Report

TRANSIENT BOILING HEAT TRANSFER IN

SATURATED LIQUID NITROGEN AND F113

AT STANDARD AND ZERO GRAVITY

Emin Oker
Herman Merte, Jr.

ABSTRACT

Transient and steady state nucleate boiling in saturated LN_2 and F113 at standard and near zero gravity conditions are investigated for the horizontal up, vertical and horizontal down orientations of the heating surface.

A semi-transparent thin gold film on pyrex glass is used simultaneously as a heater and resistance thermometer. Thermal recordings and high speed motion pictures of the nucleate boiling process are synchronized and recorded simultaneously. Test surface and bulk liquid temperatures are determined with an uncertainty of less than $\pm 1.68°F$.

The near zero gravity condition ($a/g \cong 0.004$) is obtained by the drop tower method. Heat flux is varied from approximately 300 to 30,000 $Btu/hr-ft^2$.

Two distinct regimes of heat transfer mechanisms are observed during the interval from the step increase of power input to the onset of nucleate boiling; the conduction and convection dominated regimes. The time duration in each regime is considerably shorter with LN_2 than with F113, and decreases as heat flux increases, as gravity is reduced, and as the orientation is changed from horizontal up to horizontal down.

In transient boiling, boiling initiates at a single point following the step increase in power, and then spreads over the surface. The delay time for the inception of boiling at the first site, and the velocity of spread of boiling varies depending upon the heat flux, orientation, body force, surface roughness and liquid properties, and are a consequence of changes in boundary layer temperature levels associated with changes in natural convection. Following the step increase in power input, surface temperature overshoot and undershoot occur before the steady state boiling temperature level is established.

ii

The surface superheat required for the inception of boiling is found to be independent of heat flux and orientation. It is lower at $a/g=0$ than at $a/g=1$ and is influenced by surface roughness, being higher for smoother surfaces.

The steady state nucleate boiling curve of heat flux versus surface temperature is found to be dependent on gravity and the orientation of the surface with respect to the gravity vector. The influence of gravity and orientation on the active site and average bubble population densities appear to be quite small.

The maximum bubble size and frequency of bubble departure are found to vary, depending upon the heat flux and orientation, according to the relation $(D_{max})^{1/2} \bar{f} = $ constant.

The natural convection and nucleate boiling components of heat flux are separated by using the concept of the "area of influence", and the heat transfer associated with each departing bubble is determined from the experimental measurements. The results are compared with theoretical predictions of the Latent Heat Transfer and the Vapor-Liquid Exchange models.

This report was also a dissertation submitted by the first author in partial fulfillment of the requirements for the degree of Doctor of Philosophy in The University of Michigan, 1973.

This report, along with Ref. [29], together constitute the total final report on work conducted under the subject contract.

TABLE OF CONTENTS

TABLE OF CONTENTS (cont'd.)

TABLE OF CONTENTS (cont'd.)

LIST OF TABLES

LIST OF FIGURES

LIST OF FIGURES (cont'd.)

LIST OF FIGURES (cont'd.)

LIST OF FIGURES (cont'd.)

LIST OF FIGURES (cont'd.)

LIST OF FIGURES (Cont'd.)

xiii

LIST OF APPENDICES

NOMENCLATURE

		Units
a	acceleration	ft/sec^2
a/g	dimensionless acceleration	
A	area	ft^2
C	specific heat/constant	$\dfrac{Btu}{Lbm\text{-}^\circ F}$
D	diameter	inches
E	voltage	volt
f	frequency	$\dfrac{number}{second}$
g	gravitational acceleration	ft/sec^2
H	elevation	ft
h	convective heat transfer coefficient	$\dfrac{Btu}{hr\text{-}ft^2\text{-}^\circ F}$
h_{fg}	heat of vaporization	$\dfrac{Btu}{Lbm}$
I	current	Ampere
k	thermal conductivity	$\dfrac{Btu}{hr\text{-}ft\text{-}^\circ F}$
K	constant	
L	length	ft
m	slope dT/dR Eq. (11)	$\dfrac{^\circ F}{ohm}$
n/A	average population density	$number/ft^2$
N/A	active site density	$number/ft^2$
P	pressure	Psi
Q	heat	Btu
Q/A	heat flux	$Btu/hr\text{-}ft^2$
R	radius/resistance/result	ft, ohm
t	time	hr
T	temperature	$^\circ F$, $^\circ R$, $^\circ K$
ΔT	temperature difference	$^\circ F$, $^\circ R$, $^\circ K$

		Units
V	velocity	ft/sec
W	uncertainty	
ΔE	voltage difference	volt

Greek Symbols

α	thermal diffusivity/temperature coefficient of resistance	ft^2/hr, $1/°F$
β	linear temperature coefficient of expansion/ temperature gradient (50)	$1/°F$, $°F/ft$
δ	thickness/penetration depth	ft
θ	contact angle	degree
μ	viscosity	lbm/hr-ft
ρ	density	lbm/ft^3
σ	surface tension	lbf/ft
τ	elapsed time/delay period	seconds (hr)
ν	kinematic viscosity	ft^2/hr
γ	volumetric coefficient of expansion	$1/°F$

Dimensionless Parameters

Gr	Grashof number	$\gamma g L^3 \Delta T/\nu^2$
Nu	Nusselt number	hL/k
Pr	Prandtl number	$Cp\mu/k$
Ra	Rayleigh number	$g\gamma \Delta t L^3/\alpha\nu$

NOMENCLATURE (cont'd.)

Subscripts

b	bulk
Bub.	bubble
c	calibration/cavity
dep	departure
f	fluid Eq. (14)
i	inactive/interface/summation index/initial
IB	incipient boiling
ℓ	liquid
max	maximum
min	minimum
NB	nucleate boiling/non boiling Eq. (73)
NC	natural convection
o	overshoot/reference condition
p	predicted/penetration distance Eq. (56)
s	solid
sat	saturated
sub	subcooled
T	test surface/total
u	undershoot
v	vapor
V	volume
w	wall

CHAPTER I

INTRODUCTION

A. PURPOSE

Nucleate boiling is one of the most efficient ways of transferring heat from a solid surface to a liquid, in that the temperature differences are relatively small for large magnitudes of heat flux. Advancement in space technology has increased the importance of understanding nucleate boiling at zero gravity as well as at standard gravity. Incipient and nucleate boiling have significance in the long-term space storage of cryogenic liquids. The onset of nucleate boiling, called incipient boiling, will determine the degree of superheat present in the liquid. Large liquid superheats constitute highly unstable systems and can result in undesirable effects such as sudden and large rises in pressure when vaporization begins. Because of its importance, many aspects of nucleate boiling have been extensively studied in order to learn more about the basic mechanism involved. Due to its extreme complexity, however, it remains poorly understood, as is demonstrated by the difficulty of predicting nucleate pool boiling heat transfer adequately for various surface-liquid combinations. A number of models have been proposed, but each has limitations. Many of the experimental results are somewhat incomplete and conflicting. Many experiments involved the use of small wires, so that the test surfaces were small compared to bubble diameters, raising the question as to whether the results obtained are representative of behavior with large surfaces.

The purpose of this work is to investigate the behavior of certain parameters in transient and steady-state nucleate boiling at standard

and zero gravity. Incipient boiling can be viewed as a transient process in itself, since a change in the basic mechanism is taking place. It was thus deemed pertinent that a study of the transient boiling process should be included. In space applications in particular, where finite systems are present, all phase change processes encountered will be transient. The onset of non-boiling natural convection may be anticipated to influence the inception of boiling, as will the conduction processes in both the fluid and the heat transfer surface. A complete description of transient boiling must therefore include these mechanisms.

The fluids used in this study are liquid nitrogen and Freon 113 with three different orientations of the heat transfer surface relative to the prevailing gravity field; vertical, horizontal up, and horizontal down. The boiling point of Freon 113 is 117°F at atmospheric pressure, making it convenient to use at ambient conditions. Liquid nitrogen is a reasonably typical cryogenic liquid whose attribute of inertness makes it convenient to use. In addition, both fluids are electrical non-conductors, a necessity for the experimental technique used for heating and for surface temperature measurement. The three orientations of horizontal up, vertical, and horizontal down constitute the limits commonly encountered in practice. It is recognized that orientation has no significance under true zero gravity, but true zero gravity does not exist in practice. In space solar radiation pressure produces body forces of about $a/g = 10^{-9}$, and in drop tower experiments residual body forces of about $a/g = 10^{-3}$ are present.

The objectives of the present work are stated more explicitly as follows:

1. To determine the influence of heat flux, heater surface orientation and gravity on the steady state and t. ansient nucleate boiling heat transfer processes.

2. To investigate the role or significance of the bubble microlayer in boiling heat transfer and bubble growth rates.

3. To investigate the influence of heat flux, heater surface orientation, and gravity upon the active nucleation site density, bubble population, frequency of bubble emissions, and maximum bubble departure size.

4. To test some of the existing theoretical correlations with the experimental data obtained.

B. LITERATURE SURVEY

In this present work, both the transient and steady-state behavior of nucleate pool boiling at standard and near zero gravity conditions were studied. The effects of heat flux and orientation were also investigated.

The control and response of some thermal systems, particularly nuclear reactors, depend on the transient characteristics of the boiling process. Characteristics of boiling change considerably when very short transients are considered. It is therefore important to know, for given fluids and heat transfer surface materials, the heater surface superheat, delay time, and related heat flux needed to initiate nucleate boiling. The literature on transient boiling heat transfer is relatively limited. Those available are presented below, and then followed by a summary of the relevant points in each.

Cole [1] and Rosenthal [2] investigated transient heat transfer from nickel and platinum ribbons, respectively, to subcooled water at atmospheric pressure. The test surface was used as a resistance thermometer to measure wall temperatures. Cole experimented with step power inputs while Rosenthal increased the power exponentially. A bank of 12 volt D.C. batteries was used for the power source in both studies. Cooper and Lloyd [3] measured the surface temperature fluctuations of a heated glass plate in subcooled toluene at different pressures, as individual vapor bubbles form, grow and move off. The temperatures were measured by small thin metal and semiconductor thin films. Pressure was varied from 1-2 psia, heat flux was varied between 7500-15000 BTU/HR-ft^2, and subcooling was varied between 0-15 degrees F. Garg and Patten [4] report on the temperature and pressure transients associated with bubble growth in and near the superheated layer around a 1/8" diameter heated tube in saturated water. A 20-V, 400 amp, d.c. motor-generator unit was used to supply necessary power. The average surface temperature was deduced from measured stabilized bulk liquid temperature by a 36 SWG thermocouple. Hall and Harrison [5] investigated the mechanism of boiling water with exponentially increasing heat flux. A platinum ribbon was used both as heater and resistance thermometer. A set of storage batteries controlled by a transient power generator was used as the power source. Johnson et al [6] investigated the transient pool boiling of subcooled water at atmospheric pressure. Energy was increased exponentially in platinum and aluminum ribbons, positioned both vertically and horizontally, and which were also used as resistance thermometers. The power source was similar to that used in Reference [5]. McCurdy [7] analytically studied the delay time for bubble formation in

water moderated reactors, which were reported to be in agreement with the experimental result of Ref. [6]. Lurie and Johnson [8] studied transient pool boiling of subcooled water at atmospheric pressure, on a vertical surface with a step increase in heat generation. An iron-nickel alloy ribbon was used as the heating surface and as a resistance thermometer. Power was supplied by a set of storage batteries. Klosterhouse [9] studied transient boiling using a small platinum wire as a heater and as a resistance thermometer, in saturated liquid nitrogen (LN_2) and liquid hydrogen (LH_2). A 12 volt D.C. battery was used for the step power input. Carpenter [10] made similar studies with a flat surface in liquid nitrogen, consisting of a pyrex glass substrate coated with a thin gold or nickel film and used as both a heater and a resistance thermometer. Graham [11] investigated the transient boiling of subcooled water and alcohol on a horizontal chromel ribbon cemented to a bakelite block. Surface temperatures were estimated from the readings of three thermocouples attached to the underside of the chromel strip. A 12 volt battery was used to obtain the setp power increase for the experiments.

With a step increase in imposed heat flux, what is called a surface temperature overshoot was reported [1, 8, 11], in which the heater surface temperature increases significantly above the steady state temperature corresponding to the particular heat flux, prior to the onset of nucleate boiling. Similar phenomena were observed with an exponentially increasing power input [2, 5, 6].

Once nucleate boiling is initiated, generally at a single location, it spreads rapidly across the surface because of the presence of the superheated liquid. In so doing the liquid superheat is reduced to near saturation condition, which can result in a momentary decrease in the

heater surface temperature below that of the steady temperature corresponding to the heat flux. This has been observed with a ribbon and has been termed a temperature undershoot [11]. Owing to the rapid formation of vapor, more nucleation sites most likely have been activated than can be sustained in the steady state. This undershoot has also been observed in transient boiling with small wires [9].

Time delays were observed between the imposition of the heat fluxes and the inception of boiling [2, 6-11]. It was concluded [2, 8] that the transient process taking place before nucleate boiling began was solely a conduction process. As such it is possible to predict the surface temperature superheat by solving the equation of conduction. In comparing with predictions assuming a semi-infinite solid model, it was found that predictions were low in one case, [2], and high in another [8]. In another experimental work, using a Schlieren technique in conjunction with surface temperature measurements, it was observed that both transient conduction and transient free convection processes occured prior to the onset of nucleate boiling, [11]. With a sufficiently high step increase in heat flux, the surface temperatures increased so rapidly that the process passed directly into and remained in the film boiling region [12, 13]. The surface temperature measurements of Ref. [4], while having a small response time, were highly localized and were intended to show the effects of the growth and departure of the individual bubbles.

The present work is intended to experimentally determine the nature of the time delay, overshoot and/or undershoot in wall temperature, and the types of heat transfer processes taking place up to the establishment of steady state boiling, along with the effects of body force, orientation, heat transfer rates, and the surface characteristics on these

phenomena. In addition, because of the experimental technique employed, it was possible to obtain data of interest concerning certain aspects of steady nucleate boiling.

Since it is an efficient heat transfer process nucleate boiling has a wide range of applications. Consequently a large number of research studies have been directed toward the different aspects of nucleate boiling. Many reviews of the general subject are available (e.g. Refs. [14, 15, 16]). Only those works which have a direct relation to specific aspects of the present study will be reviewed here.

Some existing experimental nucleate boiling heat transfer studies in reduced gravity fields are listed in Table 1, along with the significant parameters. A number of works reported little or no influence of the reduced body force on nucleate pool boiling process [17-23]. On the other hand, others report a distinct decrease in the heater surface superheat at a given heat flux as the body force is reduced [24-28]. For the sake of convenience, the decrease in heater surface superheat for a given heat flux will be defined as a downward shift, and the opposite as an upward shift.

The data of Clodfelter [27] indicates a downward shift of 4°F. Papell and Faber [26] report about a 5°F downward shift. Littles [24] indicates an upward shift for vertical surfaces and downward shift for horizontal surfaces. Merte et al [25] observed a downward shift for horizontal up, an upward shift for horizontal down, and no change for vertical orientations, with reduced gravity.

The seemingly contradictory results of Ref. [17-23] can be explained on the basis of the experimental procedures followed. Figure 10 in Ref. [19] indicates an upward shift of 1.5°F for $a/g = 0.20$, but the

Table 1. Nucleate Boiling Curve Shift from Standard Gravity to Near Zero Gravity

-8-

Author	Method	Test Piece	Liquid	Boiling Curve Shift
Usiskin & Siegel [22]	Drop Tower	Wire	Water	No Shift Detected
Siegel & Usiskin [23]	Drop Tower	Horizontal Flat Ribbon	Water	No Shift Detected
Sherley [18]	Drop Tower & KC-135 Aircraft	Flat Surface Upward Heating	LIQ H_2	Slight Downward Shift
Merte & Clark [19]	Drop Tower	1 & 1/2 Copper Sphere	LIQ N_2	Insignificant Upward Shift
Clodfelerter [27]	Drop Tower	Horizontal Platinum Wires & Platinum Ribbons	Water	Downward Shift
Siegel & Keshock [28]	Drop Tower	Horizontal Platinum Wires & Platinum Ribbons	Water	Downward Shift for Ribbons - Upward Shift for Wires
Schwartz [20]	Air Commander Aircraft	Horizontal Ribbon Upward Heating	Water	Slight Downward Shift
Littles [24]	Drop Tower	Flat Surface 1-Vertical 2-Horizontal Up	Freon 113	Upward Shift for Vertical Downward Shift with Horizontal
Kotake [17]	Drop Tower	Horizontal Wire	Water	No Shift
Merte et al [25]	Drop Tower	Flat Surface 1-Horizontal Up 2-Vertical 3-Horizontal Down	LIQ N_2	1-Downward Shift 2-No Change 3-Upward Shift
Lewis et al [21]	Drop Tower	1" Sphere	LIQ N_2	No Shift
Papell & Faber [26]	Magnetic Field	Horizontal Ribbon Upward Heating	Normal Heptane	Downward Shift

Authors report an uncertainty of 2°F in the data. Furthermore, the heater surface was spherical in shape, for which no preferred orientation of the acceleration vector exists. The instrumentation in the experiments of Usiskin and Siegel [22, 23] was not sensitive enough to detect tempera- ture shifts less than 6°F. There was a considerable scatter in the data of Sherley [18], most likely due to the lack of sensitivity in the tem- perature measuring technique. A least square statistical line fitted in the data of Ref. [18] by Littles [24] indicates a small shift such that the values of $\Delta T_{sat}(T_T - T_{sat})$ at zero gravity were 0.5°F smaller than the corresponding values at standard gravity, indicating a slight down- ward shift.

If nucleate boiling is relatively insensitive to buoyant forces, as reported by some of the investigators, and is controlled by inertial forces resulting from the dynamics of the bubble growth, it should also be insensitive to the orientation of the heating surfaces even at stan- dard gravity. Marcus and Dropkin [30] noticed an increase in heat flux for a given ΔT_{sat} when they rotated the surface from horizontal up to the vertical position. Similar results were observed by Githinji and Sabersky [31] when the orientation was changed from horizontal up to the vertical position, but they observed a considerable decrease in heat flux for a given ΔT when they changed the orientation of their thin ribbon surface from vertical to horizontal downward. On the other hand the highest heat flux for a given ΔT was reported with the horizontal down orientation in Freon 113 [24]. Similar results were obtained in experiments with LN_2 and LH_2 at standard gravity [25].

These latter results all indicate that nucleate boiling is influ- enced by body forces. The magnitude of the effect of reducing body forces

must be investigated more thorough,y. A trend common in each of these is seen in Fig. 2 of Ref. [25], where at lower levels of heat flux the horizontal down orientation gives the highest heat flux for a given ΔT_{sat}, and the horizontal up gives the lowest, and the vertical lies in between. A possible explanation for this effec. lies in the role that microlayer evaporation plays in bubble growth. For the horizontal down orientation the buoyant forces tend to hold the vapor bubbles closer to the surface, and thus could increase the effective area of the microlayer compared to the horizontal up and vertical orientations. Since the microlayer evaporation produces large evaporation rates with small ΔT's, the heat flux for a given ΔT_{sat} should be higher for horizontal down orientations. This s consistent with the observations of Hospeti and Mesler [32]. They report that the heat transfer associated with hemispherical bubbles is greater than that with spherical bubbles. Because of the influence of the buoyant force, horizontal down orientations tend to produce hemispherical bubbles while horizontal up orientations produce bubbles that are more spherical in shape.

The behavior at higher levels of heat flux is opposite to that at lc, levels of heat flux in that the vertical and horizontal up orientations give higher heat fluxes than the horizontal down orientations, for a given ΔT_{sat}, as is shown in Fig. 2 of Ref. [25]. The explanation for this is probably related to an increase of the bubble population density. If the bubble population density is sufficiently high the interaction between the bubbles could reduce the relative effectiveness of the microlayer mechanism. Due to "crowding", the lateral bubble growth will be restricted, therefore the possibility of the formation of a microlayer could be reduced or eliminated.

To clarify these two phenomena at the lower and higher heat flux regions it is necessary to know how the active nucleation site density, maximum bubble departure sizes, and frequency of departures are influenced by gravity, orientation, heat flux, and the heater surface superheat.

Many different models have been proposed to provide an explanation and a correlation for the nucleate boiling phenomenon. The apparatus used in the present investigation permitted simultaneous determination of heat flux, maximum bubble diameter, active site density and frequency of bubble departure for a given surface liquid combination. Therefore only the following two models which take full advantage of these results are evaluated here.

1. Latent heat transport model

It was shown by Rohsenow and Clark [33] that for bubble radii greater than 10^{-7} ft the latent heat content, Q_B, of a bubble of volume V_B is given, to a good approximation, by

$$Q_B = V_B \rho_v h_v \tag{1}$$

with properties evaluated at the saturated state corresponding to the liquid pressure. Rallis and Jawurek [36] used Eq. (1) to write an expression for the rate of energy carried away from such a surface by the bubbles, as

$$\frac{Q_{NB}}{A_T} = \rho_v h_{fg} \sum_{i=1}^{n} f_i V_i / A \tag{2}$$

Equation (2) represents the latent heat transfer by the bubbles and strictly speaking applies only to saturated nucleate boiling. In terms of time averaged measurements and assuming bubbles are spherical in

shape Eq. (2) may be expressed as

$$\frac{Q_{NB}}{A_T} = \rho_\ell \, h_{fg} \frac{\pi}{6} \, D_{max}^3 \left(\frac{N}{A}\right) f \tag{3}$$

2. Vapor liquid exchange model

Postulated by Forster and Grief [37], it is assumed that heat transfer in nucleate boiling takes place by virtue of the exchange of a volume of liquid at the bulk temperature (T_b) for a volume of liquid at the wall temperature (T_T) each time a bubble departs or collapses. This model is expressed in terms of time averaged quantities by

$$\frac{Q_{NB}}{A_T} = \rho_\ell \, C_\ell \frac{\pi}{6} D_{max}^3 \left(T_T - T_b\right) \frac{N}{A_T} f \tag{4}$$

CHAPTER II

EXPERIMENTAL APPARATUS

The data obtained in the present study are heat flux, nucleation
site densities, bubble growth rates and departure size, frequency of
departures, and test surface superheats for the transient and steady-
state nucleate pool boiling in saturated liquid nitrogen and in Freon-
113 at standard and near zero gravity conditions.

In order to study transient and steady-state boiling heat transfer
in cryogenic liquids at standard and zero gravity, the experimental appar-
atus was designed and constructed to provide the following capabilities:

1. Zero or near zero gravity conditions.

2. A test surface large enough that it can represent actual
   surfaces.

3. An optical and lighting system that permits continuous high
   speed photography of the heat transfer surface under all
   conditions.

4. Instrumentation that permits recording the surface temperature,
   bulk liquid temperature, and heat flux rates accurately and
   continuously without any time delay for all circumstances.

5. A system capable of synchronizing and sequencing 6-7 events
   in any desired order.

6. A test dewar which can hold liquids having saturation tempera-
   tures ranging from -320°F to 120°F.

7. A test package with little or no vibration as the body changes
   from standard to zero gravity condition.

In the following paragraphs a detailed description of the apparatus used for the present study will be given.

A. DROP TOWER AND DROP PACKAGE

Zero gravity condition was obtained in the drop tower shown in Fig. 1. It has a free fall distance of 32 ft (9.75 m) corresponding to a free fall time of about 1.34 sec.

Figure 2 is a sectional view of the drop package and shows the deceleration method used. The drop package had four different sections: 1) release assembly, 2) piston assembly, 3) cylinder assembly, and 4) the spike-metering pin assembly. The drop package also serves as a container for the particular test vessel being used. It has space for a vessel or system having a maximum size of 19 inches diameter by 36 inches long. Prior to release the piston is extended as shown in Fig. 2. At the end of the free fall period the cone and spike penetrate a barrel filled with sand to decelerate the cylinder. The piston continues to move, compressing the air to a predetermined pressure corresponding to the maximum desired deceleration level. At this point a metering pin attached to the bottom of the piston assembly, which constitutes a variable area orifice, vents the air at a suitable rate to maintain the pressure approximately constant. At the appropriate position the metering pin closes completely to provide a final cushion of air.

A Kistler model 808 piezoelectric crystal accelerometer was mounted on the drop package to monitor the deceleration levels. Figure 3 shows a typical result. The maximum deceleration was 25 g's, which was acceptable.

Figure 4 shows typical results of the acceleration or body force measurements (a/g) made directly on the test package during free fall. A Kistler model 303 servo accelerometer was mounted on the top cover plate, from which the entire assembly is initially supported. The vibrations of the cover plate-support assembly occuring during release were picked up by the accelerometer. The mean readings of the test are plotted in Fig. 5 and show a maximum value of a/g=0.004 for the increase of the body force during free fall, due to air resistance. This is a 50% reduction of that reported in Ref. [29], and is attributed to the installation of an aluminum fairing around the spike to give an aerodynamic shape.

The elasped time for the free fall of 28 ft 7 inches was measured as 1.345 sec. The theoretical elapsed time of free fall in vacuum for the same distance is 1.335 sec.

The calibrated zero shown in Fig. 5 arises from computing the mean output signal between a/g=1 and a/g= -1 by assuming the output from the servo accelerometer to be linear with body force, which is a severe assumption over such a wide range of output. The zero value measured by extrapolating to zero time is believed to be more realistic.

B.   TEST PACKAGE

Figures 6 and 7 show the two different views of the test package. Figure 8 shows a sectional view of the test package, which has six major components:

1. Cover Plate: Because of weight limitations and the high vacuum sealing requirements for cryogenic temperatures, the 10 3/8 inch diameter inner section of the plate was made of stainless steel and the remaining of 20 1/2 inch diameter was made of aluminum. To reduce the vibration, the 1/2 inch thick cover plate is supported by two cross bars. The cover

plate serves as a main supporting base for all of the major components of the test vessel, and mounts in the open end of the piston assembly in Fig. 2.

2. Test Vessel Assembly: Two .065" thick wall concentric stainless steel cylinders with 6.0" and 8.0" I.D.'s, closed at one end, each having four 2" dia. observation windows, make up the test vessel assembly. These are bolted to the cover plate to complete the enclosure, and 1/2" thick pyrex glasses are used to make up four separate observation windows. In order to keep the heat transfer from surroundings at an acceptable minimum level when using liquid nitrogen, the space between the inner and outer cylinders is evacuated. The acceptable vacuum pressure for sealing was between 10^{-6} - 10^{-4} mm hg. It was reduced to that level by a dual vacuum pump and continuously monitored except during the relatively short drop test.

In order to seal the vacuum space at cryogenic temperatures, teflon coated stainless steel "o" rings, .01" thick wall, were used at the windows and flanges. To compensate for any variations of the contractions between the parts when the dewar filled with LN_2, two stainless steel spring washers were installed with each bolt.

3. Test Piece Housing Tube: A 2-7/8" dia. flanged stainless steel tube with 0.065" thick wall was used to hold two relay mirrors and the test piece at the desired orientation. It is bolted to the cover plate and has the necessary openings for lighting and observation, test fluid fill line, and thermocouple and power lines.

4. Optical System: A 200 watt mercury arc lamp, a spherical reflector, two lenses with 50 mm focal length, and a mirror with 1/4 wave length flatness constitute the illumination side of the optical system.

In order to be able to illuminate the total or part of the test section at desired intensities, the system is designed such that the light source, each lens and the mirror can be moved independently. The precision movement necessary was accomplished by four sets of 1/4" x28" threaded rods and a sprocket chain assembly. Lenses and mirror were moved up and down inside a snugly fit 3-1/4" dia., .065" thick wall aluminum tube housing. The mercury lamp is located at the focal point of the 2" dia. spherical reflector, which increased the available light intensity.

The viewing side consists of a 1/4 wave-length flat mirror, a lens having 160 mm focal length and a camera relay mirror. In order to compensate for any misalignment during manufacturing of the optical system, the camera relay mirror has complete freedom of motion in every direction. The viewing relay mirror and lens are made to move similarly to their illuminating side counterparts so that any desired magnification within the capacity of the system could be obtained.

To improve the stiffness of the total system and to provide that any vibrations occurring be in phase at the test surface, relay mirrors and lenses, the tubes housing the relay mirrors and lenses are bolted to the outer test dewar at the bottom.

5. Camera Assembly: A Nova camera model 16-3 was used for taking high-speed motion pictures. It is designed to withstand up to 25 g impact loads, and has a speed range from 100 pps to 10,000 pps in the 16 mm format. The camera receives its power from a Model 1002 AC power supply. Camera speed is controlled by adjusting the voltage setting on the power supply. The camera speed/voltage setting was selected by reference to the speed charts provided by the manufacturers. Two neon timing lights within the camera were provided to record timing marks on

each edge of the film. One is operated at 60 cycles and its markings were used to calculate actual film speed. A 90 mm Mikrolor close-up lense model 16-508 is used as the camera objective lens. In some instances a 1/2" to 1" extension tube was used with the close-up lens to obtain increased magnification.

The camera was mounted rigidly on a specially built support fixture, which was supported by two rails. The support fixture had the freedom to move in two directions in a horizontal plane along the rails and along the perpendicular direction to the rails.

A Honeywell Pentax 1°/20 exposure meter is used to determine the proper film exposure needed for different speed and lighting combinations. This meter was specially adapted for high-speed photographic works of up to 50,000 pps and has an angle of acceptance of 1°, which makes it ideal for the type of back lighting used in this work.

6. Support Assembly: The complete drop package is supported by an assembly of three 3/16" dia., 6x19 stainless steel ropes, a three-armed support fixture and a release rod. Stainless steel ropes connect the support fixture to the cover plate. Figure 6 shows the support assembly. The release assembly has a circular groove in which balls are held in place by an external ring tapered on the inside. When the ring is lowered remotely by an air cylinder the balls move out of the groove releasing the drop package.

7. Drop Cable Assembly: Three drop cables link the test package to the control area. The thermocouple outputs and test surface voltage connections are connected to the recorder via one of the drop cables made of eight 24 gauge copper and six 24 gauge constantan wires. This cable was double shielded to minimize noise pick-up. D.C. power to the test

surface was supplied via a second cable. The third cable is used to supply
the power for the camera, light source, and the synchronization signals to
the neon timing lights. The cables may be seen in Figs. 6 and 7.

C.   TEST SURFACE

Test surfaces used in studies of boiling heat transfer may be grouped
into two categories:

1.   Surfaces whose dimensions are in the same order of magnitude
of the size of the bubbles growing on them. Small wires and narrow
ribbons are examples of these types of surfaces.

2.   Surfaces whose dimensions are considerably larger than the
bubbles growing on them. For example, discs, cylinders and spheres of
relatively large dimensions.

The first group of surfaces are generally used when surface temper-
ature measurements are made using the surface as a resistance thermometer.
High speed photographs of the bubbles may be obtained simultaneously,
since the small size of the heater surface usually will not generate
enough vapor bubbles to obscure the field of view. The small size of
this type of surface always raises the question as to how well it repre-
sents the behavior of large size surfaces encountered in practical appli-
cations.

With the second group of test surfaces, the surface temperatures
are generally measured with thermocouples somewhat removed spacially from
the actual heat transfer surface, giving rise to the necessity of extra-
polating temperatures and introducing time lags when dealing with trans-
ient processes. When high speed photographs of boiling at the surface
are desired, the field of view is obscured by intervening bubbles. One

possibility is to use transparent surfaces such as glass or quartz and view the boiling process from underneath. This gives information as to the number of actives sites, the frequency of the bubble formation, and the departure sizes parallel to the plane of heating surface. A difficulty arises in transferring sufficient heat through the glass for boiling to occur because of the low thermal conductivity, and in measuring the temperature of the boiling surface.

The first difficulty has been overcome in several research efforts [34, 35] by using a glass surface with a thin transparent layer of SnO_2 baked on the surface which serves as the heat source when D.C. current is passed through it. This provides a large size surface with a uniformly generated heat flux at the surface. In one case the heating surface temperature was determined by measuring the lower surface temperature with an attached thermocouple and extrapolating to the upper boiling surface [34]. However, this technique will not give accurate results under transient conditions.

In the present research, efforts were made to find suitable electrical resistive materials which could be deposited as a thin film on glass, which would be semi-transparent for optical viewing purposes, and which could serve simultaneously as a heating element and a resistance thermometer with negligible time lag.

A number of materials, including nickel, SnO_2, platinum, aluminum, and gold were investigated. The most important properties necessary to assessing the material which will serve as a resistance thermometer and heater are as follows:

1. Temperature coefficient of resistance (TCR or α) defined by:

$$R(T) = R_0 \left[1 + \alpha (T - T_0) \right] \qquad (5)$$

with

$$\alpha = \frac{1}{R_0} \frac{dR}{dT}$$

where Ro = resistance at the reference temperature T_0.

2. Temperature coefficient of expansion (TCE or β) defined by:

$$L(T) = L_0 \left[1 + \beta (T - T_0) \right] \qquad (6)$$

with

$$\beta = \frac{1}{L_0} \frac{dL}{dT}$$

where L_0 is the length at the reference temperature T_0.

3. Transparency as a function of thickness.

4. Adhesion of the film to glass.

After extensive literature studies and testing, gold was selected as most suitable. It is stable, free from oxidation, readily vacuum deposited with reproducable resistance, has a relatively high temperature coefficient of resistance (TCR), and is sufficiently transparent.

Corning Pyrex glass surfaces were coated with a semi-transparent thin layer of gold and used as the test surface. The pyrex surfaces were first coated with an approximately 300-400 A. thick gold film by vacuum deposition, and then the ends were coated with a relatively thick layer of silver as a contact area for the power supply and voltage taps. Figure 9 shows the overall dimensions used here. Thickness of the thin film was monitored during the depositing process by means of a mass sen-

sitive crystal oscillator mounted adjacent to the test surface receiving the same rate of metal deposition as the glass surface. The measured natural frequency of the crystal was then a function of the metal thickness. This device was quite sensitive on a relative basis but did not provide an accurate measure on an absolute basis. Therefore several surfaces with different thicknesses of gold film were made and tested initially. The most suitable one was selected by comparing their TCR and transparencies. Thereafter the film thicknesses were maintained approximately constant on the various surfaces used.

Figure 10 shows the design of the current and potential connections which was determined to be the most effective by a process of development.

During preliminary calibrations, to be described shortly, it was observed that the resistance of the gold surfaces varied with time but that the slope dR/dT remains constant. The resistance change was attributed to an aging effect. Moeller's work [38] dealing with the use of gold as a resistance thermometer indicates that increasing the aging temperature (or annealing temperature) makes the resistance of the film much more stable, and specimens in that work were furnace soaked up to 1080°K for 24 hours. A similar effect was reported in Refs.[39,40]. Because of the use of pyrex as a substrate in the present application, such a high temperature was not possible. After experimenting, it was found that by tempering the thin films at 275°C for 15 minutes before calibration, the variation in resistance with time was reduced considerably.

Even after tempering at an elevated temperature to accelerate the aging process to a stable level, some shifting in resistivity with time took place at any given temperature level, always increasing but at a

much smaller rate, in such a manner that the slope dR/dT still remained constant. Several effects are believed to account for the increase in resistivity of the thin gold film even after the accelerated aging process. It is possible that the aging temperature used and the time of exposure for these gold films were not sufficient to provide the stable level. The usage and handling of these surfaces probably were causing a reduction of the thickness of the gold film which would account for the increase in resistance. It was found necessary to use an intermediate th. metallic element between the gold film and the pyrex during the process of fabrication in order to improve the adhesion. Impurities in the gold and change in the properties of the intermediate material could also account for these shifts.

The continuous aging process caused no difficulty since its effect was compensated by appropriate experimental techniques, which will be described later.

A total of about 30 test surfaces were used during this investigation, all demonstrating the same behavior i. that their resistivity changed with time but the slope dR/dT remained constant.

Figure 11 shows two complete calibrations of the test surface PCG-15 in LN_2 separated by an eight-month period of time. Also shown on the same figure are two sets of single point calibrations made immediately preceding and following a boiling test. The boiling tests lasted on the order of four hours, and no shift occurred during this period of time. The two sets of calibration made eight months apart were almost parallel. Similar results were obtained with the other test surfaces used in this work and are shown in Appendix D, along with the calibration of several other surfaces, obtained in the development of the gold film technique.

Since the variation in resistivity of the thin gold films was such that dR/dT remained constant, and because a complete calibration in LN_2 requires approximately four hours a complete calibration associated with each test was impractical. Once the complete calibration of a test surface had been made, it was deemed sufficient to make only a single point calibration prior to and following each test run.

Using the slight difference in slope of the two calibration curves in Fig. 11, it is possible to compute the error involved in the temperature measurements had only one complete calibration curve been mad, followed by a single point calibration eight months later assuming that the resistivity gradient had not changed in that time interval. It can be shown that the fractional error in the measurement of a temperature by such a procedure will be given by

$$\frac{\Delta T_{error}}{\Delta T_m} = \left[\frac{(dR/dT)_2}{(dR/dT)_1} - 1 \right] \tag{7}$$

where $\Delta T_{error} = T_{computed} - T_{actual}$

$\Delta T_m = T_{actual} - T_{single\ point\ calibration}$

$(dR/dT)_2$ = resistivity slope as measured at what is taken as a single point calibration

$(dR/dT)_1$ = resistivity slope as originally measured.

For the two slopes shown in the Fig. 11 the error will be

$$\frac{\Delta T_{error}}{\Delta T_m} = \left[\frac{0.0011267}{0.0011} - 1 \right] = 0.01505 \tag{8}$$

This means that the error will be 1.5% of the difference in the temperature between that to be measured and that of the calibration point. For

a temperature 20°F above the calibration point there would be an error
of 0.3°F.

During this investigation none of the tests conducted with the same
test surface were more than four weeks apart. In addition, for experiments
lasting more than four hours, three single point calibrations were made
one immediately prior, one after and one at the midpoint of the testing.

In the calibration curve resistances are presented in terms of
ohms/square, since this quantity is proportional to the thickness of the
film and is not a function of the geometry of the particular heating
surface used. Writing the total resistance as

$$R = \rho \frac{L}{Wt} \tag{9}$$

R = total resistance

ρ = specific resistivity Ω- cm

L = resistor length

W = resistor width

t = resistor thickness

The resistance in Ω/square is given by ρ/t in the expression above. In
thin films, the resistance is no longer necessarily proportional to the
bulk resistivity divided by the film thickness, so the resistance in
ohms/square provides a more meaningful description.

During calibration of test surfaces at different temperature levels,
the D.C. current levels were varied between 5 to 95 ma to assess possible
effects of current and self-heating. The heat fluxes corresponding to
this range are less than 2 Btu/hr-ft^2, which is negligibly small. Fig-
ure 12 shows the resistance of gold film surface PCG-6 for various cur-
rents. Even though data in this and similar subsequent tests indicated

that it was not necessary to vary the current in the calibration tests, as a standard procedure the resistances of the test surface for four different current levels ranging from 5 ma to 95 ma were measured and then averaged for each calibra·n point.

During calibration the electrical resistance of the test surfaces were measured using the circuit shown in Fig. 13, with the holder inserted in various fluids to provide different known temperatures. Test surfaces were calibrated in the vicinity of two different temperature levels; the saturation temperature of F113 at atmospheric condition (about 117°F), and the saturation temperature of liquid nitrogen (about -320°F). Calibration for the F113 temperature level was done in a constant temperature oil bath. To obtain the desired constant temperature a Colora Ultra-thermostat filled with silicon oil was used. Temperature level varied from 25° to 100°C. Temperature constancy of the bath for this range was $\pm$0.005°C. Liquid temperature was measured with a Leeds and Northrup platinum resistance thermometer (serial no. 1639550) with a sensitivity of $\pm$.001°C, along with Leeds and Northrup Muller bridge with an accuracy of $\pm$0.02%. Resistance of the test surface was determined from the voltage drop across the test surface, E_T, and across the .50274Ω standard resistance, E_s, see Fig. 13. Both E_T and E_s were read on a K-3 potentiometer.

Calibration of the test surfaces at the LN_2 temperature level was performed in the apparatus used in the work reported in Ref. [41]. The test pieces were inserted in a stainless steel dewar filled with liquid nitrogen, and the liquid saturation temperature was increased with an inserted heater. A calibrated 12 inch Heise Bourdon tube gage was used to measure the vapor pressure of the LN_2. The 25 psig range was divided into 0.1 psi

steps and had a calibration accuracy of ±0.025 psi. Barometric pres-
sures were measured with a mercury barometer. Pressure in the dewar
was controlled by a mercury switch with an accuracy of ±0.02 psi. LN_2
temperature varied from 136 to 170°R and was measured by a copper-con-
stantan thermocouple calibrated earlier. Readings of the pressure gage
are used to determine the deviation of the thermocouple readings from
NBS standards.

D.   POWER SUPPLY

Figure 13 shows the power and calibration circuit diagrams, and
consists of a 0.01 ohm standard resistance, a 0-16 ohm stepwise variable
resistance and an adjustable d.c. power supply, consisting of nine 12
volt, 72 amp. hour batteries which can be switched to provide 12, 24,
or 36 volts. For test surface calibrations, the same power circuit was
used except that the 0.01 ohm standard resistance was replaced by a
0.50724 ohm standard resistance, and the 0-15 ohm variable resistance
was substituted by a 0-2400 ohm variable resistance.

Since the requirements for steady current is so stringent with the
use of thin films, any variation in resistance with temperature of the
variable resistors which may be acceptable in normal applications could
not be accommodated here. Therefore the 0-15 ohms variable resistor
elements were constructed of chromel ribbon and kept immersed in approxi-
mately ten gallons of transformer oil in order to maintain a constant
temperature at the different levels of current. The 0.50724 ohm standard
resistor was also kept in the oil bath. The 0.01 ohm resistor has a
very large surface area but was installed in an insulated box to minimize
the effects of temperature drifts in the room. To minimize contact resis-
tances, large capacity copper knife switches were used throughout.

E. INSTRUMENTATION

To calculate the instantaneous heat flux values at different temperature levels, the voltage drop (E_T) across the test surface and (E_s) across the .01 ohm standard resistance, giving the current, are recorded on a Sanborn recorder. The thermocou.le outputs, which give the bulk liquid temperature, and the synchronization and timing signals were also recorded on other channels of the Sanborn recorder.

Since the thermoelectric power of the copper-constantan thermocouples varied from 16 μV/K at liquid nitrogen temperatures to 39 μV/K at Freon 113 temperatures, and a .05 ohm change in surface resistance corresponds to a 1°K change in surface temperature, it was necessary to use highly sensitive instrumentation. Figure 14 shows a view of the instruments, power supply, and synchronizing system.

F. THERMOCOUPLES

All the thermocouples used during the experiments and test surface calibrations were made of 30 gauge copper-constantan. Prior to use they were calibrated at saturation temperature levels of F113 and LN_2. For the calibrations above room temperature, the Leeds and Northrup platinum resistance thermometer described previously was used. The deviation* from the standard tables furnished by Leeds and Northrup was less than 6 μv in the 1900 μv range. This corresponds to a deviation of less than 0.1°K in the temperature range of 290-325°K. The procedure used to calibrate the thermocouples at the saturation temperature level of LN_2 was identical with the procedure used to calibrate the test surface at at the same temperature level. The deviation from NBS thermoelectric

---

* Deviation = $E_{standard} - E_{measured}$.

tables publications (123-A, R-188) was about 4.8 μv at 5734 μv range,
which corresponds to a deviation of about .22°K in the temperature range
of 60-80°K. In determining the liquid nitrogen temperature, this devia-
tion curve is used.

Three thermocouples were used to monitor the liquid temperature.
THC I was located about 10 cms below, THC II was located at the same
level, 1/2 cm away, and THC III was located at about 10 cm above the
test surface. The thermocouple outputs were connected to a recorder via
a drop cable consisting of 24 gauge copper wires and 24 gauge constantan
wires. To minimize the noise pick up, especially when operating at high
sensitivities, all thermocouple wires were double-shielded.

G. POTENTIOMETER

For the calibration of test surfaces, temperature and the Sanborn
recorder, a Leeds and Northrup K3 potentiometer with a Rubicon Model 3550
photoelectric galvanometer was used. The potentiometer has an accuracy
of $\pm 0.015\% + 0.5 \mu v$. Therefore measured temperature uncertainties
were $\pm .1°K$ and $\pm .04°K$ in liquid nitrogen and Freon 113, respectively.
To reduce the effect of any building vibrations, the amplifier for the
null detector system was suspended from the ceiling with soft springs in
the supports. A Honeywell series 3100 galvanometer indicated the un-
balance in the circuit.

H. SANBORN RECORDER

A 7700 series 8 channel Sanborn recorder was used to record the
thermocouple outputs, and voltages E_T and E_s in Fig. 13 as a function of
time. For recording thermocouple outputs and E_s the Model 8803 high
gain d.c. amplifiers were used. The chart speed could be varied from

0.25 mm/sec to 100 mm/sec in nine steps. In these experiments a chart
speed of 100 mm/sec was used. One second timing pulses were provided by
a timing marker. The high gain amplifier had a sensitivity range from
1000 μv/div to 1 μv/div. The thermocouple outputs were recorded
at a sensitivity of 5 or 10 μv/div., and V_s was recorded at a sensi-
tivity of 50 μv/div. The non-linearity of the recorder specified by
the manufacturer was .1% of the full scale output, that is $\pm.25 \mu v$,
$\pm.50 \mu v$ and $\pm 2.5 \mu v$ at sensitivities of 5 μv/div, 10 μv/div and
50 μv/div., respectively. The recorded non-linearity contributes an
uncertainty corresponding to less than $\pm 0.03°K$ in temperature readings
and about $\pm.0025$ amps in current readings. The preamplifier was capable
of following from 10% to 90% a step change in 5 milliseconds. With the
sensitivity of 50 μv/div used, the system would follow 400 μv/sec.,
which was more than adequate for the processes encountered during this
work.

I. SYNCHRONIZING AND SEQUENCING SYSTEM

Both light intensity and camera speed are adjusted before each run,
to compensate the effects of the variation of active site density, spread
velocity, bubble frequency on film quality. Camera speeds were varied
between 1750 to 5000 pps during the present investigation. A 100 foot
roll of film will cover a time interval between 2.71 and 1.1 seconds at
these camera speeds. As indicated before the maximum time available at
the 0-G condition was about 1.4 seconds. In addition to the limited
times available for the transient processes, steady state boiling at
standard and zero gravity are successively recorded on the same roll of
film. It was thus necessary that the thermal and photographic record-

inas of the various events and the controlled variables be carefully synchronized. A highly accurate and versatile synchronizing and sequencing system was designed and constructed.

Details of the sequencing and delay circuits for the various events such as starting the camera, releasing the test package for zero gravity operation, pulsing the synchronization signal to the camera and to the Sanborn recorder, and starting the boiling process are shown in Fig. 15. The complete circuitry consisted of five sub-circuits which are connected by a 3 PDT relay switch. The first circuit is the camera power supply and camera and event synchronizer. Its function is to start the camera and any desired event with a specified delay. The camera is started first and puts the 3 PDT relay switch in operation after a set time delay. The first pole of the relay switch, which is normally open, operates the test package release mechanism solenoid. The voltage across the relay solenoid is recorded on the Sanborn recorder. The second pole of the relay, which is normally closed, turns off one of the neon timing lights in the high speed camera. Since energizing the test package release solenoid and cutting off the neon timing light occur simultaneously, these two signals are used to synchronize the Sanborn recordings with the frames on the high speed film. The third sub-circuit operates this synchronizing neon timing light at a frequency of 1000 cps via the normally closed pole of the 3 PDT relay switch. The fourth sub-circuit is another time delay switch. This circuit has a nine step time delay ranging from 77 ms to 275 ms, and controls the test surface power circuit. The total surface power circuit consists of a 0.01Ω standard resistance, a variable resistance ($0-15\Omega$), an adjustable D.C. power supply (6, 12, 24 volt) and

the test surface. The voltage drop across the test surface, R_T, and across the standard resistance, R_S, are recorded on Sanborn recorder charts simultaneously. R_T indicates the test piece surface temperature, and R_S indicates the current in the circuit.

CHAPTER III

TEST CONDITIONS

A. FLUIDS

Two different liquids, liquid nitrogen and Freon 113, were used for the present research investigation. Liquid nitrogen was selected as a representative cryogenic liquid since it is chemically inert, readily available commercially, and has properties which are well known.

Freon 113 was chosen as the test fluid for experiments in the vicinity of ambient temperature levels. It is electrically non-conductive, reasonably chemically inert, considerably less hazardous than methanol or carbon tetrachloride, and its properties are reasonably well established.

B. PRESSURE

Most of the experiments were conducted with the liquid close to or at the saturation state. Due to interference by intervening bubbles in the optical path it was necessary to conduct several of the experiments with the liquid somewhat subcooled in order to obtain better photographs, particularly for steady conditions with the horizontal-up orientations. The saturation temperature at the heat transfer surface was obtained from available vapor pressure data for each fluid, using pressures calculated according to

$$P = \frac{d}{g} \rho h + P_{vapor} \tag{10}$$

All tests were conducted at atmospheric pressure so that in general $P_{vapor} = P_{atmospheric}$.

-33-

C. LIQUID TEMPERATURES

Bulk liquid temperatures were measured continuously by three copper-constant thermocouples at different vertical locations in the liquid. The temperature indicated by the thermocouple located at the same level but removed horizontally 1/2 inch aw.y from the test surface was used as the bulk liquid temperature. Prior to each run with F113, two 200 watt immersed heaters were used to increase the liquid temperature to its saturation level, nominally 117°F.

D. HEAT FLUX

For the steady state experiments four or five levels of heat flux were used at each orientation. Four different levels were selected so as to give a reasonable spread over a range, from the minimum level where boiling starts to a level close to burnout or to the heat flux where the bubbles are too numerous to permit adequate clarity of viewing. For some cases a fifth level of heat flux was selected such that boiling could not start, but could be sustained once initiated at a higher level of heat flux. In other words, after boiling was initiated the heat flux was reduced to a level where boiling was just barely continuing.

For the transient experiments three different levels of heat flux were used at each orientation. The lowest level was selected as that heat flux which would result in complete coverage of the test surface by boiling sites within 1.4 seconds of switching the power on. This time is dictated by the zero gravity period available in the drop tower. A second heat flux was selected close to burnout, and a third one at an intermediate point.

E. TEST SURFACES

Three different test surfaces were used during this study because of unplanned burnouts on two of the surfaces. As a result several of the tests were repeated with the different surfaces in order to observe if the nominally similar surfaces produced different results. This might occur due to differences in surface characteristics. In addition, for some orientations tests were conducted at heat flux levels other than those indicated above, depending upon the results of earlier runs.

F. ACCELERATION

Two levels of accelerations were used, $a/g=1$ and $a/g=0$. As indicated previously, it is not possible to claim that true zero gravity exists in the tests conducted here. Based on the measurements shown in Fig. 5, it is possible to state only that the body force present on the drop package increases after release from some small level to a maximum value of $a/g=.004$ during the 1.4 seconds.

Due to the short time duration at $a/g=0$, nominally 1.4 seconds, it was not possible to determine decisively whether true steady state boiling existed at the end of the period, regardless of whether boiling existed at the beginning of the free fall period or was initiated during the free fall period. Two types of disturbances are used in this research which can result in transients: a step change in heat flux and a step decrease in body force.

The transient arising from a reasonably large step change in heat flux is quite obvious, both at standard gravity and at reduced gravity, and these processes are referred to as transient boiling processes. For the purpose of identification the process of a step reduction in body

force taking place with prior boiling is referred to as steady state boiling at zero gravity, even though this process is also transient in the strict sense. This terminology is justified on the basis that a seemingly steady value of temperature was present within a short time after release of the test package. Whether these results would correspond to those obtained with long term reduced gravity, say on the order of hours duration, can be answered only with experiments of long duration at reduced gravity.

A summary of the ranges of the variables are given in Table 2.

Table 2. Summary of Range of Experimental Conditions

LIQUIDS	F113			LN$_2$		
$(Q/A)_T$ Heat Flux Btu/Hr-ft^2	1500 - 30000			300 - 30000		
Orientation	Vertical	Horizontal up	Horizontal down	Vertical	Horizontal up	Horizontal down
Gravity	a/g = 1	a/g ≈ 0		a/g = 1	a/g ≈ 0	

CHAPTER IV

TEST PROCEDURE

Preliminary tests were conducted to establish a/g, the body force level on the test package during free fall, the deceleration level upon impact at the end of the free fall, and to check the optical and thermal recording systems. The tests for a/g and deceleration levels were performed only once, but the optical and thermal recording systems were checked before every run.

A. FILLING THE DEWAR

After preliminary tests were completed, the dewar was filled through specially provided lines. The depth of liquid in the test vessle was needed in order to calculate the hydrostatic pressure at the test surface which in turn was used to obtain the saturation temperature.

The depth of liquid nitrogen above the test surface was measured approximately, by means of four resistor type liquid level indicating sensors located at different levels. The locations were such that it was possible to determine the LN_2 level within 2.5 inches, and it was always kept between 15-17.5 inches above the test surface.

The depth of Freon 113 was calculated by measuring the amount of Freon 113 put into the dewar before the start of a particular series of experiments. Depending upon the orientation of the test surface the dewar was filled with 4 or 5 liters of F113, which gave between 5-7" of liquid height above the test surface. At the end of the experiments the amount of liquid remaining in the dewar was measured. The variation in liquid level for any series of runs was always less than 1".

B.   CALIBRATION

Once the dewar was filled, a calibration procedure was followed prior, during, and following each test. This included calibration of the thermocouples and the test surface at the prevailing temperature of the liquid, and of the recorder. If the series of experiments took more than two hours, single point calibration of the test surface was performed three times; prior to, at the middle and at the end of the experiments. For series lasting less than two hours, single point calibration of the test surface was made twice; immediately before the start of and after the end of the experiments.

The output of the thermocouples in the saturated liquid was measured with a potentiometer and used to find the deviation of the thermocouple output from the standard tables, assuming the deviation of the thermocouple outputs to vary linearly from the liquid temperature to the reference temperature (ice bath).

For each recorder channel used, the amplifier gain was calibrated by supplying a known input from the potentiometer and observing the corresponding deflection on the recorder. After each amplifier was calibrated, the appropriate zero suppression was applied again using the potentiometer as the signal source. After zero suppression the amplifier gain was checked once more. In addition, recorder outputs were checked against the potentiometer before and after each run.

C.   CAMERA AND LIGHTING ADJUSTMENT

Prior to the start of a series of experiments, the test surface was illuminated at the desired intensity by adjusting the light source and illuminating lenses. Then the camera, relay mirrors, and viewing lenses

were adjusted for focusing and desired magnification. After focusing,
the camera and relay mirrors were secured on their supports to prevent
any motion due to impact and vibration. Then the liquid was heated to
its saturation temperature corresponding to the pressure at test surface,
and boiling was initiated at the desi.ed heat flux level. While boiling
continued, the light intensity at the test surface was measured with a
light meter, and the correct camera speed was determined for an f/2
aperture opening. The camera close-up lens was always set at its maximum
aperture opening (f/2), which provided the largest surface coverage for
a given magnification. Then camera power supply voltage was set for
the desired camera speed. Camera speed was not critical as long as it
was greater than 1500 pps.

D.   SEQUENCING AND DELAY

For a selected camera speed the approximate running time for 100
feet of film was obtained from speed charts supplied by the manufacturers.
For experiments at steady state conditions the event and camera synchron-
izer, (see Fig. 15), was set to start the camera first, and then operate
the test package release mechanism at about 1.4 seconds before the end
of the film, thus making it possible to photograph both 1-G and 0-G
boiling on the same roll of film. The timing signal generator was turned
on, and neon lights in the camera were checked for proper operation.

After settings, adjustments, and calibrations were completed, a
trial run was conducted at a low recorder speed (5-10 mm/sec) to check
for proper operation, including signal connections, sequencing and zero
suppressions. The film was then installed in the camera, the observation
window removed, the test package lifted and connected to the release

mechanism, the liquid brought to its saturation temperature, and power
turned on manually with enough time allowed to establish steady state
boiling. Steady state test conditions were considered to have been
reached when the outputs of E_T and E_s reached a constant level and
remained there. At this point the one second timer was turned on,
recorder speed was increased to 100 mm/sec, and the event synchronizer
was put in operation with a remote control button, sequencing the events
as planned. The camera starts first, and at an appropriate time the
release mechanism is actuated, which releases the test package for 0-G
condition with about a 10 millisecond delay. The instant of release is
marked on the recorder chart by a signal provided by a dry cell in the
package release circuit, and a corresponding signal is recorded on one
of the film edges by turning off one neon signal light.

For experiments with transient boiling, the synchronizer operated
in a similar way with the additional function of turning the power on
according to the pre-set sequencing schedule. The recorder is started
manually, and the camera and event synchronizer is activated by remote
control, which in turn starts the camera, releases the test package,
registers the synchronizing signals on both the film and recorder, and
finally turns the power on at a set time.

The release signal on the recorder and the synchronization signal
on the film are recorded about 10.3 milliseconds apart, and are used to
synchronize the film frames with the thermal recordings.

After the run was completed at impact the package was hoisted back
into position, and the film removed and marked with an identifying num-
ber. For each run the above operations were repeated.

CHAPTER V

DATA REDUCTION

In these experiments, as in all measurements, errors are associated with determinations of test surface temperature, bulk and saturation liquid temperatures, heat flux, site density, bubble frequency, and the maximum bubble size. The detailed calculation of the related uncertainties in these quantities is given in Appendix B. In the following sections the methods used for calculating these quantities are described.

A. TEST SURFACE TEMPERATURE (T_T)

Test surface temperature was determined from the measured test surface resistance, R_T, the single point calibration resistance R_c, and the corresponding temperature T_c, and the slope of a calibration curve, $m = dT/dR$, according to the equation

$$T_T = T_c + m\left(R_T - R_c\right) \tag{11}$$

The values of E_T and E_s were obtained from the recorder charts using appropriate zero suppression and the sensitivity value at which the recorder was operated.

The level of the zero-suppression applied was varied for each test dependent upon the E_T and E_s range and the sensitivity of the recorder. Sensitivity of the recorder was selected such that all variations during the various types of experiments (transient, zero gravity, etc.), could be recorded in the linear range available on the recorder chart with a minimum of noise pickup. Test surface voltage drops E_T were recorded by a low gain amplifier, at a sensitivity of 0.005 volts/div. and standard resistance voltage drops E_s were recorded by a high gain amplifier,

with 50 μv/div. sensitivity. The standard resistance R_s was .01 ohm for all cases.

As explained in Appendix B, the values of R_T, R_c, T_c and dT/dR were determined with uncertainties of $\pm$.051%, $\pm$.033%, $\pm$.028% and $\pm$1.46%, respectively. Therefore, wall temperatures were determined with an uncertainty of $\pm$1.33°F for the worst case with F113. For liquid nitrogen the uncertainty was less than $\pm$1.68°F for the worst case.

It should be emphasized here that since the resistance of the total surface area is measured, the corresponding temperature represents only the mean temperature over the entire area. This mean will differ from the representative surface temperatures only in those cases where highly localized differences in behavior occur, such as during the spreading of nucleate boiling across the surface.

B. BULK LIQUID TEMPERATURE (T_ℓ)

Bulk liquid temperature was measured by copper-constantan thermocouples, using both the K3 potentiometer and the recorder. The Sanborn recorder was operated at a sensitivity of 5 μv/div. The maximum uncertainty in the bulk liquid temperature was $\pm$.076% corresponding to less than $\pm$.09°F for the worst case.

C. SATURATION TEMPERATURE IN THE TEST SURFACE (T_{sat})

The saturation temperature of liquid at the test surface was deduced from the pressure at that location. Pressure at the test surface was obtained by adding hydrostatic pressure at the test surface to local atmospheric pressure. The main source of error in determining saturation temperature came from uncertainty in the liquid depth. The uncertainty

in the liquid level was less than ± 1 inch for F113 and ± 2.5 inches for liquid nitrogen, corresponding to $\pm .18°F$ for F113 and $\pm .05°F$ for LN_2.

D. HEAT FLUX

The heat flux to the liquid at the heat transfer surface in the steady case was calculated from the total power generated on the surface, subtracting the heat transfer to the glass substrate.

$$
\begin{aligned}
(Q/A)_\ell &= (Q/A)_T - (Q/A)_{loss} \\
&= \frac{E I}{A} - (Q/A)_{loss}
\end{aligned}
\qquad (12)
$$

Since the test surfaces were kept in a snugly fitted teflon holder, heat losses through the edges are neglected. For steady state runs heat transfer to the glass substrate in F113 and LN_2 is obtained from the curves given in Fig. 16 and 17, respectively. These curves were generated from the solution of the heat transfer problem shown on them, involving boiling, conduction, and convection. The uncertainty associated with total heat flux measurements were less than $\pm 1\%$. The uncertainty in values of $(Q/A)_{loss}$, comes from the uncertainty associated with determination of wall temperature and uncertainty associated with natural convection correlations, the latter contributing the most.

E. ACTIVE SITE AND POPULATION DENSITY

The active site density and average population density were determined from the 16 mm high speed motion picture films, using a Vanguard motion analyzer. The active site density is the number of active nucleating sites per unit area present under the given conditions. The average population density is the average number of bubbles present on the surface per unit area at any given time. During the growth period, which

is also called the active period, a bubble will be present at the site. No bubble is present at the site during the waiting period, and thus the population density is always less than the active site density. After the film was threaded on the analyzer the synchronization signal was brought onto the screen and the frame counter was set to zero. The release of the test package takes place about 10-11 ms after the release signal, corresponding to 20-55 frames for film speeds of between 2000-5000 pps. Pictures after these 20-55th frames pertained to zero gravity boiling, while all earlier ones pertained to standard gravity boiling.

Each frame of the film corresponding to a/g=1 was studied carefully by running the film on the analyzer backward and forward until all the active sites for standard gravity were located. After site counting at standard gravity was completed, the zero gravity part was analyzed. Since bubbles stay on the surface and continue to grow under zero gravity conditions, they coalesce as they grow, covering some of the sites on the surface, and the short time at zero gravity makes it impossible to determine all the active sites at zero gravity. Therefore only the newly activated sites were located and counted. The number of additional new sites activated during 0-G was added to the total of active sites counted during the 1-G condition. A new total was thus obtained and used to calculate the active site density for the 0-G conditions. Therefore, the active site density values for 0-G are always larger than for 1-G condition. It is not possible to state that all the sites active at 1-G would continue to be active at 0-G, but as may be seen in the experimental results in Fig. 79, for example, the surface temperatures are higher at 0-G than 1-G for a given heat flux, and it thus seems reasonable to assume that all the sites active at 1-G would therefore remain active at 0-G.

More than 50% of the surface area was photographed and enlarged more than 50 fold on the analyzer, and every frame of the 100 foot roll of film was viewed independently. For one test run the film was analyzed by three individuals at different times. The maximum variation in the active site density between the three results was less than 7%. It is assumed that the portion of the surface photographed was representative of the total test surface.

Population densities were obtained from 20 arbitrarily selected frames of the film. In each of these randomly selected frames the number of bubbles attached to sites were counted. The average of the randomly selected 20 frames was used to calculate the average population density. To find the representativeness of the sample size selected, average population densities were determined for 5, 10, 20, 30 arbitrarily selected frames from the same runs. The variation between using 5 and 10 frames was ±6%, the variation between using 10 and 20 frames was ±2.3%, the variation between using 20 and 30 frames was ±.75%. In order to keep data reduction time as low as possible and still obtain accurate results, 20 frames is chosen as a basis to determine the population site density.

F. BUBBLE FREQUENCY

The period of the cycles between bubble emissions was determined by a detailed examination of the films projected on the analyzer screen. Depending upon the heat flux levels, the fraction of the total active sites that were used for determination of the bubble cycle period varied between 10-95%. This variation was dictated by two factors. At high heat flux levels so many active sites existed that it became impractical to follow each site. Secondly, the increase in the number of total sites

with high heat flux reduces considerably the number of sites where the bubble growth period can be followed for at least one complete cycle, because of the periodic obscuring of portions of the surface.

In the determination of bubble frequencies, the growth of a single vapor bubble at each site was followed frame by frame. The time intervals between bubble initiation, departure, and the initiation of the next bubble at the same site were obtained. The elapsed time between initiation and departure of the vapor bubble was called the active period, and the time from departure to initiation of the next bubble was called the inactive period. For each site analyzed, bubble growths are followed for at least 2 or 3 cycles until variations in the periods were reasonably well determined. The average cycle length was used as the period for that site. The frequency of vapor bubble emission was obtained by taking the reciprocal of this quantity. Figure 18 shows a typical bubble appearance, growth and departure in LN_2 at standard gravity. The smallest diameter plotted corresponds to the frame in which the bubble first appeared. This means that the growth initiated some time in the interval of the previous frame. An inherent uncertainty thus exists in the origin of the growth period. This is discussed in Ref. [46].

G. BUBBLE SIZE

The departure and the maximum diameter attained by the vapor bubble while attached to the heat transfer surface was measured,along with the bubble periods, from the films projected on the analyzer screen. The photographed area was enlarged 50-60 times on the screen, corresponding to a 7-8 power linear magnification. The film was again analyzed frame by frame and when the diameter of the vapor bubble attached to the sur-

face reached a maximum size it was measured in two mutually perpendicular directions by means of crosshairs on the analyzer, using a scale graduated in thousandths of an inch. The average value of these two measurements was taken to be the maximum bubble diameter. Measurements of bubble sizes were taken for at least 2 or 3 consecutive periods to determine the variation in measured diameter, and to obtain better accuracy by reducing the chance of missing the maximum bubble size if it had been attained in the interval of time separating two consecutive frames.

Two 46 gauge wires, spaced nominally .1 inch apart, were visible in the field of view for every run. The precise spacing was measured by a traveling microscope each time the test surface was installed.

H. TRANSIENT PERIODS

Two built-in neon lights were used to record timing and synchronization marks on the edges of the film. In the transient runs, power was turned on automatically about 54.6 ms after the synchronization signal was recorded, as indicated by turning off one of the neon lights. The actual film speed was calculated from the recorded 60 cps signals on the second edge of the film.

Figure 19 shows a typical representation of the transient surface temperature behavior occuring with a step change in heat flux. The various domains are believed to represent distinct physical phenomena taking place and are defined as follows:

τ_1 - is the time delay between the beginning of power input and onset of natural convection. It is thus the elapsed time in the conduction dominated regime.

$\mathcal{T}_{IB}$ - is the elapsed time between the beginning of power
input and the inception of the first boiling site as ob-
served on the photographs.

$\mathcal{T}_2$ - is the elapsed time in the convection dominated regime,
and is terminated when the surface temperature begins to de-
crease because of the spreading of nucleate boiling.

$\mathcal{T}_1$ + $\mathcal{T}_2$ - is the elapsed time between the beginning of power
input to the maximum surface temperature.

$\mathcal{T}_3$ - elapsed time from T_{max} to the end of spreading of
nucleate boiling over the surface.

$\mathcal{T}_s$ - represents the elapsed time from beginning to the end
of the spreading of nucleate boiling over the surface.

$\mathcal{T}_1$ + $\mathcal{T}_2$ + $\mathcal{T}_3$ - represents the total elapsed time from the
step power input to the completion of the boiling spread over
the test surface.

$\mathcal{T}_1$ values were obtained from thermal recordings of V_T or from T_T
vs time plots as in Fig. 20, which presents data obtained with a verti-
cal orientation in F113 at standard gravity, for various levels of heat
flux. $\mathcal{T}_1$ is an approximate value since the rate of increase in the
surface Temperature T_T does not change sharply with the onset of convec-
tion. It tapers down slowly.

$\mathcal{T}_{IB}$ values were obtained from the films. Since only 50-80% of the
area of the test surface was photographed $\mathcal{T}_{IB}$ values could not be ob-
tained with the same accuracy for all cases. The symbol "IB" in Fig. 20
indicates the point at which the first nucleating site is activated.
When boiling was initiated outside the observed viewing area exact values

of T_{IB} were not obtainable. Values for those cases are taken as the time of appearance of the first bubble, thus giving values of T_{IB} larger than may actually exist.

T_2 values were not determined alone. Instead the sum of $T_1 + T_2$ values are measured. If T_2 values were needed these can be obtained by subtracting T_1 from $T_1 + T_2$. $T_1 + T_2$ were determined from the Sanborn recordings. Power was turned on 64.9 msec. after the Sanborn synchronization signal. Recorder speed was always kept at 100 mm/sec. $T_1 + T_2$ values were obtained by counting the number of divisions from power on to the point that surface temperature reached a maximum value.

T_3 values were determined from the thermal recordings. It corresponds to time between the time when surface temperature reaches its maximum value and the end of spread of boiling . τ_s values were determined from photographic films by observing the time between the beginning and the end of the spread of nucleate boiling. In addition to the spread times, T_3 and T_s, the rate of boiling spread over the surface can be represented by the percent area covered by active sites versus time values and by determining the spread velocity. The fraction of the surface area covered by nucleating sites is obtained by dividing the area covered by active sites at a given time by the total photographed area. Typical photographs of the spread of the active sites are shown in Figs. 95 and 96 of Appendix C.

Spread velocity values, V_s, are obtained in two steps. The distance traveled by the bubble front from the starting point in two different directions were obtained and plotted against time. The average spread velocities are then obtained by averaging the slopes of these curves.

Total delay time values, $T_1 + T_2 + T_3$, were obtained by counting the timing signals from the frame where power was turned on to the frame whose surface was covered completely by the active bubble sites. This quantity was also independently obtained from the thermal recordings by observing the variation of test surface temperature, as may be seen in Fig. 20. The variation between these two results for the majority of cases was not more than a few percent, with the temperature results giving larger values. This was reasonable since it was not possible to photograph the total area of the test surface, and the spread of boiling may have continued beyond the observed area. This unobserved part of the boiling was reflected in the thermal recordings.

CHAPTER VI

RESULTS AND DISCUSSION

In this section, the results of the experimental measurements are
presented and discussed under two main headings: Transient and Steady
State Boiling Heat Transfer. These are presented in the form of graphs
showing the influence of heat flux, orientation gravity and in some
cases surface roughness on boiling heat transfer in F113 and LN_2. An
index of all tests conducted is presented as Appendix F.

A. TRANSIENT BOILING HEAT TRANSFER RESULTS

During the transient part of the process between the step power
input and the point where the surface is completely covered by active
boiling sites, three distinct regimes of heat transfer mechanisms were
observed: the conduction, convection and boiling dominated regimes.
The elapsed time in each regime varied depending on the heat flux, orien-
tation, body force and liquid used, which constitute the independent
variables. The dependent variables are the transient test surface
temperature, the various defined delay periods, the spread velocity, and
the fractional coverage of the surface by nucleating sites.

At the outset of this study, it was anticipated that the timewise
activation of nucleation sites as the boiling spread over the surface
would be determined. However, in viewing the films it appears that once
nucleation takes place in a particular region, the boiling spreads by
a process in which a vapor layer grows within the superheated liquid
layer adjacent to the heating surface. Once the vapor front has passed
a particular region, removing the superheat in the liquid, surface ten-

-52-

sion forces then result in the formation of bubbles and the normal nucleate boiling process follows. During the spreading of the vapor layer it was thus not possible to discern active nucleating sites.

1. Test Surface Temperature Results

Transients of the test surface temperatures are presented in the form of plots of surface temperature, T_T, versus time with levels of heat flux, orientation, body force, and the liquid used as parameters. Figures 20-23 and 24-27 depict the transient surface temperature results obtained with F113 and LN_2, respectively. The effects of heat flux, orientation, reduction of the gravity and different surfaces are presented in these figures. Figure 28 shows the transient wall superheat for both F113 and LN_2 for the vertical surface at $a/g=1$.

These all show a definite wall temperature overshoot, ΔT_0, as has been observed elsewhere [5,6,8-11]. The results reported in Refs. [8-11] should be considered most comparable since step increases in power inputs were used.

It appears that the amount of the step increase in heat flux has some effect on the degree of overshoot. Variation of ΔT_0 with heat flux for vertical surface in F113 and LN_2 can be seen in Figs. 20 and 24, respectively. These results along with others are replotted as ΔT_0 vs. $(Q/A)_T$ in Fig. 29 for convenience, where the increase of ΔT_0 as heat flux increases is more clearly noted. Similar results, the increase of ΔT_0 with increasing heat flux, have been observed in transient boiling studies with water [6].

On the other hand, Ref. [8] reports diminishing overshoot with increasing heat generation rate. Also, Refs. [8] and [11] report no sur-

-54-

face temperature overshoot with saturated boiling, which is contrary to the results of the present study and Refs. [9], [10]. These discrepancies could be due to the differences in surface roughness and heat capacity of the surfaces used, and the sensitivity of the temperature measurements. As will be discussed later, surface roughness has a pronounced effect on ΔT_0: smoother surfaces result in a higher degree of overshoot in order for bubble nucleation to take place. Since no information about the surface roughnesses is given in Refs. [8,11], it is not possible to assess this effect. Furthermore, an insensitivity of about $\pm 5°K$ in temperature measurements was reported in Ref. [8]. A narrow chromel ribbon 1/16 inches wide cemented to a bakelite block served as the heater in Ref. [11], and temperatures were measured by three thermocouples attached to the underside of the chromel strip. No information is given about the method of attachment and the accuracy of the temperature measurements, which give only local temperatures at the points of attachments. In addition to the possible inaccuracies and time delays in the temperature measurements, it was not possible to substantiate a conclusion of "no overshoot at saturated boiling" from Fig. 3 of [11], where transient surface temperatures for 45°, 23° and 6° subcooling are shown.

As reported in Ref. [8], the lack of observation of any temperature overshoot in Refs. [8] and [11] could be attributed to the heat capacity of the test surfaces used. Metallic ribbons were used as a heating surface, with a volumetric heat generation compared to a virtual plane heat generation with the thin gold film in the present investigation. Thus, for a given power input, the rate of temperature rise of the ribbons will be lower than that of the thin gold film even with the

presence of the glass substrate, which has a relatively low thermal diffusivity. Transient effects in the liquid may thus be masked by transients in the heater surface, in the case of solid metallic surfaces.

Transient surface temperatures with the vertical, horizontal-up and horizontal-down orientations at $a/g=1$ are presented in Figs. 20, 22 and 23 for F113 and in Figs. 24, 26 and 27 for LN_2. Since different test surfaces are used in the experiments with F113, comparison of Figs. 20, 22 and 23 to determine the effect of orientation on ΔT_0 must be made with caution. On the other hand, surface PCG 29 was used in the experiments with LN_2 for all orientations, and the results presented in Figs. 24, 26 and 27 can be compared to determine the effect of orientation on ΔT_0. For convenience, the ΔT_0's are replotted vs $(Q/A)_T$ in Fig. 29. Figure 29 indicates that the effect of heat flux on ΔT_0 is more pronounced with horizontal-up orientations and the vertical than the horizontal-down orientations. At the lower heat flux levels the highest ΔT_0 occurs with vertical surfaces, while at the higher heat flux levels, ΔT_0 is highest with the horizontal-up orientations. ΔT_0 is lowest for horizontal-down orientations for all heat flux ranges except at one data point. This discrepancy may be related to the surface temperature oscillations which occurred during that run, as may be observed in Fig. 27.

These differences observed between ver. cal and horizontal-up orientations may be due to variations in the non-boiling convective heat transfer arising with these orientations. Convective heat transfer is higher with horizontal-up than vertical orientation. Therefore, for a given heat generation rate a larger heat transfer rate will occur by

conduction and convection with the horizontal-up orientation. This difference is more significant at the lower heat generation rates and results in a lower ΔT_0 for the horizontal-up orientation. On the other hand, the differences in convective heat transfer with orientation do not effect the outcome at the higher heat generation rates because as heat generation rates are increased the transient periods get smaller, and eventually a point is reached where boiling starts even before convective currents are initiated.

As indicated in Figs. 23 and 27, for F113 and LN_2, respectively, the transient surface temperatures at higher heat flux levels behave differently with the horizontal down orientation than with the horizontal up and vertical up orientations. With the inception of boiling the surface temperature drops sharply. However, since the vapor generated is held against the heater surface by buoyant forces the surface temperature increases until the trapped vapor escapes from the edges of the heating surface, at which point the surface temperature reduces sharply as boiling again takes place when liquid comes into contact with the heater surface. The process then repeats itself.

This periodic coverage of the surface with vapor slugs is observed in the photographic films, and is in synchronization with the thermal recordings. At highest heat flux levels ured here the surface temperature drops somewhat with the inception of boiling, but the vapor generation rate is so rapid that the surface becomes continuously covered with vapor slugs, causing the surface temperature to increase sharply toward the burnout point, as is noted in Fig. 27.

The effect of reduced gravity on the surface temperature transients is shown in Figs. 21-23 and 25-27 for all three orientations in F113 and LN$_2$, respectively. The level of ΔT_0 is considerably reduced with a reduction in gravity for the horizontal up and vertical orientations, but is virtually unchanged with the horizontal-down orientation. With the inception of boiling at zero gravity the surface temperature begins to decrease but then the generated vapor bubbles remain on the surface, preventing any further drop in surface temperature and eventually causing the surface temperature to increase, as shown for example in Fig. 21. Since the vapor bubbles are held against the surface by body force with the horizontal down orientation at a/g=1, reduction of gravity has little effect other than the elimination of the oscillation in the surface temperature created by the periodic escaping of vapor slugs at standard gravity.

As Figs. 21, 23, 25 and 27 illustrate, a continuous increase in surface temperature occurs for the horizontal down orientation at both a/g=1 and a/g=0, while this occurs only at a/g=0 for the other orientations, indicating the invariance of the results with orientation at zero gravity. The high speed photographs show that bubbles stay on the surface at zero gravity, at least for the period of the observation in these experiments. This would tend to reduce heat transfer from the surface to the liquid which, for an imposed heat flux, leads to an increase in surface temperature, as is noted in Figs. 23 and 27.

Though not as pronounced as the temperature overshoot, a temperature undershoot is observed in some cases in Figs. 20-26. Different speeds of recovery to the steady state values may be noted. Similar

observations of temperature undershoot have been reported [6,7, and 11].
At the initial inception of boiling, it is believed that the higher sur-
face and liquid film superheat activates more sites than the steady
state boiling can sustain, and the surface temperature reduces below
the steady state temperature for the given heat flux. The number of
active sites then reduces and the surface temperature rises to the steady
state level.

The transient surface temperatures of two different test surfaces,
PCG 23 and PCG 29, for the vertical orientation with F113 are plotted in
Fig. 20. The temperature overshoot of PCG 29 is higher than the over-
shoot of PCG 23. This is more apparent in Fig. 29 where the results
are plotted in the form of ΔT_o vs. $(Q/A)_T$. The only difference in the
experimental conditions for these two sets of data was the roughness of
the surfaces used. The pyrex substrate of PCG 29 was polished before
being coated with the thin gold film whereas the substrate of PCG 23
was coated as it came. The effect of polishing is indicated by the RMS
profilometer readings, which varied between 1.6-2.0 microinches for
PCG 23 and .09-.1 microinches for PCG 29. Thus, the surface temperature
overshoot is larger with smoother surfaces than rougher ones. This is
reasonable, if the profilometer surface roughness measurements provide
an indication of cavity sizes influencing the nucleation characteris-
tics. As will be shown below, smaller cavities require higher surface
temperatures to become active nucleating sites.

The transient surface temperature for both LN_2 and F113 are com-
bined in Fig. 28 for the same surface, PCG 29, with the vertical orien-
tation. For a given heat flux not only the temperature overshoot but

the steady state surface superheat as well are higher with F113 than with LN_2. A comparison of the temperature overshoot between two fluids may also be made in Fig. 29.

The differences of ΔT_{sat} with F113 and LN_2, and also with PCG 23 and PCG 29 for F113 can be explained on the basis of the relationship between ΔT_{sat}, the surface characteristics, and the liquid properties. Assuming that a vapor nucleus trapped in a cavity is hemispherical in shape and has the same radius as the cavity, it is possible to calculate the superheat necessary for the nucleus to grow from the cavity, using the analysis as presented by Hsu [43]. The pressure difference between the vapor within the bubble and the surrounding liquid is given by

$$P_v - P_l = \frac{2\sigma}{R_c} \tag{13}$$

The Clausius-Clapeyron equation relates the vapor pressure to the physical properties as

$$\frac{\Delta P}{\Delta T} = \frac{h_{fg}}{T(V_f - V_v)} \tag{14}$$

Combining Eq. (13) and (14), and assuming that $V_v \gg V_f$ will give the minimum superheat necessary for a hemispherical vapor bubble to grow.

$$\Delta T_{SAT} = T_l - T_{SAT} = \frac{2\sigma T_{SAT}}{R_c h_{fg} \rho_v} \tag{15}$$

Equation (15) can be used to explain qualitatively the effect of surface roughness and the different liquids on ΔT_{sat} and ΔT_0. Since the cavity radii are not known, and the surface used in the experiments most likely do not contain cavities of a uniform size, Eq. (15) cannot be used for a direct check.

Equation (15) shows that, for a given fluid and heater surfaces having different roughness, the heater surface superheats necessary for the initial formation of vapor bubbles should be inversely proportional to the prevailing cavity sizes, as

$$\frac{(\Delta T_{sat})_1}{(\Delta T_{sat})_2} = \frac{(R_c)_2}{(R_c)_1} \tag{16}$$

Assuming that the profilometer RMS values of roughness are indicators for R_c for the two surfaces, and substituting the mean measured RMS values for R_c

$$\frac{(\Delta T_{sat})_{29}}{(\Delta T_{sat})_{23}} \cong \frac{1.8}{.09} = 20 \tag{17}$$

The numerical result given by Eq. (17) can only be interpreted as an indicator, and has no meaning other than indicating that smoother surfaces require higher superheat for the inception of boiling. This can account for the larger overshoot observed for the surface having the smaller RMS profilometer readings, PCG 29, in Fig. 20.

Equation (15) also can be used to compare $\Delta T_{sat}(T_{IB}-T_{sat})$ required for inception of boiling with F113 and LN_2. The ratio of the heater surface superheats necessary for the initial formation of vapor with the two fluids is given from Eq. (15) as

$$\frac{(\Delta T_{sat})_{F113}}{(\Delta T_{sat})_{LN_2}} \cong \left(\frac{\sigma\, T_{sat}}{h_{fg}\rho_v}\right)_{F113} \bigg/ \left(\frac{\sigma\, T_{sat}}{h_{fg}\rho_v}\right)_{LN_2} \tag{18}$$

Substituting the appropriate properties into Eq. (18) gives

$$\frac{(\Delta T_{sat})_{F113}}{(\Delta T_{sat})_{LN_2}} = \frac{(16.07)(527)}{(63.2)(94.35)}\bigg/\frac{(8.82)(140)}{(85.6)(50.4)} = 5.48 \tag{19}$$

Inception of the first site is shown by the symbol IB in Fig. 20, and was determined from viewing the high speed photographs. These indicate

that boiling is initiated before the surface temperature reaches its maximum value. In other words, $(T_{IB}-T_{sat})$ is less than ΔT_o $[=(T_{max}-T_{sat})]$. Figures 30 and 31 are plots of $T_{IB}-T_{sat}$ vs. heat flux for F113 and LN_2, respectively, and illustrate the effects of heat flux, orientation, gravity and surface roughness on superheat for incipient boiling. These indicate that $T_{IB}-T_{sat}$ is effected only by surface roughness and the liquid used, which is consistent with Eq. (19), which predicts that the superheat is five times higher with F113 than with LN_2 for inception of boiling. The experiments indicate that the superheat with F113 is 3-4 times higher than with LN_2. Considering the approximations made for the derivation of Eq. (15) this is very reasonable agreement.

In an approach similar to this, a value of 9.4 was calculated for the ratio of superheat required for the inception of boiling in LN_2 and LH_2 (liquid hydrogen) [41]. The experimental values of this ratio varied between 2.3 and 9.1, depending upon the surface polish. Polished copper surfaces gave results closer to the calculated values than polished stainless steel or 600 grit steel surfaces, supporting the results obtained in the present research.

2. Delay periods

In this section, the experimental results related to delay periods T_1, T_{IB}, $(T_1 + T_2)$, T_3, $(T_1 + T_2 + T_3)$, percent boiling area coverage and boiling spread velocities are presented and discussed in chronological order.

1. Delay period, τ_1:

This period is the conduction dominated regime. The predicted temperature rise of the gold film during this period is plotted in Fig. 32 and 33 from Eqs. (48) and (49) of Appendix A, for F113 and LN_2, respectively, along with the experimental values obtained. The derivation of these equations, which are solutions of the problem of two semi-infinite solids with a step increase in a plane heat source at the boundary of these two solids, is given in Appendix A. The difference between the predicted temperature rise and the experimental value increases with time, the experimental temperature being below the predicted values. The linearity of the experimental data and the good comparison at small times indicate that heat transfer is in the conduction regime during the early time periods.

The next process which occurs in a gravitational field prior to the inception of boiling is the onset of natural convection. The detailed analysis of the theoretical relations predicting the delay time for the onset of natural convection as a function of heat flux for the horizontal up and vertical surfaces are given in Appendix A.

Equations (54) and (55) in Appendix A are the theoretical relations predicting the onset of natural convection for the horizontal up orientations in LN_2 and F113, respectively, for a given critical Rayleigh number, Ra=800. The theoretical relations with critical Ra numbers of 1100 and 1700 are tabulated in Table 4 in Appendix A. As described in Appendix A, a critical Ra=800 corresponds to a constant wall heat flux while Ra=1100 and 1700 correspond to constant wall temperatures with free and solid upper boundaries, respectively. Assuming that the end of the conduction period marks the beginning of natural convection, it is

possible to compare the experimental results showing its variation with heat flux with those predicted by the equations tabulated in Table 4 in Appendix A. These are shown in Figs. 34 and 35 for F113 and LN_2, respectively, for horizontal up orientations. The agreement appears to be quite good. The experimental results in both Figs. 34 and 35 fall between the two theoretical relations obtained using the critical Rayleigh numbers of Ra=800 and Ra=1100. This is reasonable, since the boundary conditions in the tests conducted in the present study are neither constant wall temperatures nor constant heat flux in a strict sense. This result provides further indication for the existence of a conduction dominated regime for horizontal up orientations. The existence of a convection regime prior to boiling has been observed elsewhere [11, 42]. In a photographic study with a horizontal up orientation, columnar instabilities rather than the classical Benard cells were observed [11]. Using five different liquids, it was established that free convection begins after the critical Rayleigh number of 1700 is surpassed [42].

Equations (57) and (58) in Appendix A are the theoretical relations predicting the onset of natural convection for vertical orientations in LN_2 and F113, respectively. Figures 36 and 37 show the comparisons between the experimental results obtained with vertical orientations in F113 and LN_2 with those predicted by the theoretical equations (57) and (58), respectively. In both cases, the agreement is reasonably good for the lower levels of heat flux. As heat flux is increased, the experimental values deviated from the theoretical predictions more and more. For both liquids, the experimental values were always lower than the predicted results, and may be anticipated on the basis of the following: As explained in Appendix A, the transition from conduction to convection

on a vertical surface begins only when some effect from the leading edge
is propagated up the plate to the particular point in question. Before
this leading edge effect has propagated to that point, the region ef-
fectively does not know that the plate has a leading edge. Therefore,
the delay time τ_1 in Eqs. (58) and (59) is the total time necessary for
the convection to be established over the entire surface. It is the
elapsed time necessary for the disturbance coming from the leading edge
to reach the upper edge of the surface. Convection at a point begins
when the disturbance coming from the leading edge reaches that point,
and with the transient heating process taking place, a reduction in the
rate of increase of the surface temperature may take place before the
delay time has reached the maximum possible value, corresponding to the
vertical height of the surface, due to the increased heat flux being
carried away by convection. The experimental values presented in Figs.
36 and 37 correspond to that time when the rate of increase in the
average surface temperature begin to reduce, and the experimental values
of τ_1 are less than predicted, as expected. In addition, as the heat
flux level is increased, boiling may start before convection has become
established over the entire surface. When heat fluxes are sufficiently
high, the surface temperature may rise so rapidly that boiling is es-
tablished before any convection can take place. This is probably why
the existence of a convection dominated regime was not observed in some
experimental works [2,8]. Heat flux levels in the range of 10^5-2×10^6
BTU/HR-FT^2 were used in experiments with water [2,8], which goes above
the burnout heat flux, whereas the heat flux levels were kept below the
burnout point in the present experiments and varied between 3×10^3-1.5×10^4
BTU/HR-FT^2 with LN$_2$ and F113.

11. Delay period for inception of boiling, $\mathcal{T}_{IB}$:

$\mathcal{T}_{IB}$ is the time elapsed from a step change in heat flux to the appearance of the first bubble. Figures 38 and 39 illustrate the effect of heat flux and gravity on the elapsed period, $\mathcal{T}_{IB}$, for vertical surfaces in F113 and LN_2, respectively. The results indicate that $\mathcal{T}_{IB}$ decreases with increasing heat flux and with reduction of gravity. The difference in the $\mathcal{T}_{IB}$ values at a/g=1 and a/g=0 become less as heat flux increases. One might expect that at sufficiently high heat fluxes the body forces no longer will have an effect. These effects are related to the amount of energy available to heat the liquid film adjacent to the test surface and can be explained as follows:

Hsu and Graham [42, 43] have postulated and experimentally verified that a bubble will not grow until the liquid surrounding the bubble nucleus is warmer than the equilibrium superheat temperature as given by Eq. (15). Thus, the delay time $\mathcal{T}_{IB}$ depends on the transient growth of a very thin thermal layer adjacent to the heating surface. As heat flux increases, the liquid film temperature increases more rapidly and $\mathcal{T}_{IB}$ becomes smaller. Similarly, with the reduction of gravity convection effects are reduced or eliminated, and more energy is available to heat the liquid film adjacent to the surface. As heat flux increases, the delay time shortens and the effect of convection is reduced, and the effect of gravity on $\mathcal{T}_{IB}$ thus becomes smaller.

The values of $\mathcal{T}_{IB}$ for a vertical surface in F113 and N_2 at a/g=1 and a/g=0 are presented in Fig. 40 along with the delay times for the onset of spreading of nucleate boiling. The delay time, $\mathcal{T}_{IB}$, is considerably shorter with LN_2 than with F113. Although the thermal diffusivities of both liquids are similar, F113 requires a heater surface

superheat about five times larger t an LN_2 for the inception of boiling, accounting for the longer delay time with F113.

The flagged symbols in Fig. 40 are the delay times from the step input in power to the beginning of spreading of the active boiling sites, as observed in the high speed photographs. Boiling initiates first at a few sites, and the increase in the number of active sites on the surface does not take place until an additional delay period. These additional delay periods are the differences between the flagged and unflagged symbols in Fig. 40. The surface superheat, when spreading begins, is higher than the incipience of the first sites. This phenomena occured only with LN_2. With F113, the spread of boiling sites immediately followed the appearance of the first bubble site. It is also observed in the photographs that the inception of boiling on vertical surfaces begin at t' per edge and penetrates downward. This can be seen in the film samples shown in Fig. 95 of Appendix C. As discussed earlier, convection occurs at the upper part of the test surface at a later time, which allows the liquid boundary layer near the upper edge to be heated to a higher temperature than that below. In addition, the liquid film temperature in the upper parc is always higher due to the upward motion of the convection currents. Therefore, boiling may be expected to begin preferentially at the upper side of the surface provided that the cavity size distribution is uniform over the entire surface. On horizontal surfaces, boiling is observed to begin near the center of the test surfaces and spread outward. Vest and Sweeney [44] showed, using holography, that the liquid temperature is highest at central locations for a heated horizontal surface facing upward, which explains the fact that the ini-

tiation of first boiling sites takes place at the central part of the test surfaces facing upward.

iii. Delay period for maximum surface temperature, (T_1 + T_2)

The test surface temperature rises at its highest rate during the conduction period, and tapers off with the onset of convection. It tapers off further with the activation of the first few nucleating sites, but still continues to increase until a certain percent of the area is covered with active boiling sites. T_{IB} is the delay time from the power input to the activation of first site, and (T_1 + T_2) is defined as the delay time from the power input to the point where surface temperature reaches its maximum value. These are compared for various levels of heat flux on Figs. 41 and 42 for a vertical surface with F113 at standard and zero gravity, respectively. These indicate that the surface temperature continues to rise even after the activation of the first nucleating site. This is also shown in Fig. 20 where activation of the first site is identified by the symbol "IB". Actually, as shown in Figs. 95 and 96 in Appendix C, the test surface temperature continues to increase until enough sites are activated such that the heat transfer by conduction, convection and boiling is equal to the power input. (T_1 + T_2) depends on: (1) the rate of increase of temperature on the nonboiling portions of the heat transfer surface and (2) the rate of spreading of the active sites. The surface temperature as measured is a mean value, and it is determined from the total resistance of the surface. The surface resistance at any time is equal to the sum of the resistance of the boiling part R_B and the resistance of the nonboiling part R_{NB} of the surface. A relationship between the boiling and non-

boiling surface temperatures and the boiling and nonboiling surfac :
areas can be found for the condition when the surface temperature reaches
its maximum value. The relation is given by Eq. (81) in Appendix E,
which indicates that the surface temperature continues to increase until
a certain percent of the area is covered by active sites.

Figures 43 and 44 show the effects of heat flux and gravity on
($T_1 + T_2$) for surfaces in F113 in the horizontal up and horizontal down
orientatians, respectively. As Figs. 41-44 illustrate, ($T_1 + T_2$) de-
creases a $(Q/A)_T$ increases. The difference between the energy gen-
erated and the heat transfer by conduction and ...nboiling convection
becomes larger as $(Q/A)_T$ is increased. This in turn increases surface
temperature at a faster rate and b.ings the liquid film superheat to a
boiling level sooner.

Figure 43 and comparisons of Figs. 41 and 42 show that reduction in
gravity reduces ($T_1 + T_2$) for the vertical and horizontal up surfaces.
Comparing Figs. 41-44 also shows that ($T_1 + T_2$) is shortest for the
horizontal down orientation. The reduction of gravity has an effect
similar to that of rotating the surface to the horizontal down orien-
tation in that the convection part of the heat transfer is reduced or
eliminated. Therefore, as may be seen in Fig. 44, ($T_1 + T_2$) does not
vary significantly from a/g=1 to a/g=0 with the horizontal down orien-
tation. The explanation for the effect of gravity and orientation on
($T_1 + T_2$) is similar to that given for T_{13}, and is due to the influ-
ence in convection effects.

Behaviors similar to these occurred with LN_2 although the values
of ($T_1 + T_2$) are considerably shorter. These are shown in Figs. 51-53,
along with other delay times to be discussed shortly.

iv. Spreading periods, τ_3 and τ_s:

τ_3 is the elapsed time from the point when surface temperature reaches its maximum value to the time when spreading of nucleate boiling over the surface ends. τ_s is the elapsed time from the beginning to the end of spreading of nucleate boiling over the surface. For most cases the difference is negligibly small. Since, as explained before, surface temperature continues to increase after spreading started τ_s is always greater than τ_3.

The starting point, direction and velocity of boiling spread vary depending on heat flux, orientation, liquid media and the test surfaces used. Figures 45 and 46 are plots of heat flux versus elapsed time, τ_3, for F113 with vertical and horizontal up orientations, respectively. τ_3 values for LN_2 for various orientations are shown in Figs. 51-53. They show the effect of gravity and $(Q/A)_T$ on τ_3, which decreases with increasing $(Q/A)_T$ and reduction of gravity. Increasing $(Q/A)_T$ increases the rate of heating of the boundary layer, producing more superheat which, in turn, speeds the activation of the sites on the surface. Reduction of a/g decreases the convection heat transfer, which also increases the rate of heating the boundary layer of sites, and thus also reduces τ_3.

Figures 59-61 and 62-64 show the effect of heat flux and gravity on τ_s for various orientations in F113 and LN_2, respectively. In terms of the relationship between time and the fraction of surface area covered by nucleate boiling, as observed from the high speed photographs. These will be considered further shortly. The effects of heat flux, gravity and orientation on τ_s in LN_2 are similar to the effects in F113. The difference is that values of τ_s are smaller with LN_2 than F113, i.e. for vertical orientation with $(Q/A)_T = 2800$ BTU/HR. $(\tau_s)F113/(\tau_s)LN_2 = .13/.03 = 4.33$.

As Eq. (18) indicates for a given cavity size about one fifth the superheat is needed in LN_2 as compared to F113 for a bubble to grow. This may be the reason for the faster spread of active sites in LN_2 than in F113.

v. Delay period ($T_1 + T_2 + T_3$):

For some thermal systems, particularly nuclear reactors, the elapsed time between the initiation of power input and the complete coverage of the test surface by boiling sites could be very critical. This period is represented by $T_1 + T_2 + T_3$. Figures 47-49 show the effect of heat flux, gravity and surface roughness on the total elapsed time, $T_1 + T_2 + T_3$, for each orientation with F113, while Fig. 50 is a composite plot of the results presented in Figs. 47-49. Figures 47 and 48 indicate that the total delay time decreases with increasing heat flux and with reduction of gravity for the vertical and horizontal up orientations. While reduction of gravity has a considerable effect on the total delay time with the horizontal up and vertical orient tions, its effect with the horizontal down orientation is insignificant in Fig. 49. This phenomena is more apparent in Fig. 50, which also indicates that at a/g=0 the total delay time is insensitive to orientation. Figures 47-50 also indicate that a reduction of gravity has less and less influence as heat flux is increased. Since the total delay time $T_1 + T_2 + T_3$ is the sum of the individual components T_1, T_2 and T_3, the explanation for the effects of heat flux, gravity and orientation on the total delay time is the same of that given for the individual components, and is due primarily to the increased rate of heating of the boundary layer resulting either from the increased $(Q/A)_T$ or the decreased nonboiling convection effects.

Experimental results of the total delay time obtained with LN_2 are presented in Figs. 51-53 for each orientation at a/g=1 and a/g=0. These include plots of ($T_1 + T_2$) and T_3 for LN_2, which were discussed earlier in connection with F113. The general results are similar to effects observed with F113.

The total delay time results obtained with LN_2 and F113 at a/g=1 for each orientation are presented in Figs. 54-56 for comparison. Results obtained at a/g=0 for all orientations are presented together in Fig. 57. These figures indicate that the total delay time in F113 is about 5-6 times that for LN_2 at any given heat flux. The difference in the total delay time in LN_2 and F113 is most likely due to the property diff rences of surface tension, latent heat and saturation temperature which gave rise to differences in ($T_1 + T_2$) and T_3.

Both ($T_1 + T_2$) and T_3 are larger for F113 than for LN_2.

A rapid decrease in the total delay time with increasing heat generation rate was also reported for water [8], and is plotted with the results of the present study in Fig. 58. Comparisons between these are tenuous due to the differences in the test surfaces and liquids, but the linearity of log-log scale indicating exponential relations is interesting, and perhaps can be exploited for estimating purposes.

3. Percent area coverage and spread velocity

Figures 59-61 show the spreading of active sites over the test surface as the percent area covered versus time, at a/g=1 and a/g=0 for three orientations in F113. As heat flux is increased and gravity is reduced the boiling sites activate at a faster rate and the test surfaces are covered by active sites in shorter time. Comparison of Figs. 59-61 in-

dicate that a reduction of gravity has the highest effect in reducing the area coverage time with hor*.ontal up orientation and lowest effect with horizontal down orientation, with a reduction in this effect occuring as heat flux increases. This is consistent with the relationship between natural convection and T_3 discussec previously.

The percent area coverage by active sites along with the delay time for inception of boiling in LN_2 at a/g=1 and a/g=0 for the vertical and horizontal up orientations are shown in Figs. 62 and 63, respectively. Percent area coverage for the horizontal down orientation is shown in Fig. 64. Increasing the heat flux has similar effects on the spreading of active sites in LN_2 and F113, in that T_s decreases. The effect of gravity on the boiling spread is more pronounced with F113 than with LN_2. In fact, upon close examination of Figs. 62-64, one can say that reduction of gravity has no effect on either the incipient boiling point or the rate of formation of active nucleating sites. If this is a general characteristic of cryogenic liquids, this could have significance in future research directions connected with heat transfer for space applications. After the inception of first site boiling spreads *: LN_2 at a faster rate than in F113. The effect of orientation on boiling spread is more pronounced with F113 than with LN_2. The explanation for the effect of $(Q/A)_i$, gravity and orientation on the boiling spread is similar to that given for T_3, and is due to increased heating rate of the boundary layer by either the increased heat flux or reduced convection effects.

Comparison in the rate of spreading with the two test surfaces PCG 23 and 29 in F113 may be made in Fig. 59 for the vertical orient: ion. Comparison between PCG 24 and 29 with the horizontal down orientation

may be made in Fig. 61. Profilometer RMS values for PCG 29, 23, and 24
are between .09-.1, 1.6-2.0 and 3.0-10.0 microinches, respectively.
As shown in both Figs. 59 and 61, after the inception of the first site,
additional boiling sites activate or spread at a faster rate on the
smoother surfaces. This is as might be expected. According to Eq. (15),
smoother surfaces, which are presumed to have smaller cavities, require
higher superheats for the inception of boiling, thus raising the test
surface temperature to a higher value, which in turn speeds the spread
once boiling is initiated.

The effect of heat flux and gravity on T_{IB}, (T_1 + T_2),
T_1 + T_2 + T_3 and percent area for a vertical surface in F113 are
shown together for convenience in Fig. 65. The arrows on Fig. 65 indi-
cate the percent of the surface area covered by the active sites at the
delay periods T_{IB} and (T_1 + T_2). The percent area covered by active
sites at the delay time (T_1 + T_2) increases with heat flux and with
reduction of gravity. Up to elapsed time (T_1 + T_2) the surface tem-
perature increases and after this time the surface temperature decreases.
The slope of the curves is a measure of the rate of boiling spread,
which increases with increasing heat flux and with a reduction in gravity.

The average velocity at which the spreading of nucleate boiling
took place was determined from the high speed photographs. Two direc-
tions are chosen from the point at which the initial bubble forms, one
corr. ponding to the maximum rate of spreading, the other the minimum
rate of spreading. The spreading speed in these two directions are then
averaged. The spreading speed in any direction is not constant but
varies from region to region, giving a large deviation from average
values. Figure 66 shows the average boiling spread velocity for all

orientations in F113, at a/g=1 and a/g=0, and Fig. 67 shows the corresponding results for LN_2. These can be used for qualitative purposes only, however, because of the relatively large variations observed, which are represented, typically, by the vertical dotted lines in Fig. 66. The spread velocity is faster with LN_2 than F113 and, for a given heat flux, the spread velocity increases with reduction of gravity. In Figs. 66 and 67, the darkened symbols correspond to a/g=0 for the same orientation, at a/g=1 represented by the open symbols. In all cases, both fluids and all orientations, the darkened data points lie above the open ones, indicating that the spread velocity increases with reduced body force. The explanation for this effect was given before with the discussions of T_3, T_s and the percent area coverage. Since the spread velocity is related to T_s, which is the boiling spread time, the same factors govern both.

B. STEADY STATE NUCLEATE BOILING HEAT TRANSFER RESULTS

In the steady state part of the present study the following parameters were measured: 1) heat flux, 2) test surface temperature, 3) active site and population density, 4) bubble frequency, and 5) maximum bubble size. The step power input, body force (gravity) and the liquid used were independent variables. The results are discussed under the related headings. Comparisons between some of the existing nucleate boiling models with results of the present work are also included in this section.

1. Heat Transfer Results

The heat transfer results are presented in the form of plots of heat flux versus superheat for different orientations and body forces. Figures 68-70 show the heat transfer results obtained at $a/g=1$ and $a/g=0$ for the three orientations in F113. They also include the natural convection correlation equations for comparison purposes. The effect of the various orientations are compared in Fig. 71 for $a/g=1$ and in Fig. 72 for $a/g=0$. Figure 73 is heat flux versus ΔT_{sat} for LN_2 and illustrates the effects of both orientation and body force on nucleate boiling heat transfer.

Experimental results obtained with two different surfaces, PCG 23 and 29, at about two months apart are presented together in Fig. 68 for the vertical orientation and in Fig. 70 for horizontal down orientations. The consistency of these results, which were obtained with different surfaces at different times, demonstrate the reproducibility of the data.

Figure 71 indicates that, for a given ΔT at lower levels of heat flux, the horizontal down orientations provide the highest heat flux, the horizontal up provide the lowest, and the vertical orientation falls between, for F113 at $a/g=1$. Similar results were obtained with LN_2 and are presented in Fig. 73. These results showing the effect of orientation are consistent with the results of Refs. [24-28], which also show that results obtained with the thin gold films compare well with those obtained with conventional metal heat transfer surfaces such as ribbons and discs [24-28]. Figure 2 of Ref. [25], in which a copper disc was used as test surface, is replotted in Fig. 74 for comparison. The var-

iation in heat flux with orientation for a given ΔT is believed related to the effect of "microlayer evaporation" at the base of the bubbles. At the lower levels of heat flux, with the horizontal down orientation buoyant forces tend to hold the vapor bubbles closer to the surface, thus increasing the size of the microlayer. With the horizontal up orientation the buoyant forces tend to decrease the size of the microlayer trapped beneath the vapor bubble, thus decreasing the heat flux for a given heater surface superheat. This is consistent with the experimental observation by Hospeti and Mesler [32] that heat transfer associated with a hemispherical bubble is greater than that with a spherical bubble, due to the larger microlayer trapped with hemispherical bubbles than the spherical ones. Due to the buoyant forces, the horizontal down orientation tends to produce hemispherical bubbles while the horizontal up position favors spherical bubbles.

Experimental results for all three orientations in F113 and LN_2 consistently fall above natural convection correlations, Figs. 68-71, 73. Photographic results indicate that boiling was present for all data points shown in these figures, and since the heat flux is higher with nucleate boiling than with natural convection, this is to be expected. The lowest data points in Figs. 68 and 70 are results obtained with induced boiling as indicated. The induced boiling points correspond to such low heat flux levels that a step increase to that level does not result in nucleate boiling on the test surface, but once boiling has been initiated at a higher heat flux level, it continues when the heat flux is reduced to that level. This procedure for obtaining boiling at lower heat flux levels is an example of the hysteresis effect, which

moves the boiling curves toward left (e.g. Ref. [47]). Figure 71 indicates that the horizontal down orientation requires the lowest heat flux to sustain the induced boiling and the horizontal up requires the highest. This is related to the effect of natural convection heat transfer, discussed in Section A-2 for the transient process.

As indicated in Figs. 68-70, for a given heat flux the boiling surface superheat increases with the reduction of gravity from $a/g=1$ to $a/g=0$ for the vertical and horizontal down orientations, whereas it decreases with the horizontal up orientation. Reduction of gravity reduces or eliminates the natural convection effects, and it might be expected that the nucleate boiling performance should be independent of orientation. That this is the case is illustrated in Fig. 72 for F113, where heat flux versus surface superheat is plotted for all orientations at $a/g=0$.

2. Test Surface Superheat Results

Figures 75-79 are plots of surface superheat versus time for the different constant levels of power input and the various orientations used with F113 and LN_2, and show the transient surface temperatures during the transition from steady state at $a/g=1$ to the lower gravity level, $a/g=0$. It is possible that a new true steady state condition is not yet reached during the 1.4 second free fall period, but examination of the surface temperature behavior in any of the Figs. 75-77, for example, would appear to support the idea that a new steady state is reached even within such a short time. The experimental results of surface temperatures at $a/g=0$ presented in Figs. 68-73 were obtained from such plots as Figs. 75-79, and show that surface superheat increases with a reduction of gravity for vertical and horizontal down orientations (see Figs.

75, 76). The effect of reducing the gravity drastically becomes more pronounced as the heat flux is increased. As illustrated in Fig. 78, when the heat flux is high enough at a/g=0, the surface temperature increases continuously toward the burnout point. Similar results were reported by Littles [24] in experiment. with F113 at atmospheric pressure, in that an increase in surface temperature occured with the vertical and horizontal down orientations, and a decrease occured with the horizontal up orientations as gravity was reduced from a/g=1 to a/g=0.01. Figure 77, where surface superheat versus time for the horizontal down orientation is given, illustrates that the surface temperature fluctuations caused by escaping vapor bubbles from the sides at a/g=1 are damped by a reduction of gravity to a/g=0, and reappear when standard gravity condition is resumed after the impact. The different behavior of the test surface temperatures with reduction of gravity for the various orientations are caused by combinations of several phenomena: 1) reduction of gravity reduces or eliminates the convection heat transfer, increasing the rate of energy transfer by boiling alone which, in turn, increases the ΔT_{sat} necessary. 2) As shown in Fig. 98 in Appendix C, which is a typical sample of high speed photographs of steady state boiling at a/g=0, departure of vapor bubbles from the vicinity of the heating surfaces ceases shortly after gravity is reduced from a/g=1 to a/g=0, and the bubbles remain on the surface and continue to grow there. Vapor bubbles remaining in the vicinity of the heat transfer surface behave as thermal insulators, and thus the test surface temperature increases. 3) The third phenomena may be a succeeding consequence of the first two effects. As the surface temperature increases, sites with smaller critical radii become activated. The addition of new active sites then decreases the

average test surface temperature, as was discussed earlier with regard
to transient boiling. 4) The reduction of gravity from a/g=1 to a/g=0
makes the bubble shapes similar for the different orientations, during
the growth period, because of the elimination of the buoyant forces.
The bubble shapes become more hemispherical for all orientations at
a/g=0. Thus, the microlayer trapped under the growing vapor bubbles
increases with a reduction of gravity where this hemispherical shape is
promoted. The maximum increase occurs with the horizontal up orienta-
tion, where bubbles growing at a/g=1 are primarily spherical. The in-
creased microlayer area means more rapid liquid evaporation, and a higher
rate of heat transfer resulting in a larger surface temperature drop.
The net results of these opposing phenomena depends on the initial orien-
tation at a/g=1.

3. Active Site Density and Bubble Population Results

Figures 80 and 81 present the results of the photographic study in
which the active site densities in nucleate boiling were determined for
F113 and LN$_2$, respectively. The results are presented in the form of
plots of active site density versus heat flux for a/g=1 and a/g=0 and
for the vertical, horizontal up, and horizontal down orientations. The
active site densities shown represent the number of nucleation sites
per unit area which were observed to be active during the entire length
of the film. Included for reference on Fig. 80 are the approximate
burnout, minimum incipient and induced boiling heat flux values. Figures
81 and 82 present the average population densities along with the active
site density for LN$_2$ and F113, respectively. The average population den-
sities represent the average of the bubble populations on the surface at

any given instant of time. The vertical bars on each data point indi-
cate the observed variations associated with each of the mean values.
It is noted that the active site densities are always larger than the
average population density. This occurs because of the fact that at
any instant of time a number of the active sites may be in the "waiting"
period.

The results of present investigation shown in Figs. 80-82 indicate
that the active and population site densities increase considerably with
heat flux. The linearity of the plots indicates the existence of an
exponential relation between the active site density and heat flux such
as

$$\frac{N}{A} = \text{CONSTANT} \left(\frac{Q}{A}\right)^{a} \qquad a \gg 1 \qquad (20)$$

The relationship between heat flux and active nucleation site density has
been noted by numerous investigators, observing that increasing the heat
flux results in the activation of additional nucleating sites in order
to facilitate the transfer of the additional heat. The results of West-
water and Kirby [45] for carbon tetrachloride boiling on an artificially
roughened oxide coated glass surface and the results of Judd and Merte [34]
for F113 boiling on a smooth oxide coated glass surface are shown in Fig.
83, along with the results of the present work, for purposes of comparison.
It is noted that a considerable discrepancy exists between the present
work and that of Judd and Merte [34](for a given heat flux Ref. [34]
reports an active site density four times as large) even though a smooth
glass surface was used in both cases. This discrepancy could reflect
the difference in the coatings used, a vacuum deposited gold film in the
present case as compared to a fixed oxide coating in [34]. The discrep-

ancy could also be due to procedural differences used in determining the site densities. Figure 97 is a representative series of high speed photos taken during the course of the present research for steady state boiling on a vertical surface. These show that the distribution of sites is not uniform over the surface. Therefore, depending upon the section of the area chosen for site counting, the results could vary manyfold. In the present work, as explained before, measurements were made over 50-80% of the surface, whereas in Ref. [34] only approximately 3% of the test surface was viewed for determination of the site densities. It is possible that the sample size used in Ref. [34] was not large enough to provide a meaningful result for the site density.

In addition to the effects described in the above, Figs. 81-82 indicate that even though the change is not large, the active site density increases slightly with a reduction of gravity, while the population density decreases slightly with a reduction of gravity. The increase of N/A is to be expected, if the heat transfer per site remains constant, or if it does not increase enough to compensate for the increase of heat transfer by boiling, owing to the elimination of convection heat transfer accompanying the reduction of gravity from a/g=1 to a/g=0. On the other hand, the decrease in population density could result from the inaccuracy in the determination of n/A at a/g=0. Since the bubbles stay and grow on the surface at a/g=0, neighboring sites may become covered by the adjacent growing bubbles, preventing an accurate count of the sites active at any instant of time.

Figures 80 and 81 indicate that orientation, like gravity, do not appear to have large effects on the active site densities. The active site density is slightly larger with the horizontal up orientation and

slightly lower with the vertical orientation. This could be related to the microlayer effect. Bubbles generated on surfaces at the horizontal up orientation generally are more apt to be spherical in shape, and thus have a minimum microlayer contribution, and each bubble results in less heat transfer. Therefore, for a given heat flux more active sites may be required with the horizontal up orientation. On the other hand, as noted in Fig. 80, the active site density for the horizontal down orientation is slightly higher than for the vertical orientation, which seems contradictory to the argument given above. Since bubbles generated on the horizontal down surfaces are more apt to be hemispherical in shape, and thus have larger microlayer contribution, each bubble should contribute more to the heat transfer. For a given heat flux fewer active sites should therefore be required with the horizontal down orientation. On the other hand, for a given heat flux a reduction of convective heat transfer increases the rate of energy transfer by boiling. It is therefore possible to increase the active site density, provided that the heat transfer per site and the frequency of departure remain constant or not increase accordingly. Finally, growing vapor bubbles remain close to the surface in the horizontal down orientation until they escape from sides, and behave as thermal insulators. The surface temperature thus increases which, in turn, activates additional sites at the smaller cavities.

4. Maximum Bubble Size Results

Bubbles attain their maximum sizes at departure from the surface in nucleate boiling with a saturated liquid, whereas in subcooled boiling the departure sizes may be smaller than the maximum size attained during

the growth period due to partial collapse before departure from the surface.

Figure 84 is a plot of the maximum bubble diameter as a function of heat flux for the horizontal up and vertical orientations with Fl13 at atmospheric pressures. The vertical bars represent the observed variations of the maximum bubble sizes. The results indicate a slight decrease in average maximum bubble diameters with increasing heat flux. Beckman, Merte [46] and Gaertner [47] have also observed a small decrease in bubble diameters with increasing heat flux in their experiments with water. The decrease in bubble diameter could be due to momentum effects associated with the bubble growth.

Figure 84 also indicates that the average maximum bubble diameters are larger with the horizontal up orientations than with vertical, in Fl13, and may be a consequence of the induced velocity sweeping the bubbles off sooner with the vertical surface.

Figure 85 presents results obtained for the vertical and horizontal down orientations with LN_2. With the horizontal down orientation there is no departure diameter in the conventional sense, because buoyant forces hold the bubbles against the surface until the vapor slugs that cover the surface escape from the sides. In the present experiments with LN_2, the test surface is tilted about 3-5° from the horizontal to help vapor bubbles to move off the site more frequently, which then made it possible to observe the maximum bubble diameters presented in Fig. 85. The maximum bubble diameters decrease slightly with heat flux in LN_2 as in Fl13. As shown in Fig. 85 the average maximum bubble sizes are higher with the horizontal down orientations than with vertical. This could be due to the distortion of the bubble shapes by buoyant forces, or also for the

reason that the bubbles may be swept away sooner by the convection currents on vertical surfaces.

The bubble departure diameter was first formulated by Fritz [48], based on the work of Bashfort and Adams [49] from a static force balance of surface tension and buoyancy for es, who obtained the following equation

$$D = 0.0119\,\theta\,\sqrt{\frac{\sigma}{(\rho_\ell - \rho_v)}}\tag{21}$$

Equation (21) is plotted in Fig. 84 for an arbitrary constant contact angle $\Theta = 24°$ for comparison. Equation (21) has been shown to predict departure diameters reasonably well at low heat fluxes [46]. Since the dynamic forces were ignored, Fritz' equation does not predict the departure diameter well at higher heat flux levels. Among others, Staniszewski [50] found that the bubble departure diameter depends on the growth velocity in the last stages of growth and suggested a correction to include the dynamic effects, resulting in

$$D = 0.0071\,\sqrt{\frac{2\sigma}{g(\rho_\ell - \rho_v)}}\left(1 + 0.435\,\frac{dD}{dt}\right)\tag{22}$$

Both Eqs. (21) and (22) include the $\sigma/(\rho_\ell - \rho_v)$ term as a multiplier. This term can be considered to represent the ratio of the surface tension to buoyancy forces, and can be used to obtain an indication of the expected maximum bubble sizes in two different liquids. Taking the ratio of Eq. (21) for two liquids and assuming that the contact angle is the same for both

$$\frac{D_{LN_2}}{D_{F113}} \sim \frac{\sigma_{LN}}{\sigma_{F113}}\cdot\frac{(\rho_\ell - \rho_v)_{F113}}{(\rho_\ell - \rho_v)_{LN_2}}\tag{23}$$

Substituting the properties of F113 and LN$_2$, in Eq. (23) gives

$$\frac{D_{LN_2}}{D_{F113}} \sim 1.22 \tag{24}$$

In saturated boiling the bubbles attain their maximum sizes at departure, and the experimental results could be used for comparison with the value of Eq. (24). Substituting the departure sizes from Figs. 84 and 85 for Q/A=9000 BTU/Hr-Ft^2 will give

$$\frac{D_{LN_2}}{D_{F113}} = \frac{26}{15} = 1.7 \tag{25}$$

The result given by Eq. (25) agrees reasonably well with the predicted results of Eq. (24).

5. Bubble frequency results

Figures 86 and 87 present the results of the analysis of the photographs in which the average frequency of departure of bubbles in nucleate boiling were determined for F113 and LN$_2$, respectively. The results are presented in the form of plots of average frequency of bubble departure versus heat flux for each orientation at a/g=1. The results indicate that the frequency of vapor bubble emission varies as a power of the heat flux.

As the photographic samples in Appendix C and Fig. 18 indicate, a bubble period consists of two parts: the active period, or elapsed time from the appearance to the departure of a bubble, and the waiting period, or elapsed time between the departure to the appearance of the next bubble at the same site. The waiting period depends on how rapidly the new liquid boundary layer can be heated to the minimum superheat necessary for the next bubble to grow. The required superheat for the formation of a

bubble, as discussed earlier, depends on the cavity size, surface tension, saturation temperature, etc. Therefore, for a given liquid the waiting period depends on the amount of the excess heat flux over the amount transfered by conduction and convection. The growth period of a bubble depends on the bubble growth rate, which is dependent upon the surface temperature and the temperature of the fluid adjacent to the test surface, both of which increase with increasing heat flux. Therefore, as heat flux is increased both the waiting period and the growth period decrease thus increasing the frequency of bubble departure. As observed previously, however. the maximum size decreases somewhat.

Figures 86 and 87 also indicate that the average frequency of bubble departure is higher with the vertical orientations than the horizontal up orientations. As shown in the previous section dealing with departure sizes (e.g. Figs. 84 and 85) the vapor bubble sizes are larger on departure for the horizontal down and horizontal up orientations than for the vertical orientations. If the growth rates remain comparable for the different orientations, then the growth period will be longer for the horizontal surfaces than for the vertical surface, which will in turn reduce the frequency of departure for the horizontal surfaces. In addition, buoyant forces tend to hold bubbles on the surface with the horizontal down orientations, inhibiting their departure, and thus become the major contributing factor in reducing the frequency for that orientation. Furthermore, for a given heat flux the energy transfer rate by boiling is less with the horizontal up orientation than with the vertical orientation due to the higher convection heat transfer which, in turn, results in a reduction in the frequency of departure.

Figure 86 includes the results of [34] for F113 for the sake of comparison. Considering that the present results were obtained at about 2° subcooling, which, according to the results of Ref. [34] reduces the frequency of bubble departure, agreement with [34] is excellent.

As reported by Jakob [51], when the frequency of bubble departure was plotted against the departure diameter a hyperbolic relation was observed such that

$$f \cdot D_{Dep} \simeq \text{CONSTANT} \tag{26}$$

Later Zuber [52] proposed the following relation involving surface tension and buoyancy forces:

$$f \cdot D_{Dep} = \frac{1.18}{2} \frac{\left[\sigma g (\rho_l - \rho_v) \right]^{1/4}}{\rho_l} \tag{27}$$

McFadden and Grassmann [53] demonstrated the inadequacy of Eq. (27) for their experimental results with LN_2. They developed the following relation with dimensional analysis, coupled with available experimental data

$$f \cdot D_{Dep}^{1/2} = \text{CONSTANT} \tag{28}$$

Later Staniszewski [50] and Perkins and Westwater [54], among others, also experimentally showed that the product $f \cdot D_{dep}$, given by Eq. (26), remains constant for certain liquids and for certain conditions.

Since Eqs. (26) and (28) are commonly used and indicate a reduction in frequency as the departure diameter increases, both relations are plotted in Fig. 88, using the present experimental results obtained for various orientations with F113 and LN_2. The results indicate a marked increase in the $f \cdot D_{max}$ products with increasing heat flux. This agrees

with the findings of Ref. [46]. On the other hand the $f \cdot D_{max}^{1/2}$ products do not vary significantly with increasing heat flux and almost remain constant, which agrees with the findings of McFadden and Grassmann [53].

C. EVALUATION OF NUCLEATE BOILING MODELS

Up to this point the experimental results related to the various parameters such as surface temperature, active site density, average population density, frequency of vapor bubble emission and maximum bubble size have been discussed. In this section discussion is directed towards theoretical models. First the separation of the natural convection and nucleate boiling components of heat flux is presented. Then two theoretical models, whose validity it is possible to check with experimental data obtained during this investigation, are considered.

Merte and Clark [55] considered that natural convection and nucleate boiling act independently of each other on a given surface, and that the heat transfer by nucleate boiling, Q_{NB}, and heat transfer by natural convection, Q_{NC}, were confined to the related area fractions A_{NB}/A_T, and A_{NC}/A_T, respectively. Therefore, the total heat transfer to the liquid could be written as

$$Q_\ell = Q_{NB} + Q_{NC} \qquad (29)$$

and the total heat flux to the liquid Q_ℓ /A_T could be written as

$$\frac{Q_\ell}{A_T} = \left(\frac{Q_{NB}}{Q_\ell}\right)\left(\frac{Q_\ell}{A_T}\right) + \left(\frac{Q_{NC}}{A_{NC}}\right)\left(\frac{A_{NC}}{A_T}\right) \qquad (30)$$

Rearranging for Q_{NB}/Q_ℓ , the nucleate boiling heat transfer fraction, gives

$$\frac{Q_{NB}}{Q_\ell} = 1 - \left[\frac{(Q_{NC}/A_{NC})}{(Q_\ell/A_T)}\right]\left(\frac{A_{NC}}{A_T}\right) \qquad (31)$$

Approximate relations for the natural convection heat flux fractions, $(Q_{NC}/A_{NC})/(Q_\ell/A_T)$, are tabulated in Table (3), using appropriate natural heat transfer correlations for each orientation along with properties of the two fluids used. The measured surface-fluid temperature differences are substituted into the natural convection heat flux fractions given in Table (3) for the tests conducted with F113 and LN_2 at a/g=1 and plotted in Fig. 89 as a function of heat flux to the liquid.

As could be anticipated, Fig. 89 indicates that the natural convection heat flux fraction decreases with increasing heat flux, since the active site density and frequency of bubble departure increases with heat flux, thus a greater portion of the increased imposed heat flux will be transfered by the boiling process. A similar trend was observed with a horizontal up orientation in F113 [34].

The natural convection area fraction A_{NC}/A_T is obtained as in Ref. [34] by subtracting the total area occupied by vapor bubbles at a given instant of time from unity

$$\frac{A_{NC}}{A_T} = 1 - \frac{A_{NB}}{A_T} = 1 - \left[K\left(\frac{\pi}{4}\right)\left(D_{max}\right)^2\left(\frac{\eta}{A}\right)\right] \qquad (32)$$

The total surface area occupied by vapor bubbles is given by the measured projected area of vapor bubbles, the average population density (η/A) and a constant to compensate for the area of influence of the bubbles. Han and Griffith [56] reported that the area influenced by the departure of a spherical bubble in the water had approximately twice the diameter of the sphere, which suggests a value of K=4. On the other hand, Ref. [34] obtains unreasonable results with K=4 and suggests using K=3. K=1 is a lower limit and K=4 could be the upper limit. In order

Table 3. Natural Convection Heat Flux Fractions

LIQUID	ORIENTATION	NATURAL CONVECTION HEAT TRANSFER CORRELATION	NATURAL CONVECTION HEAT FLUX FRACTION $(Q_{NC}/A_{nc})/(Q_\ell/A_T)$
Freon-113	Vertical	$Nu=0.555\,(Gr \cdot Pr)^{1/4}$	$\dfrac{15.81\,(T_T-T_\ell)^{5/4}}{(Q_\ell/A_T)}$
	Horizontal Up	$Nu=0.14\,(Gr \cdot Pr)^{1/3}$	$\dfrac{14.06\,(T_T-T_\ell)^{4/3}}{(Q_\ell/A_T)}$
	Horizontal Down	$Nu=0.27\,(Gr \cdot Pr)^{1/4}$	$\dfrac{7.69\,(T_T-T_\ell)^{5/4}}{(Q_\ell/A_T)}$
Liquid Nitrogen	Vertical	$Nu=0.555\,(Gr \cdot Pr)^{1/4}$	$\dfrac{41.76\,(T_T-T_\ell)^{5/4}}{(Q_\ell/A_T)}$
	Horizontal Up	$Nu=0.14\,(Gr \cdot Pr)^{1/3}$	$\dfrac{43.09\,(T_T-T_\ell)^{4/3}}{(Q_\ell/A_T)}$
	Horizontal Down	$Nu=0.27\,(Gr \cdot Pr)^{1/4}$	$\dfrac{2\mathrm{J}.3\,(T_T-T_\ell)^{4/3}}{(Q_\ell/A_T)}$

to compare the results of the present work with the results of Ref. [34]
K=3 is also used in the present work.

Using K=3 in Eq. (32) along with experimental results of D_{max} and
n/A, A_{NC}/A is calculated. Substituting the values obtained for the nat-
ural convection area fractions and the natural convection heat flux frac-
tions obtained into Eq. (31), the nucleate boiling heat flux fractions
are determined, and plotted in Fig. 90 as a function of a dimensionless
heat flux, defined as the ratio of the heat flux to the burnout heat
flux for that liquid. The results in Fig. 90 indicate that Q_{NB}/Q_ℓ in-
creases toward unity with increasing heat flux, which is expected since
the natural convection heat flux fraction decreases as the imposed heat
flux increases.

The next step is the determination of the total bubble heat trans-
fer, Q_{Total} , defined as the quantity of heat transfered by the growth
Bubble
and departure of a single bubble. This quantity is needed to show the
significance of the microlayer contribution and to assess the adequacy
of several nucleate boiling models. The overall nuc   boiling heat
flux is obtained by multiplying Eq. (31) with Q_ℓ /A_T, ...e total heat
flux to liquid.

$$\frac{Q_{NB}}{A_T} = \frac{Q_{NB}}{Q_\ell} \frac{Q_\ell}{A_T}$$

(33)

Q_{NB}/A_T is the total heat flux associated with the action of bubbles and
is plotted in Fig. 91 as a function of heat flux to the liquid. It shows
the effect of heat flux and orientation on the nucleate boiling heat flux.
The 45° line on Fig. 91 represents the results that would have been ob-
tained at absolute zero gravity a/g=0 condition, and is approached quite
closely by the horizontal down orientation, where the influence of nat-

ural convection is a minimum. Q_{NB}/A_T increases with heat flux, and for a given heat flux it is slightly higher with vertical orientations than with horizontal up orientations.

Finally, dividing the nucleate boiling heat flux, Q_{NB}/A_T, by the active site density and the frequenc, of vapor bubble formation gives the total heat transfer associated with a single bubble. This is defined as the total bubble heat transfer and given by

$$Q_{\substack{Total \\ Bubble}} = \frac{Q_N \cdot /A_T}{(N/A_T)f} \tag{34}$$

Figure 92 shows the variation of the heat transfer associated with a single bubble with heat flux and orientation for both F113 and LN_2 respectively. In contrast to the findings of [34] for saturated F113, Fig. 92 indicates that $Q_{\substack{Total \\ Bubble}}$ decreases with increasing heat flux. This could be due to a more rapid increase of N/A and f than the heat flux itself. As discussed in earlier sections, both N/A and f increase as power functions of the heat flux (e.g. Figs. 8;-84) while heat flux itself increases linearly. There is no significant difference in $Q_{\substack{Total \\ Bubble}}$ between the vertical and horizontal up orientations, $Q_{\substack{Total \\ Bubble}}$ is considerably higher with the horizontal down orientation. Several factors may contribute to this difference: 1) A higher microlayer contribution with the horizontal down orientations, discussed previously; 2) buoyancy forces hold the vapor bubbles against the surface, thus increasing the contact time of each bubble with the test surface, which results in larger bubble diameters and at the same time reduces the frequency of the bubble departure. All these effects increase the heat transfer associated with the individual bubbles.

The results of Ref. [34] are also shown in Fig. 92 for comparison.
The difference between the result of the present investigation and the
results of [34] is due mainly to the difference in the determination of
site densities where for a given heat flux Ref. [34] reported an active
site density about four times as large with oxide coated glass in F113.
The explanation for the discrepancy was given in Section B-2. Figure 92
also indicates that a similar decrease in $Q_{Total \atop Bubble}$ with increasing heat
flux occurs in LN_2 as with F113. $Q_{Total \atop Bubble}$ for LN_2 is somewhat higher
than with F113, which could be due to the higher latent heat of vapori-
zation of LN_2 compared to F113.

Now that values of $Q_{Total \atop Bubble}$ are determined from the experimental
measurements of surface temperature, active site and average population
densities, frequency of vapor bubble emission and maximum bubble size
obtained in this present investigation, it is possible to compare these
results with the following models.

1. Latent Heat Transfer Model

It was first suggested by Jakob [51] that the rate of heat transfer
in nucleate boiling is related to the bubble volume of the latent heat.
This theory has been supported by the recent experimental results of
saturated water boiling on a horizontal wire [36]. In terms of time
averaged measurements obtained in the present investigation the latent
heat transfer model may be expressed as follows

$$\left(\frac{Q_{NB}}{A_T}\right)_{Latent \atop Heat} = \rho_v \, h_{fg} \, V_{Bubble} \left(\frac{N}{A_T}\right) f \tag{35}$$

$$Q_{\substack{Total \\ Bubble}} = \frac{Q_{NB}/A_T}{(N/A_T)f} = \rho_v \, h_{fg} \, V_{Bubble} \tag{36}$$

The experimental results of the present investigation and Ref. [34], along with results predicted by Eq. (36) are presented in Fig. 93 for comparison. According to Fig. 93 the latent heat transfer model predicts values considerably lower, indicating that other mechanisms of heat transfer are acting, such as pumping action and increased forced convection due to change in the momentum of liquid particles as a result of bubble growth and departure. According to Fig. 93 the horizontal down orientation gives results closest to those predicted by Eq. (36). With the horizontal down orientation the superheated liquid layers remain near the surface, and the pumping and forced convection actions by the bubbles become less effective. Therefore, the contribution of the latent heat transport to the total is larger with the horizontal down orientation than with the vertical and horizontal up orientations.

2. Vapor Liquid Exchange Model

In this model, postulated by Forster and Grief [37], heat transfer by nucleate boiling was described as the exchange of a bubble volume of liquid at temperature T_T for a bubble volume of liquid at the bulk temperature T_ℓ due to the action of bubble departure and collapse expressed by

$$\frac{Q_{NB}}{A_T} = \beta \, C_\ell \frac{\pi}{6} \left(D_{max}\right)^3 \left(T_T - T_\ell\right) \left(\frac{N}{A_T}\right) f \tag{37}$$

or

$$Q_{\substack{Total \\ Bubble}} \Big/ V_{Bubble} = \frac{Q_{NB}/A_T}{(N/A)f} = \rho_\ell C_\ell (T_T - T_\ell) \tag{38}$$

Figure 94 presents the experimental results of $Q_{\substack{Total \\ Bubble}}$ along with the theoretical predictions computed from Eq. (38). The results of Ref. [34] are also included for comparison.

As Fig. 94 indicates, the vapor liquid exchange model largely over-predicts the heat transfer per bubble. A similar conclusion is reached in Ref. [34]. Part of the deviation could come from the fact that the liquid near the surface is not uniformly at the wall temperature, as the model assumes. The deviation is largest with the horizontal down orientation and smallest with the vertical orientations. Due to less mixing action the temperature gradient may be expected to be highest within the liquid with the horizontal down orientation, resulting in the large deviation observed.

CHAPTER VII

CONCLUSIONS

1. This research has demonstrated that semi-transparent thin gold films, properly calibrated, can be used simultaneously as a heater and resistance thermometer for temperatures ranging from -320°F to +250°F, with better than ±2°F accuracy and producing heat flux levels up to burnout in LN_2 and F113. The resistance of the gold film surfaces increases with time, but the slope dR/dT remains constant. Therefore, once a complete calibration of a test surface has been made, it is sufficient to make only a single point calibration prior to each test run.

2. From the step increase of power input up to the initiation of boiling two distinct regimes of heat transfer mechanisms exist; the conduction and convection dominated regimes. The time duration in each regime is considerably shorter with LN_2 than with F113, and decrease as heat flux increases, as gravity is reduced, and as the orientation is changed from horizontal-up to horizontal-down. These changes are a consequence of changes in boundary layer temperature levels associated with changes in natural convection.

3. With a step increase of power input, boiling initiated first at a single point and then spreads over the surface. The delay time for the inception of boiling at the first site decreases as heat flux increases, as gravity is reduced and as the orientation is changed from horizontal up to horizontal down. The delay time depends on the transient growth of a thermal boundary layer. Therefore, as heat flux is increased, the liquid film temperature increases more rapidly. Similarly, with a reduction of gravity or changing orientation from horizontal up to horizontal down, convection effects are reduced or eliminated, and more energy is available

-96-

to heat the boundary layer. The delay time also depends on the liquid properties, being shorter with LN_2 than F113. The spread velocity of nucleate boiling increases with increasing heat flux, and with a reduction of gravity. It is larger with LN_2 than with F113, and is larger with smoother surfaces.

4. With a stepwise increase in power input, a heater surface temperature overshoot and undershoot occur before the steady state boiling temperature level is established. The degree of overshoot varies depending upon the heat flux, gravity, orientation and surface characteristics. It is higher with smoother surfaces and increases with increasing heat flux. The effect of orientation on the degree of overshoot depends on gravity and the heat flux level. At lower heat flux levels the highest overshoot occurs with vertical surfaces, while at the higher heat flux levels, it is highest with the horizontal up orientations. It is lowest for horizontal down orientations for all heat flux levels.

5. The surface superheat at the inception of boiling is independent of heat flux and orientation. It is a function of gravity, however, being smaller at $a/g=0$ than at $a/g=1$. It also appears to be a function of surface roughness.

6. While the active site and average population densities increase as a power function of the heat flux, these are influenced by orientation and gravity to a minor extent, only.

7. Experimental results indicate that the maximum bubble size and the frequency of bubble departure are correlated for various levels of heat flux and orientation by the relation, $(D_{max})^{1/2} \bar{f} = $ constant.

8. The heat transfer associated with each departing vapor bubble, $Q_{Total \atop Bubble}$, decreases as heat flux increases.

EXHAUST FAN

TEST PACKAGE

ELEVATOR
TOWER

CO_2 JETS

SHEET
ALUMINUM
LINING

SHAFT HEAD
CHAMBER

SHEET ALUMINUM
SHAFT

32 FT.

CO_2 JETS

BUFFER
CHAMBER

SAND
BOX

SHEET ALUMINUM
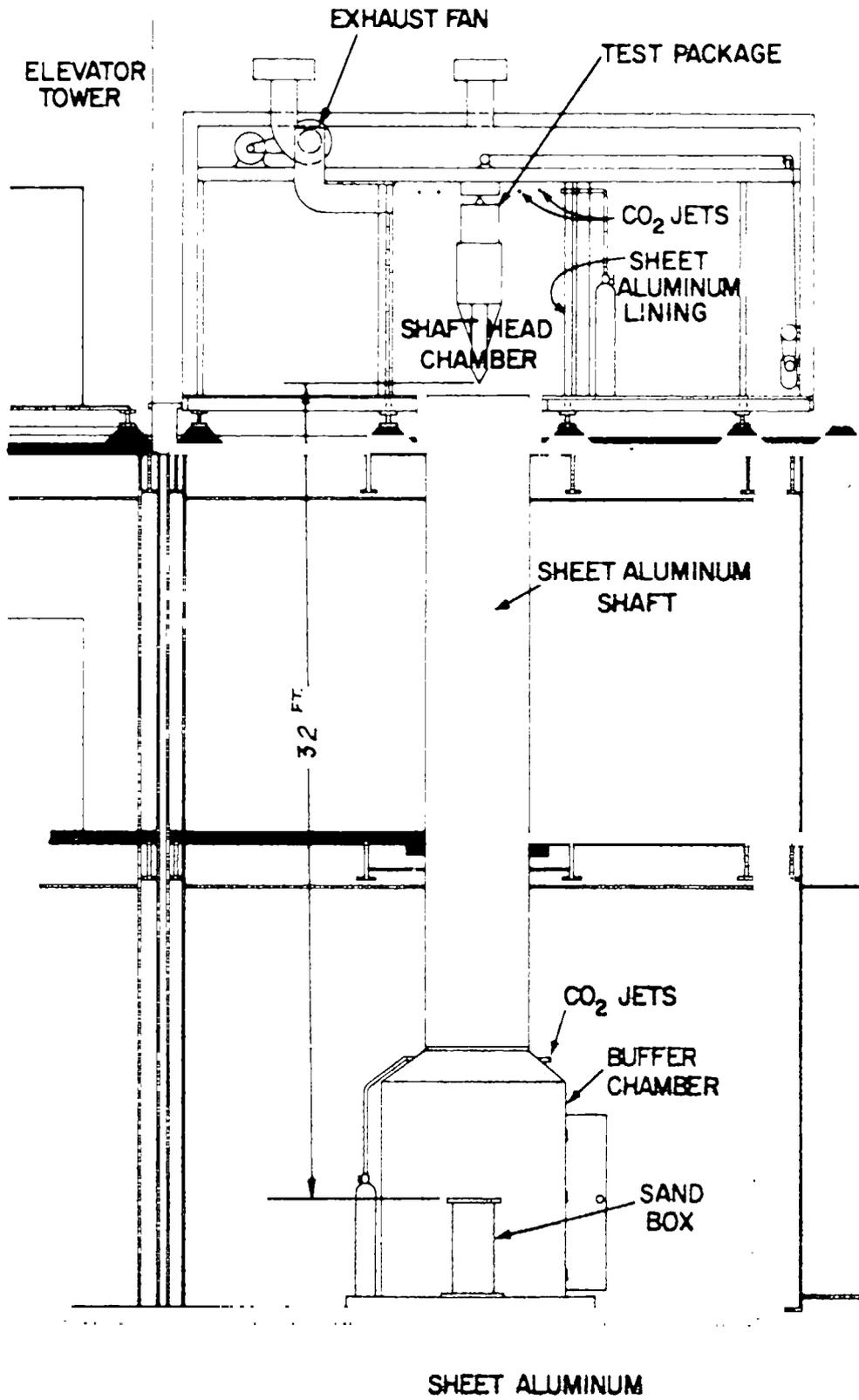
Fig. 1. Drop tower-elevation
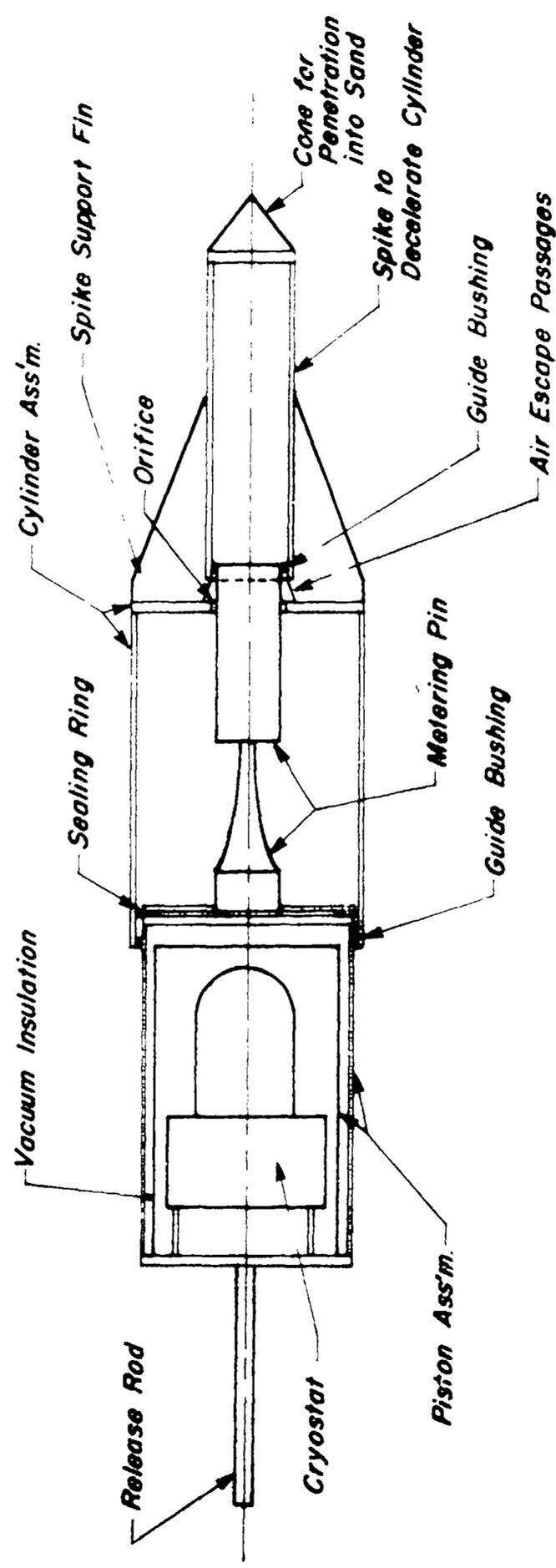
Fig. 2. Deceleration assembly for test package

Release Rod

Cryostat

Piston Ass'm.

Vacuum Insulation

Sealing Ring

Cylinder Ass'm.

Spike Support Fin

Orifice

Cone for Penetration into Sand

Spike to Decelerate Cylinder

Guide Bushing

Air Escape Passages

Metering Pin

Guide Bushing

Scale: 1" = 18"
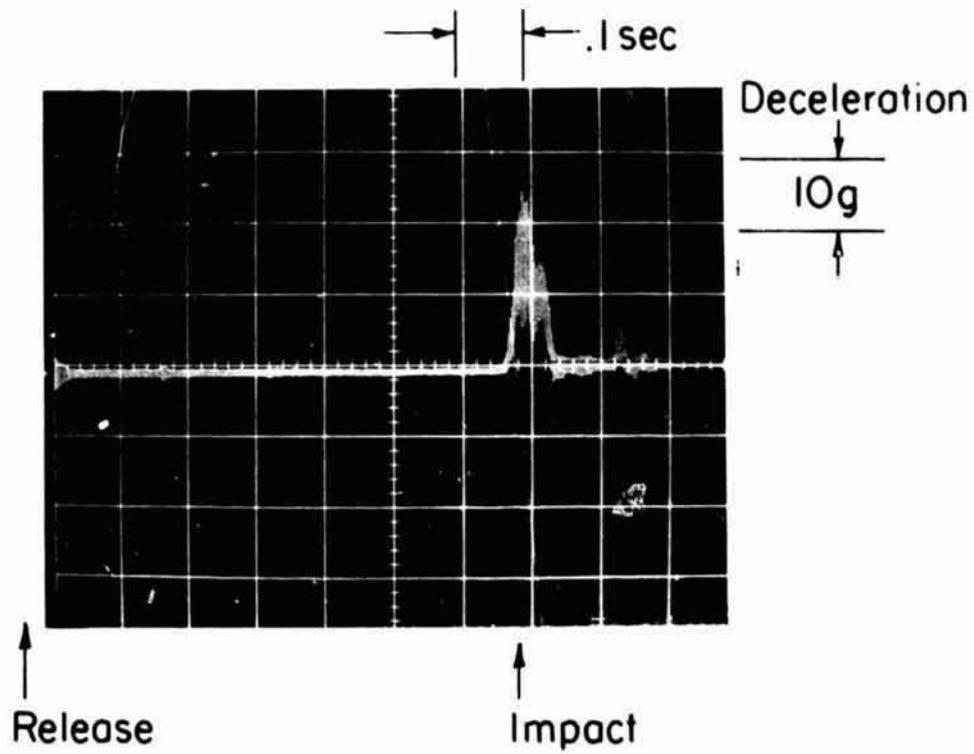
Fig. 3. Drop package deceleration

RELEASE   IMPACT

.01
SEC.

1.345 SEC.

a/g =.010

TIME
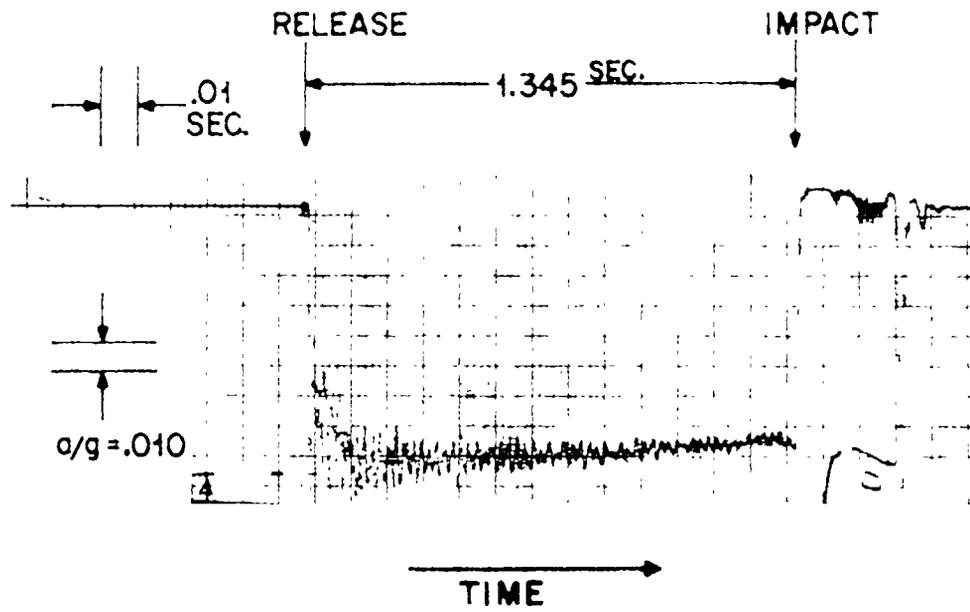
CHART SPEED = 50 MM/SEC.
SENSITIVITY = 10 MV/DIV
a/g = 1
SIGNAL = -5074 MV

Fig. 4.   Accelerometer measurements with free fall
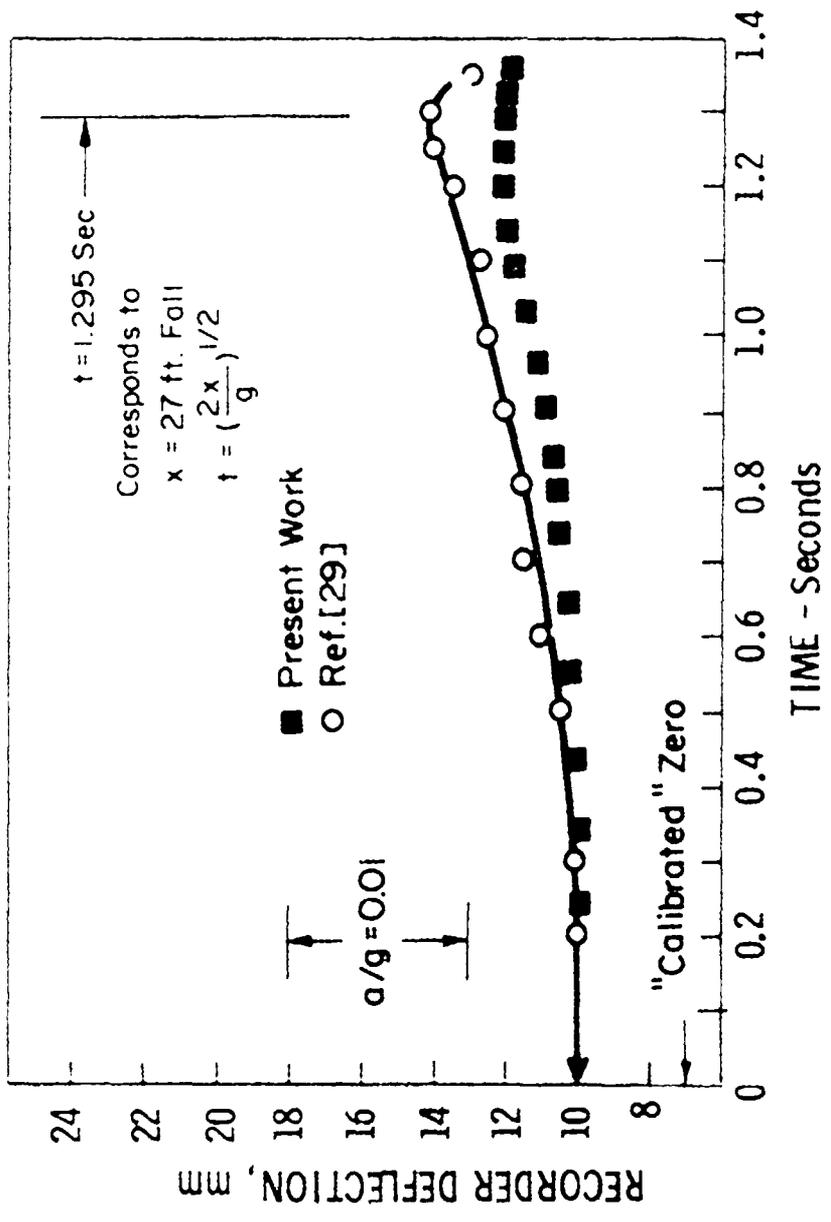
Fig. 5. Smoothed plot of free fall acceleration measurement
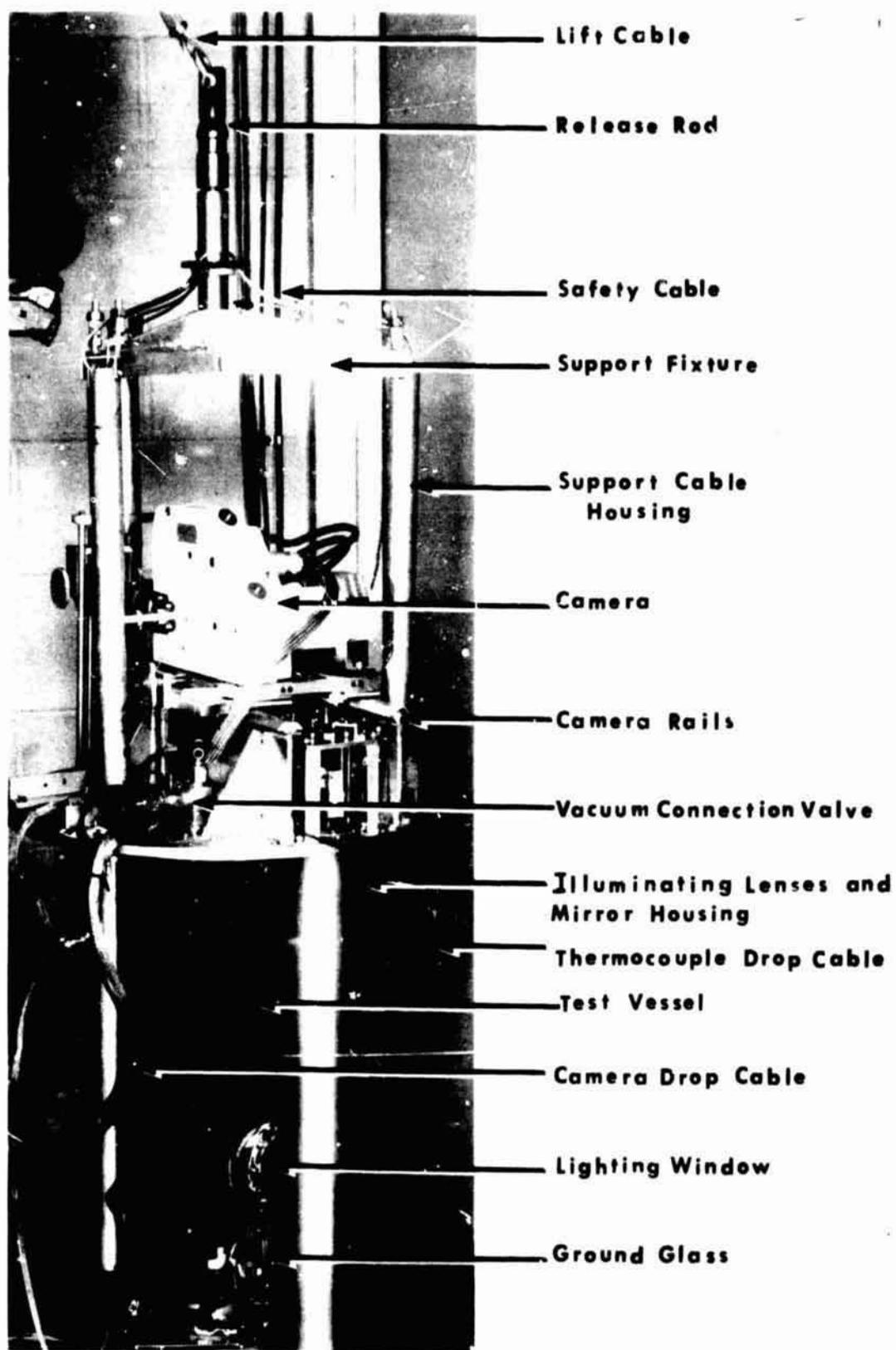
Fig. 6. Test package - view A
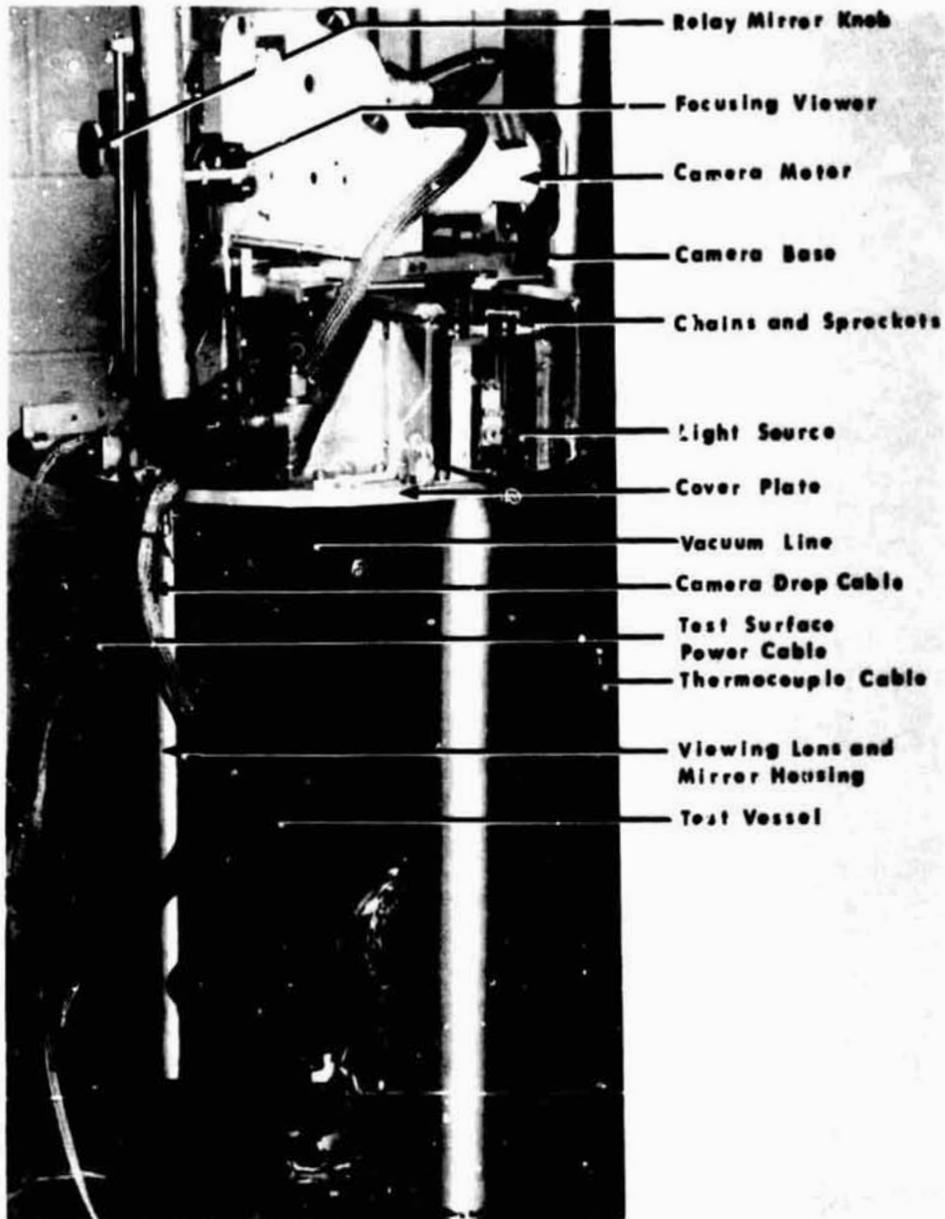
Fig. 7. Test package - view B
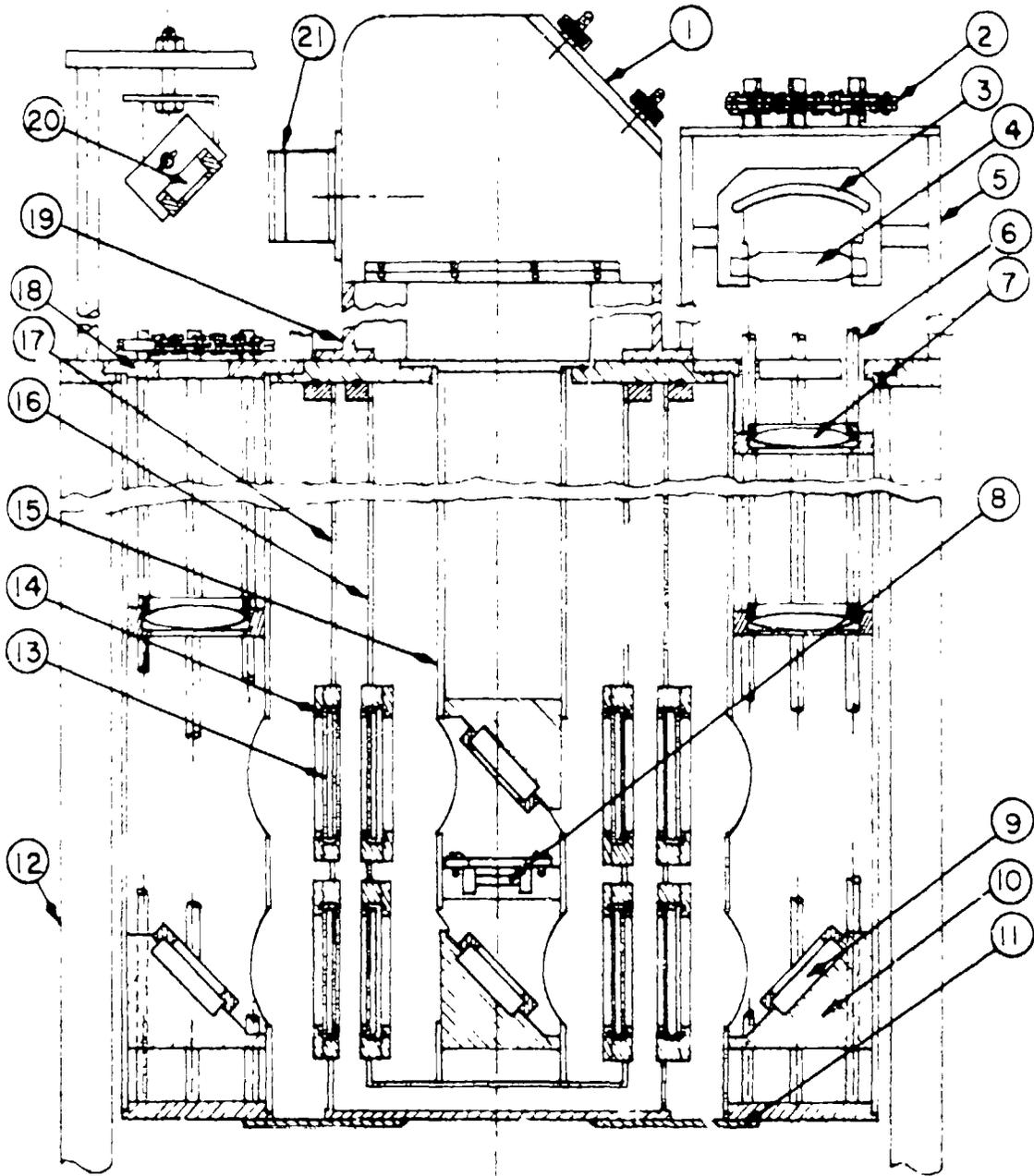
1. Camera
2. Sprocket & Chains
3. Spherical Reflector
4. Mercury Arc Lamp
5. Light Source Housing
6. Thread Rods
7. Lighting Lens
8. Test Surface
9. Relay Mirror
10. Mirror Holder

11. Cross Bar
12. Drop Package
13. Viewing Window
14. "O" Ring
15. Test Tube
16. Inside Dewar
17. Outside Dewar
18. Flange
19. Camera Rail
20. Relay Mirror
21. Camera Lens

Fig. 8. Test vessel and package
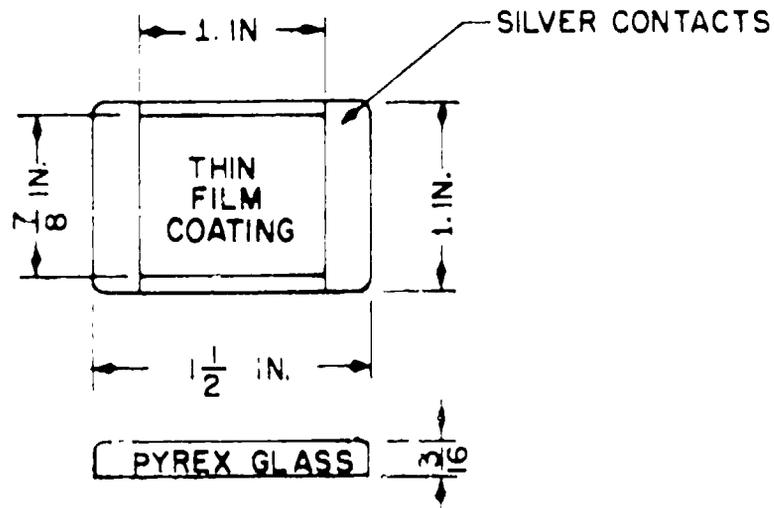
Fig. 9. Thin film surface dimensions
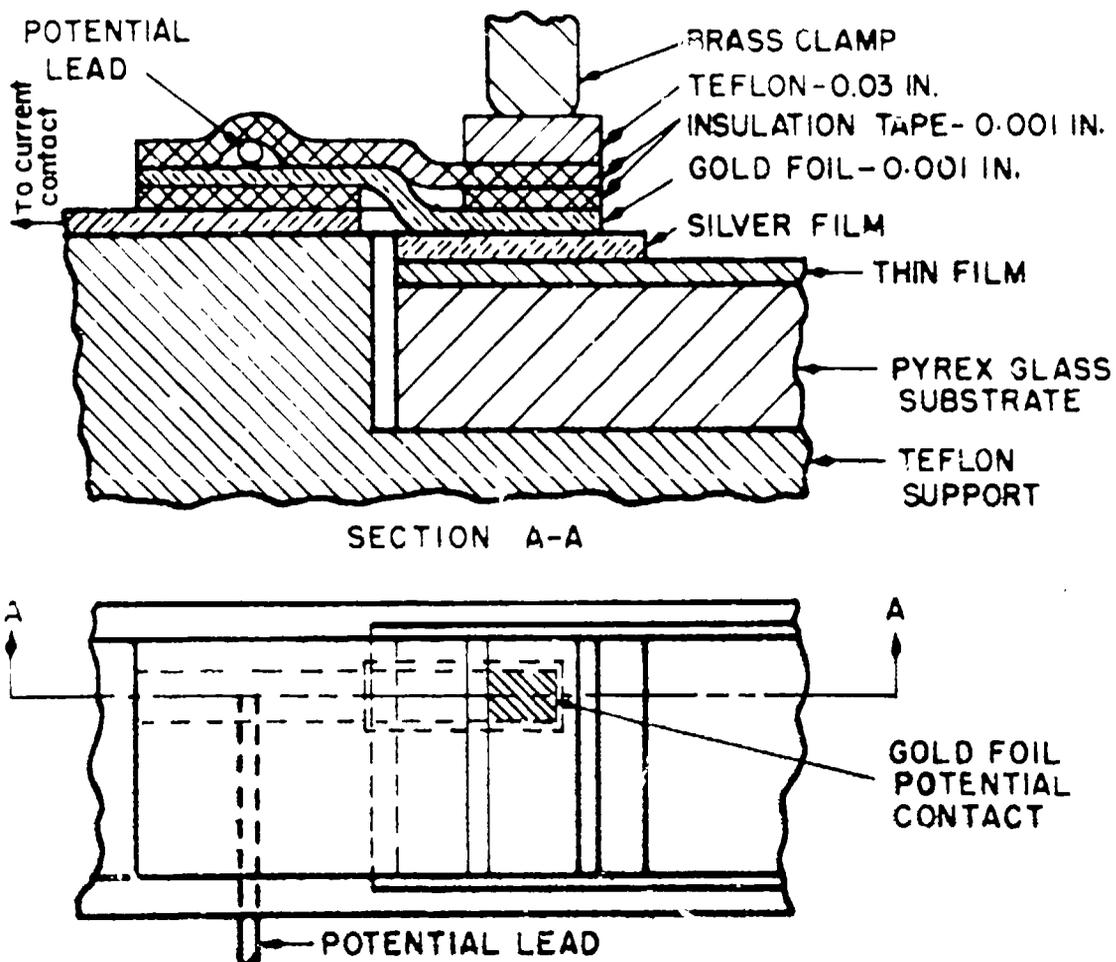
Fig. 10. Current potential connections on thin films
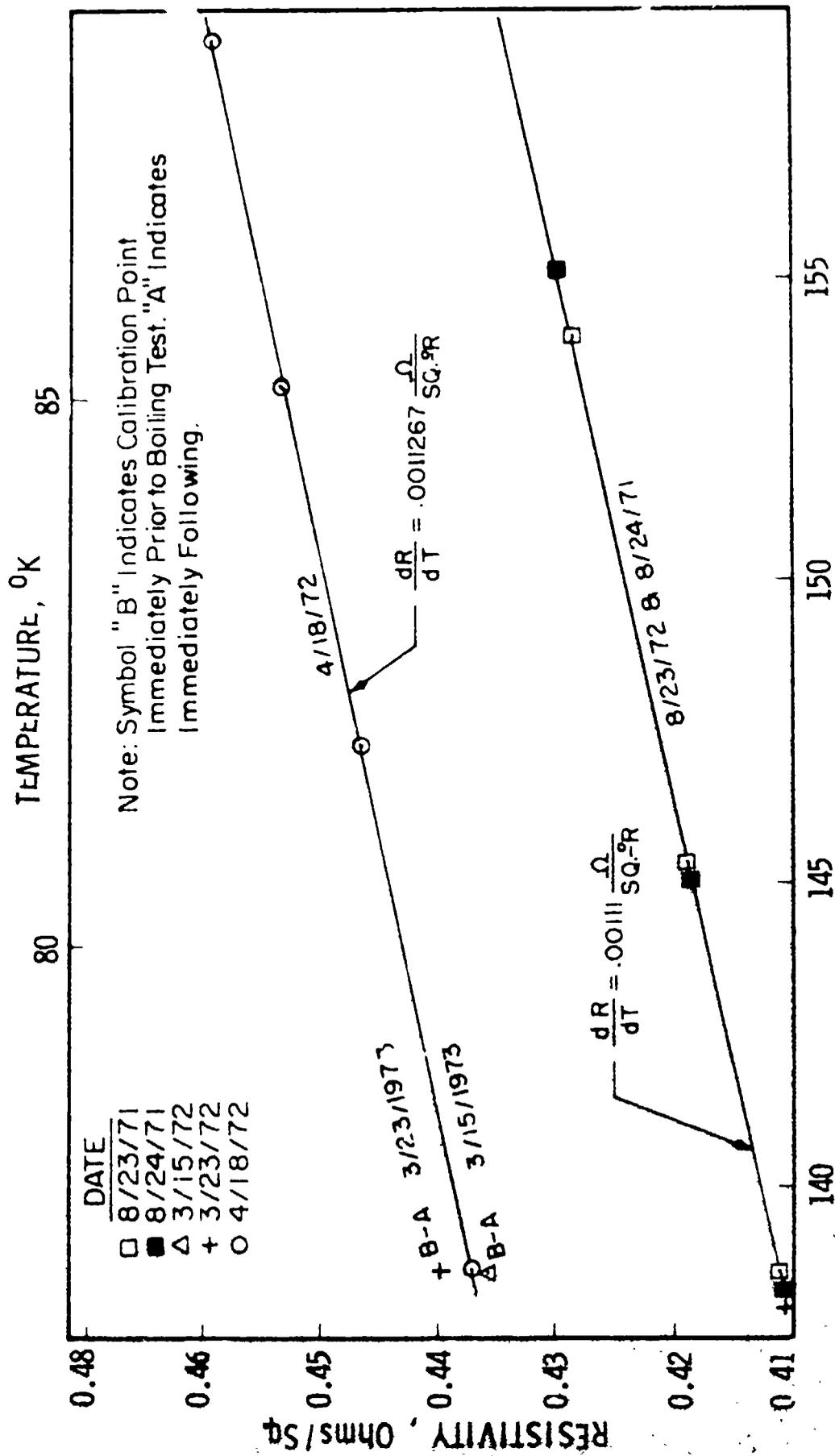
Fig. 11. Calibration shift with time (PCG-15) in LN₂
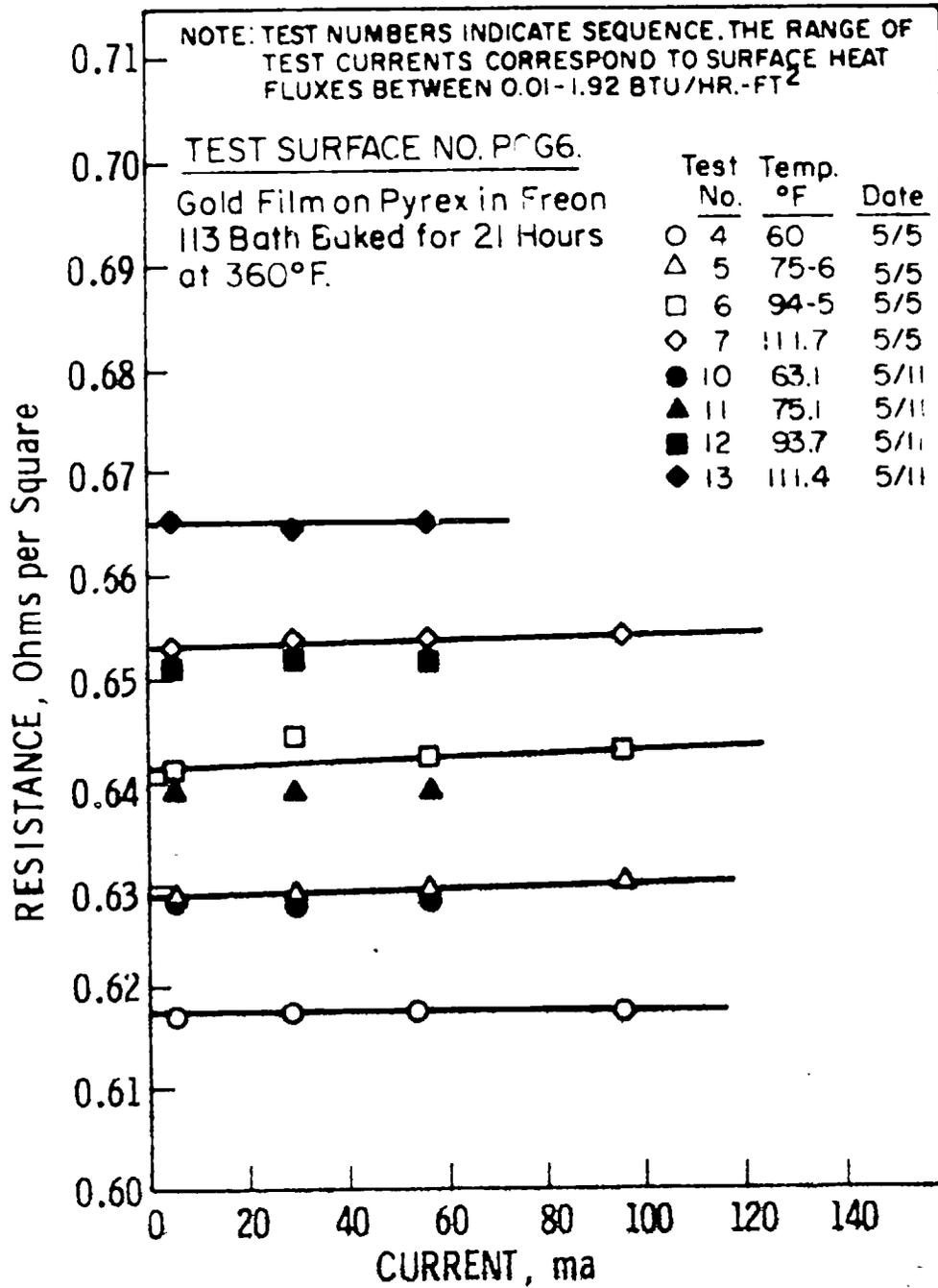
Fig. 12. Calibration test, gold film PCG 6
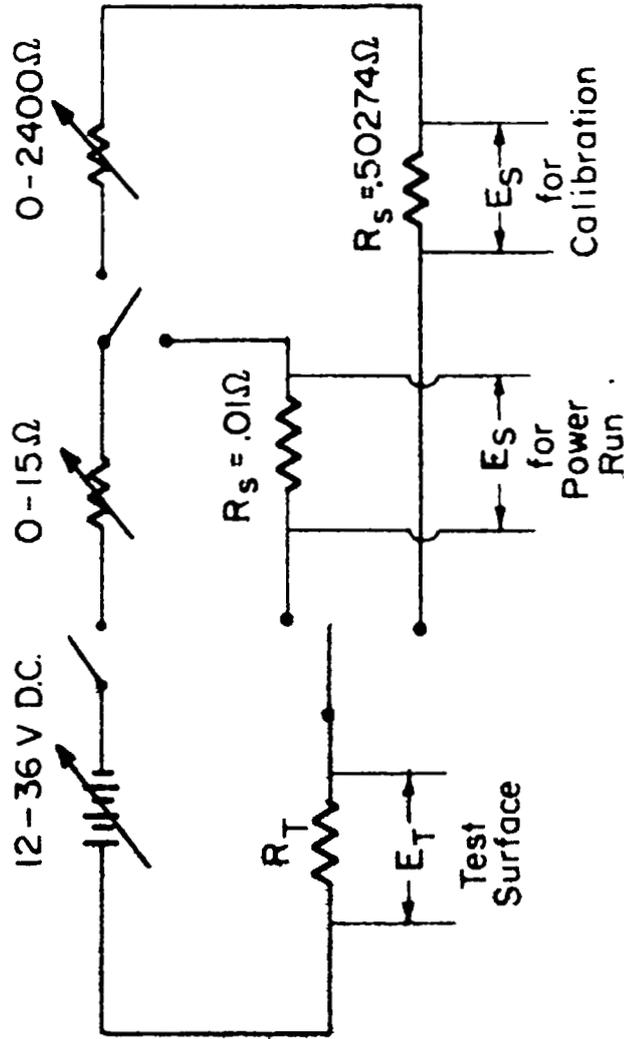
Fig. 13. Calibration and power circuit

1. Test Package
4. Liquid Level Indicator
7. Millivolt Meter
10. .01 Ohm Standard Resist.
13. Sanborn Recorder
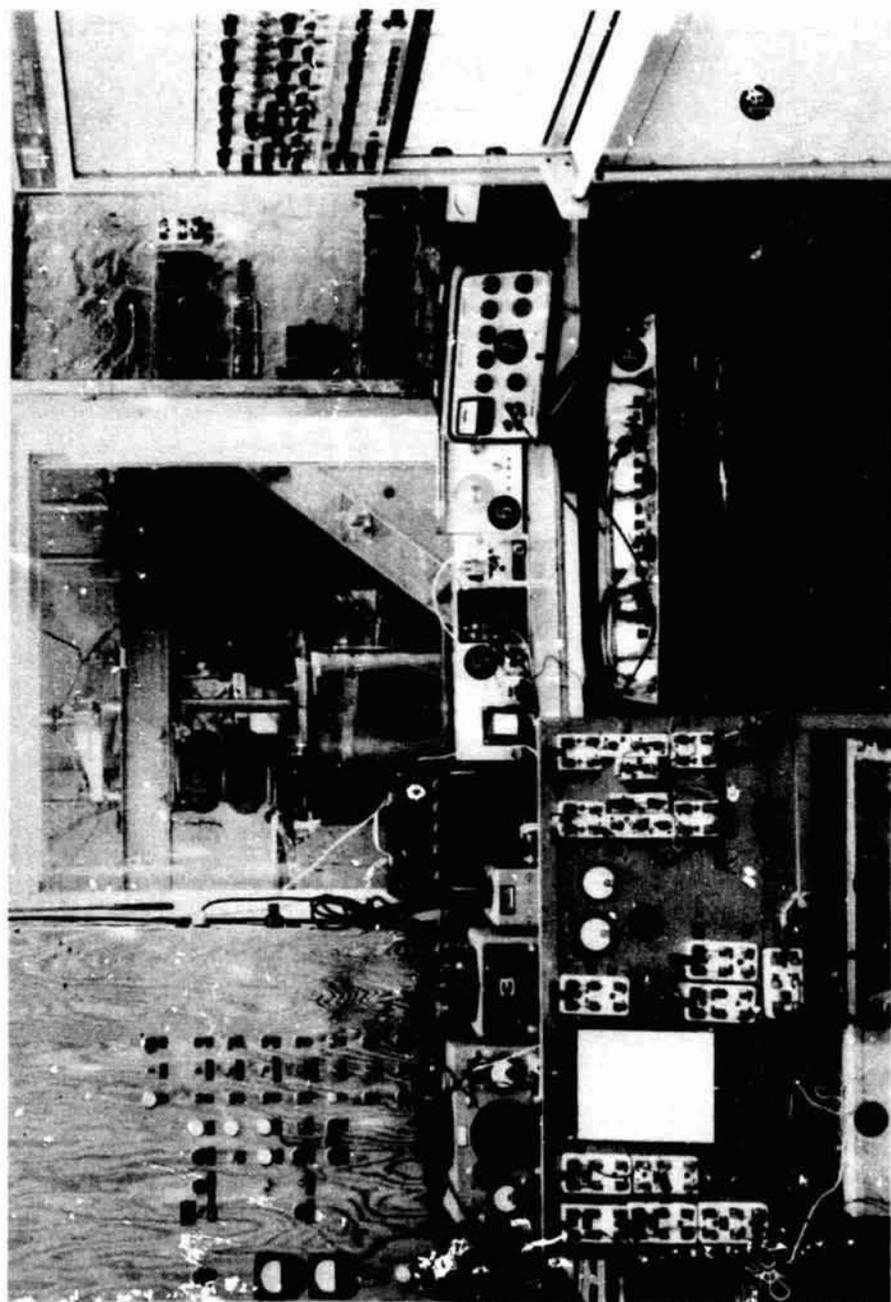
2. Camera Power Supply
5. Delay Circuit
8. Remote Control Switch
11.~16 Ohm Variable Resist.

3. Camera and Event Synchronizer
6. Square Wave Generator
9. D-C Power Source
12. K-2 Potentiometer

Fig. 14. Instrumentation and power supply
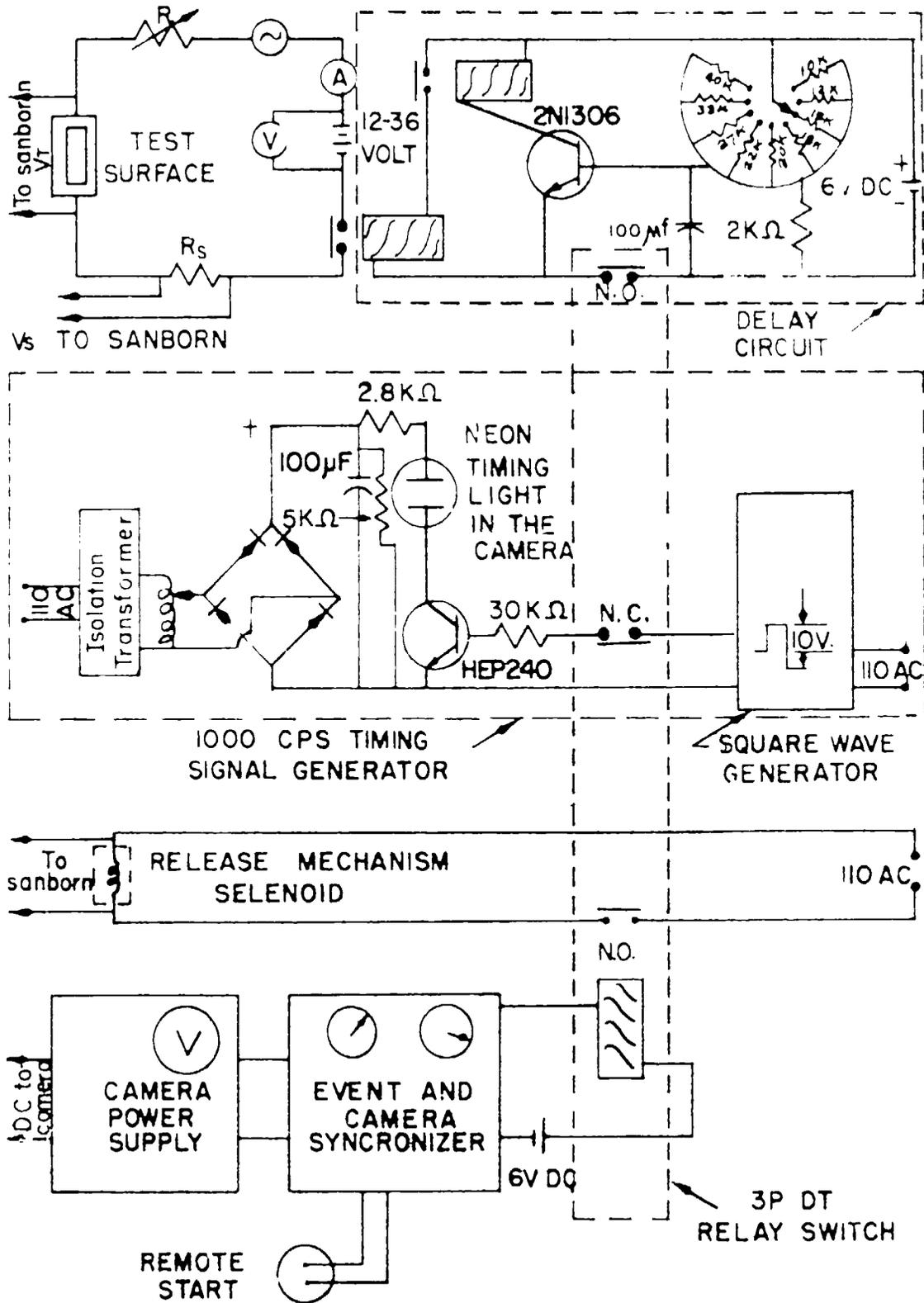
Fig. 15. Sequencing and delay circuit
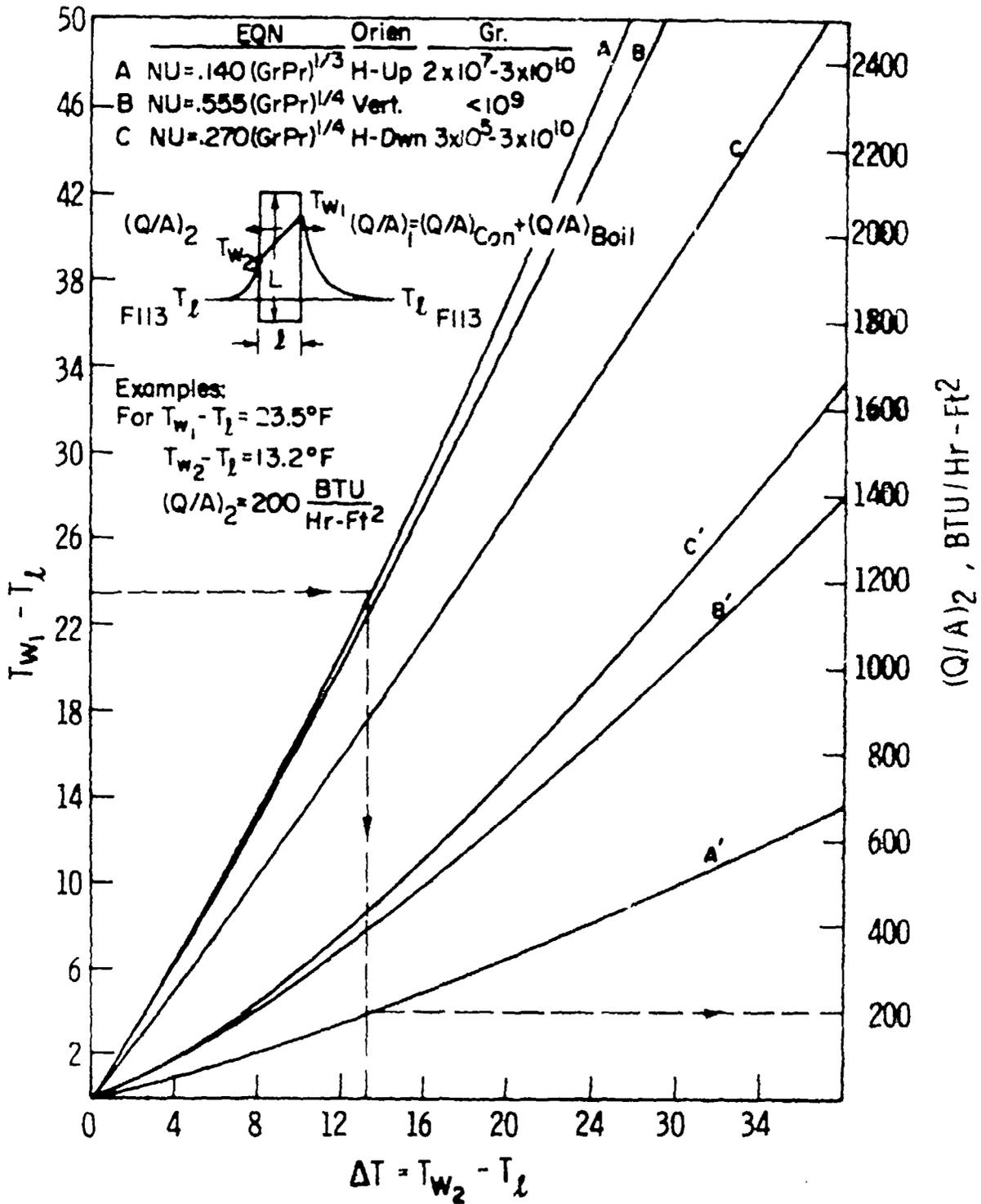
Fig. 16. Heat loss through glass substrate, F113
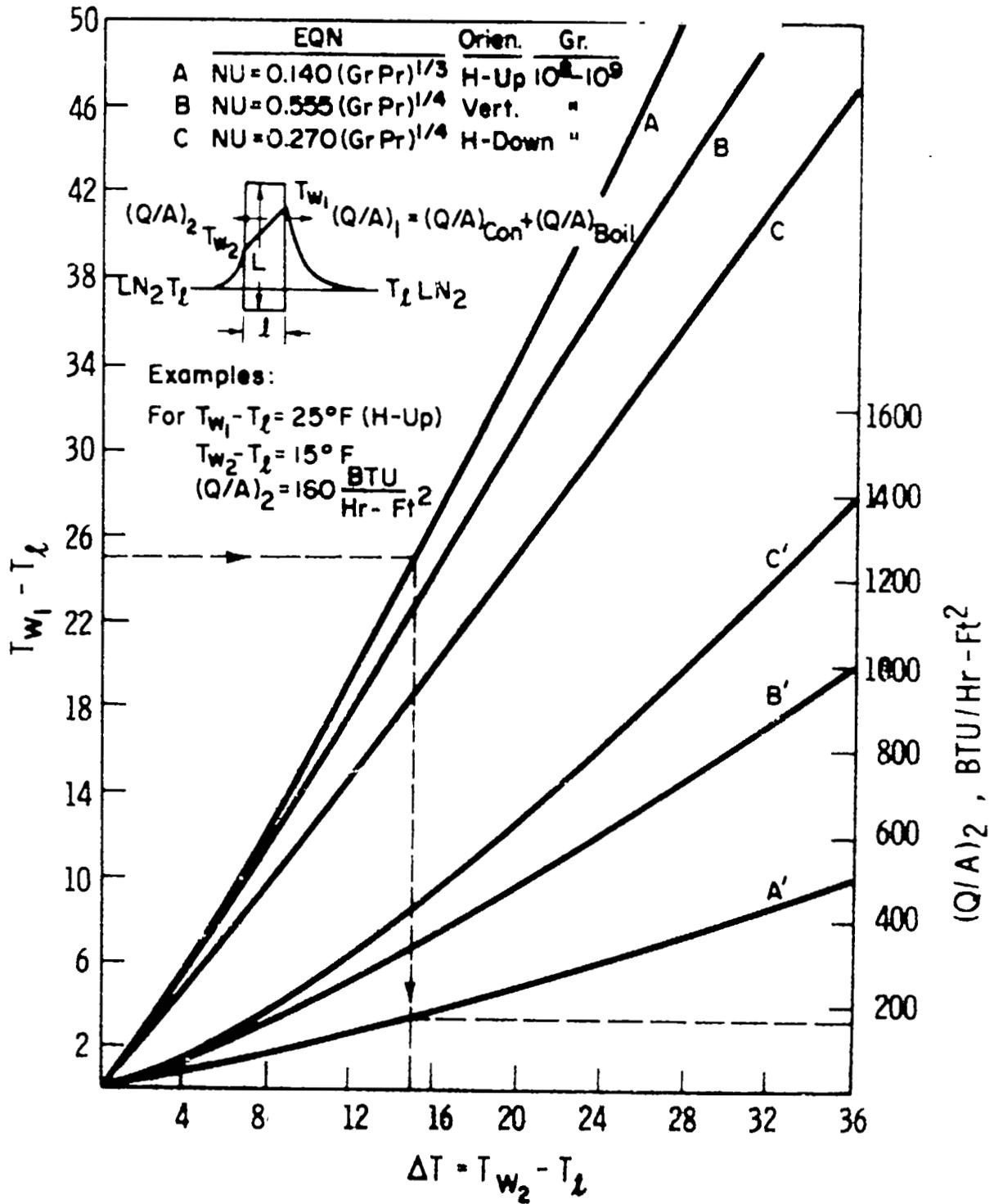
Fig. 17. Heat loss through glass substrate, LN_2
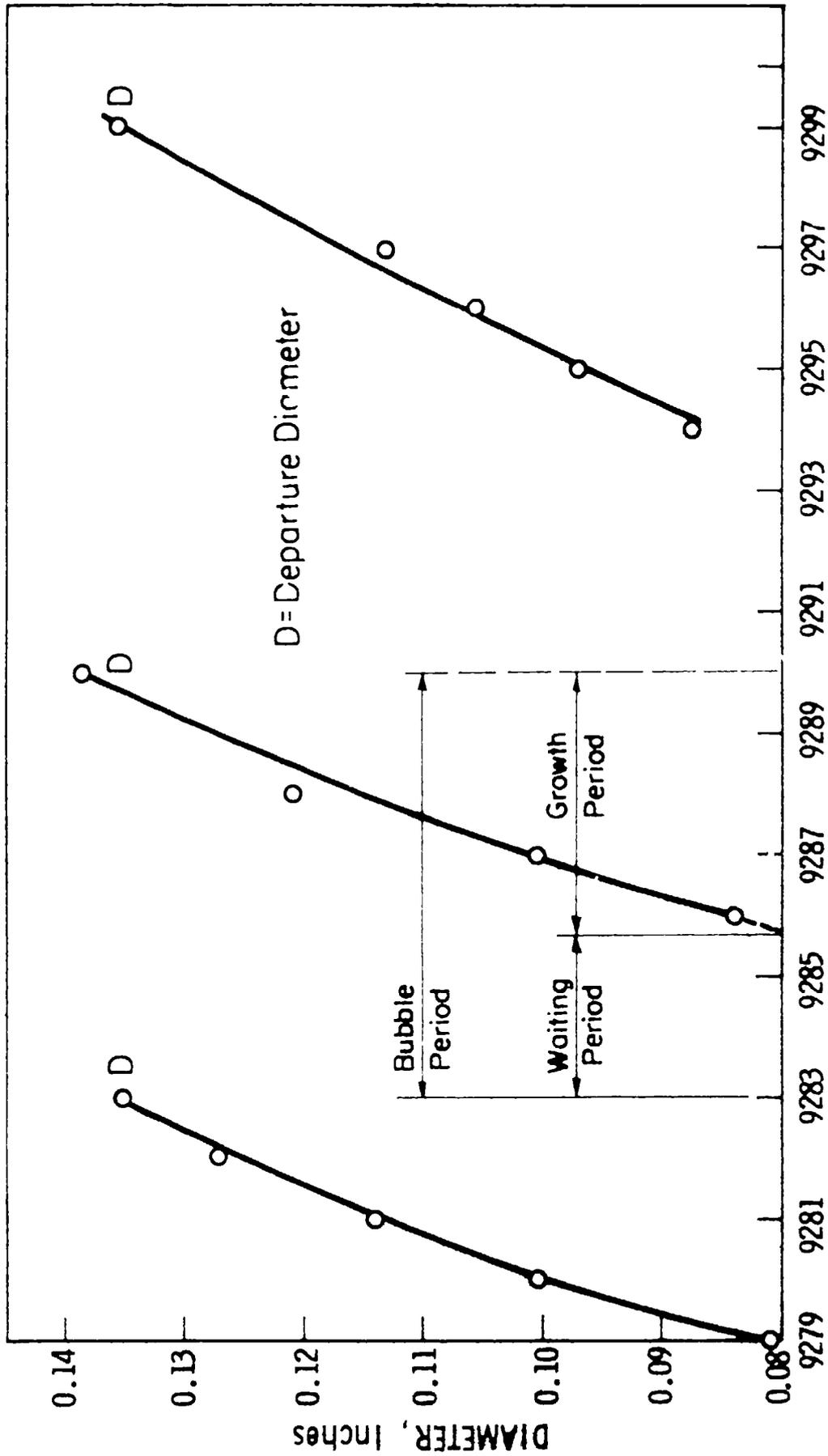
Fig. 18. Typical bubble growth at a/g=1, LN$_2$
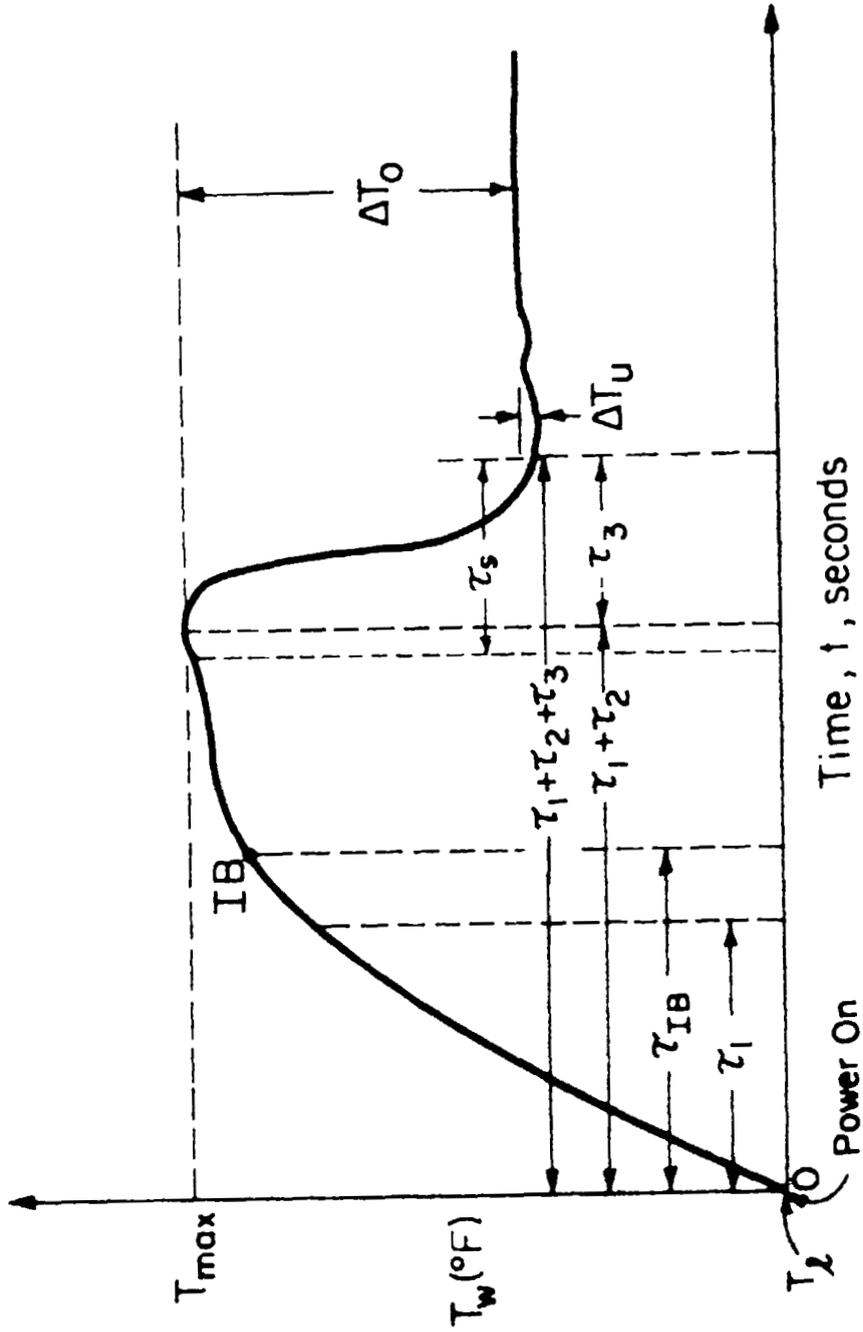
Fig. 13. Typical transient wall temperature
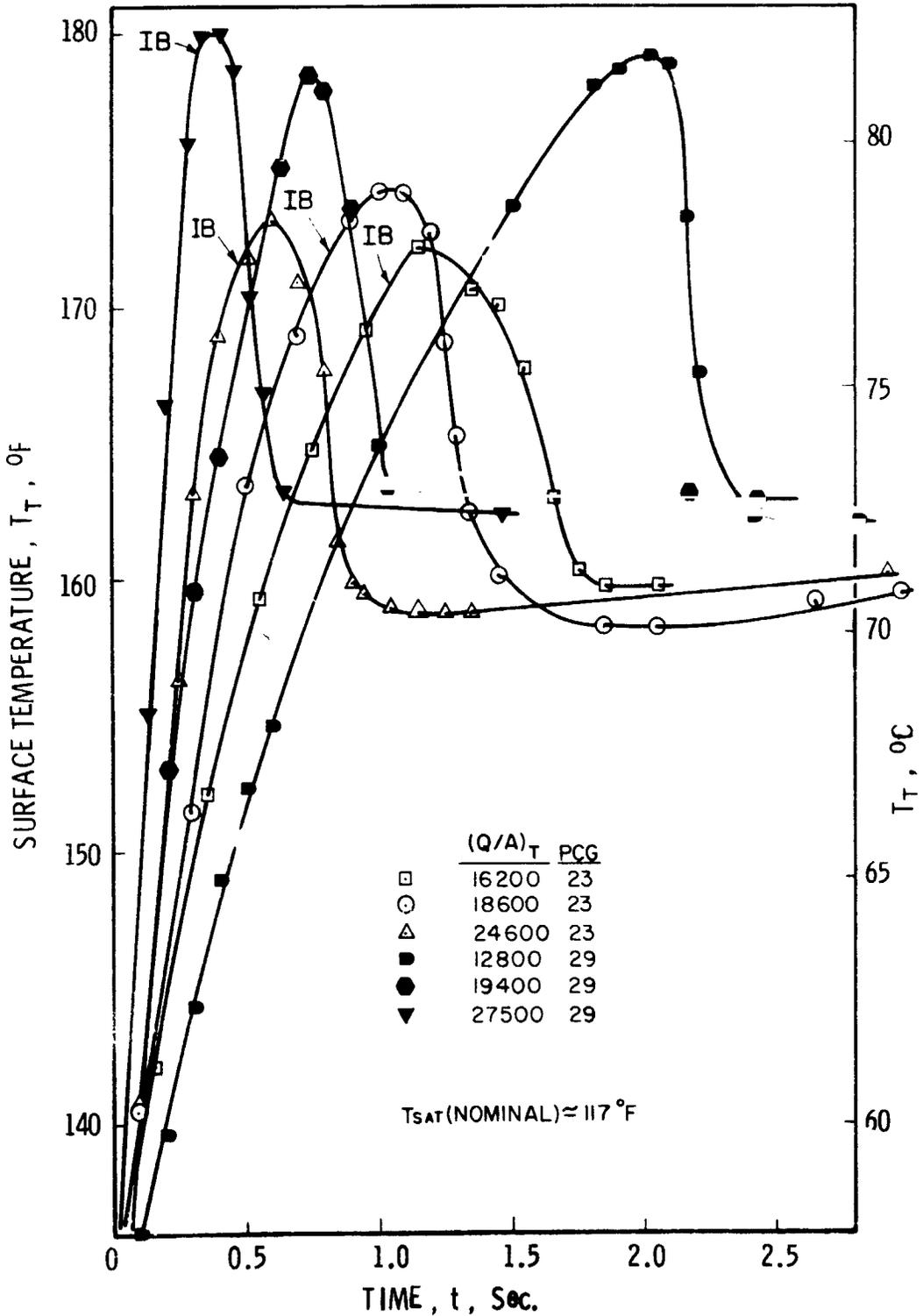
Fig. 20. Transient surface temperature, F113, vertical, a/g=1
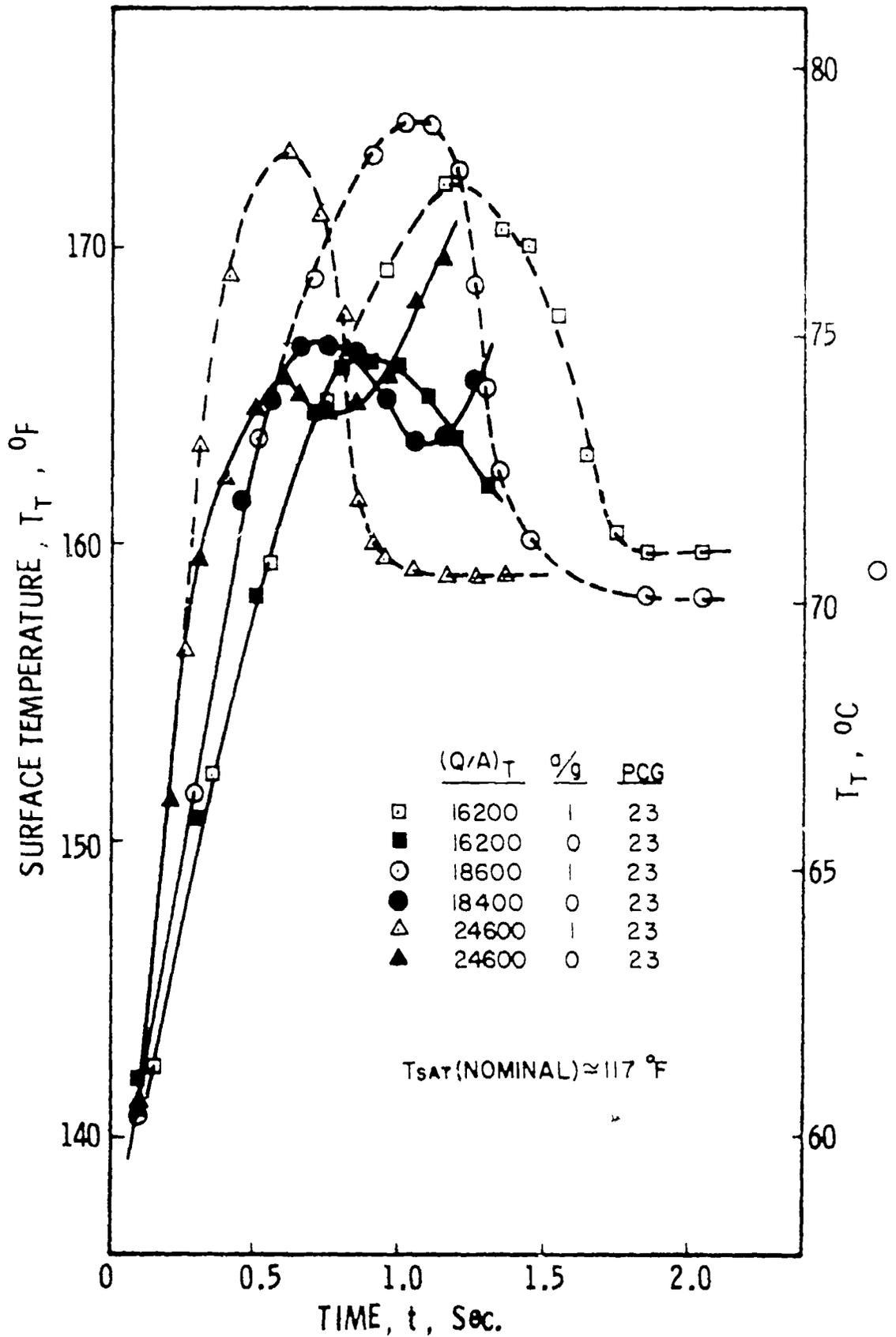
Fig. 21. Transient surface temperature, F113, vertical, a/g=1 and ≃ 0
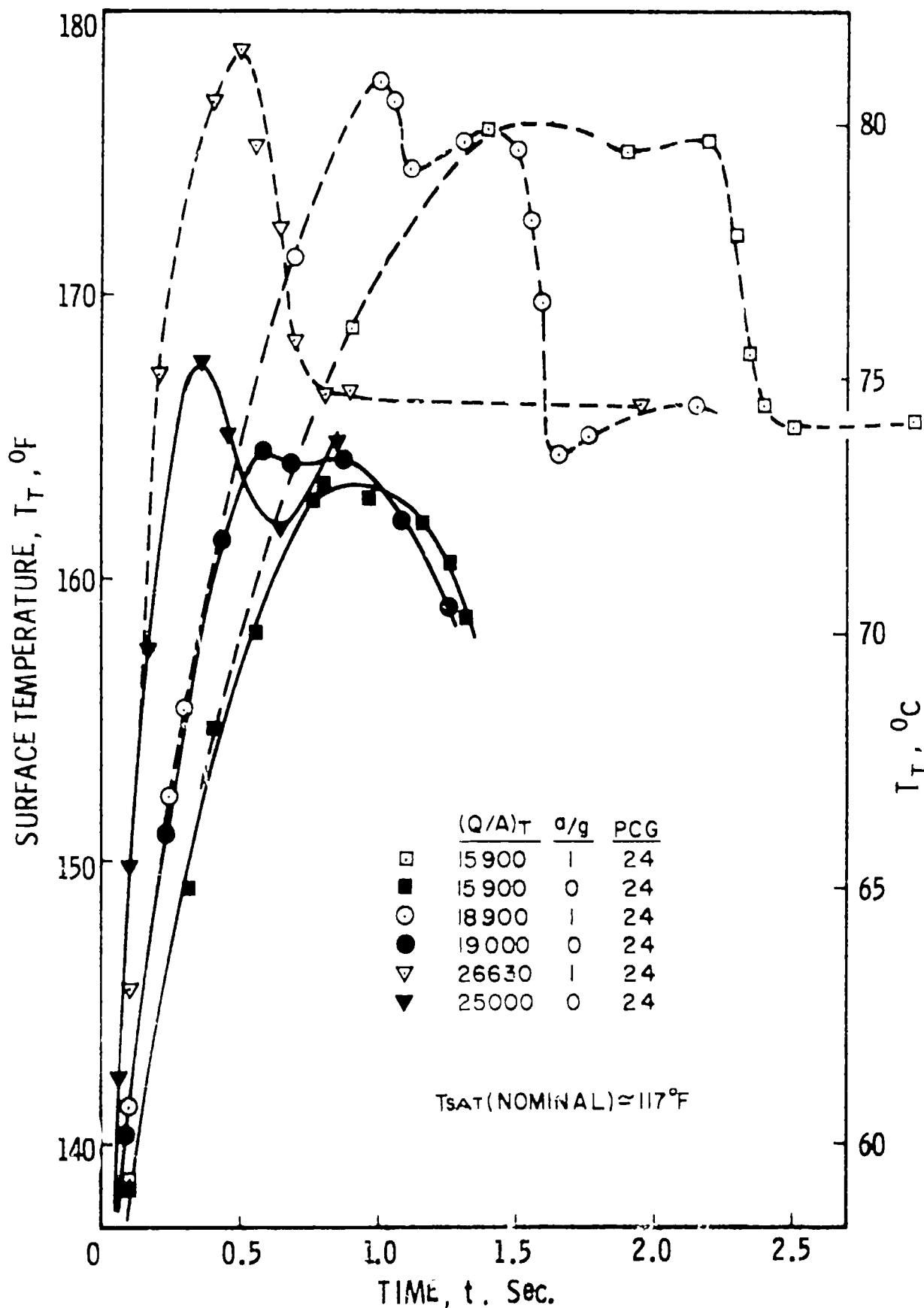
Fig. 22.   Transient surface temperature, F113, horizontal-up, a/g=1 and ≃ 0
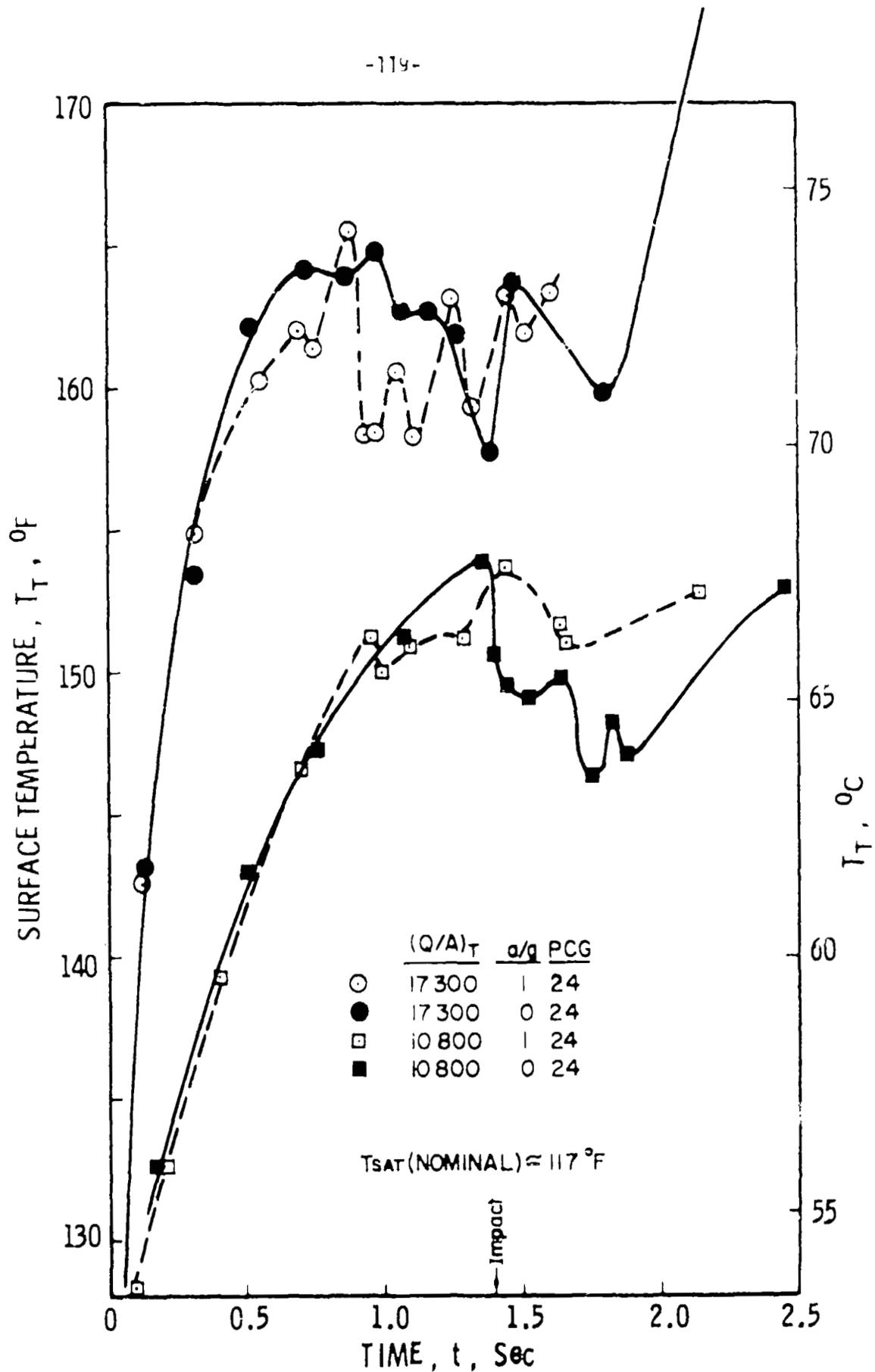
Fig. 23.   Transient surface temperature, F113, horizontal-down, a/g=1 and ≅ 0
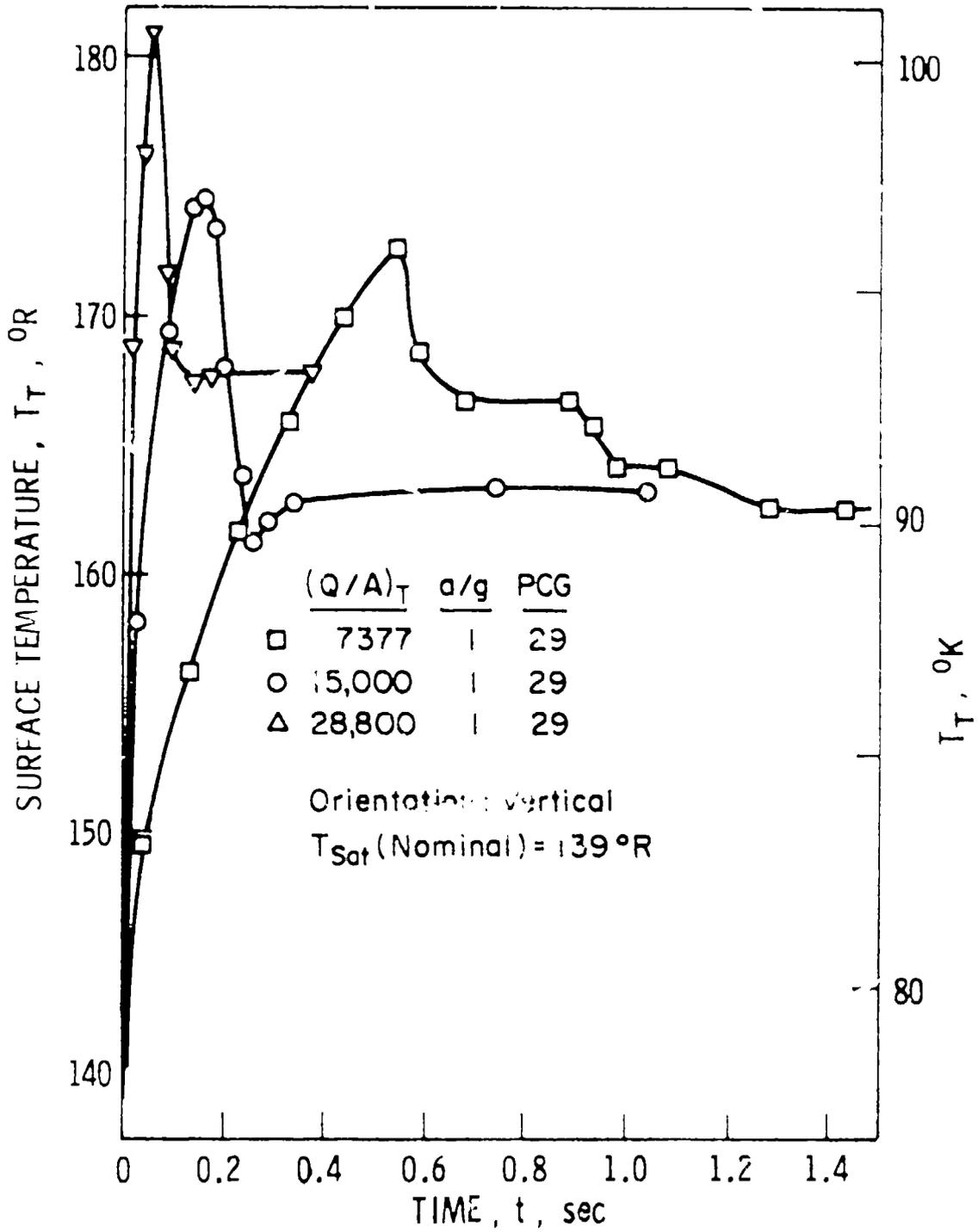
Fig. 24. Transient surface temperature, LN_2 vertical, a/g=1
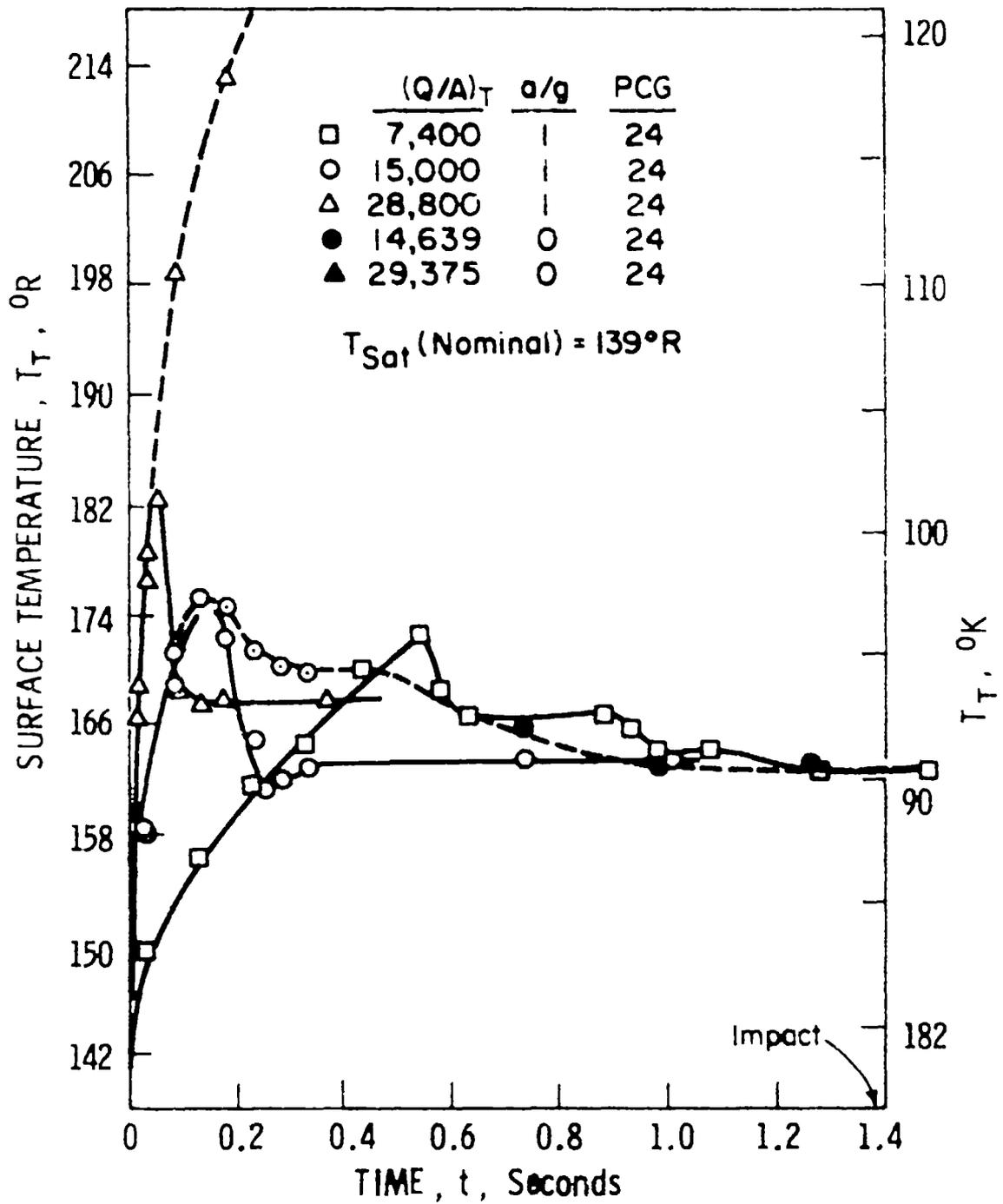
Fig. 25. Transient surface temperature, LN₂, vertical, a/g=1 anr≈0
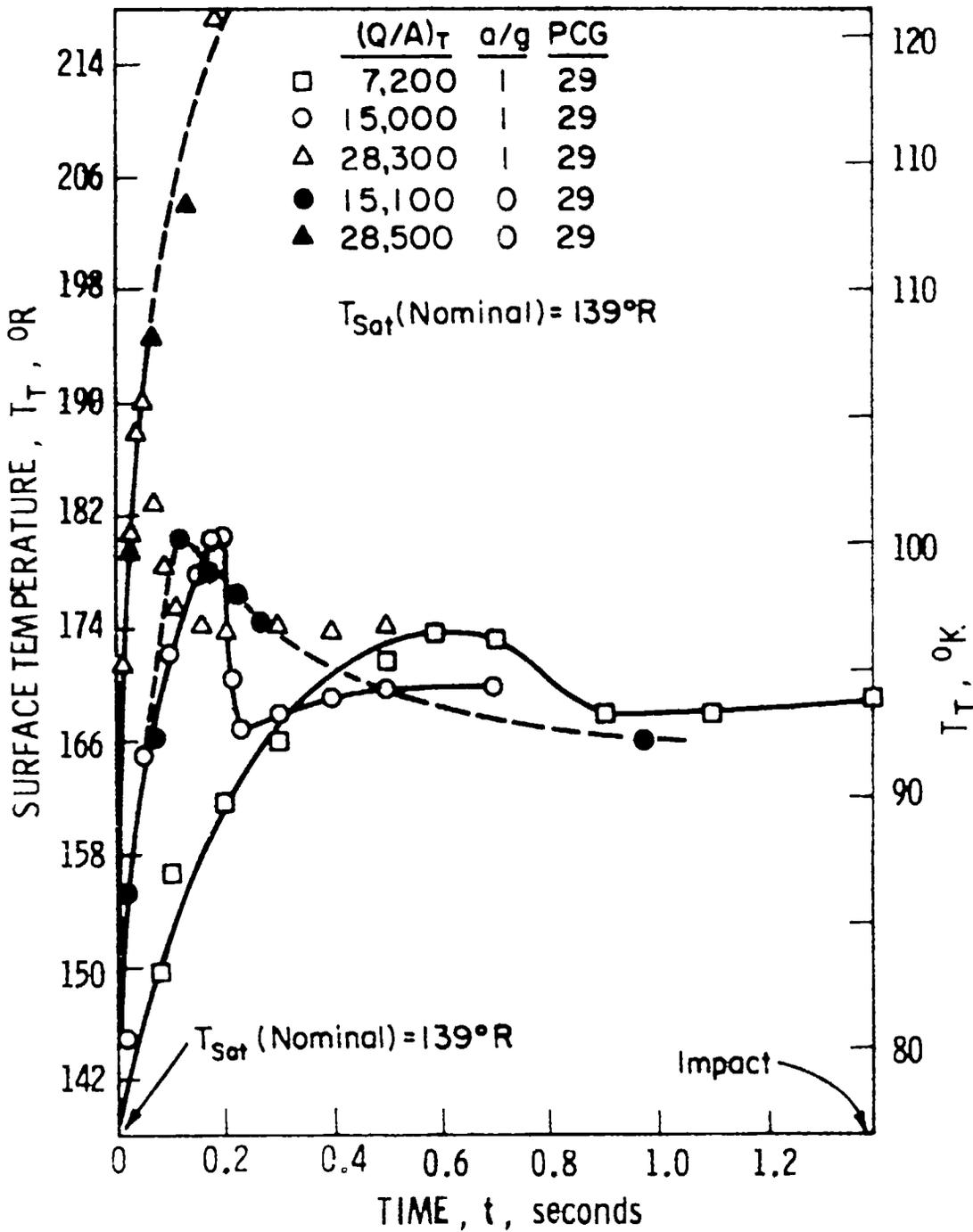
Fig. 26. Transient surface temperature, LN_2, horizontal-up, $a/g=1$ and $\simeq 0$
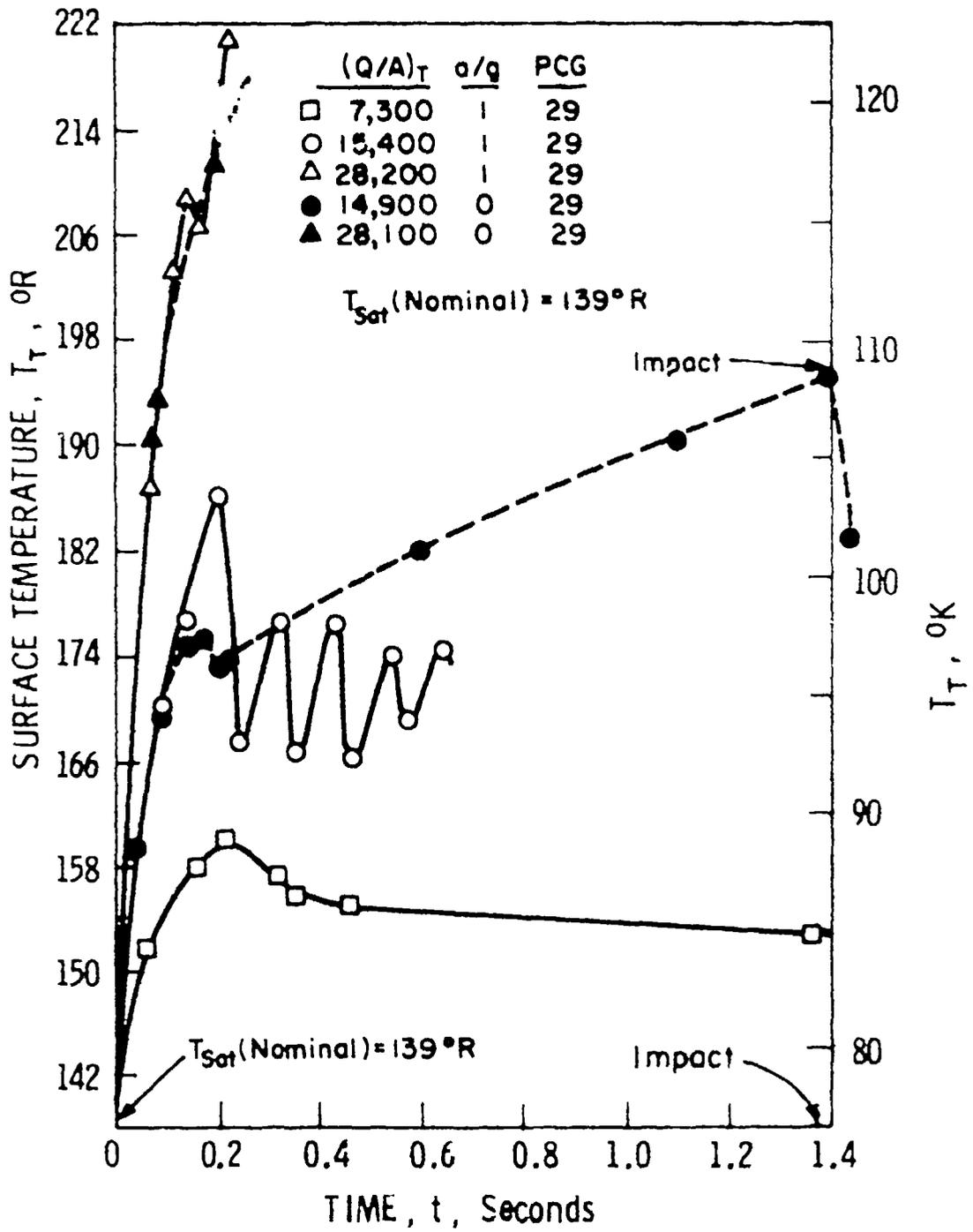
Fig. 27. Transient surface temperature, LN_2, horizontal-down, $a/g=1$ and $\simeq 0$
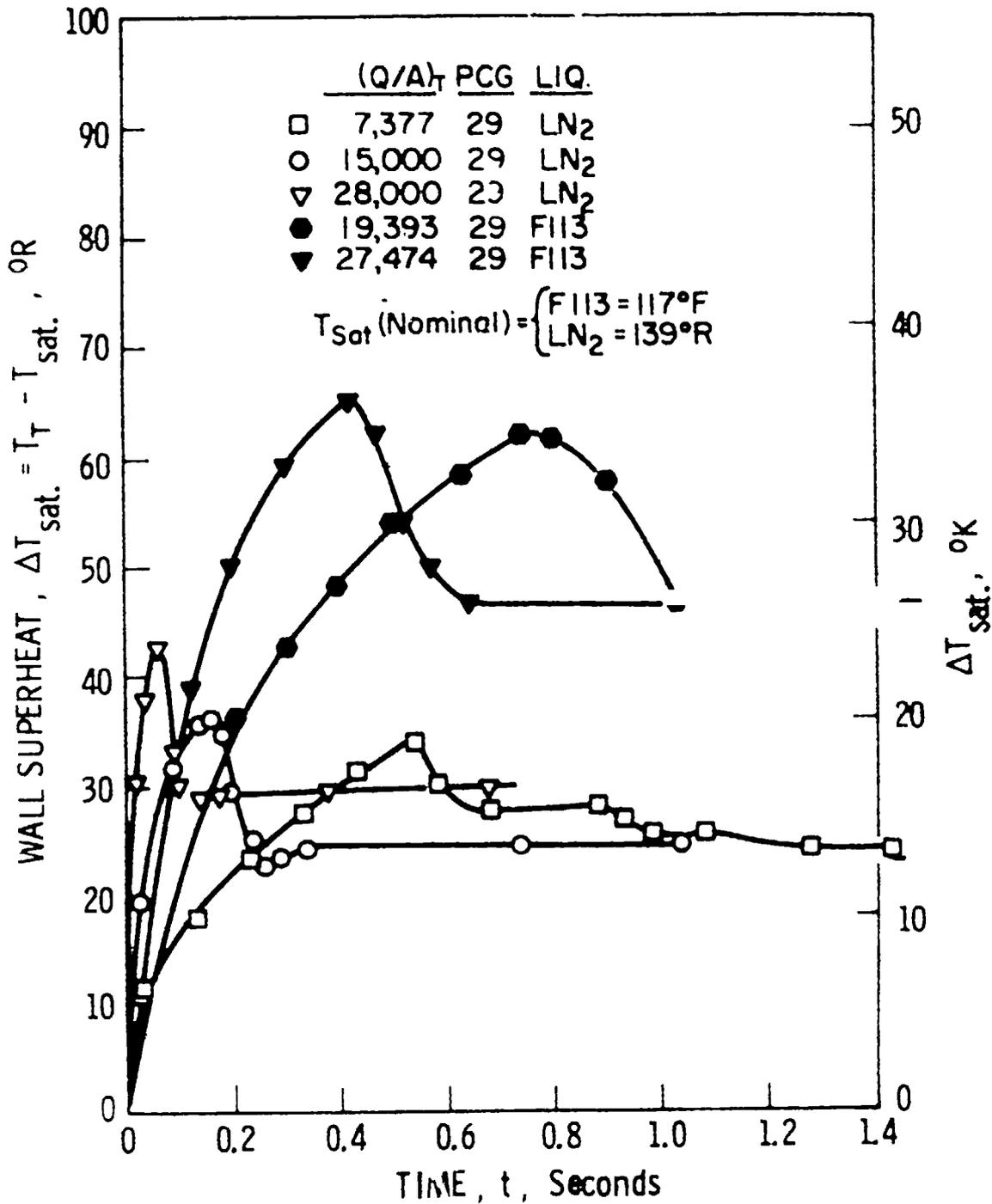
Fig. 28. Comparison of transient surface temperature of a vertical surface in F113 and LN$_2$, a/g=1
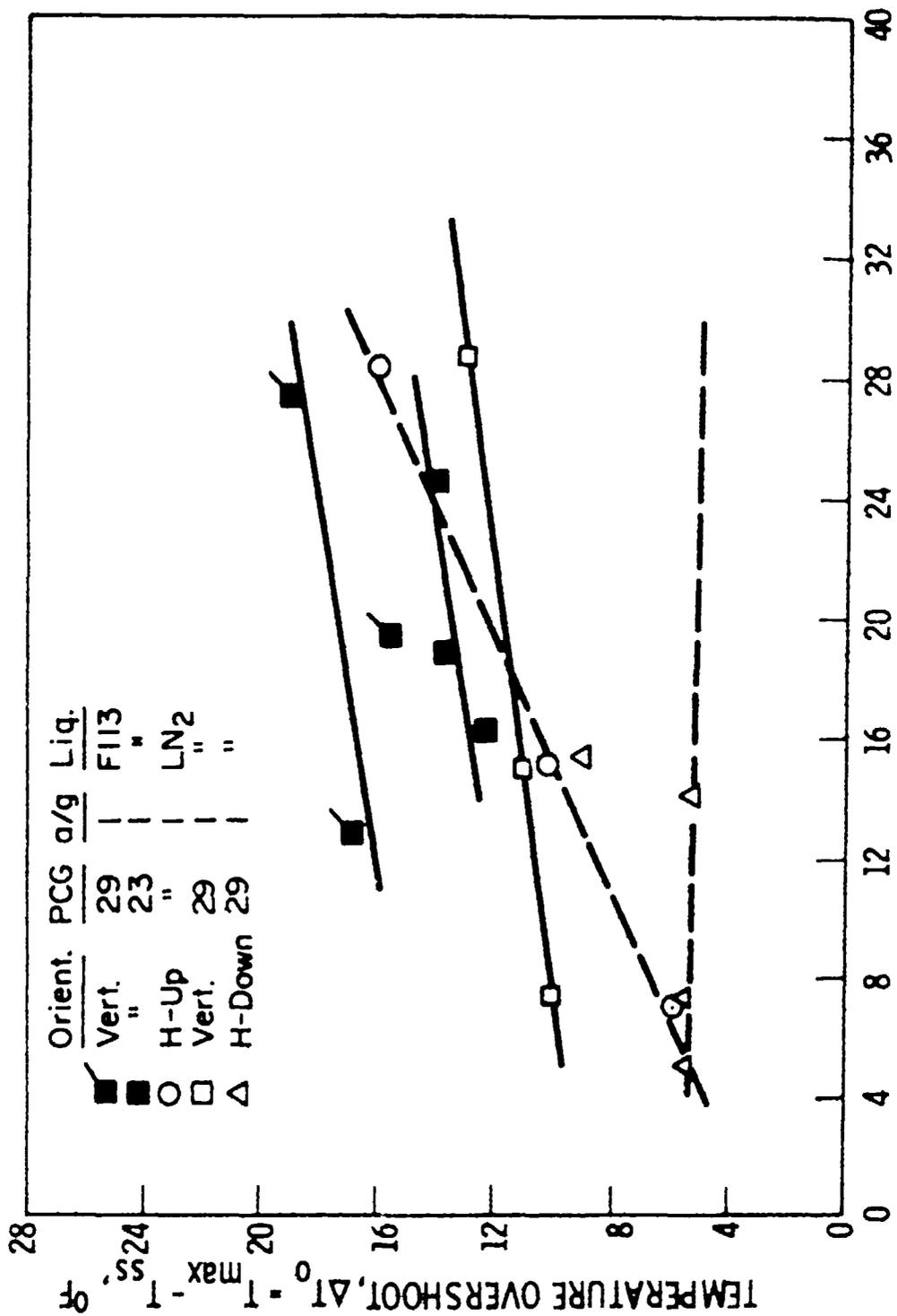
Fig. 29. Effect of heat flux, orientation and gravity on temperature overshoot
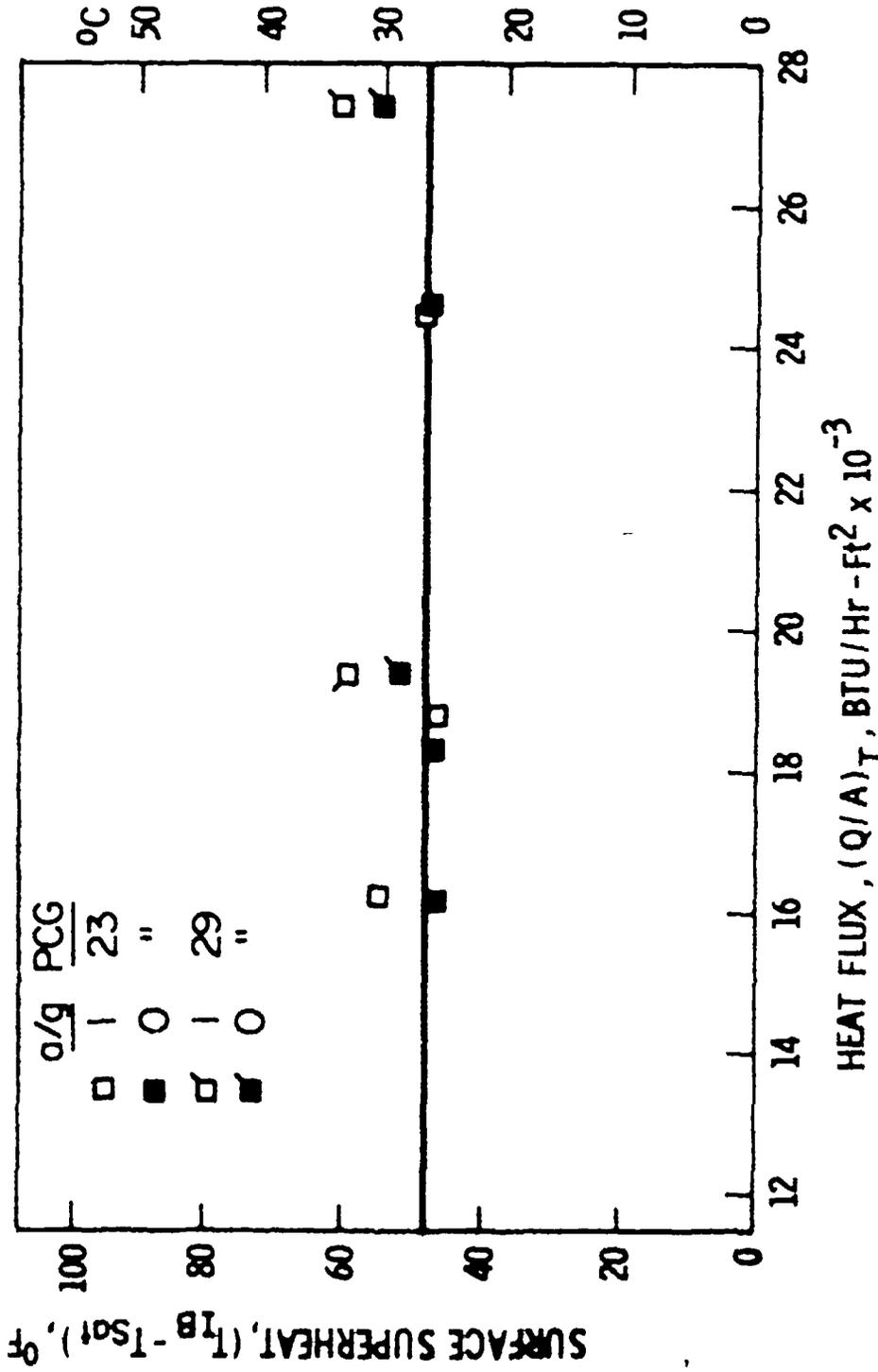
Fig. 30. Surface superheat for incipient boiling, F113, vertical, a/g=1 and ≈ 0
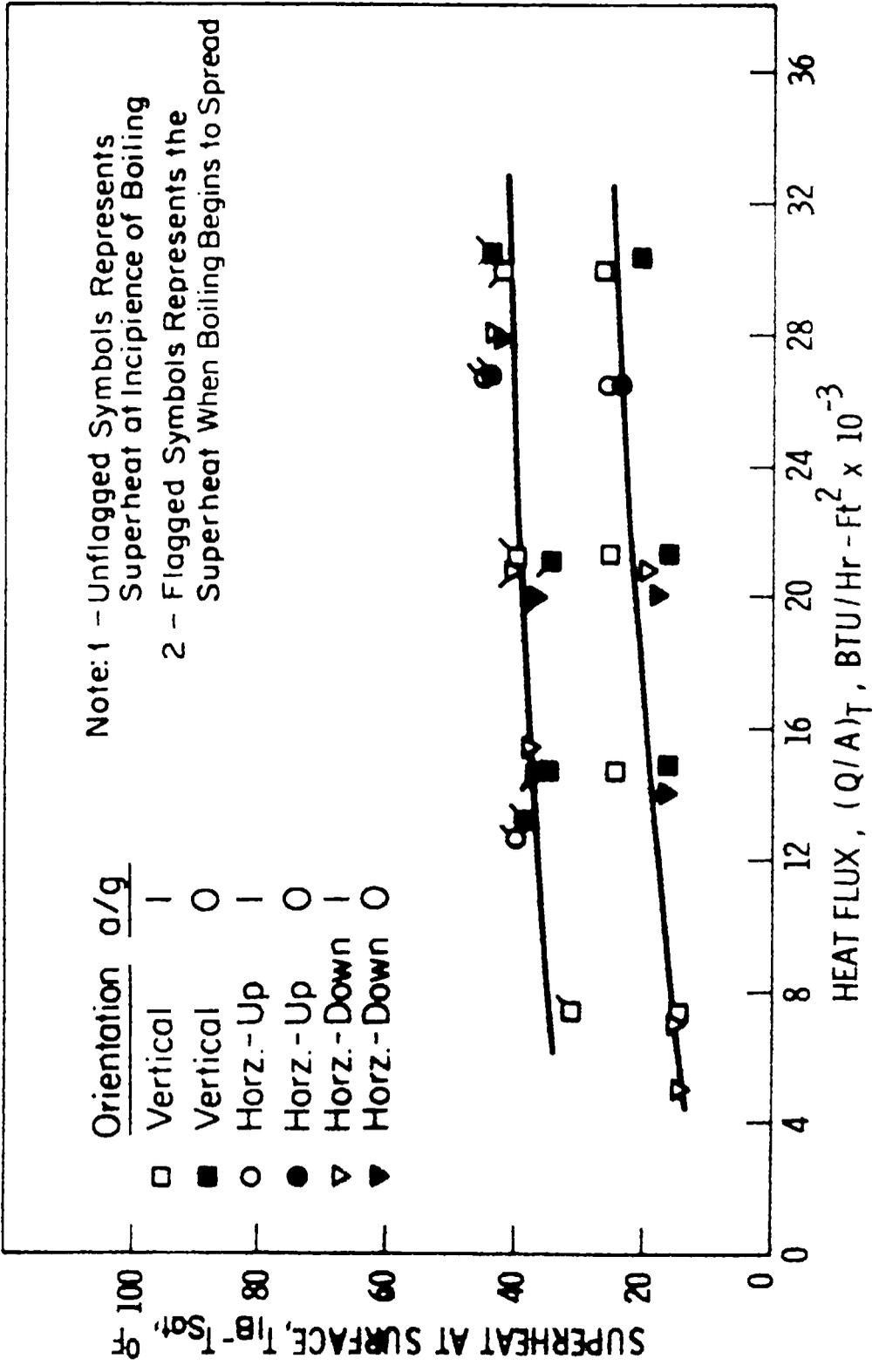
Fig. 31. Surface superheat for incipient boiling, LN₂, all orientations, a/g=1 and ≅ 0

$$\frac{T_T - T_i}{(Q/A)_\ell} = .0223\ t^{\frac{1}{2}}$$

TIME t IN SECONDS

$(Q/A)_\ell$	ORIENT.	a/g
16 300	Vert.-Up	1
27 400	Vert.-Up	1
15 900	Horiz.-Up	1
26 600	Horiz.-Up	1
17 300	Horiz.-Down	1
25 100	Horiz.-Down	1
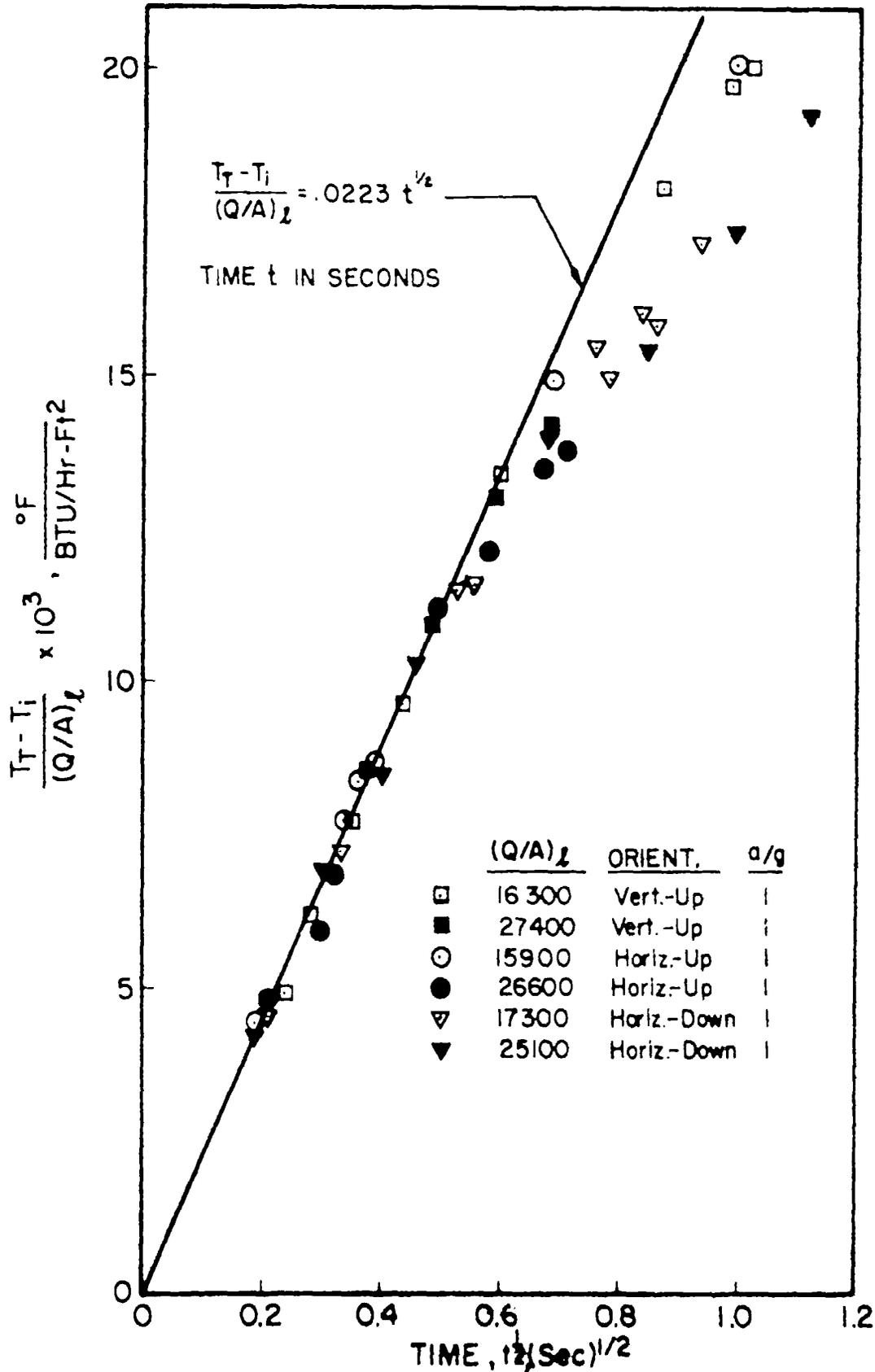
Fig. 32. Comparison of computed and measured transient thin film temperature, F113

	$(Q/A)_T$	$(Q/A)_\ell$	Orientation	Run No.
□	7,300	3,600	Vertical	111
■	7,100	3,500	Horz.-Up	127
○	15,000	7,400	Vertical	110B
●	15,100	7,500	Horz.-Up	126
△	28,800	14,200	Vertical	112
▲	28,300	13,900	Horz.-Up	131B
▽	28,300	13,900	Horz.-Down	145B
⊓	15,400	7,600	Horz.-Down	136B
◇	7,300	3,600	Horz.-Down	145A

Theoretical Equation

$$(T_T - T_i)/(Q/A)_\ell = .0069\, t^{1/2}$$
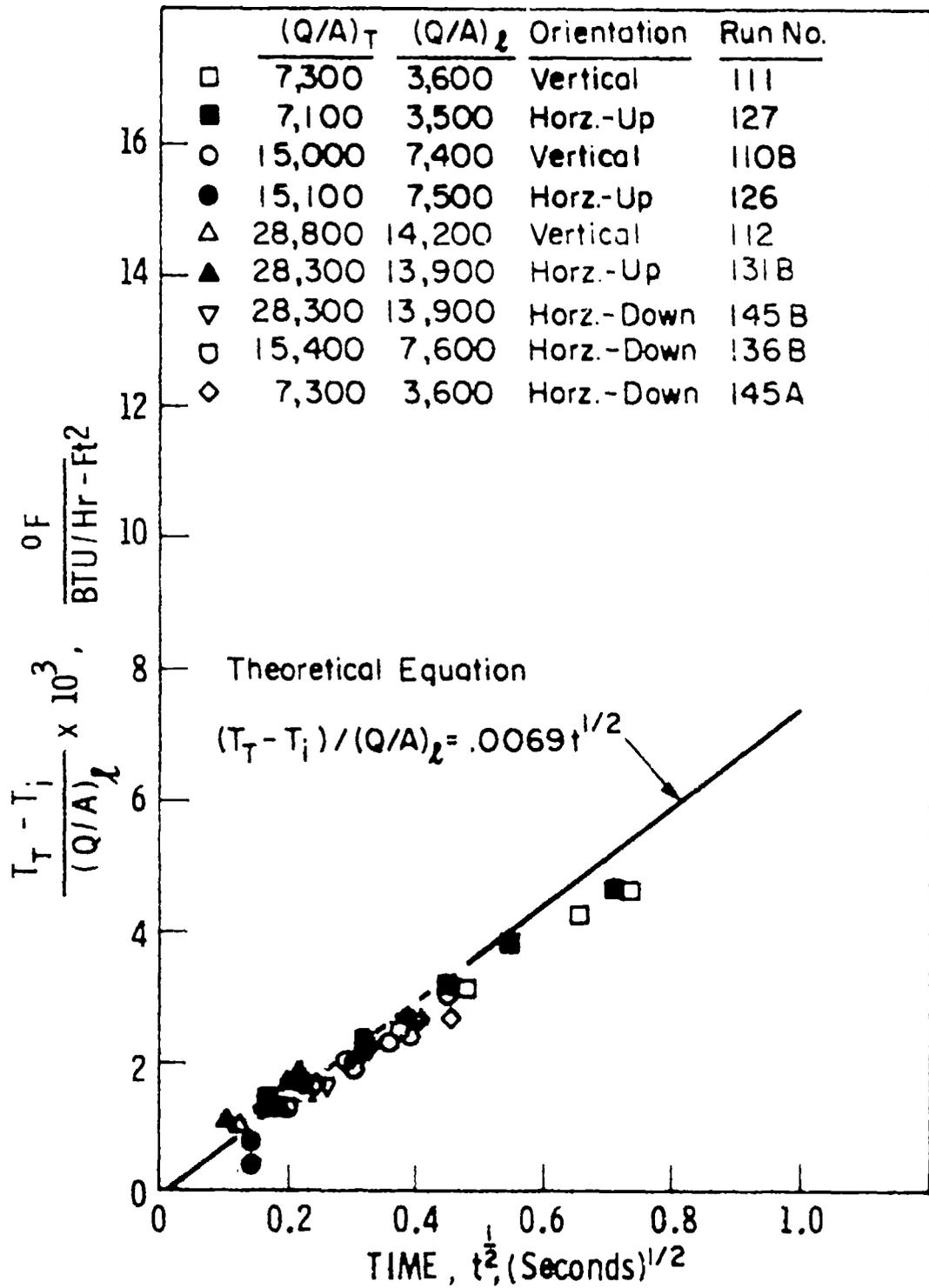
Fig. 33. Comparison of computed and measured transient thin film temperature, LN_2
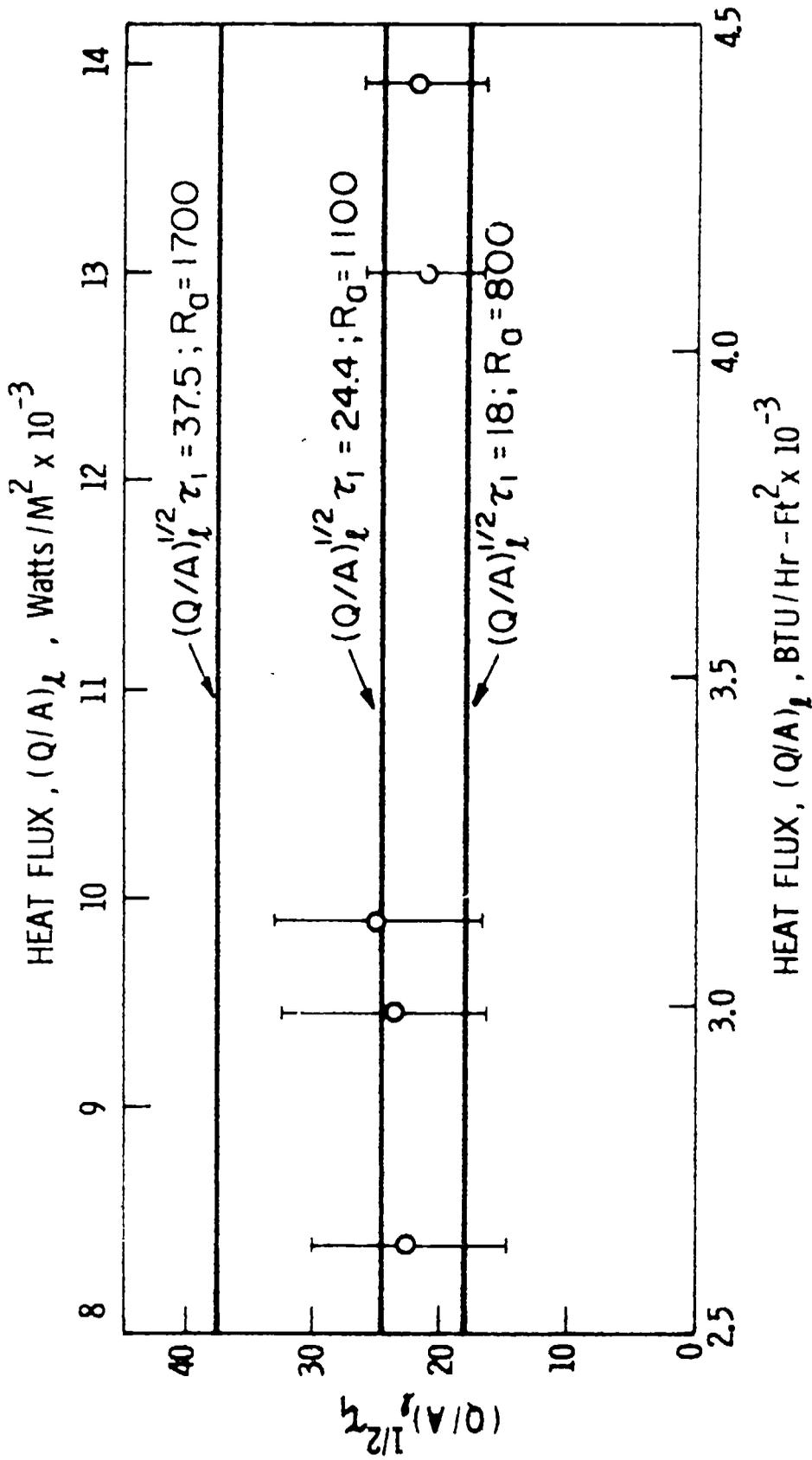
Fig. 34. Onset of convection, F113, horizontal-up, a/q=1
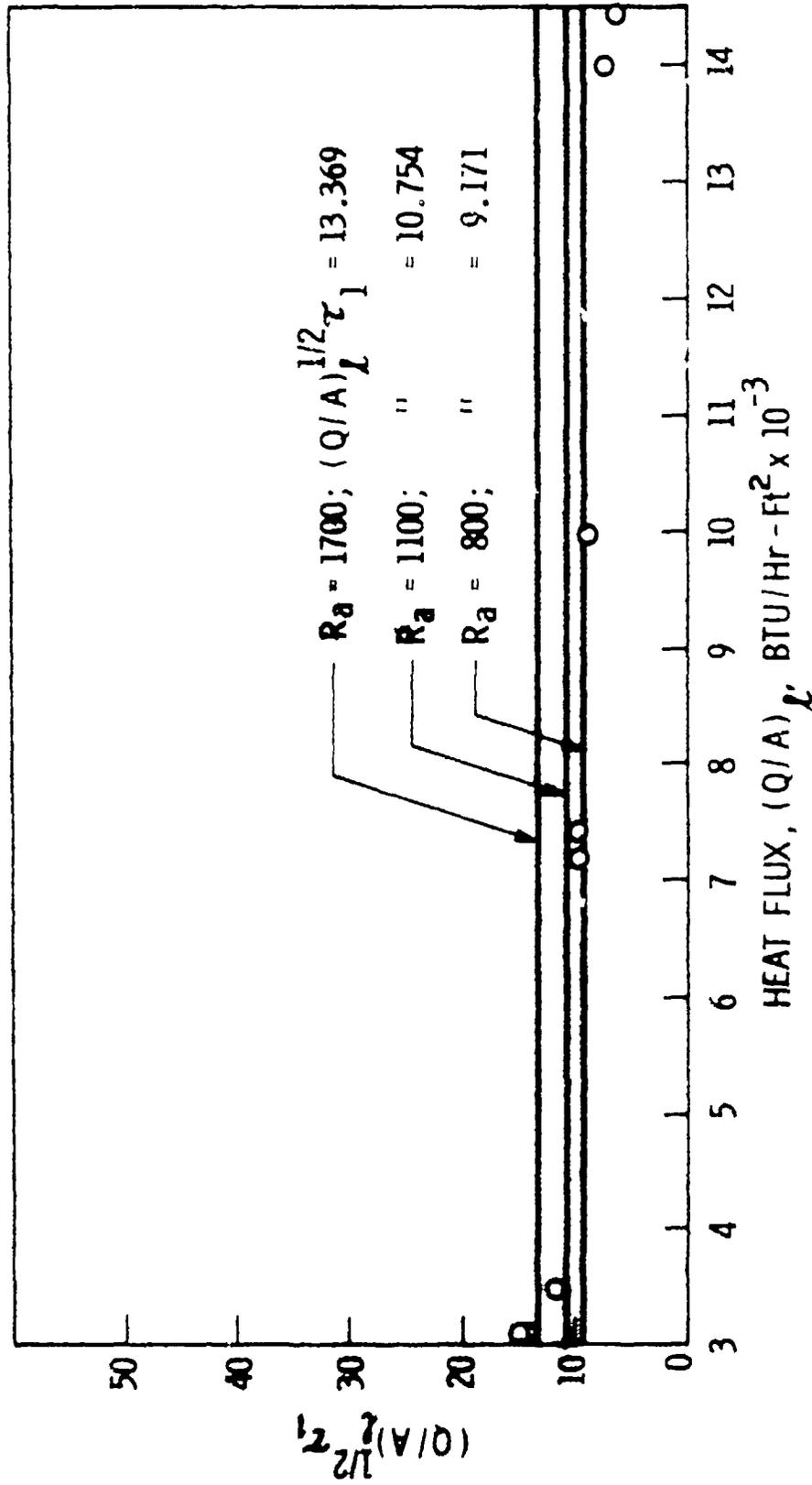
Fig. 35. Onset of convection, LN_2, horizontal-up, $a/g=1$
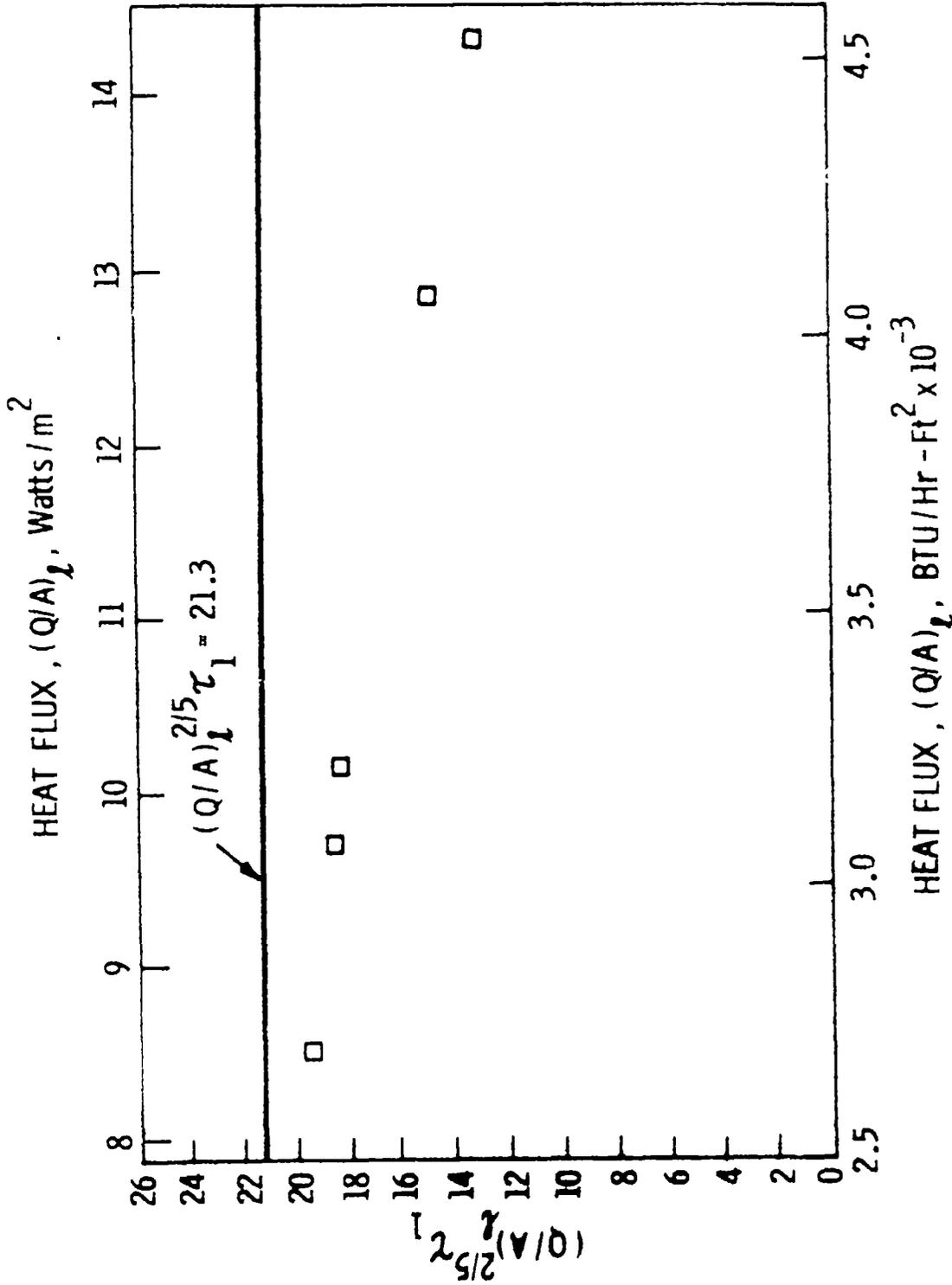
Fig. 36. Onset of convection, F113, vertical, a/g=1
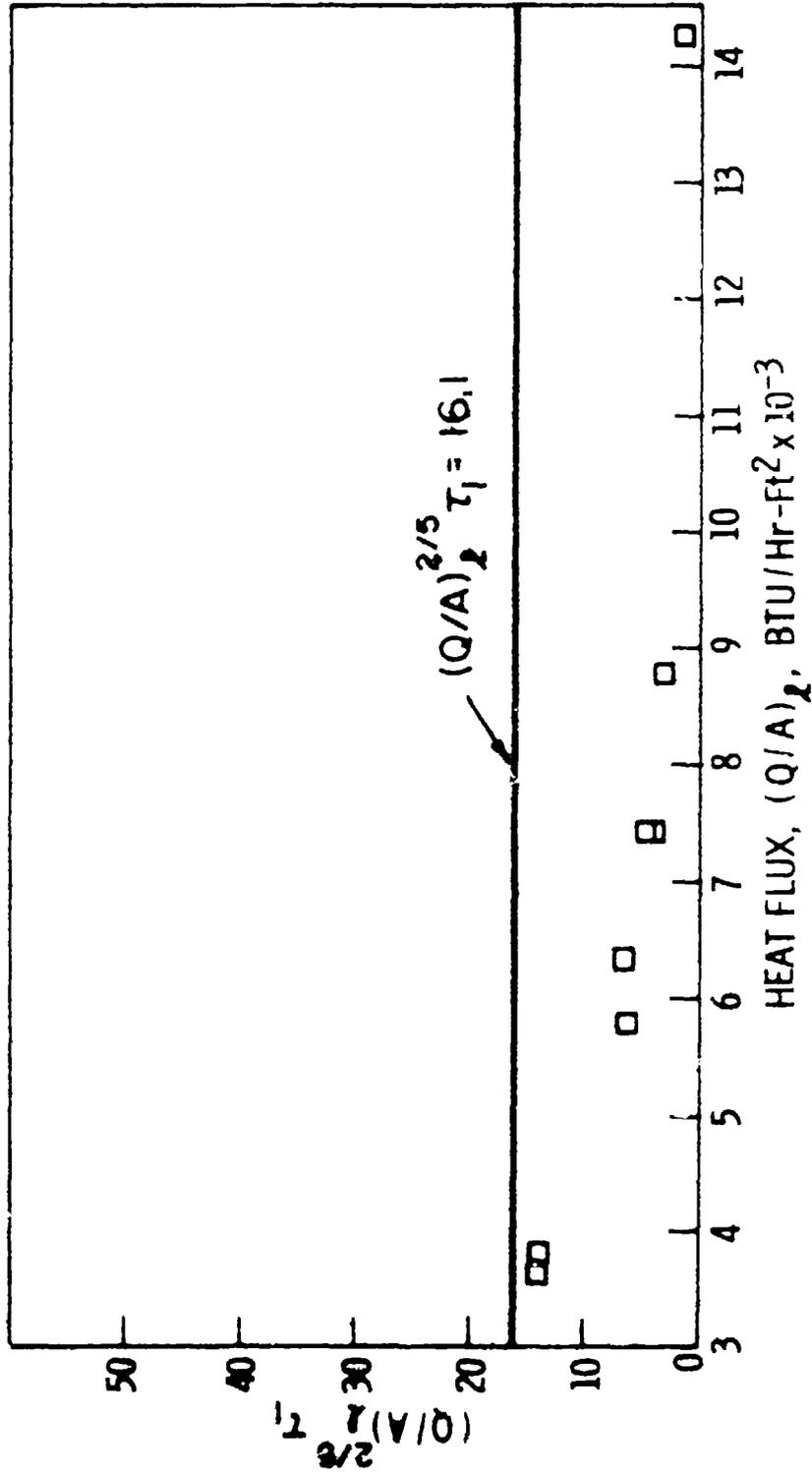
Fig. 37. Onset of convection, LN_2, vertical, $a/g=1$
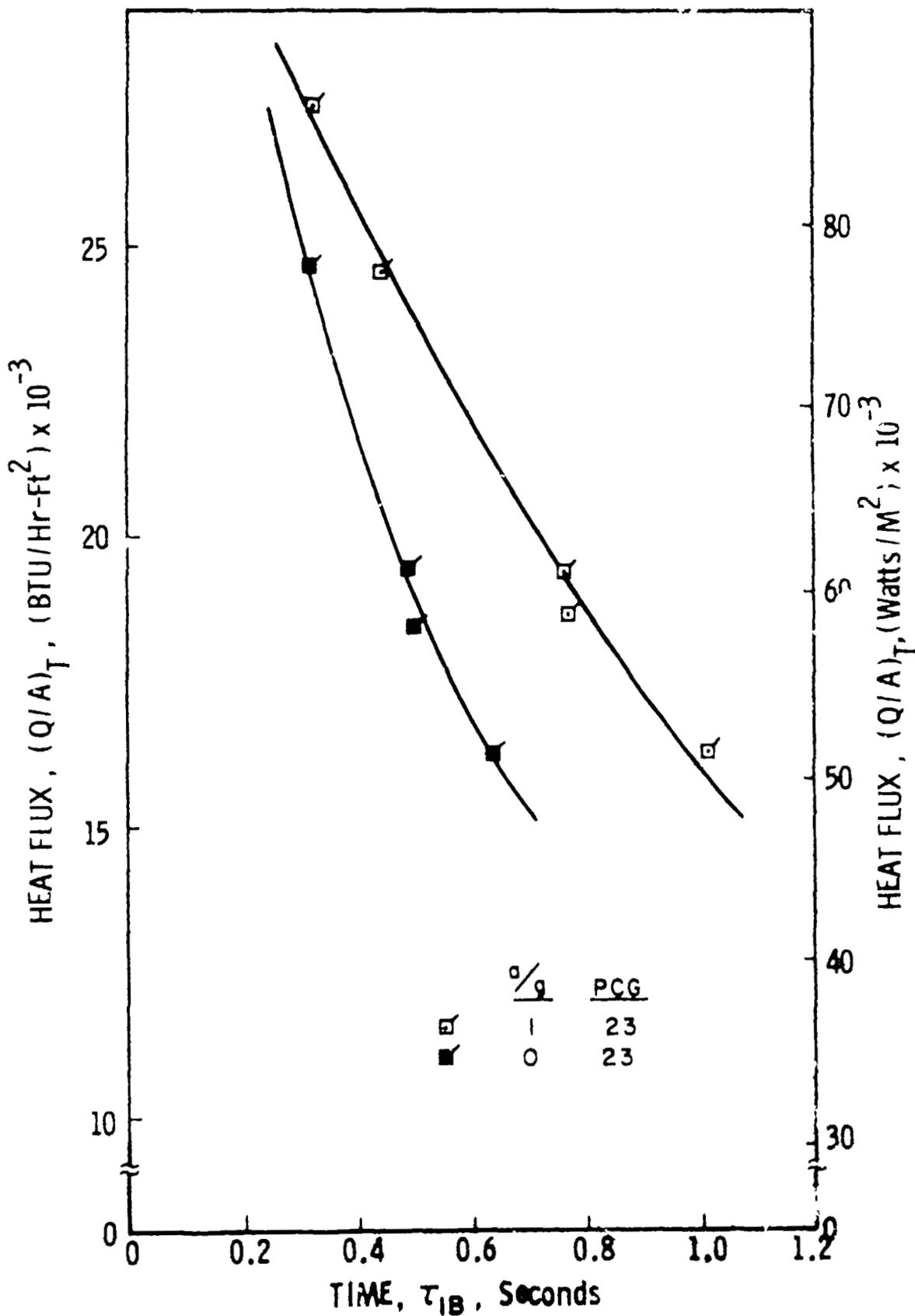
Fig. 38. Elapsed time for incipient boiling, F113, vertical, a/g=1 and ≈0
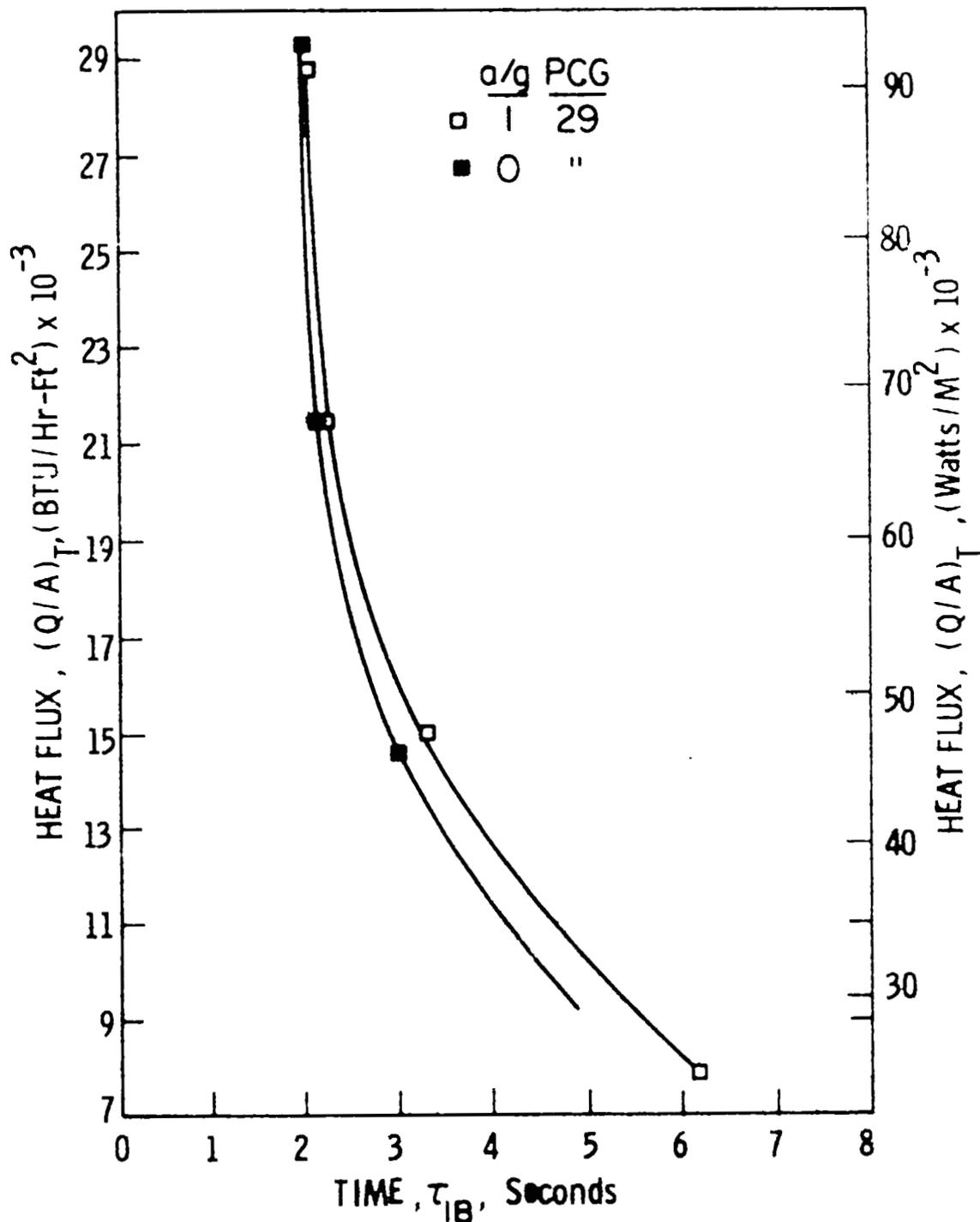
Fig. 39. Elapsed time for incipient boiling, LN_2, vertical, a/g=1 and ≈0
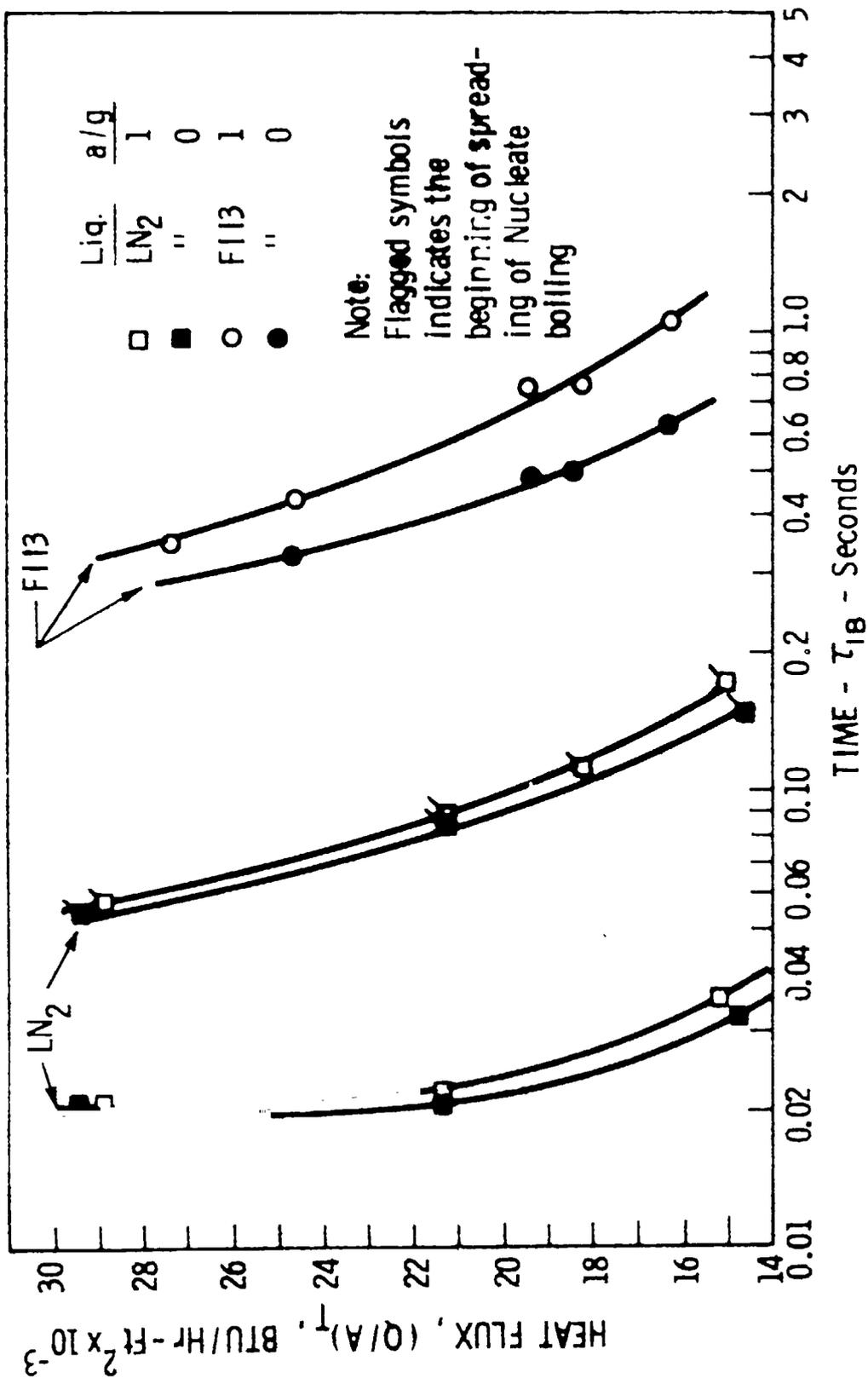
Fig. 40. Elapsed time for incipient boiling, F113 and LN_2
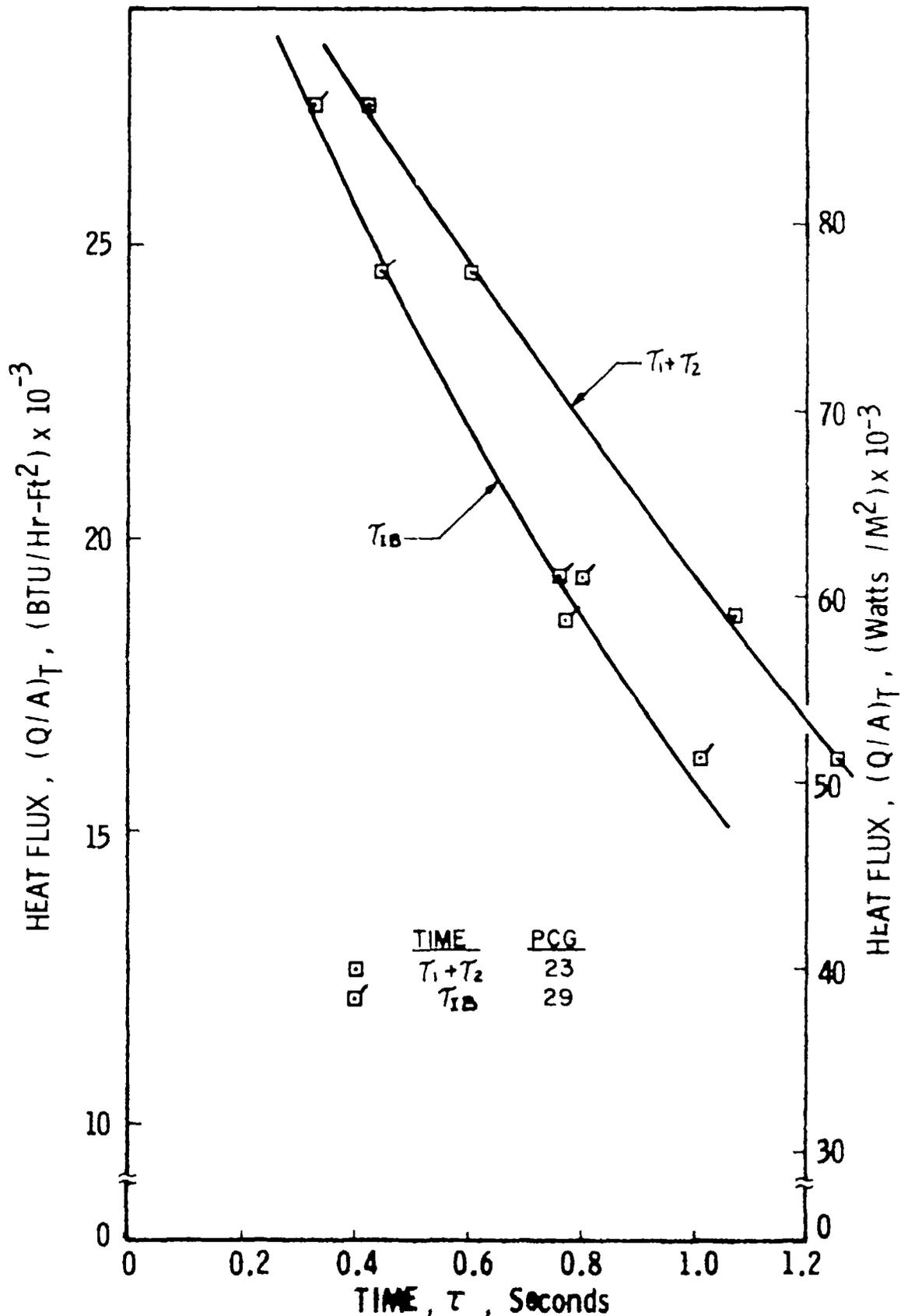
Fig. 41. Elapsed time for incipient boiling, and maximum surface temperature, F113, vertical, a/g=1
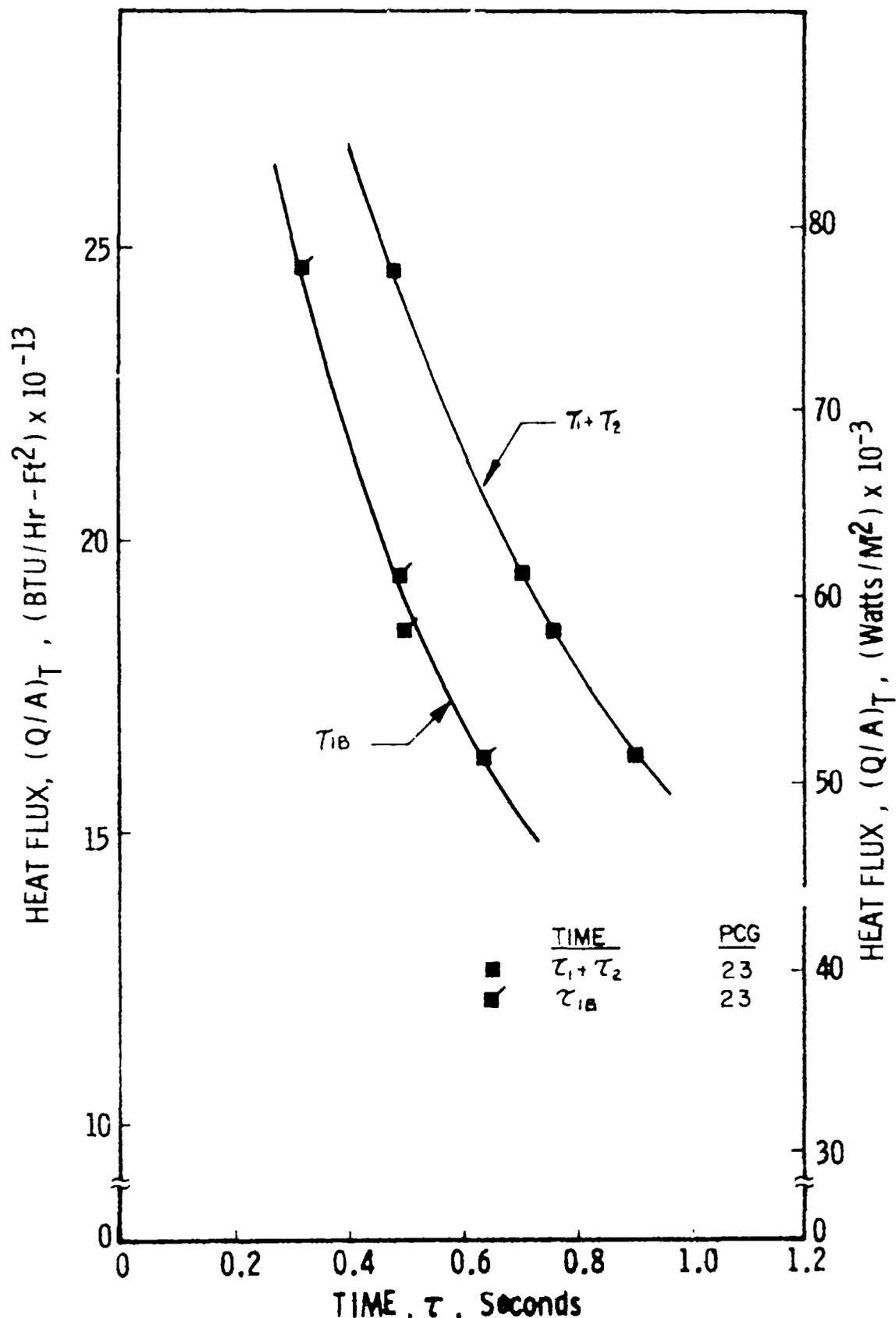
Fig. 42. Elapsed time for incipient boiling, and maximum surface temperature, F113, vertical, a/g ≠ 0
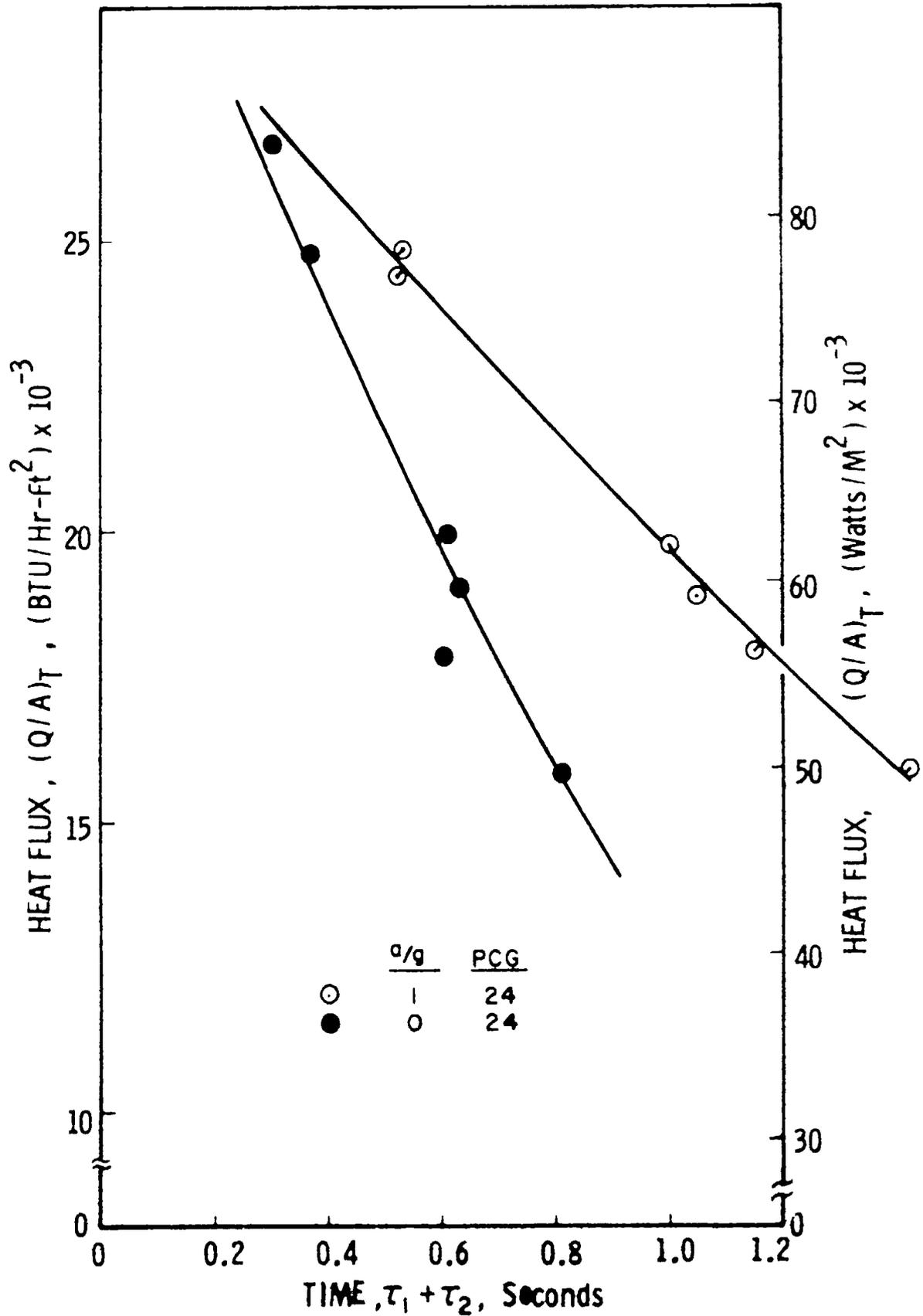
Fig. 43. Elapsed time for maximum surface temperature, F113, horizontal-up, a/g=1 and ≈ 0
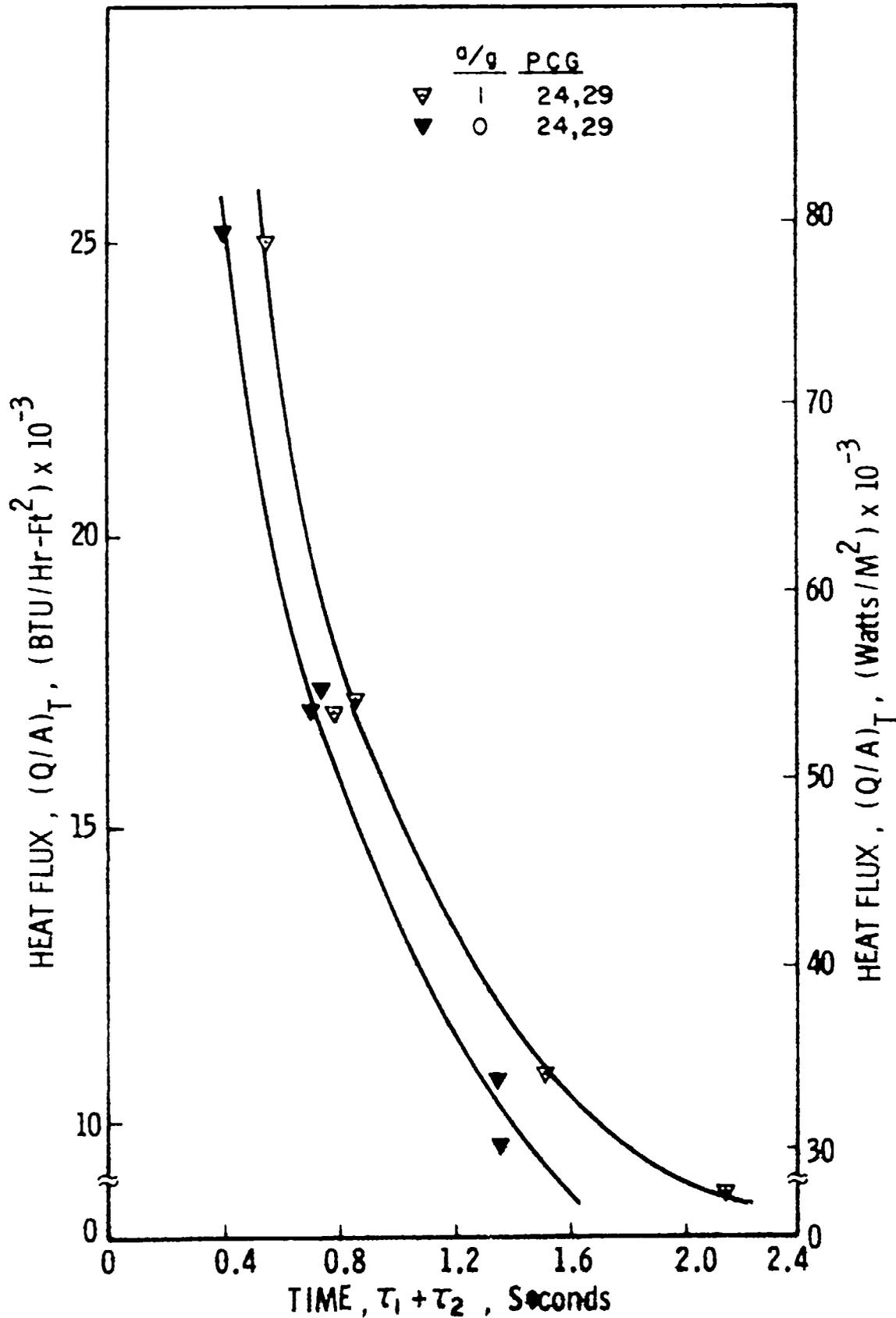
Fig. 44. Elapsed time for maximum surface temperature, F113, horizontal-down, a/g=1 and ≃ 0
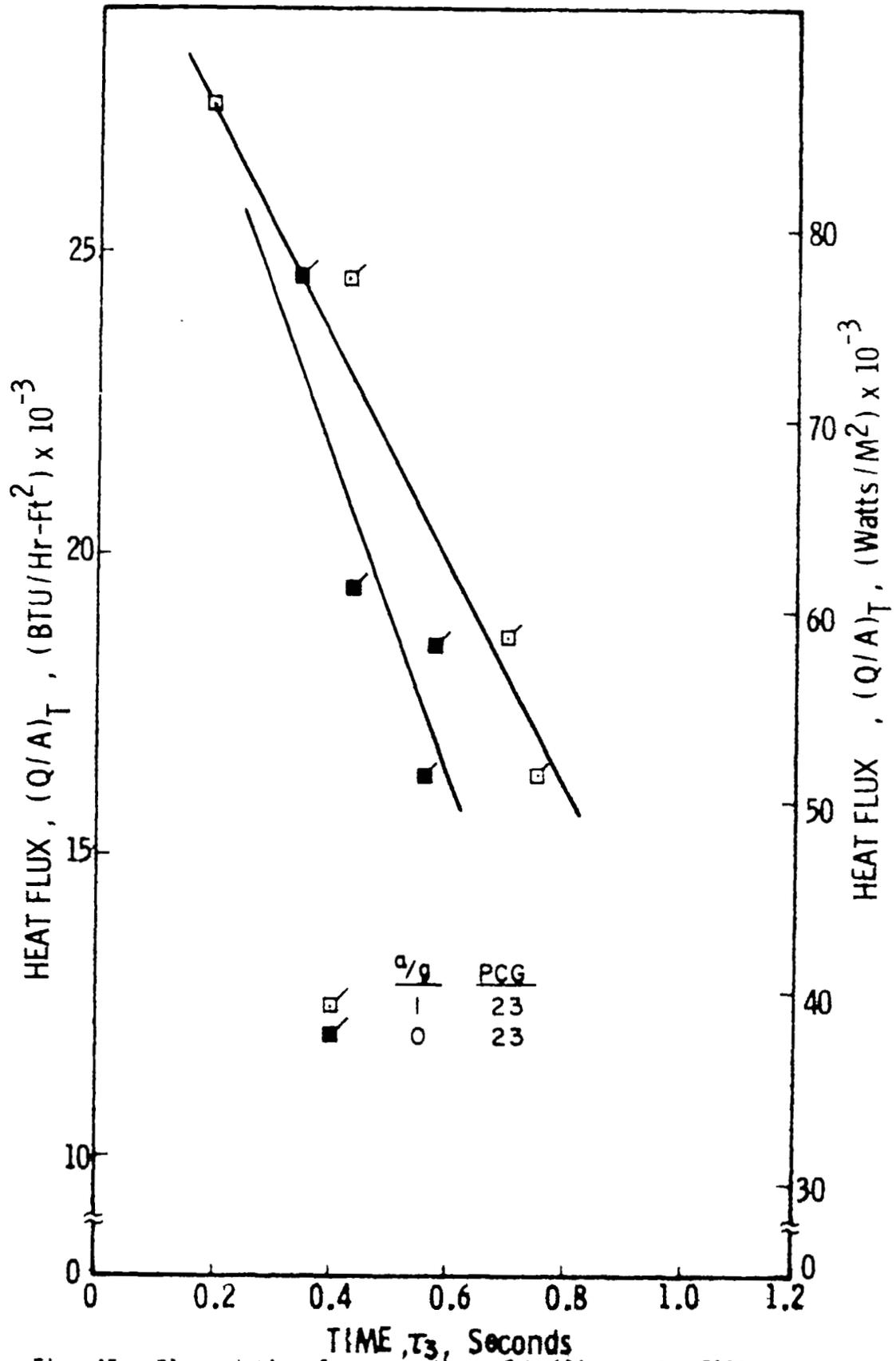
Fig. 45. Elapsed time for spreading of boiling, τ_s, F113, vertical a/g=1 and $\neq$ 0
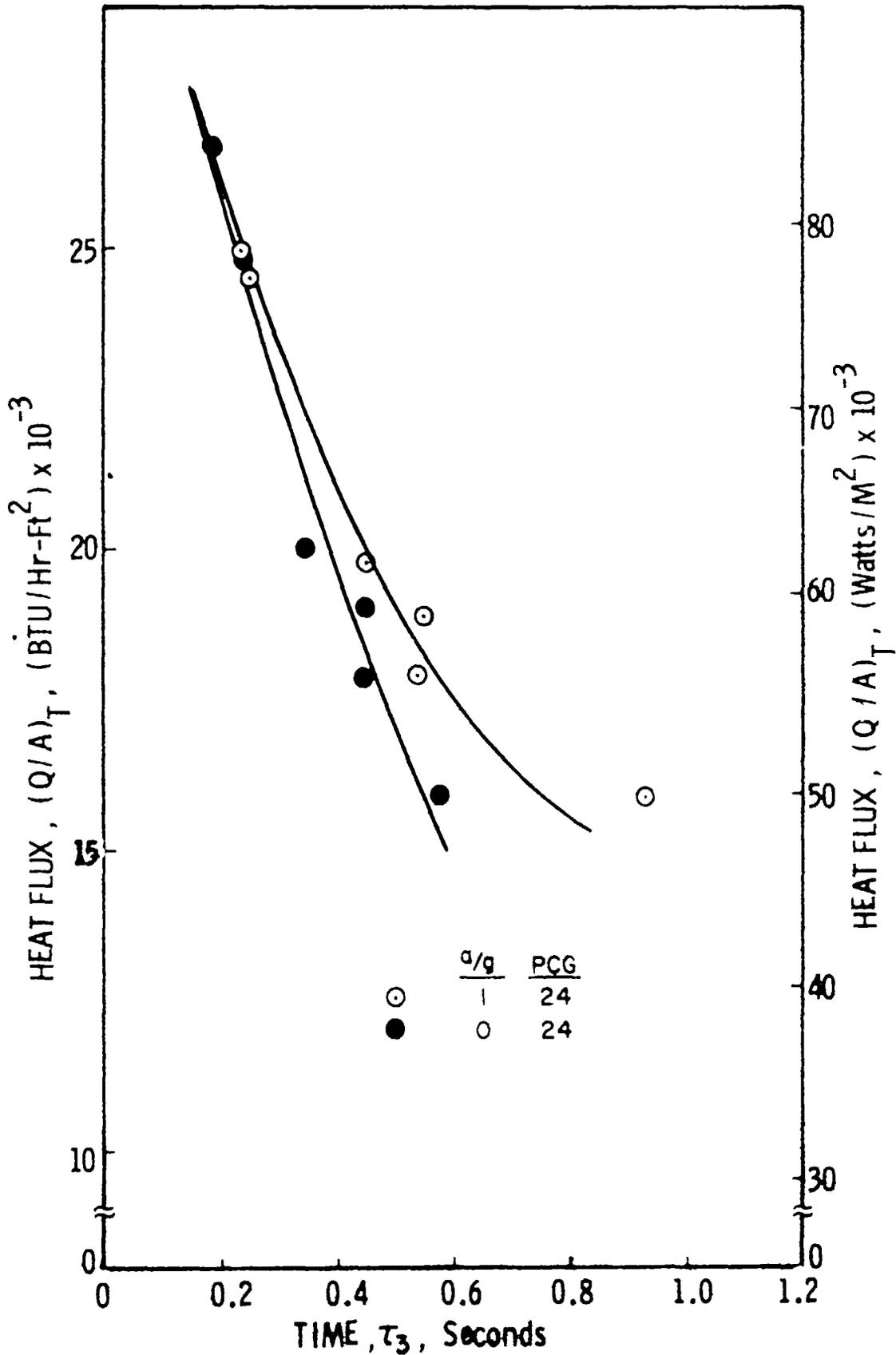
Fig. 46. Elapsed time for spreading of boiling, τ_s, F113, horizontal-up, a/g=1 and $\propto$ 0
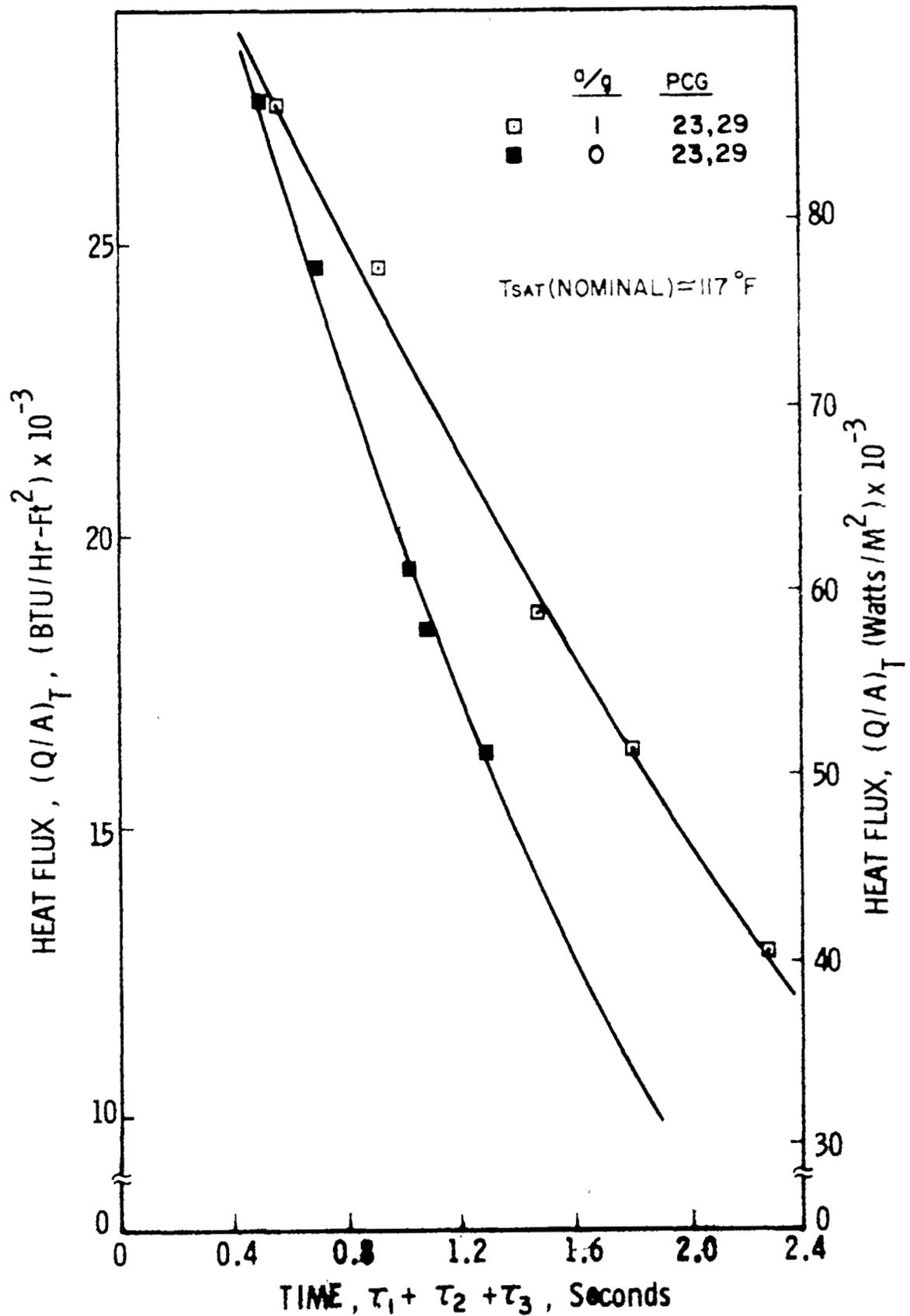
Fig. 47. Elapsed time to establish steady state nucleate boiling, F113, vertical, a/g=1 and ≈ 0
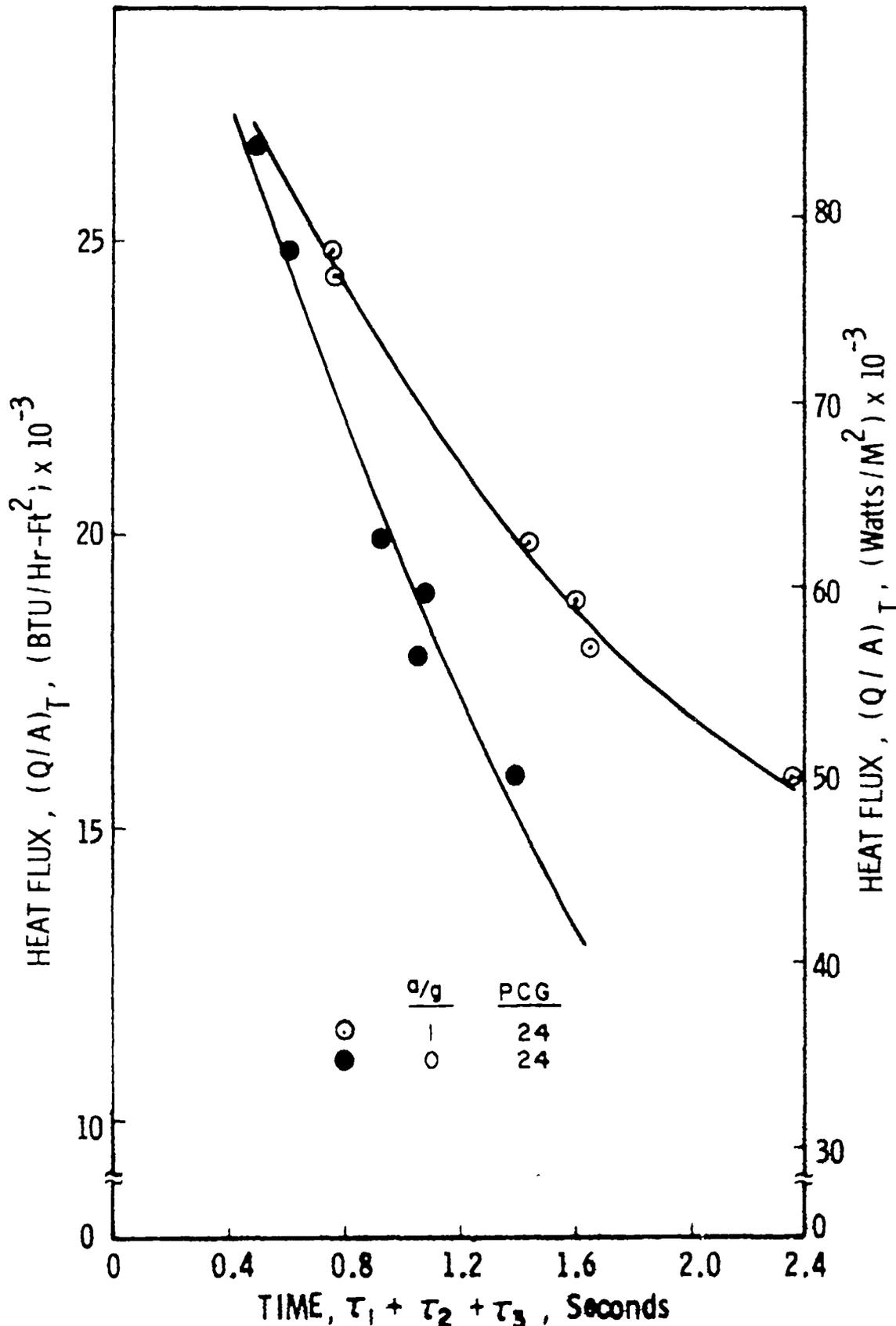
Fig. 48. Elapsed time to establish steady state nucleate boiling, F113, horizontal-up, a/g=1 and ≈ 0
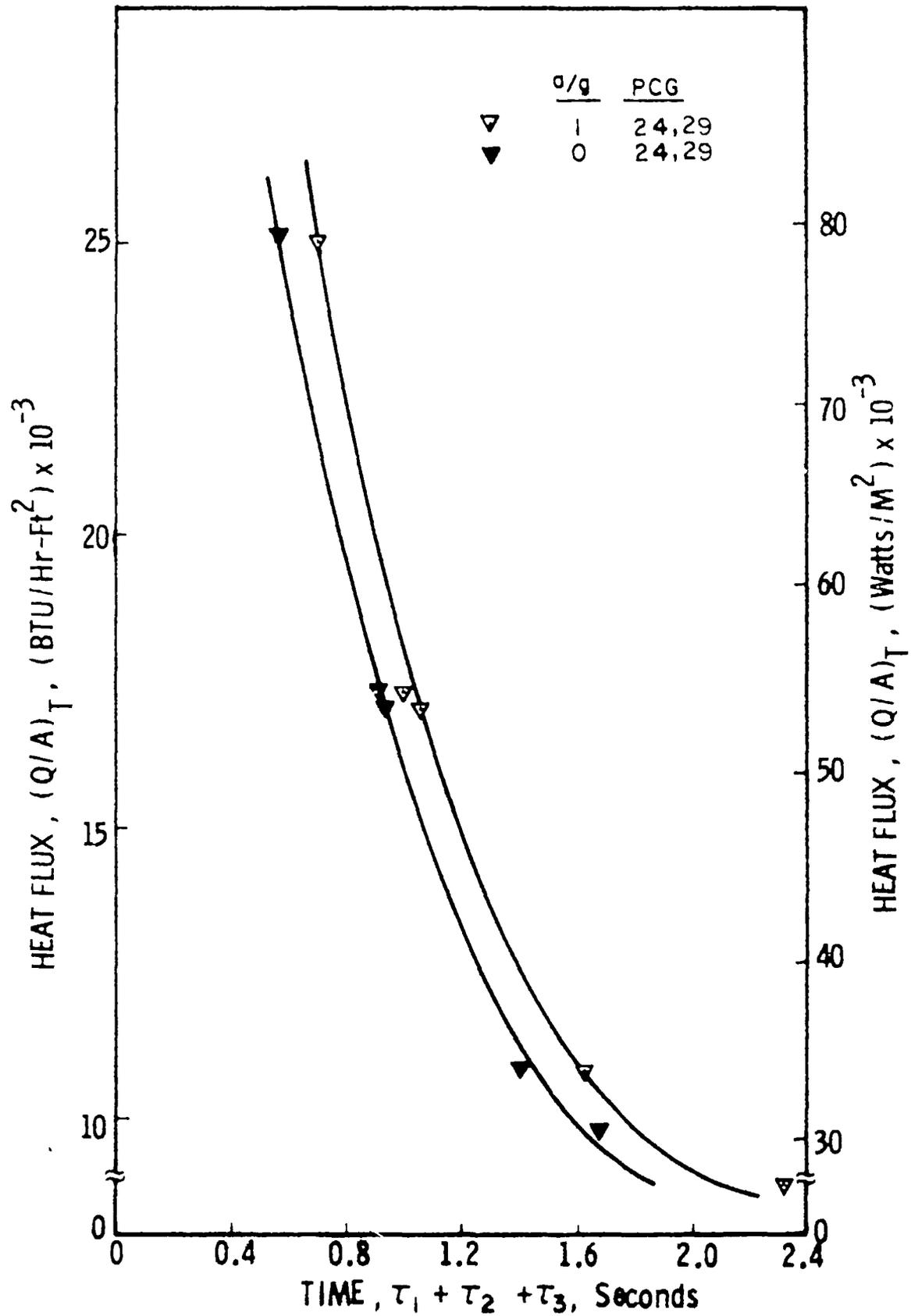
Fig. 49. Elapsed time to establish steady state nucleate
boiling, F113, horizontal-down, a/g=1 and ≃ 0
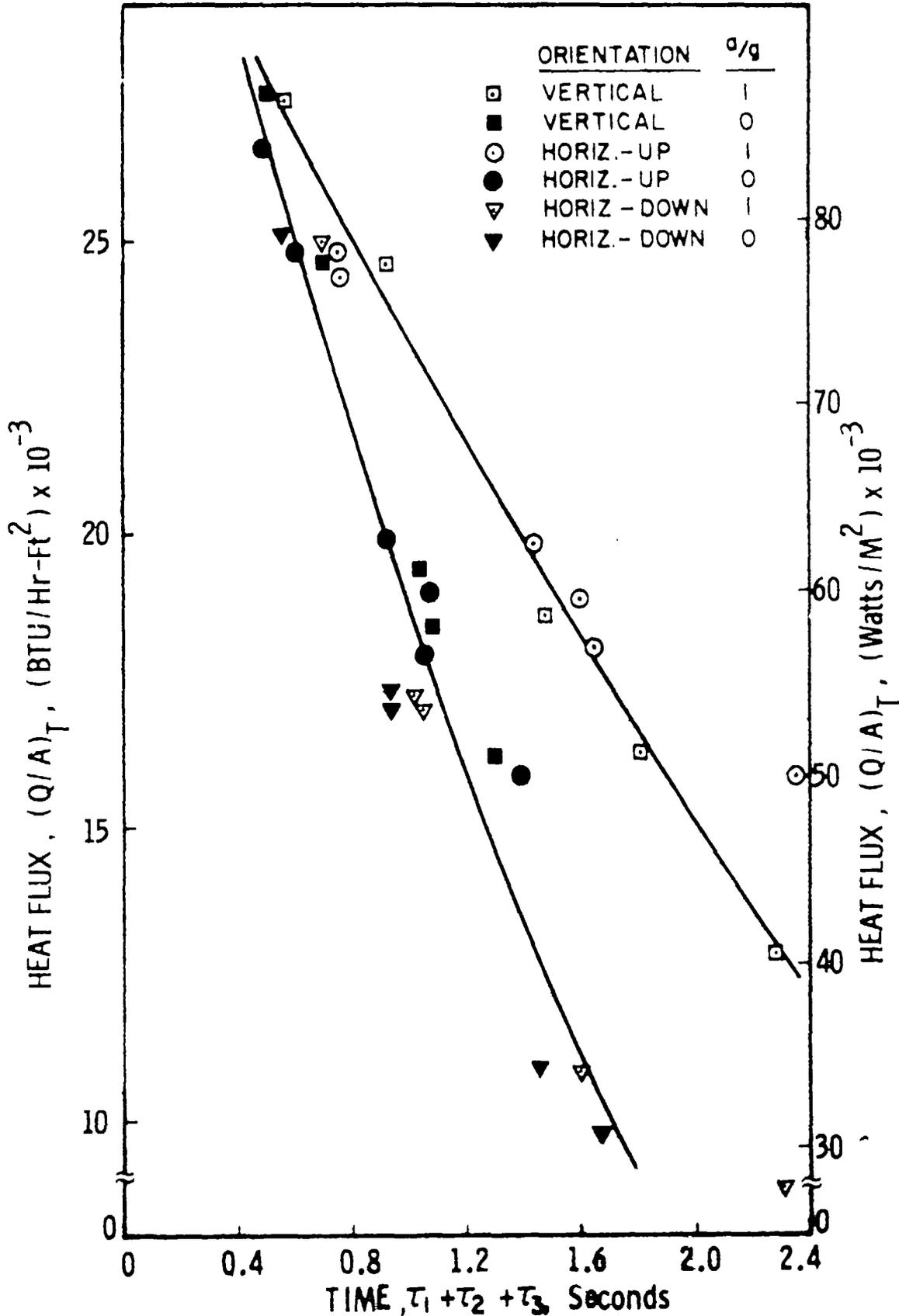
Fig. 50. Elapsed time to establish steady state nucleate boiling, F113, all orientations, a/g=1 and ≃ 0
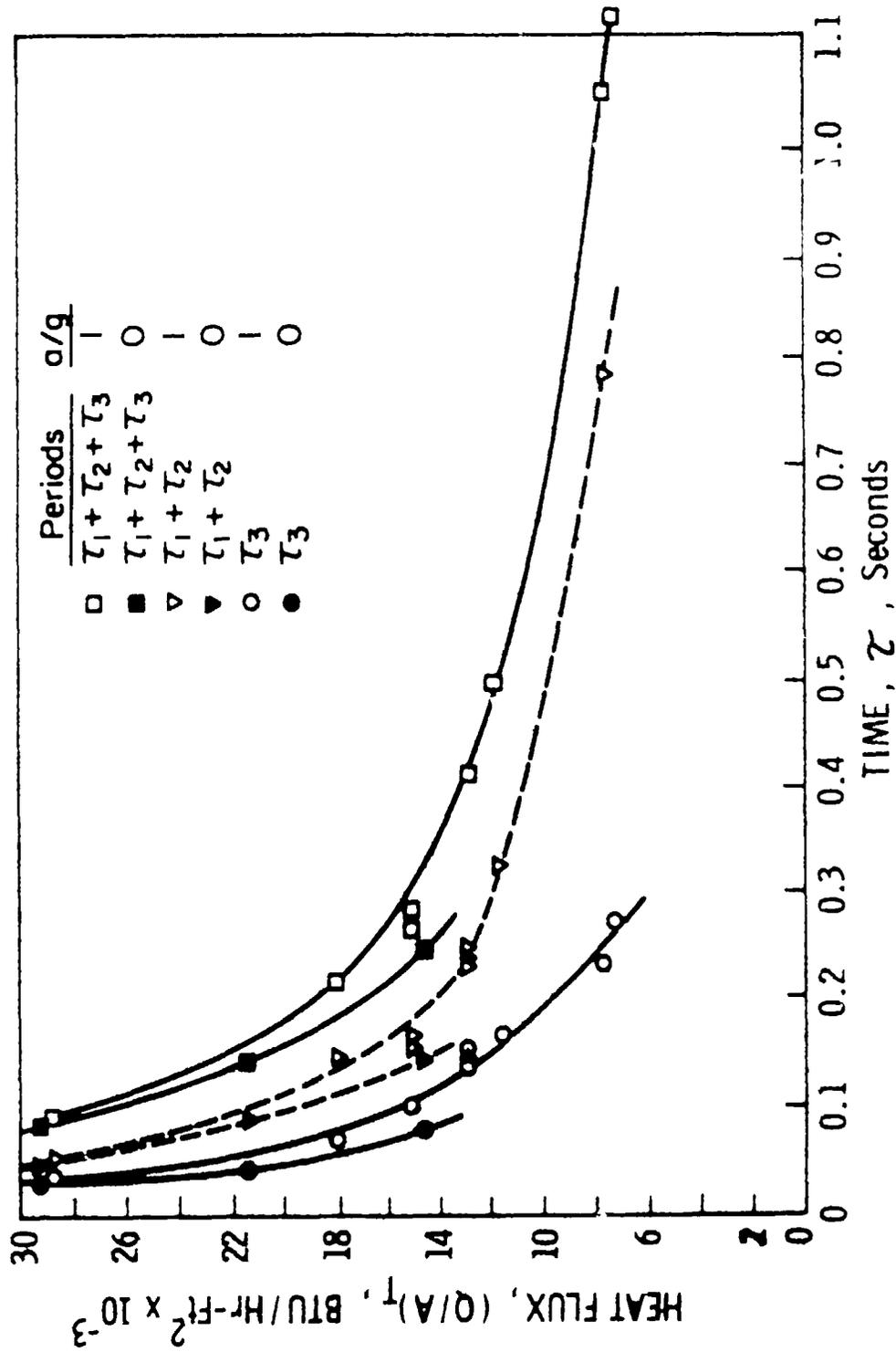
Fig. 51. Transient periods, LN_2, vertical, $a/g=1$ and ≈ 0
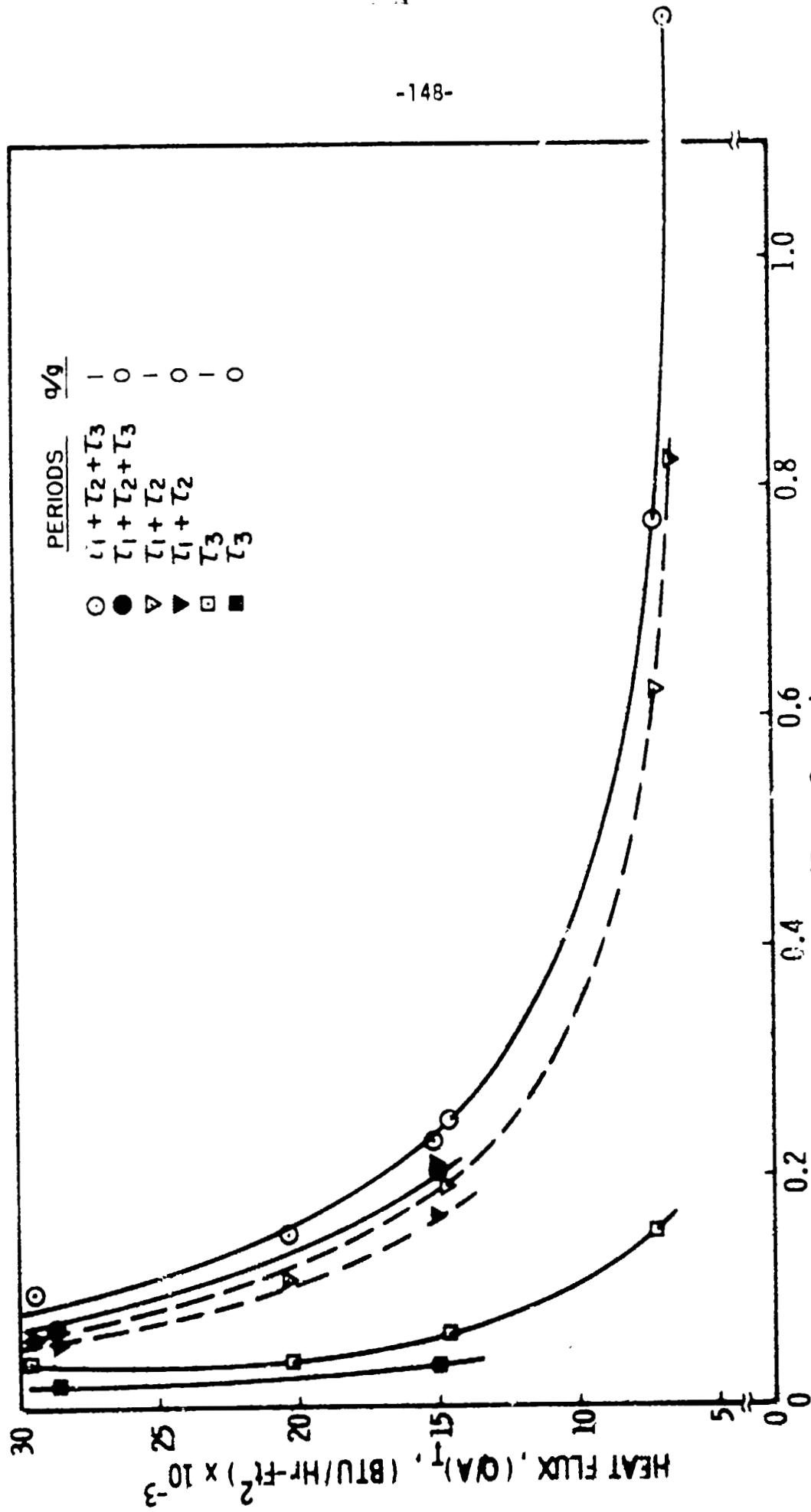
Fig. 52. Transient periods, L''_2, horizontal-up, $a/q=1$ and $\cong 0$
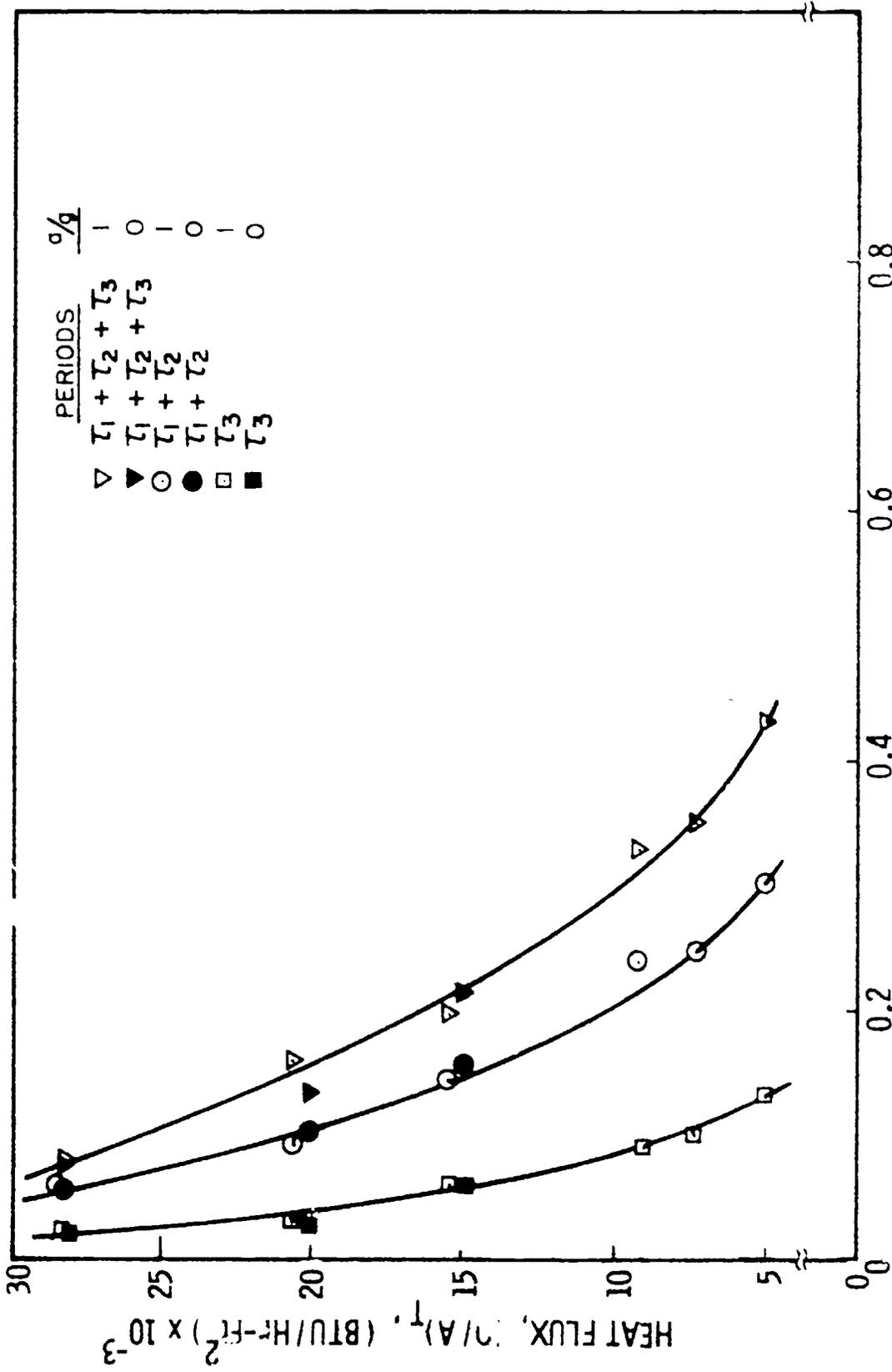
Fig. 52. Transient periods, LN_2, horizontal-down, $a/g=1$ and $\cong 0$
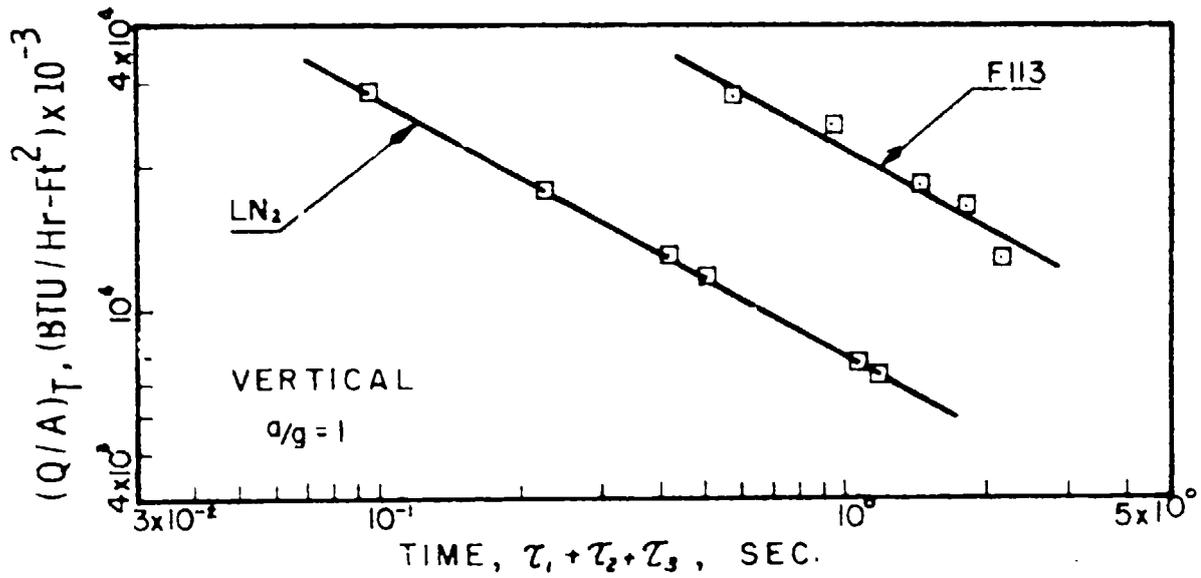
Fig. 54. Elapsed time to establish steady state nucleate boiling, F113 and LN₂, vertical, a/g=1
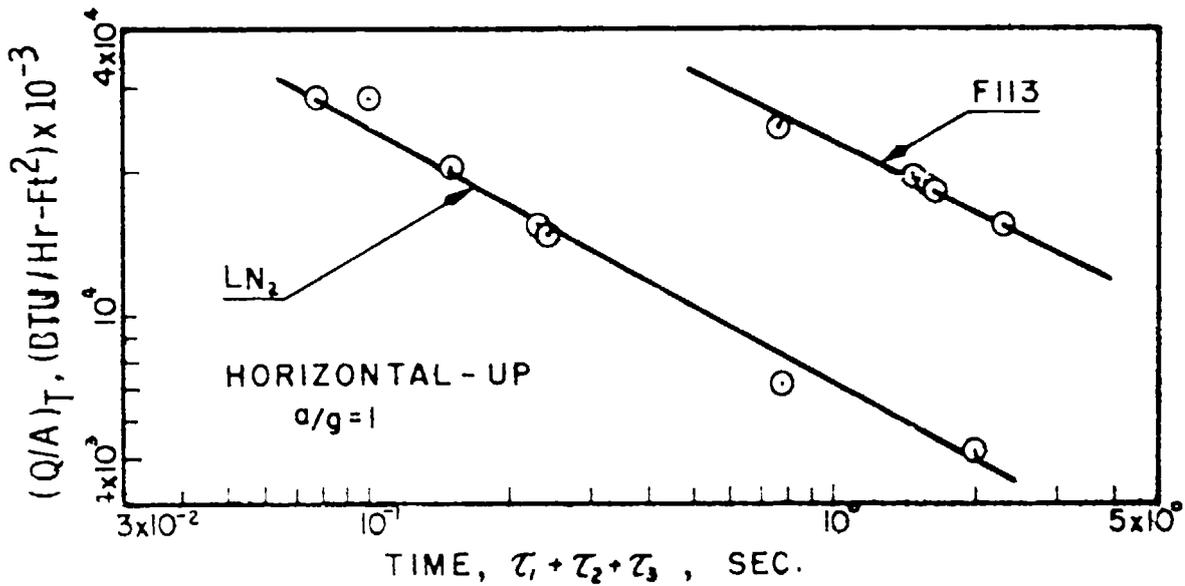
Fig. 55. Elapsed time to establish steady state nucleate boiling, F113 and LN₂, horizontal-up, a/g=1
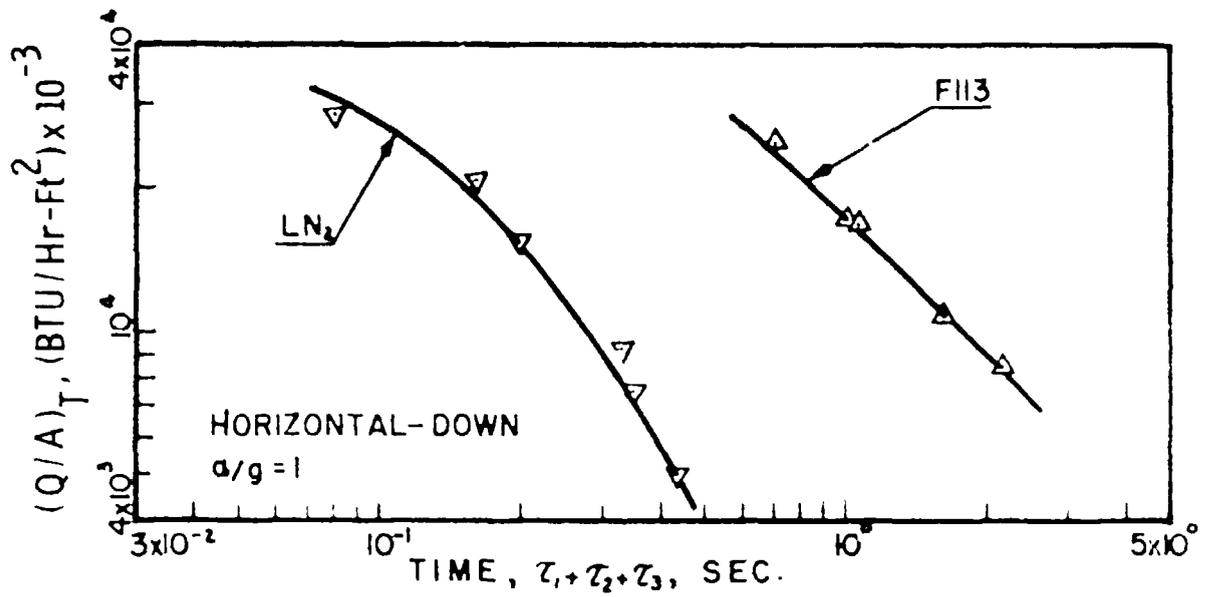
Fig. 56. Elapsed time to establish steady state nucleate boiling F113 and LN_2, horizontal-down, a/g=1
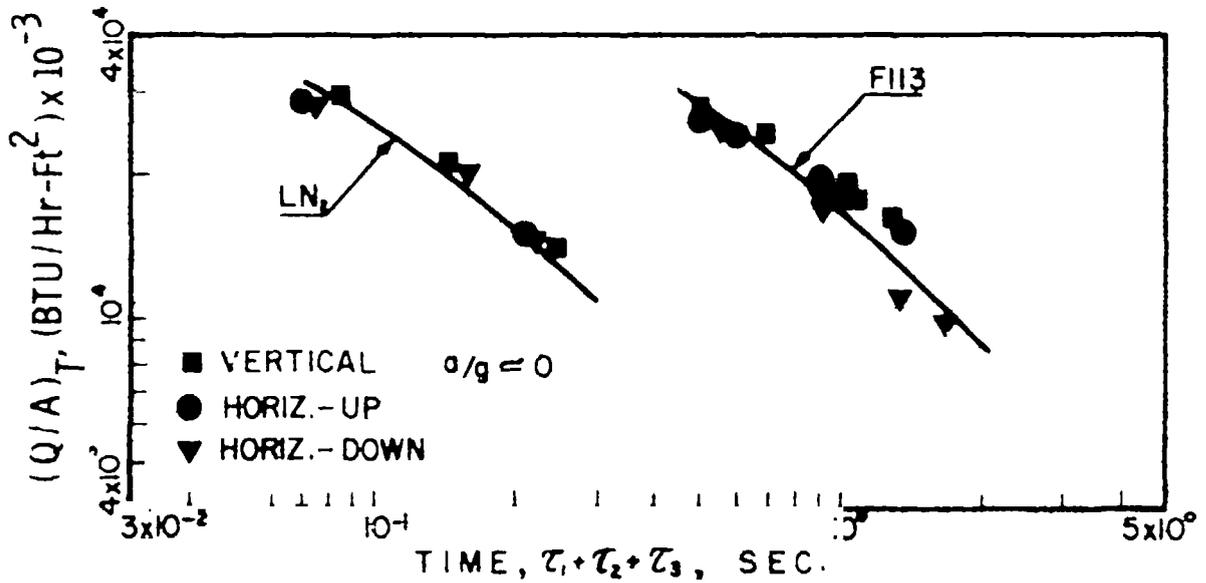
Fig. 57. Elapsed time to establish steady state nucleate boiling F113 and LN_2, all orientations, a/g - 0
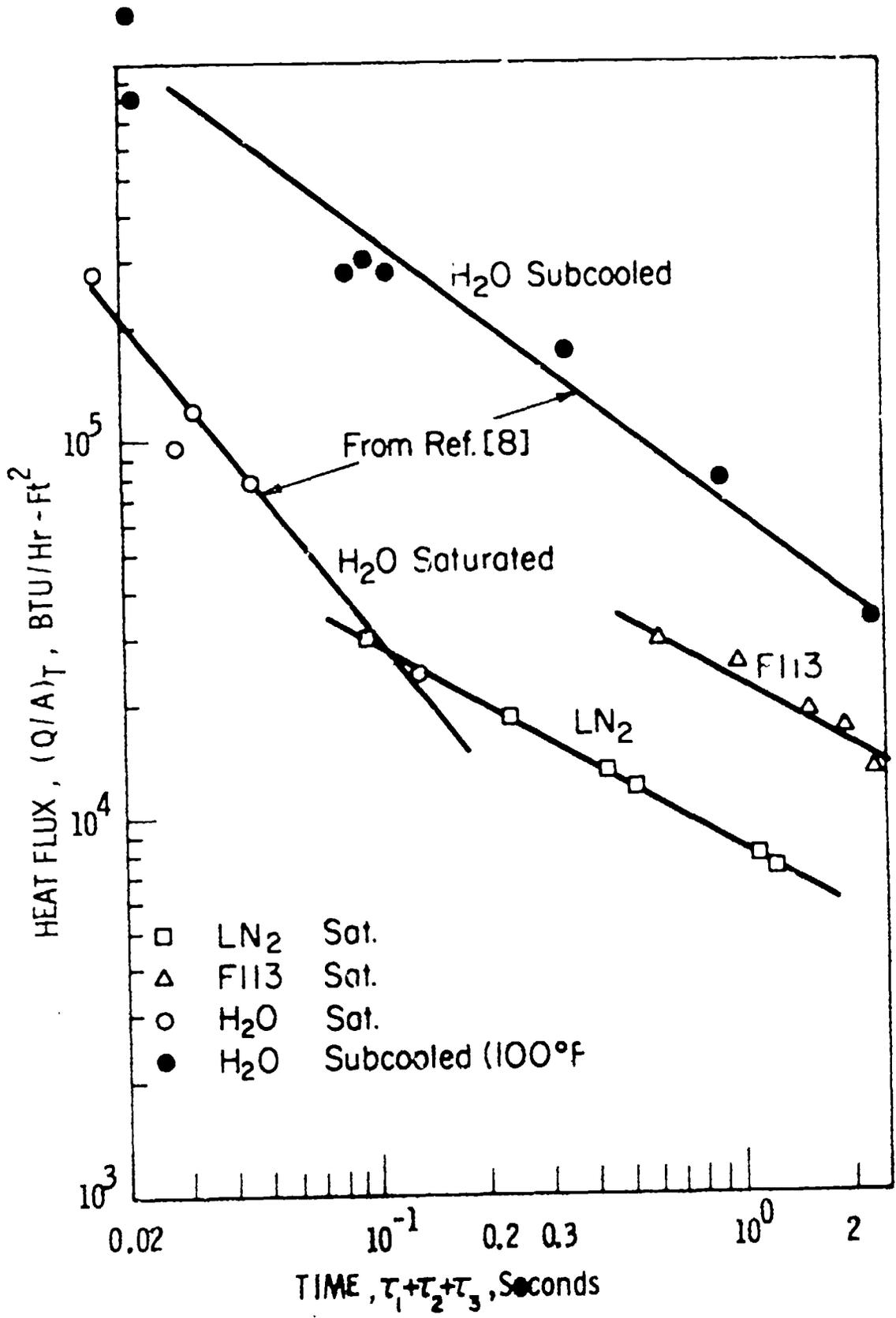
Fig. 58. Elapsed time to establish steady state nucleate boiling, F113, LN_2 and H_2O, a/g=1
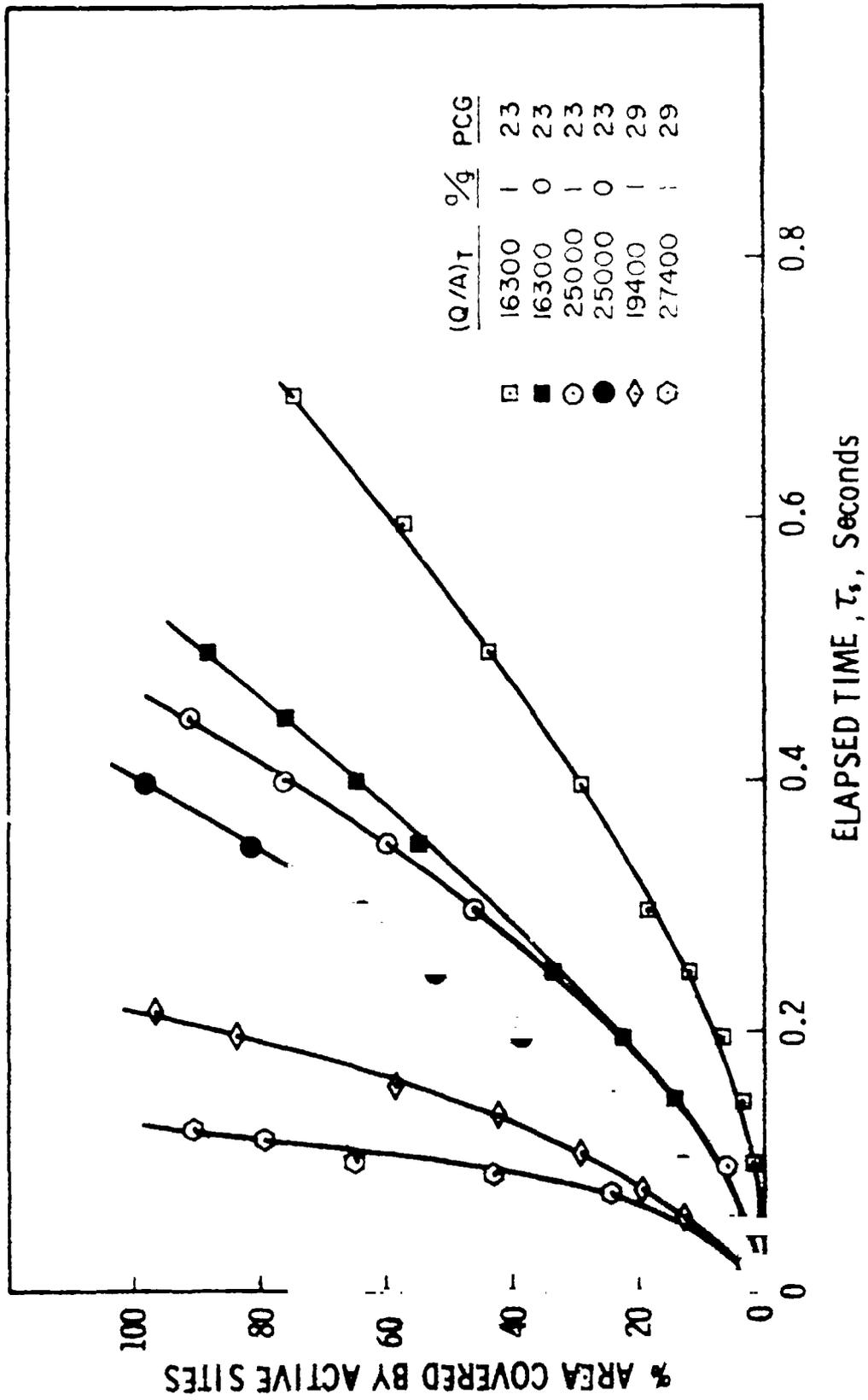
Fig. 59. Spreading of active boiling sites, F113, vertical, a/g=1 and ≃ 1
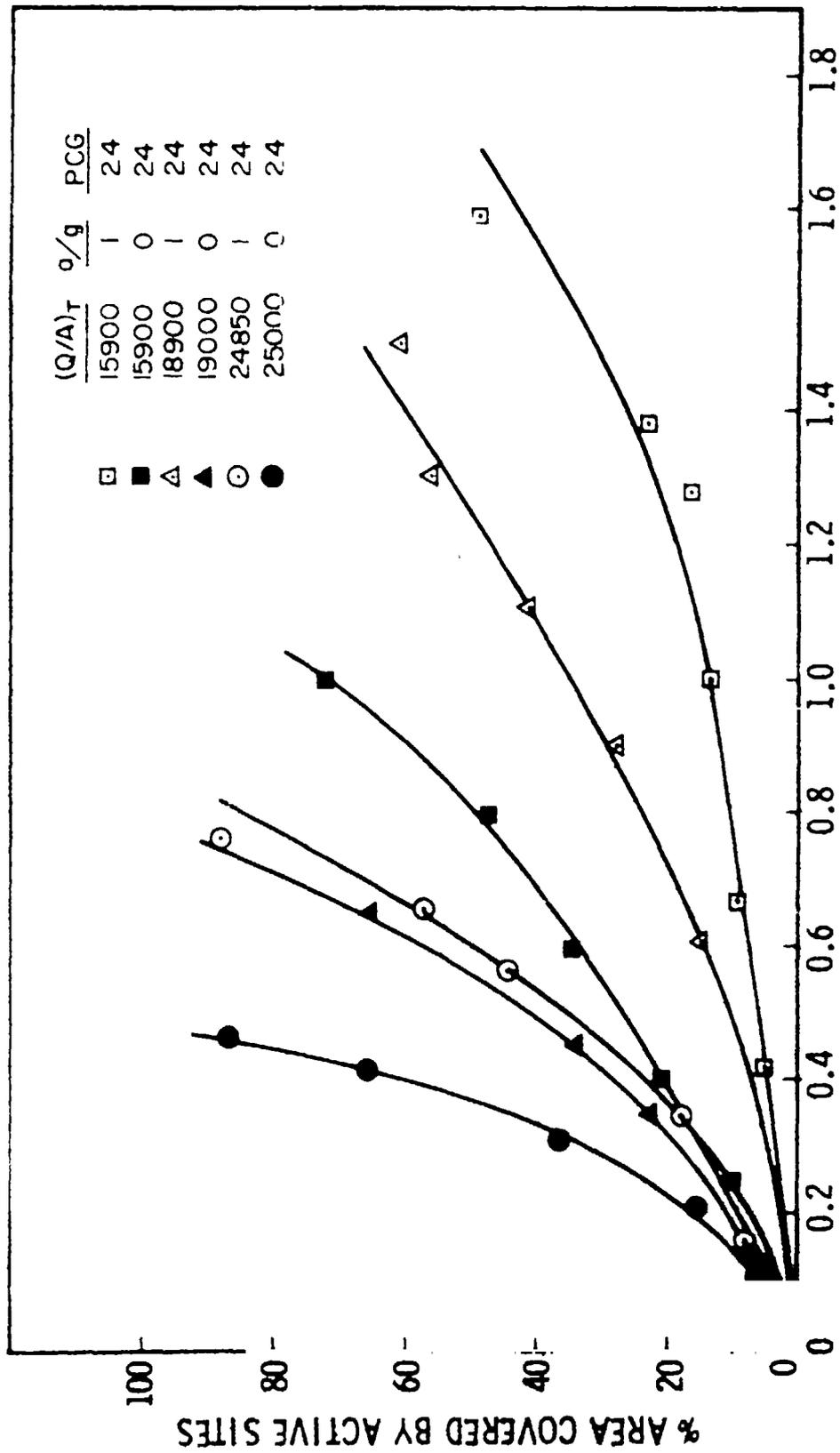
Fig. 60.   Spreading of active boiling sites, F113, horizontal-up, a/g=1 and ≃ 0
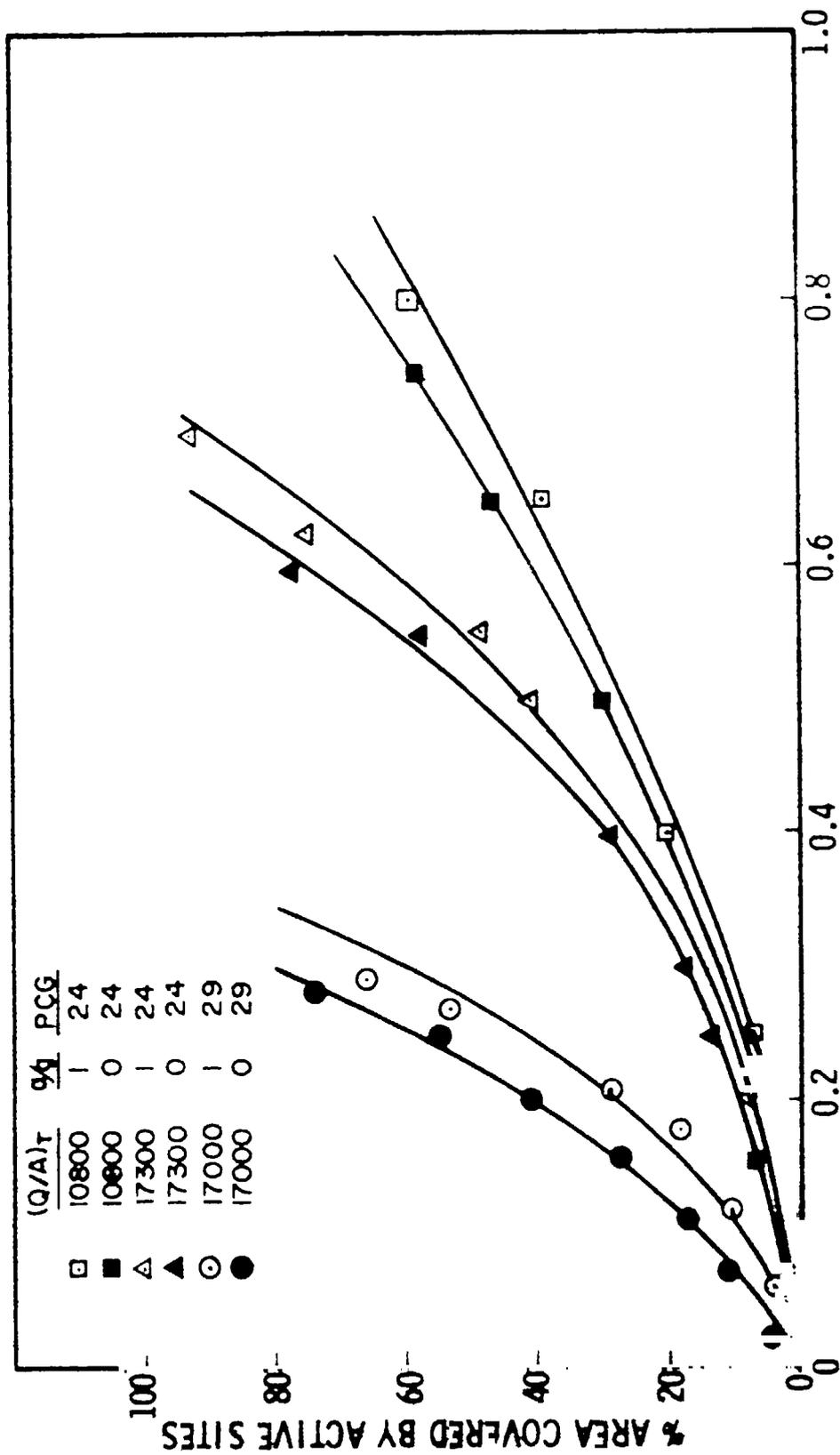
Fig. 61. Spreading of active boiling sites, F113, horizontal-down, a/g=1 and ≅ 0
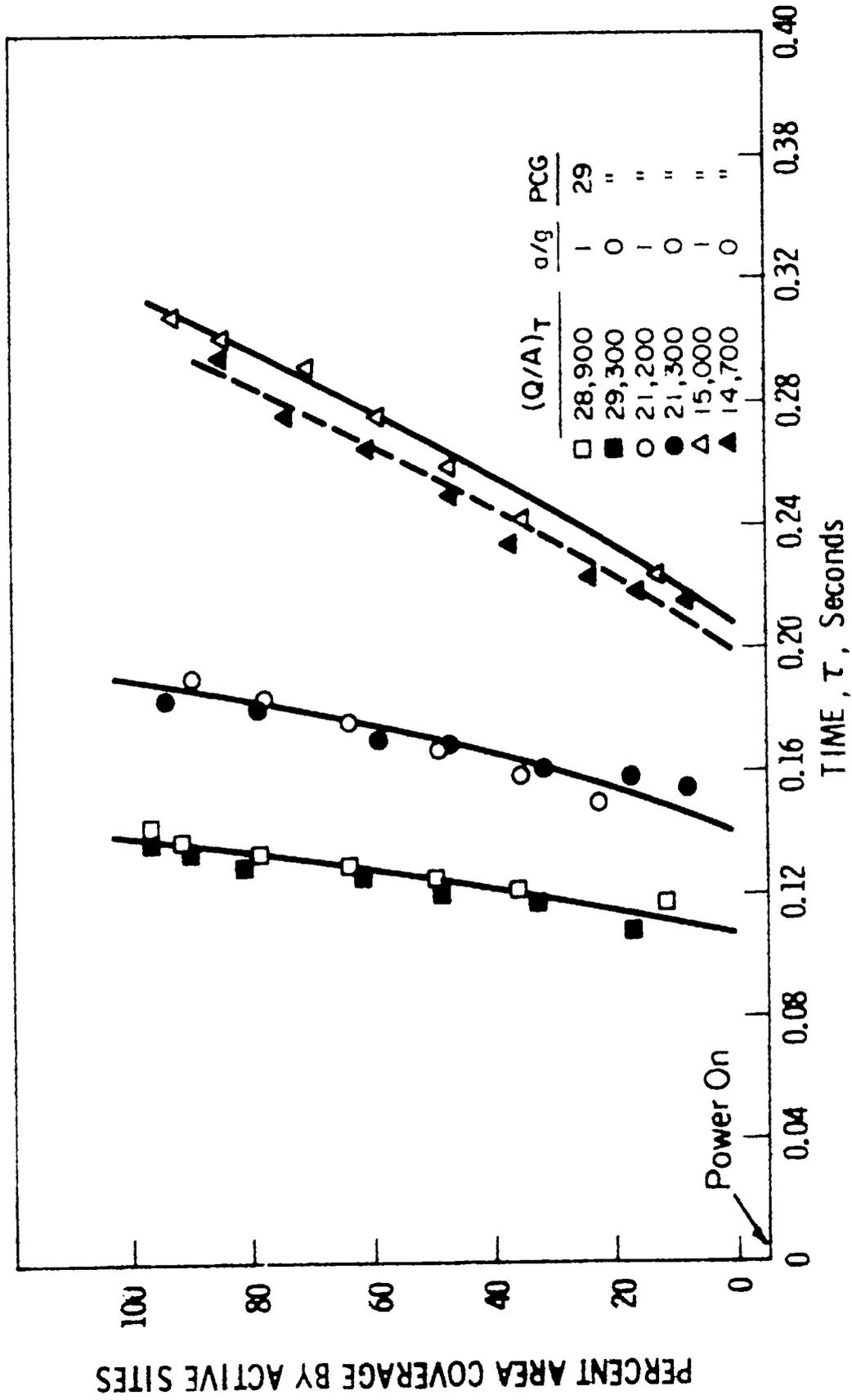
Fig. 62. Incipient and spread of boiling sites, LN_2, vertical, $a/g=1$ and $\cong 2$
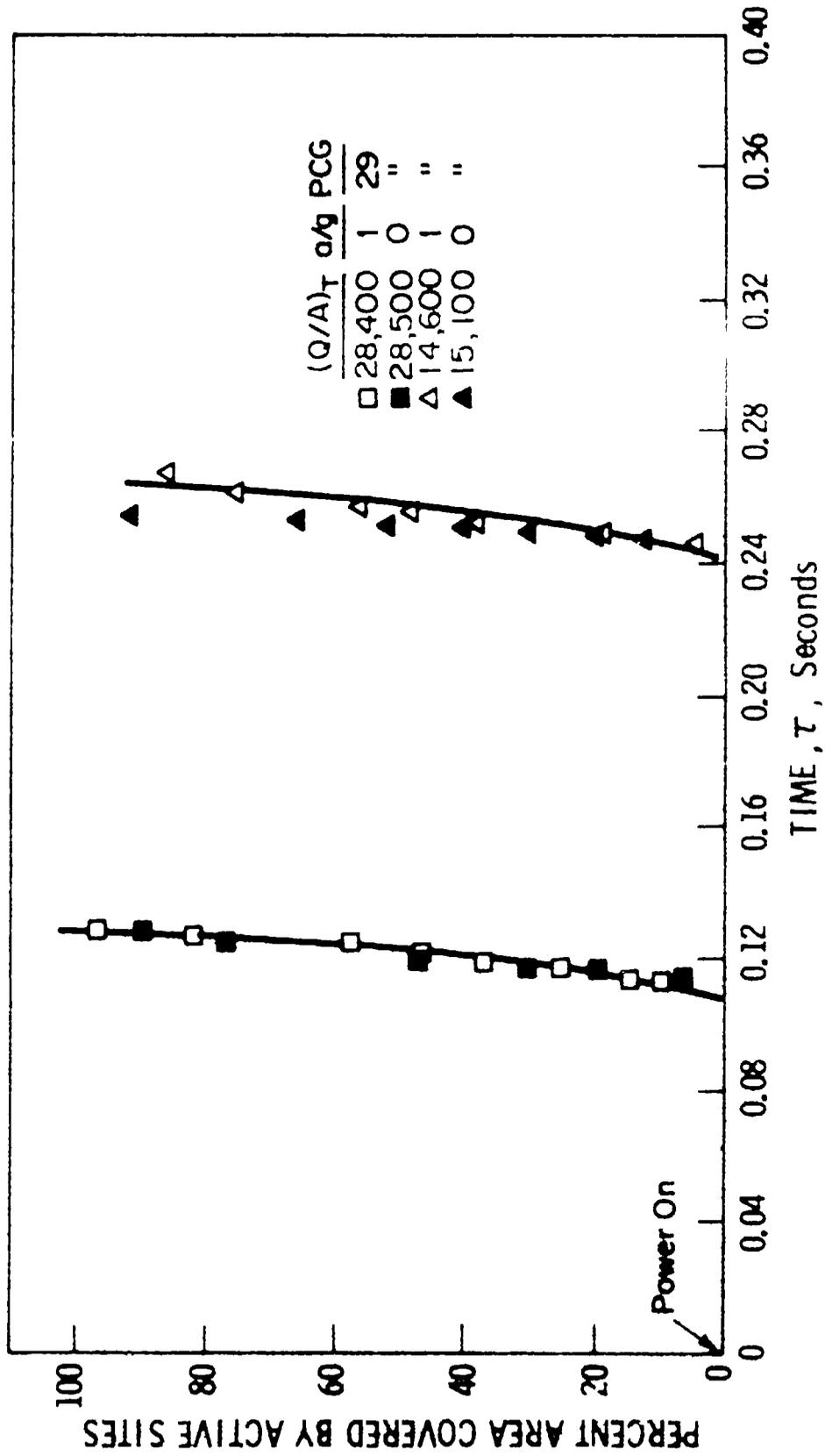
Fig. 63. Incipient and spread of boiling sites, LN$_2$, horizontal-up, a/g-1 and $\cong$ '/
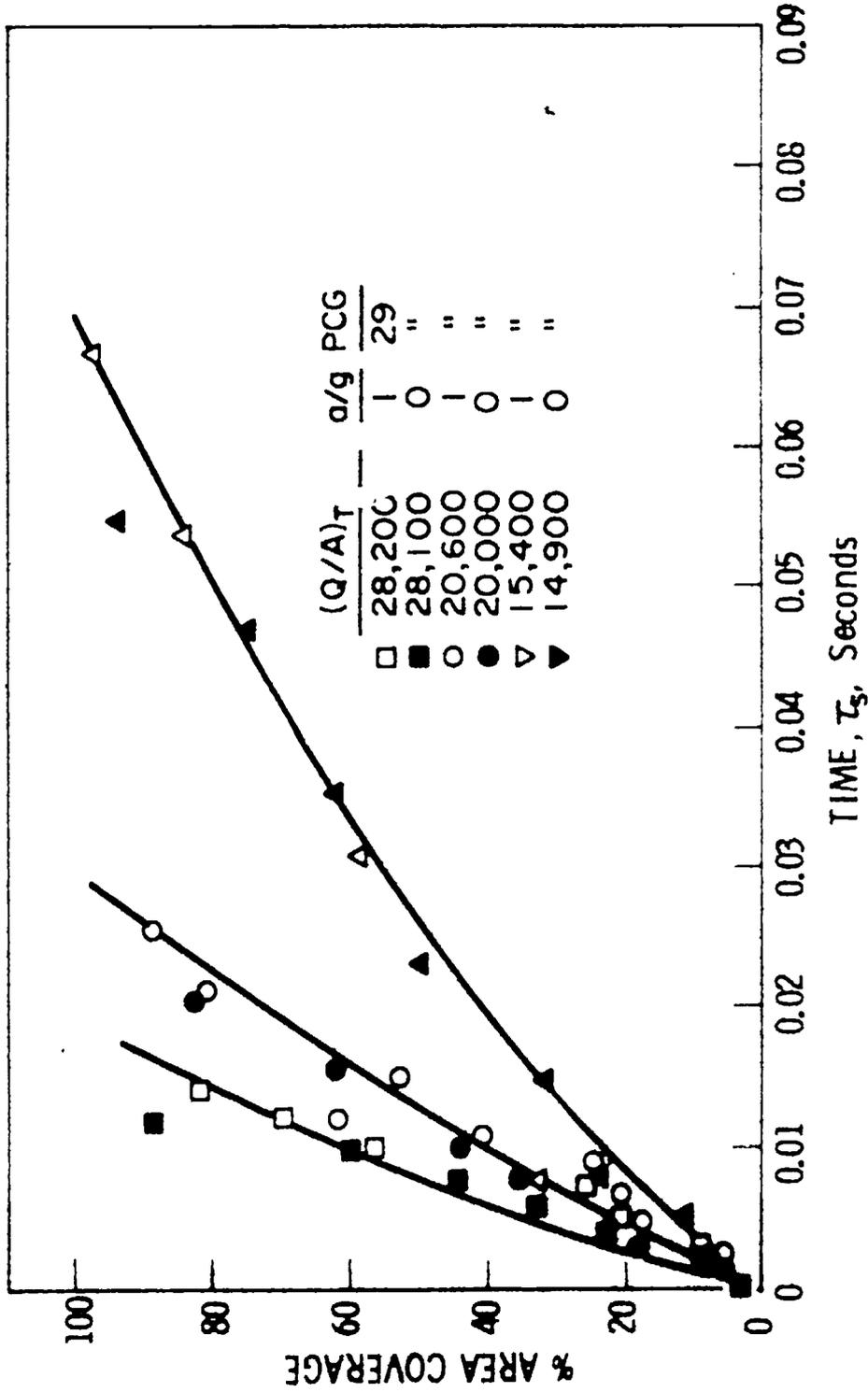
Fig. 64. Spreading of active boiling sites, LN_2, horizontal-down, $a/g=1$, and $\cong$?
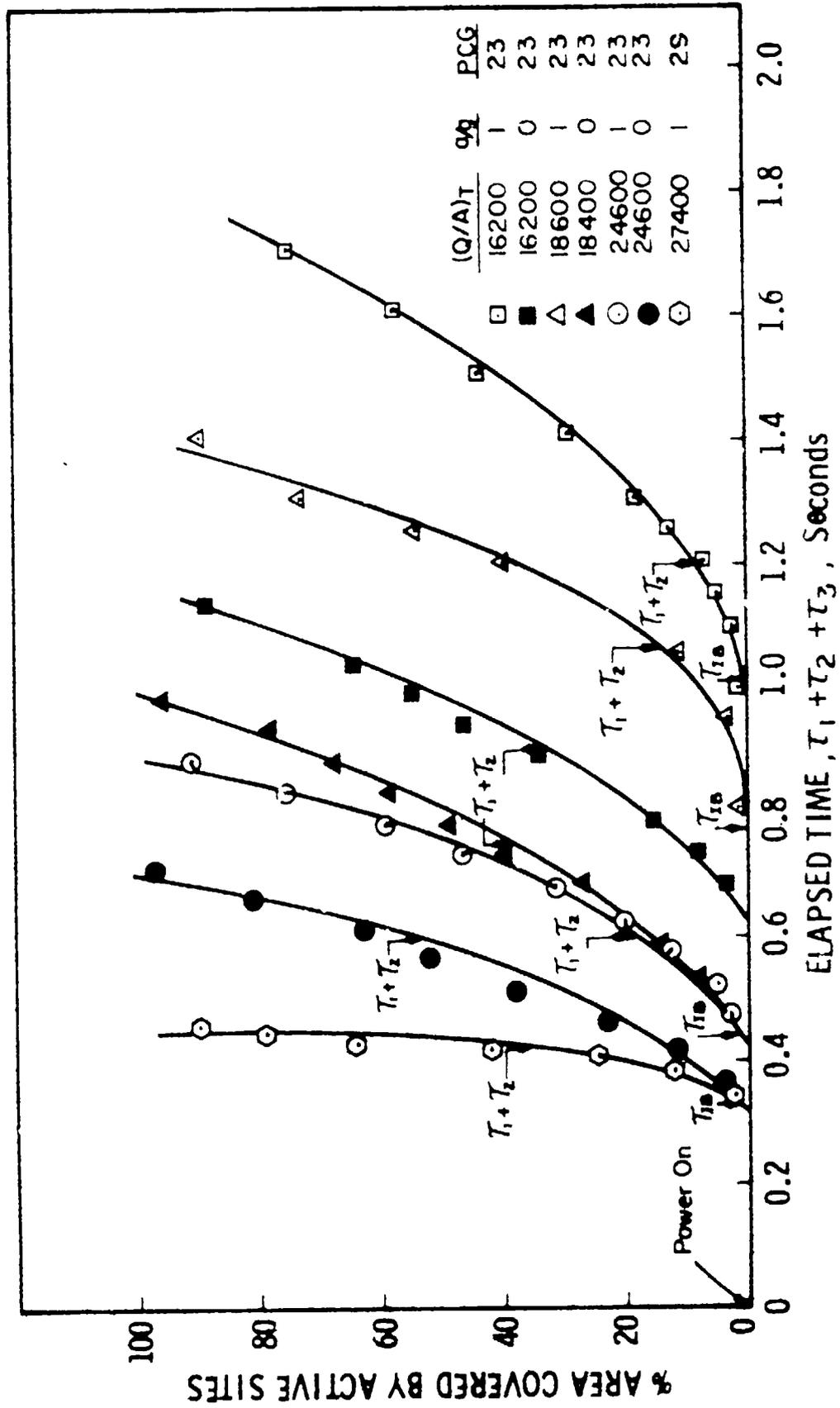
Fig. 65. Incipient and spread of boiling sites. F113, vertical, a/g=1 and ≃ ?
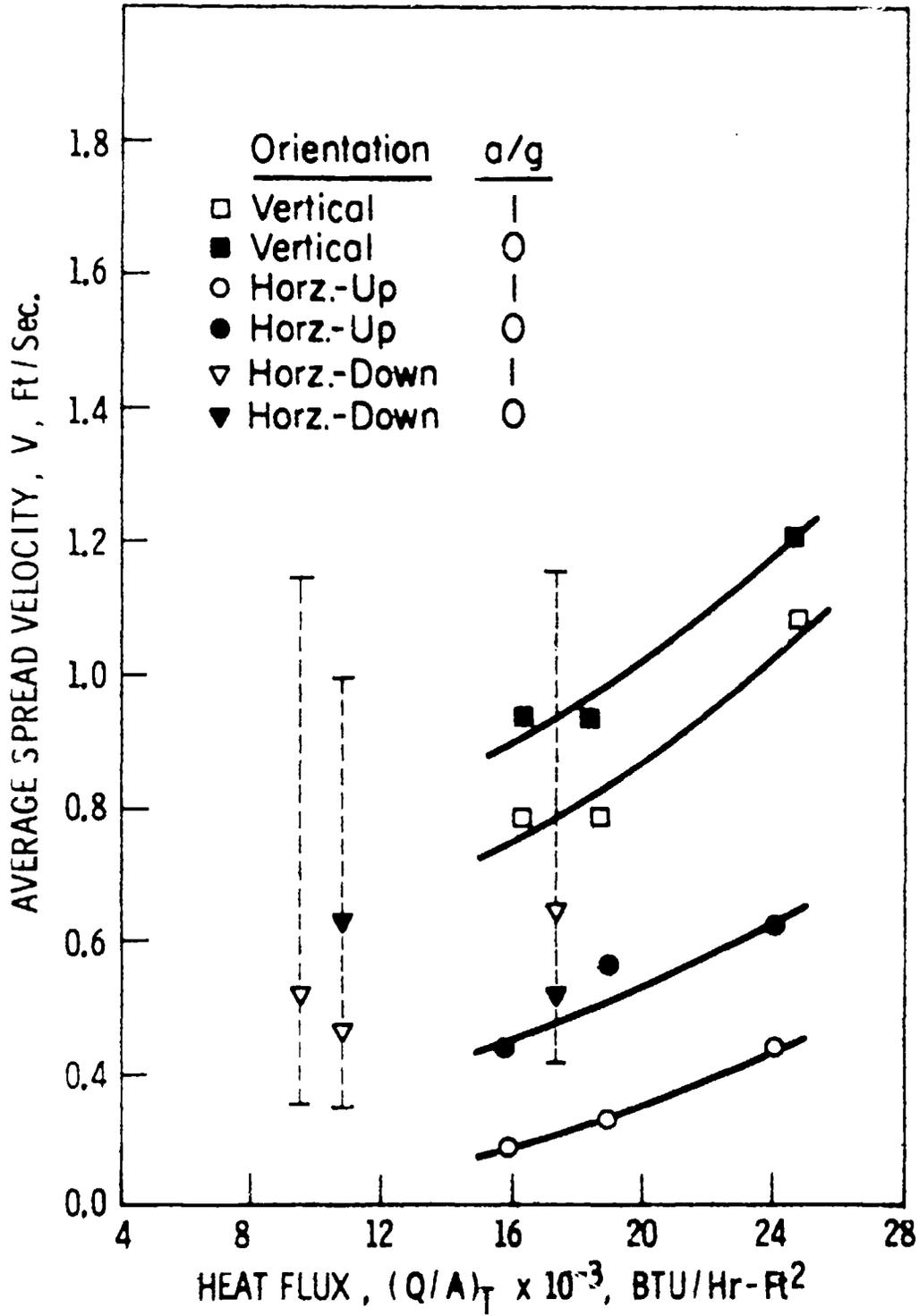
Fig. 66. Average boiling spread velocity, F113, all orientations, a/g=1 and ≈ 0
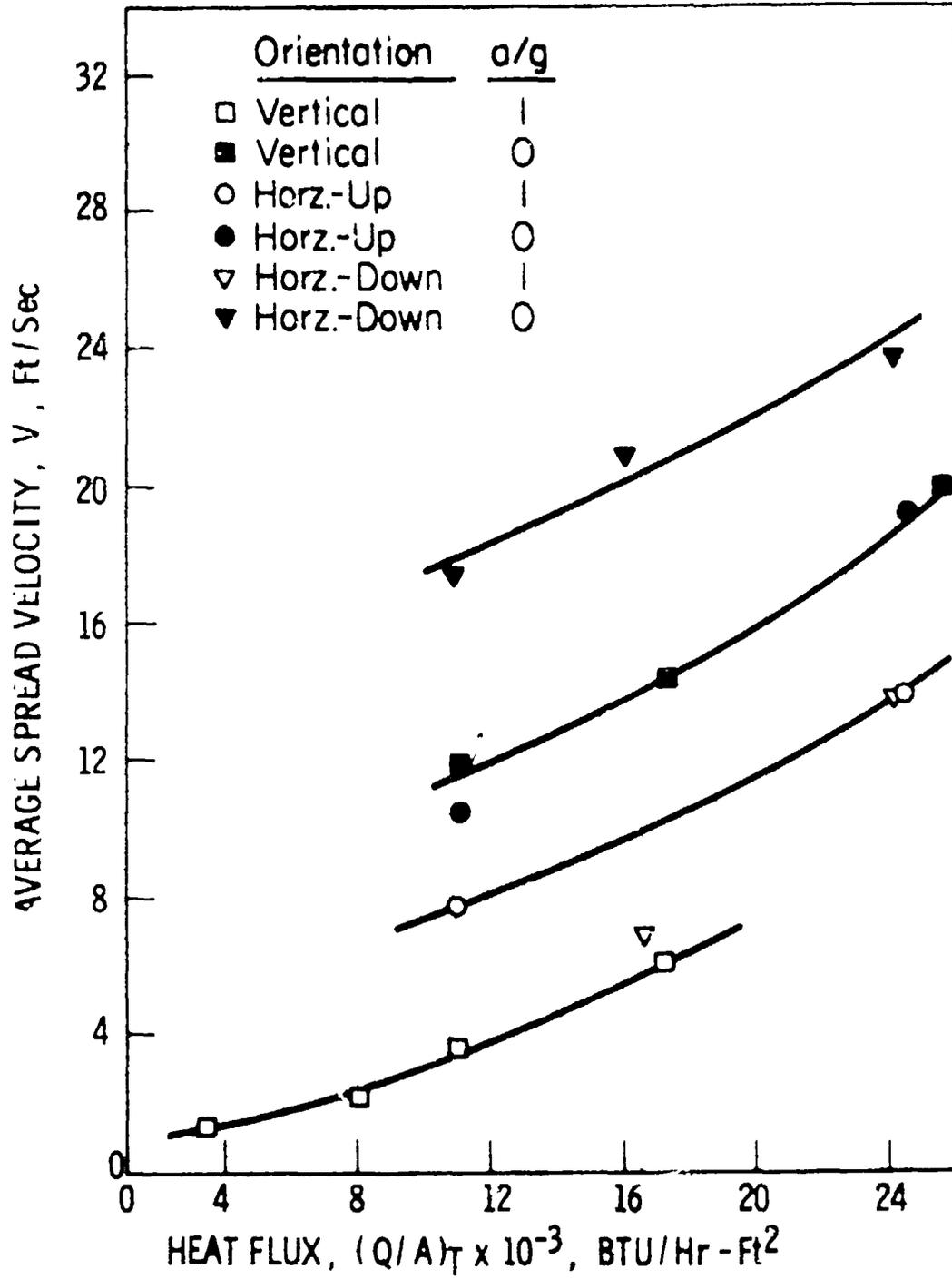
Fig. 67. Average boiling spread velocity, LN_2, all orientations $a/g=1$ and ≈ 0
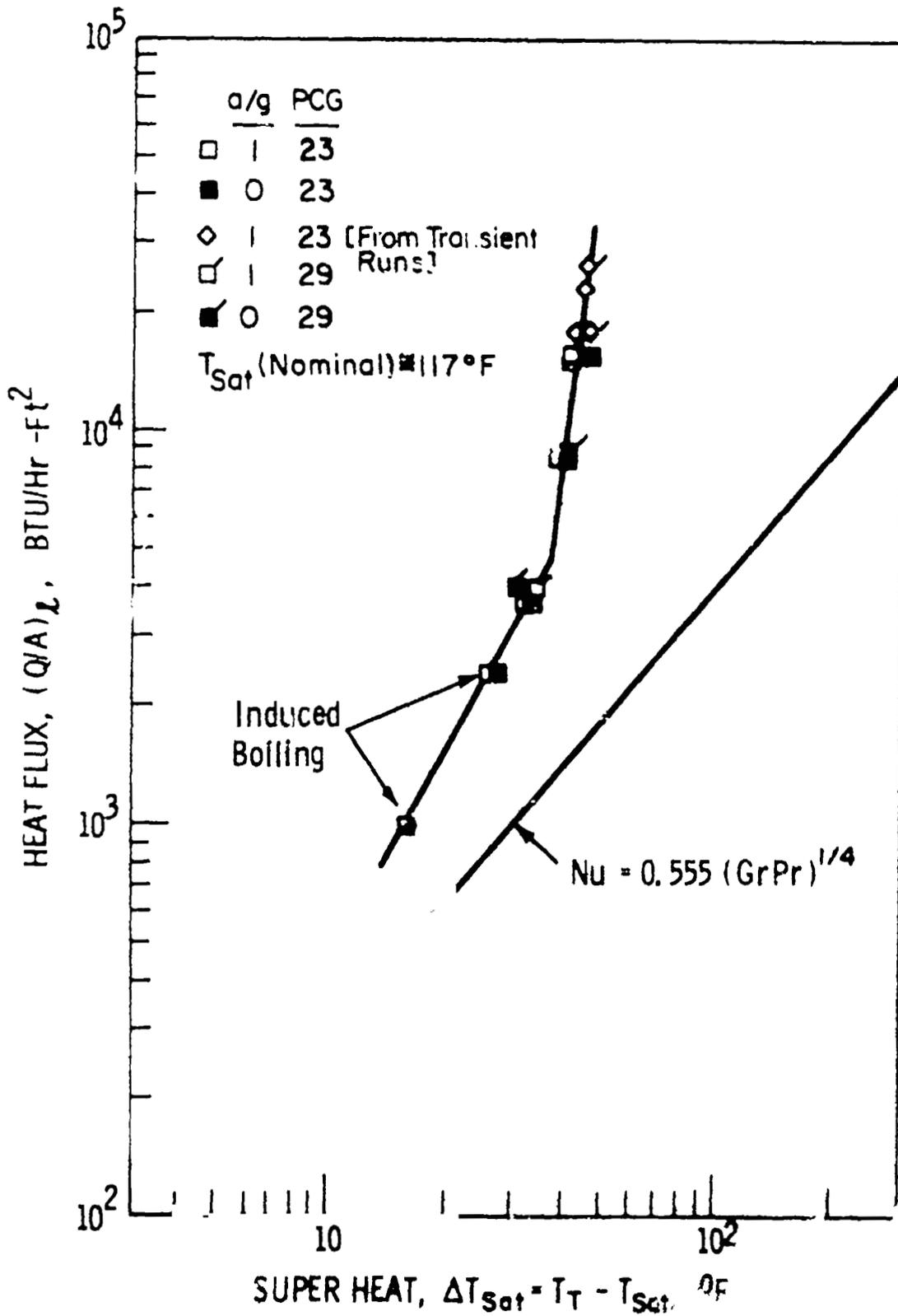
Fig. 68. Saturated nucleate boiling heat transfer, F113, vertical, a/g=1 and ≃ 0
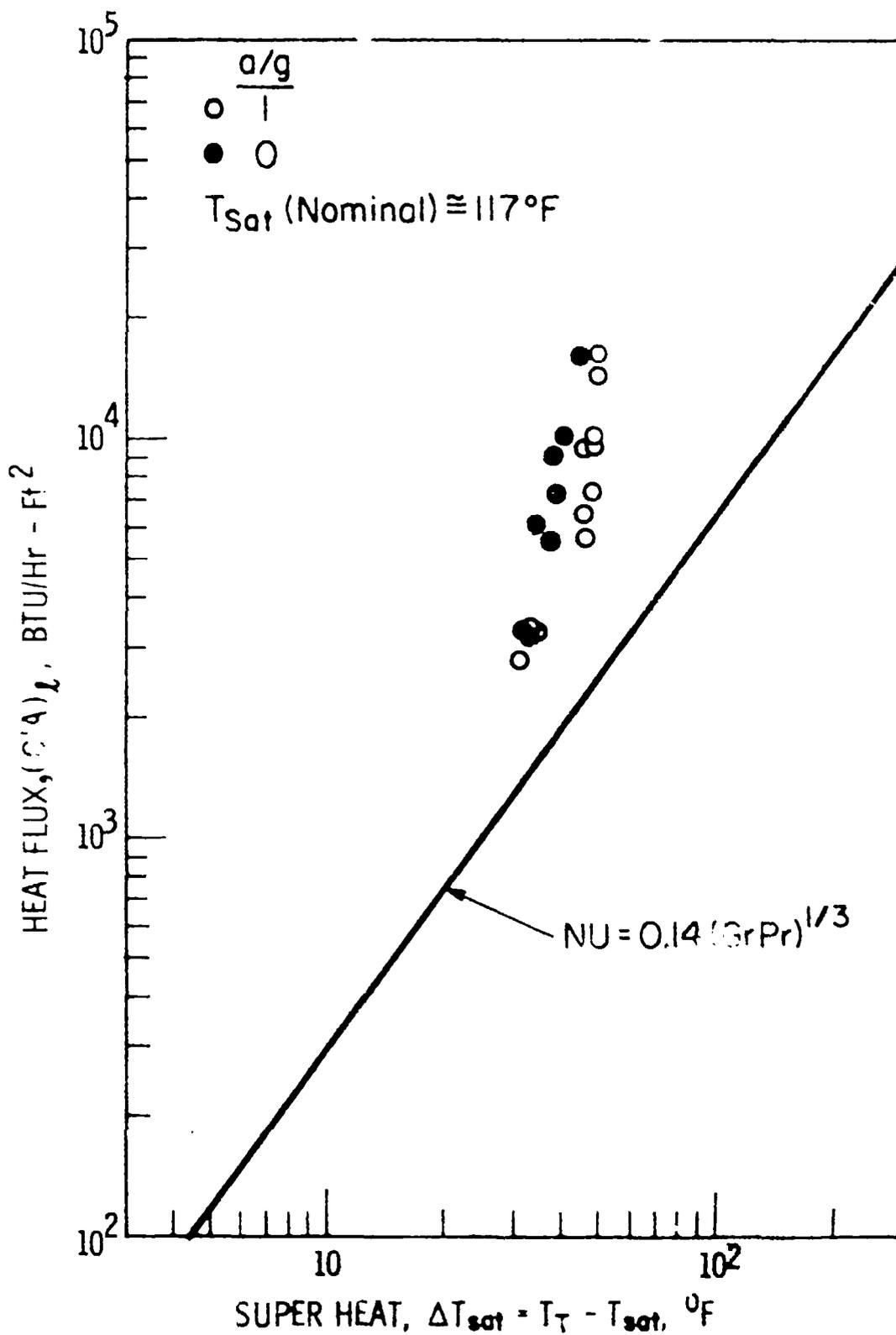
Fig. 69. Saturated nucleate boiling heat transfer, F113, horizontal-up, a/g=1 and ≈ 0
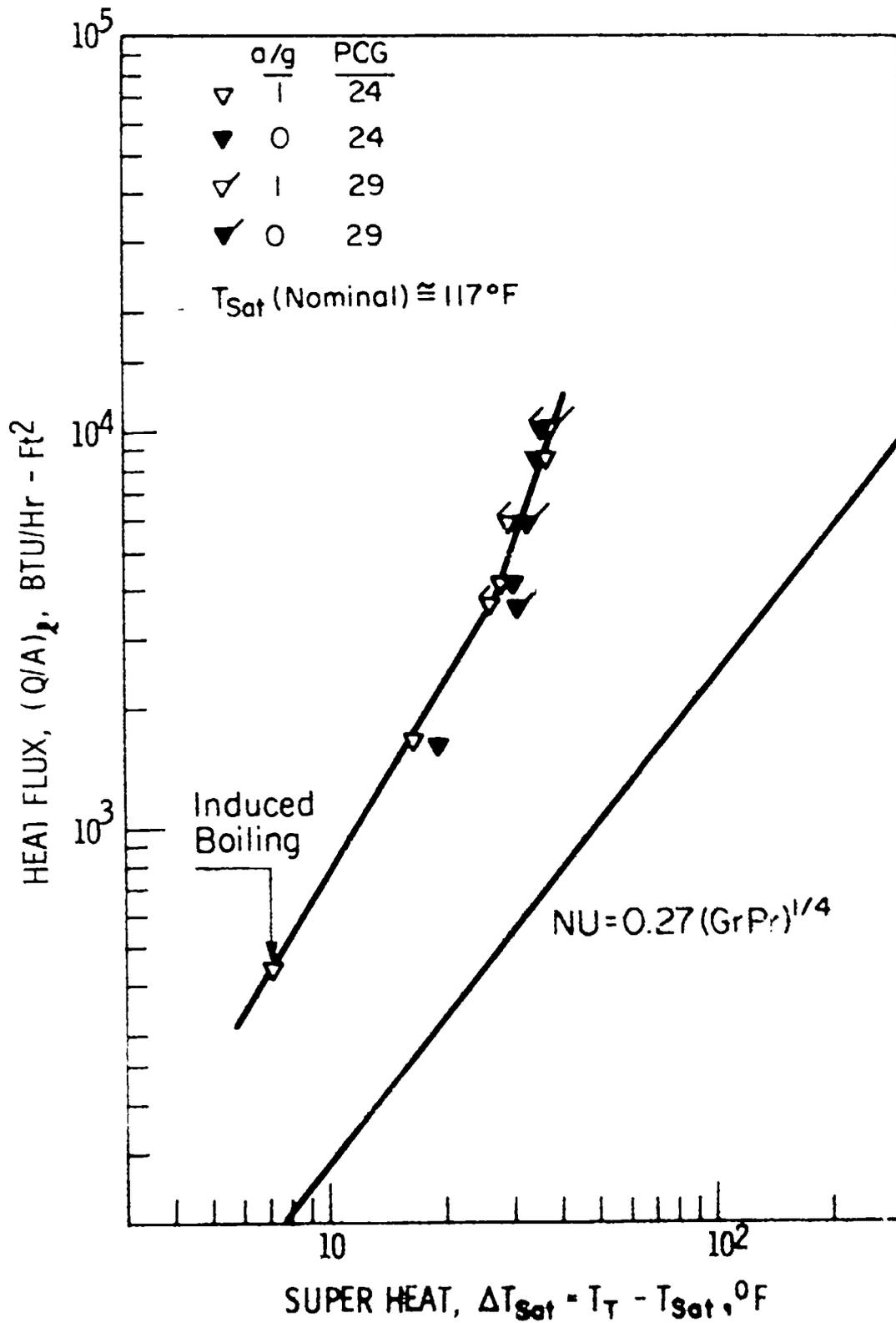
Fig. 70. Saturated nucleate boiling heat transfer, F113, horizontal-down, a/g=1 and ∝ 0
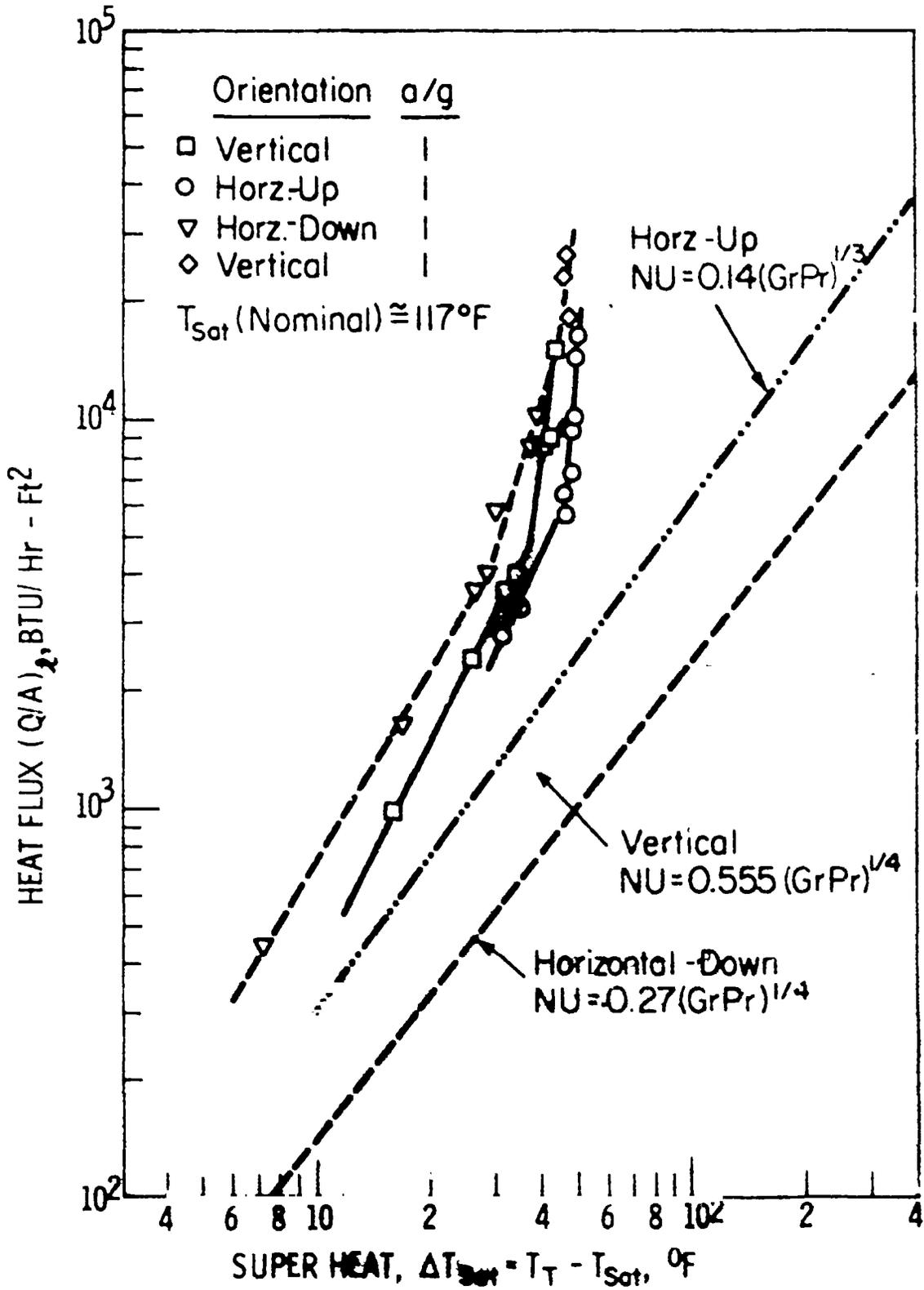
Fig. 71. Saturated nucleate boiling heat transfer, F113, all orientations, a/g=1
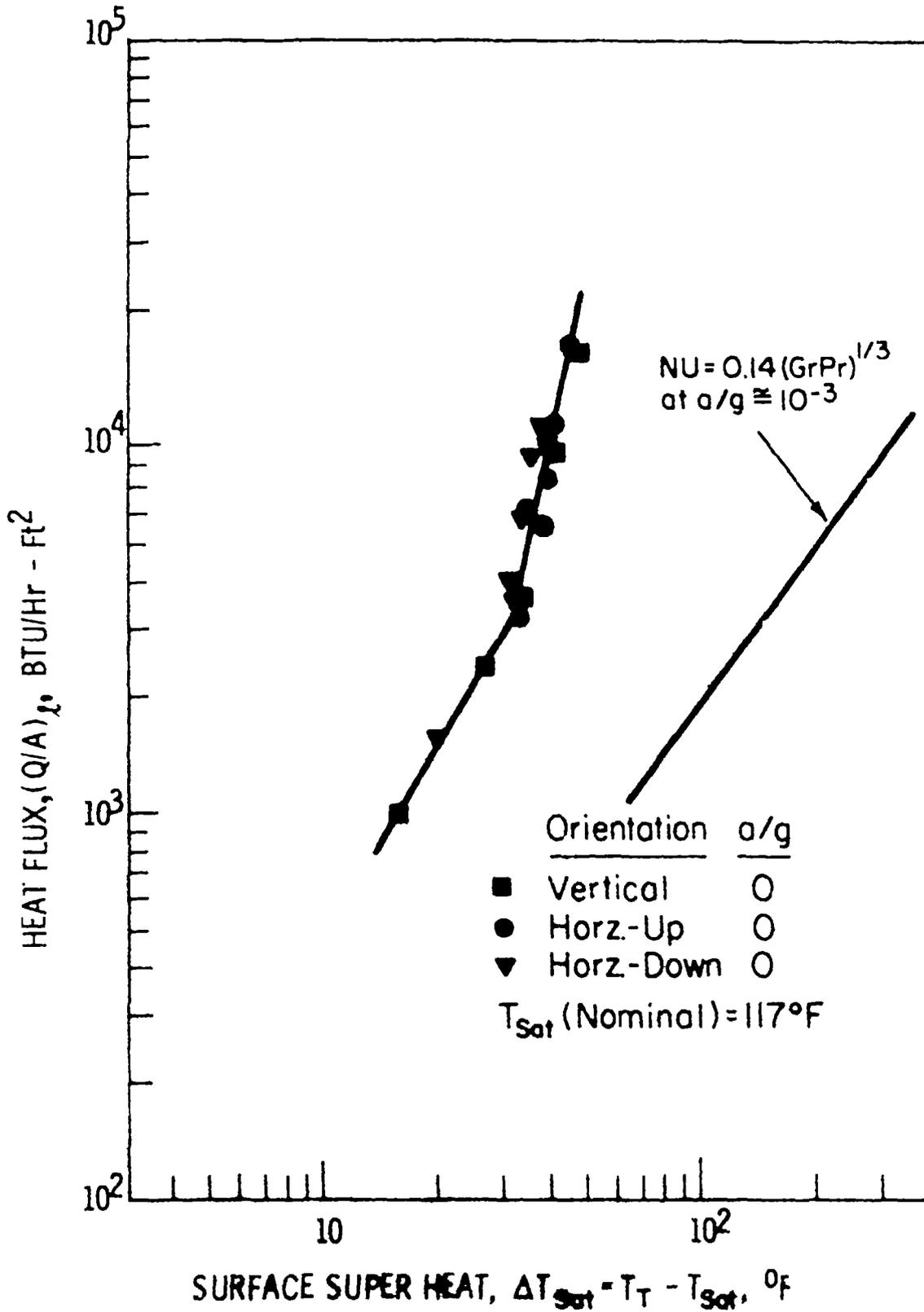
Fig. 72. Saturated nucleate boiling heat transfer, F113, all orientations, a/g ≠ 0
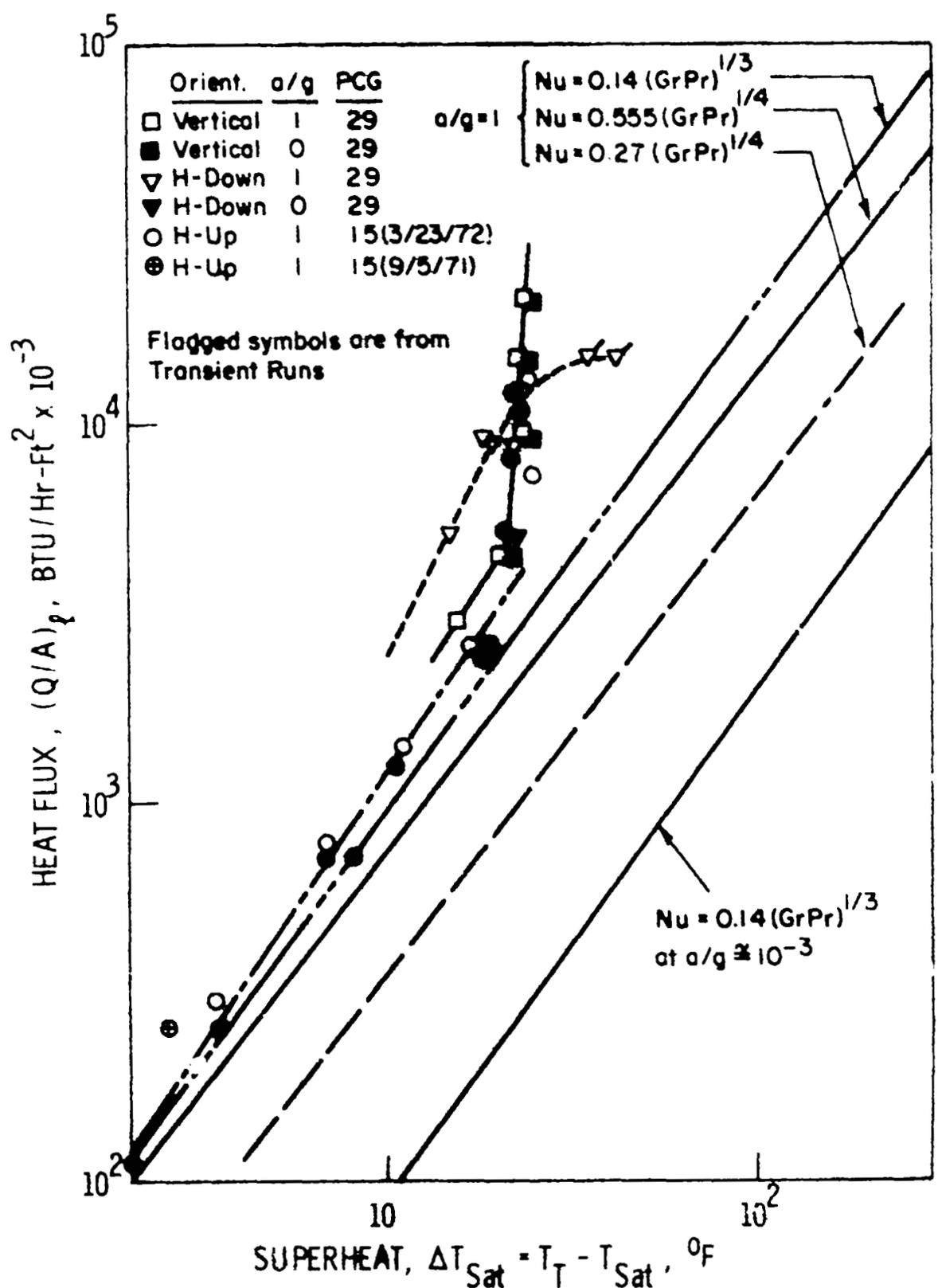
Fig. 73. Saturated nucleate boiling heat transfer, LN_2, all orientations, a/g=1 and $\simeq$ 0
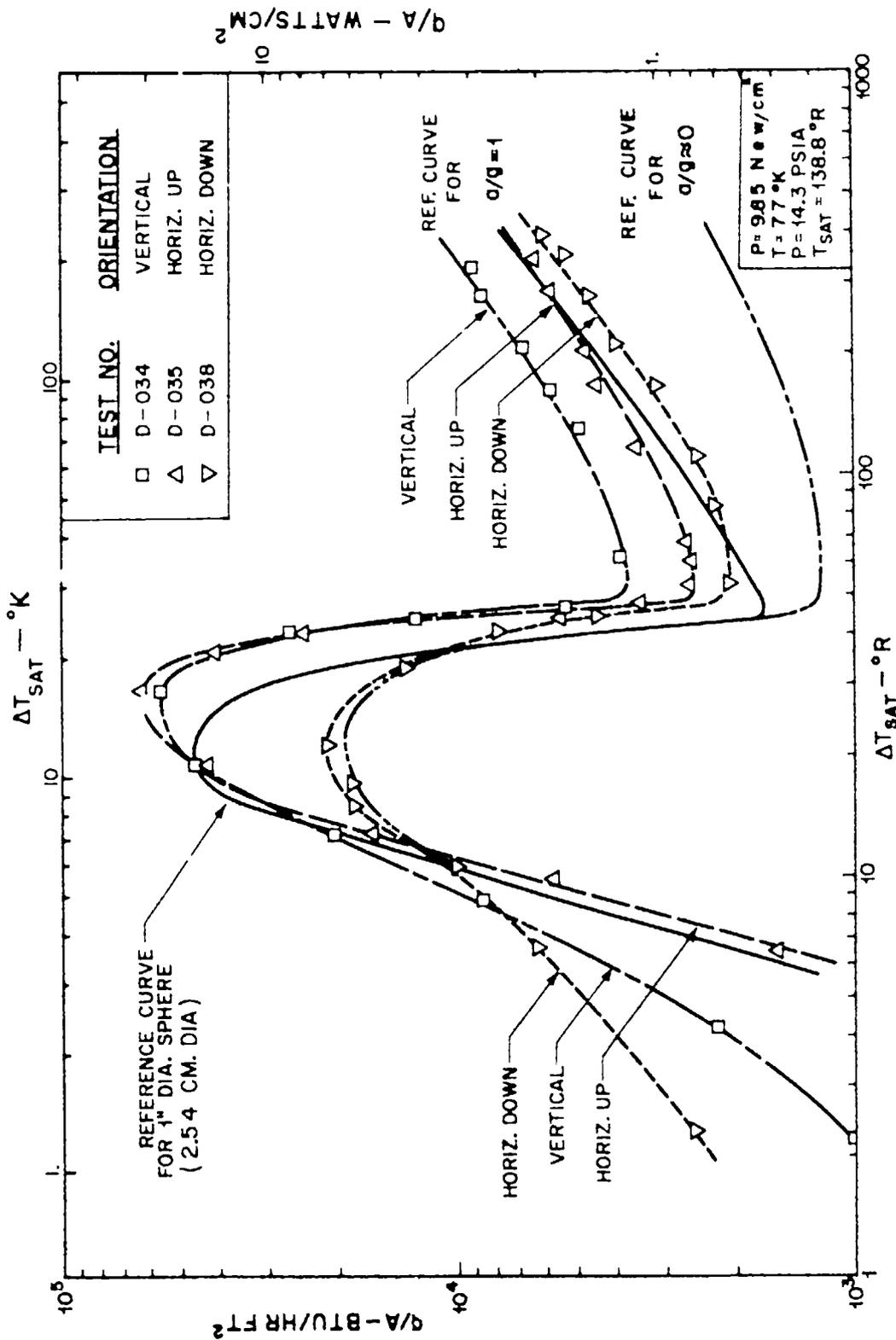
Fig. 74. Surface superheat in a boiling disc, LN₂, all orientations, a/g=1. Ref. [25]
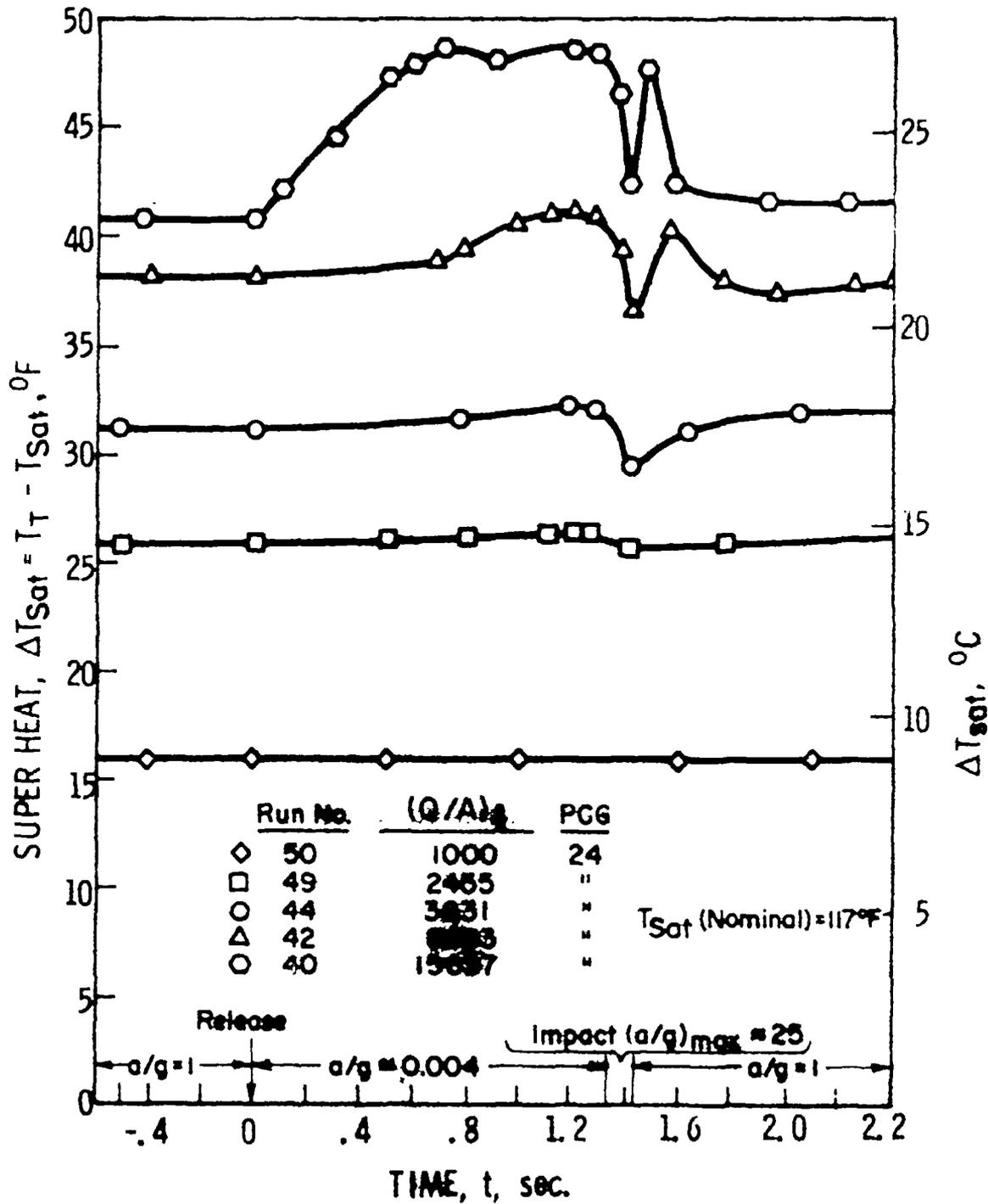
Fig. 75. Surface superheat in a nucleate boiling,
F113, vertical, a/g=1 and ⪬ 0
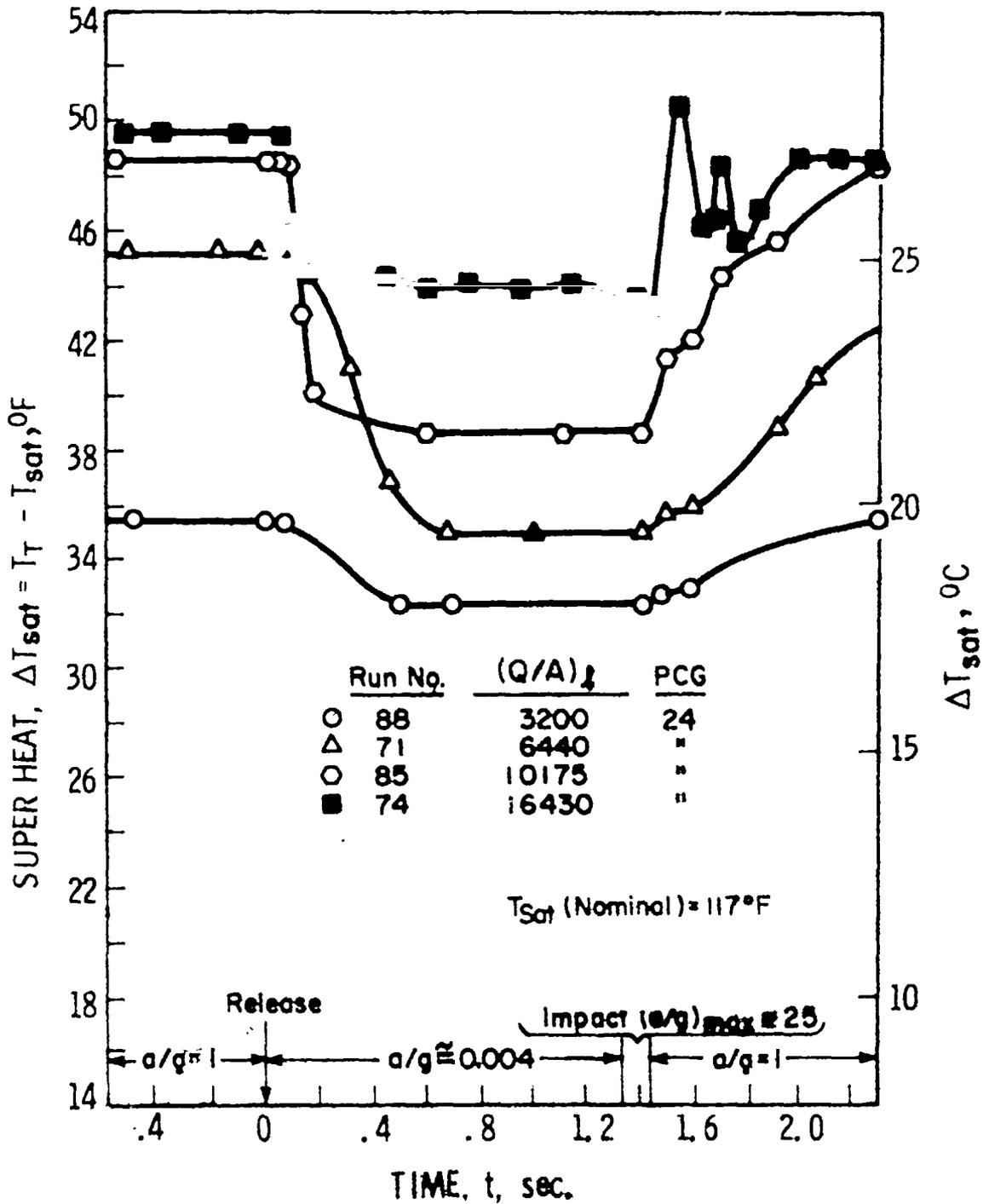
Fig. 76. Surface superheat in a nucleate boiling,
₣₁13, horizontal-up, a/g=1 and ≈ 0
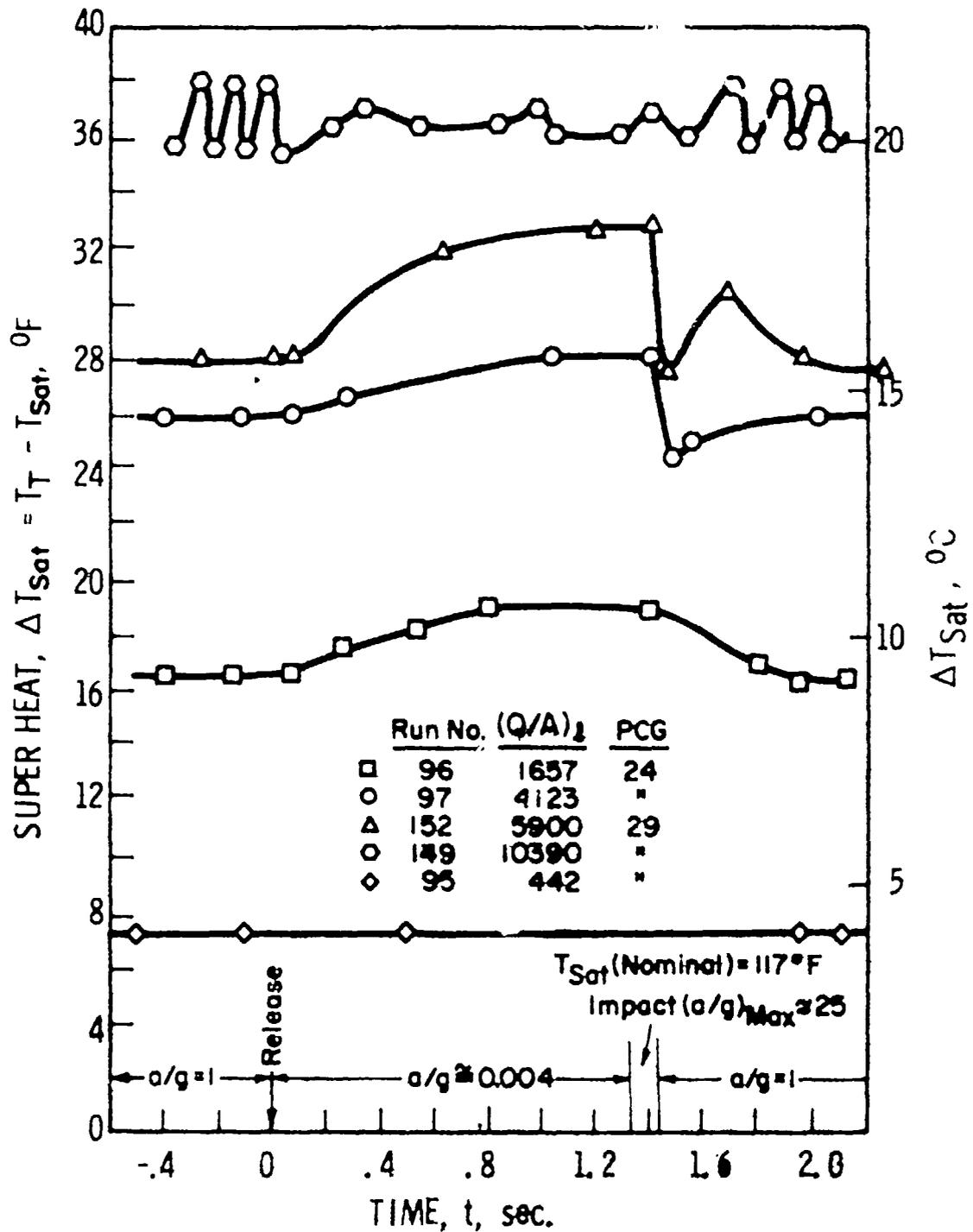
Fig. 77. Surface superheat in a nucleate boiling,
F113, horizontal-down, a/g=1 and ≈ 0
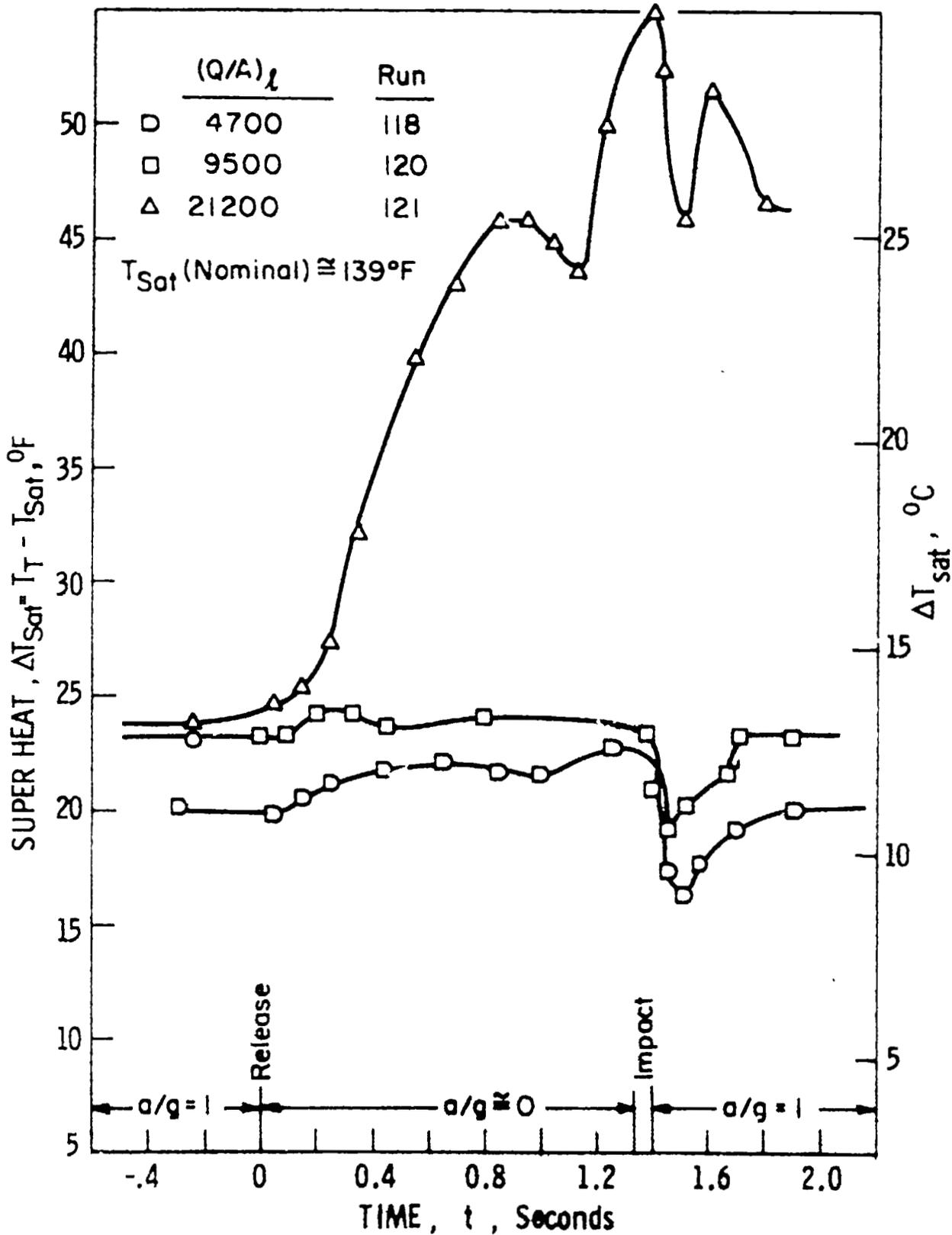
Fig. 79. Surface superheat in a nucleate boiling, LN₂, vertical, a/g=1 and ≃ 0
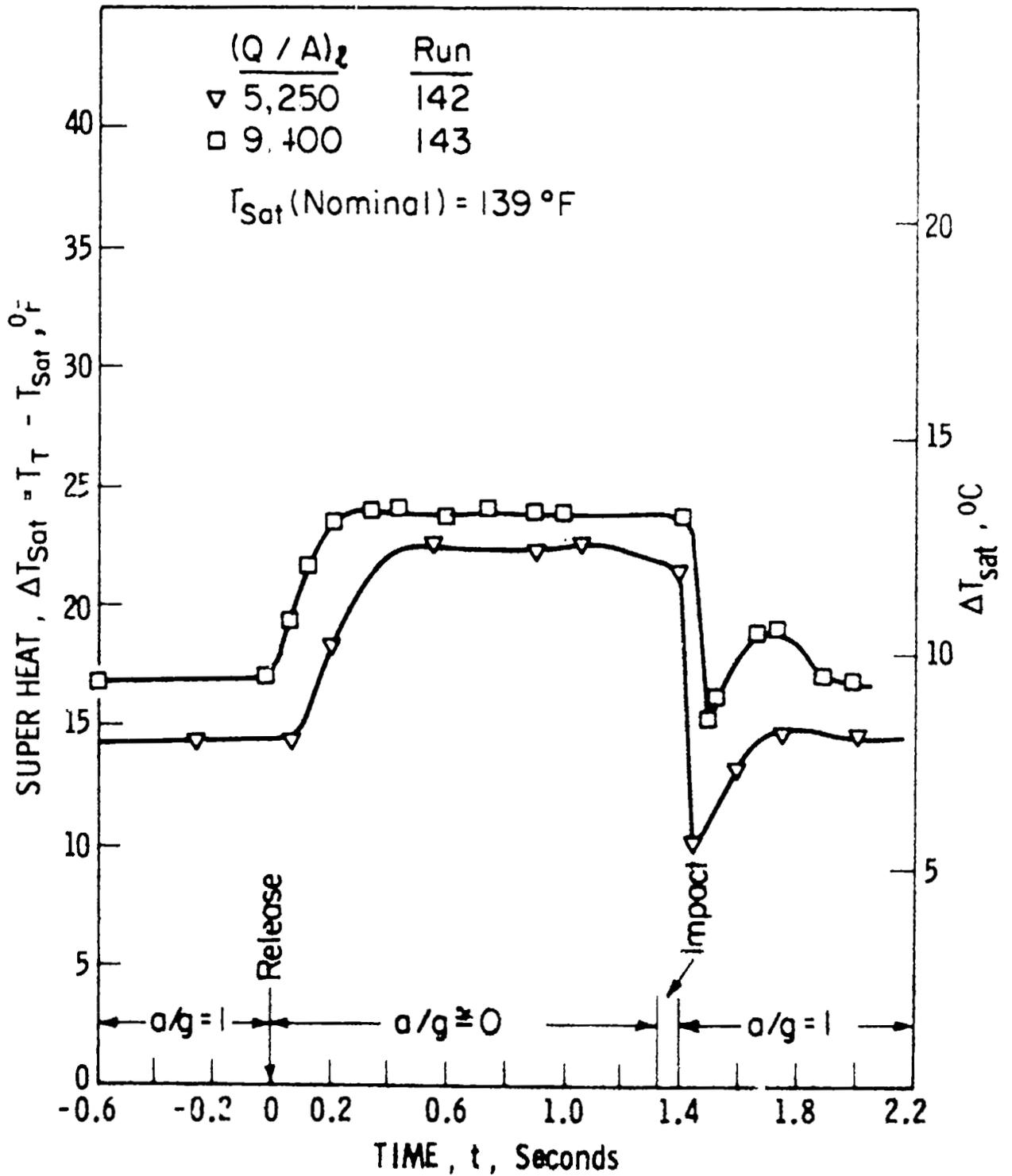
Fig. 79. Surface superheat in a nucleate boiling, LN$_2$, horizontal-down, a/g=1 and $\asymp$ 0
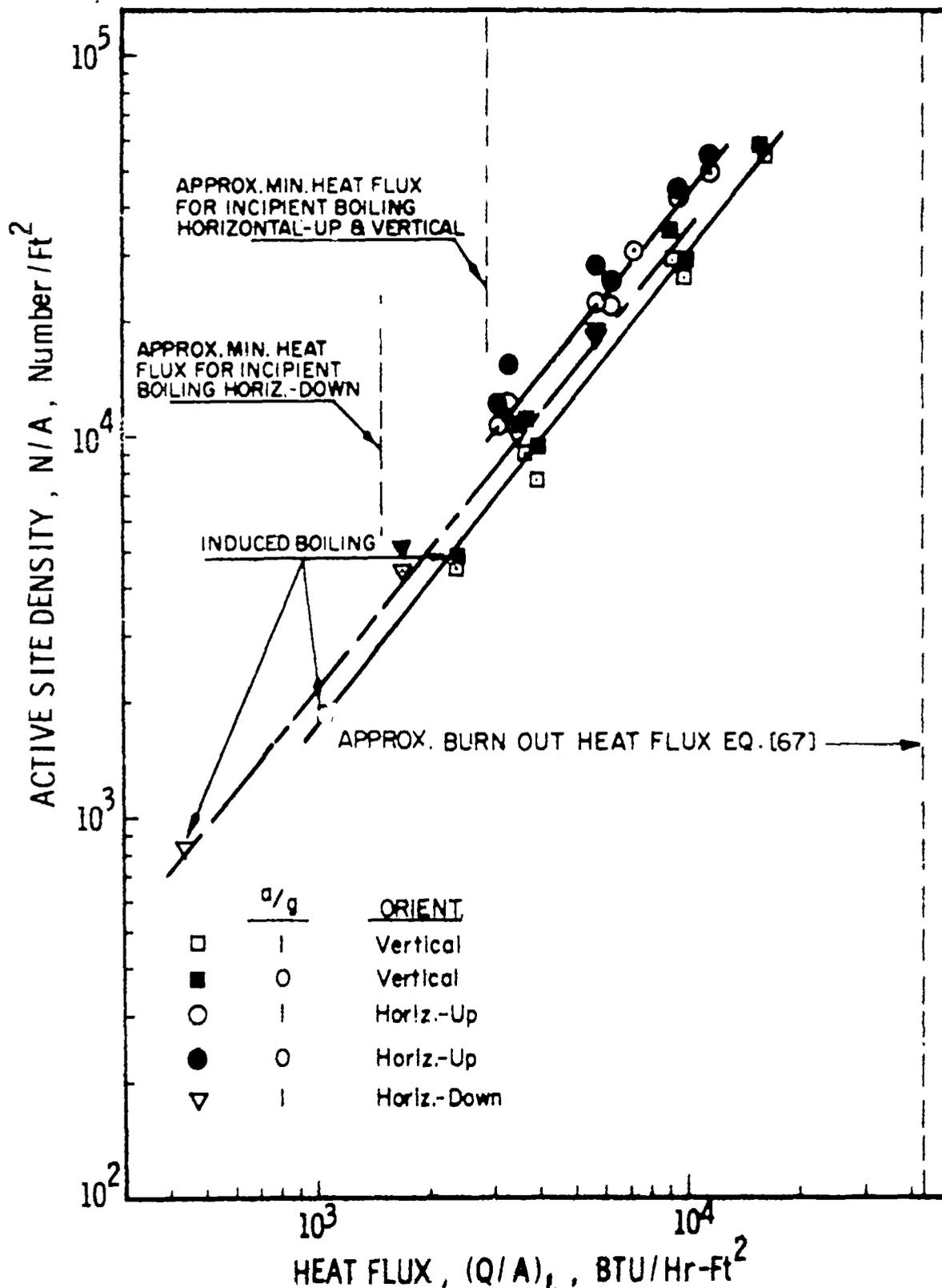
Fig. 80. Active site density in nucleate boiling, F113, all
orientations, a/g=1 and ≅ 0

Fig. 81. Active site density, N/A, and average population density, n/A, LN$_2$, vertical and horizontal-down, a/g=1 and $\approx$ 0
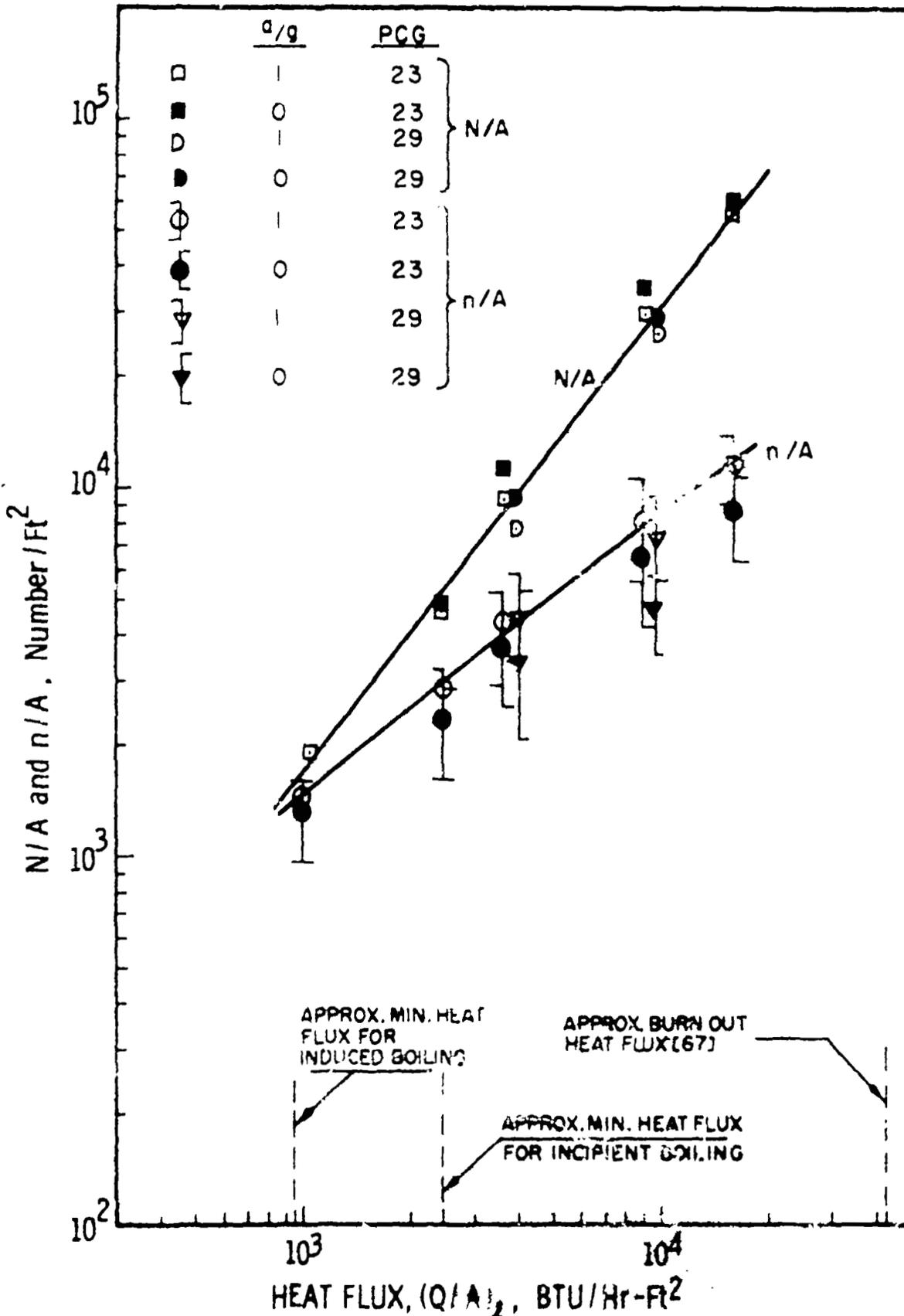
Fig. 82. Active site density, N/A, and average population
density. n/A, F113, vertical, a/g=1 and ≈ 0
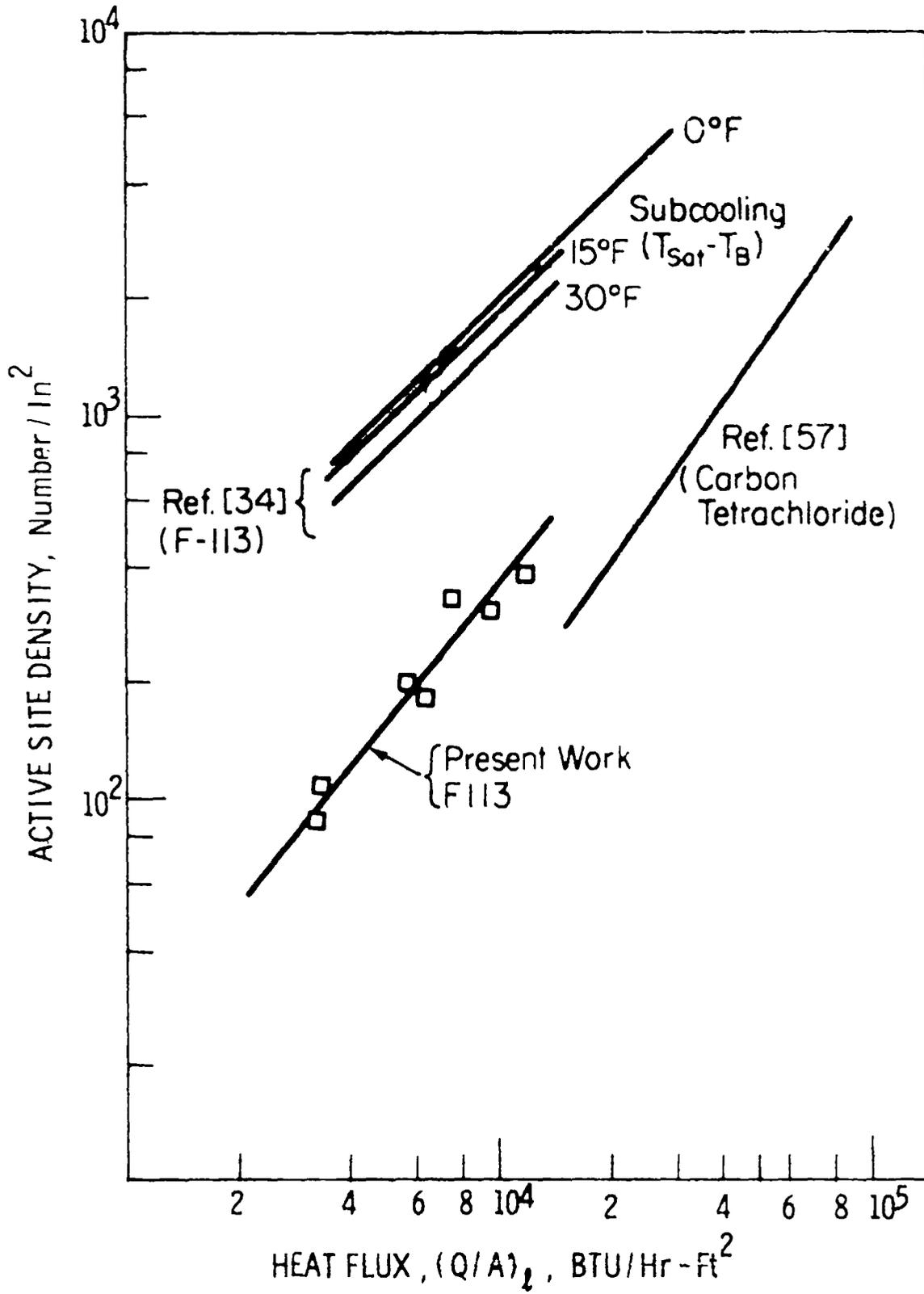
Fig. 83. Active site density results
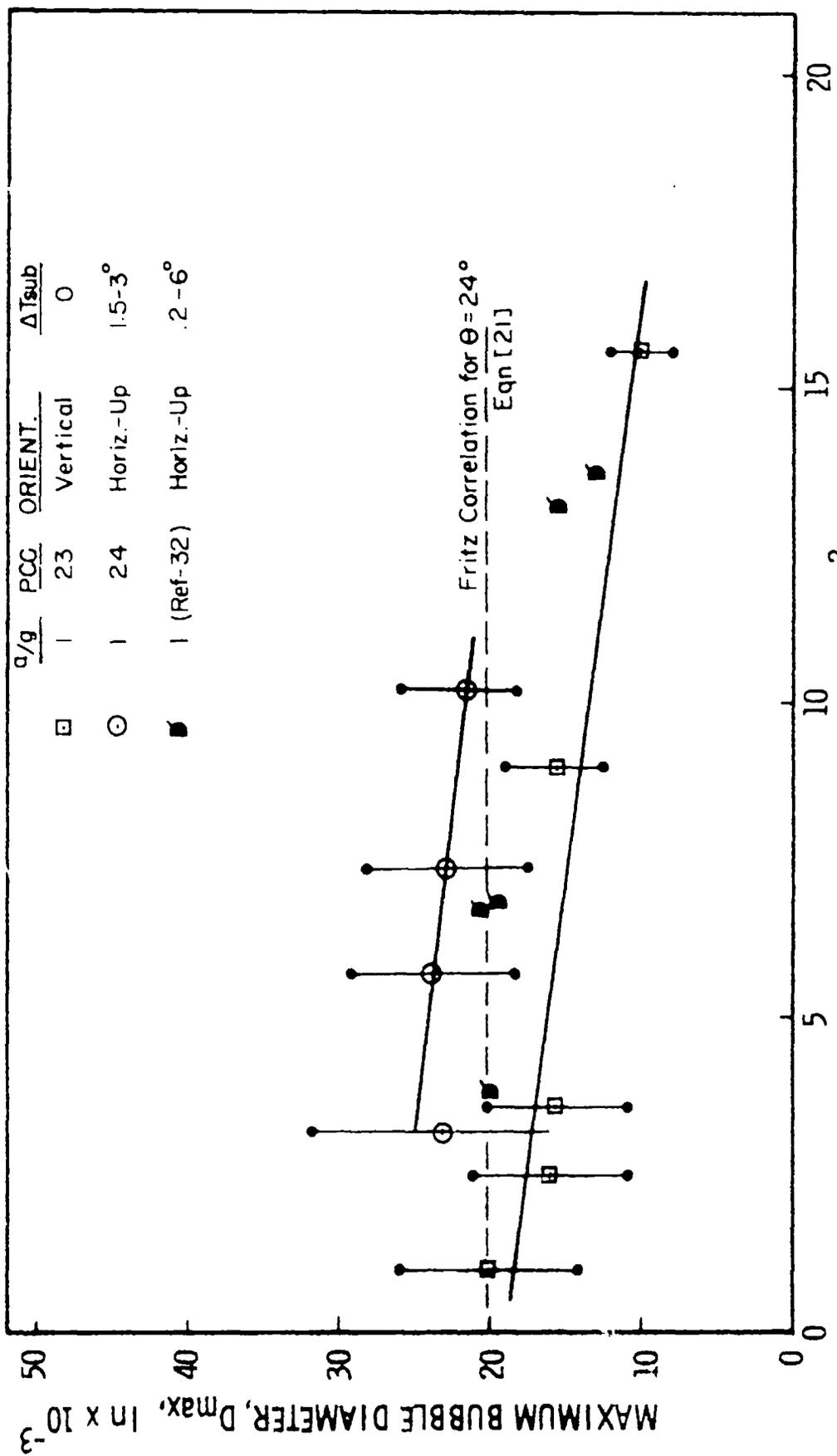
Fig. 84. Maximum bubble diameter, F113, horizontal-up and vertical, a/g=1
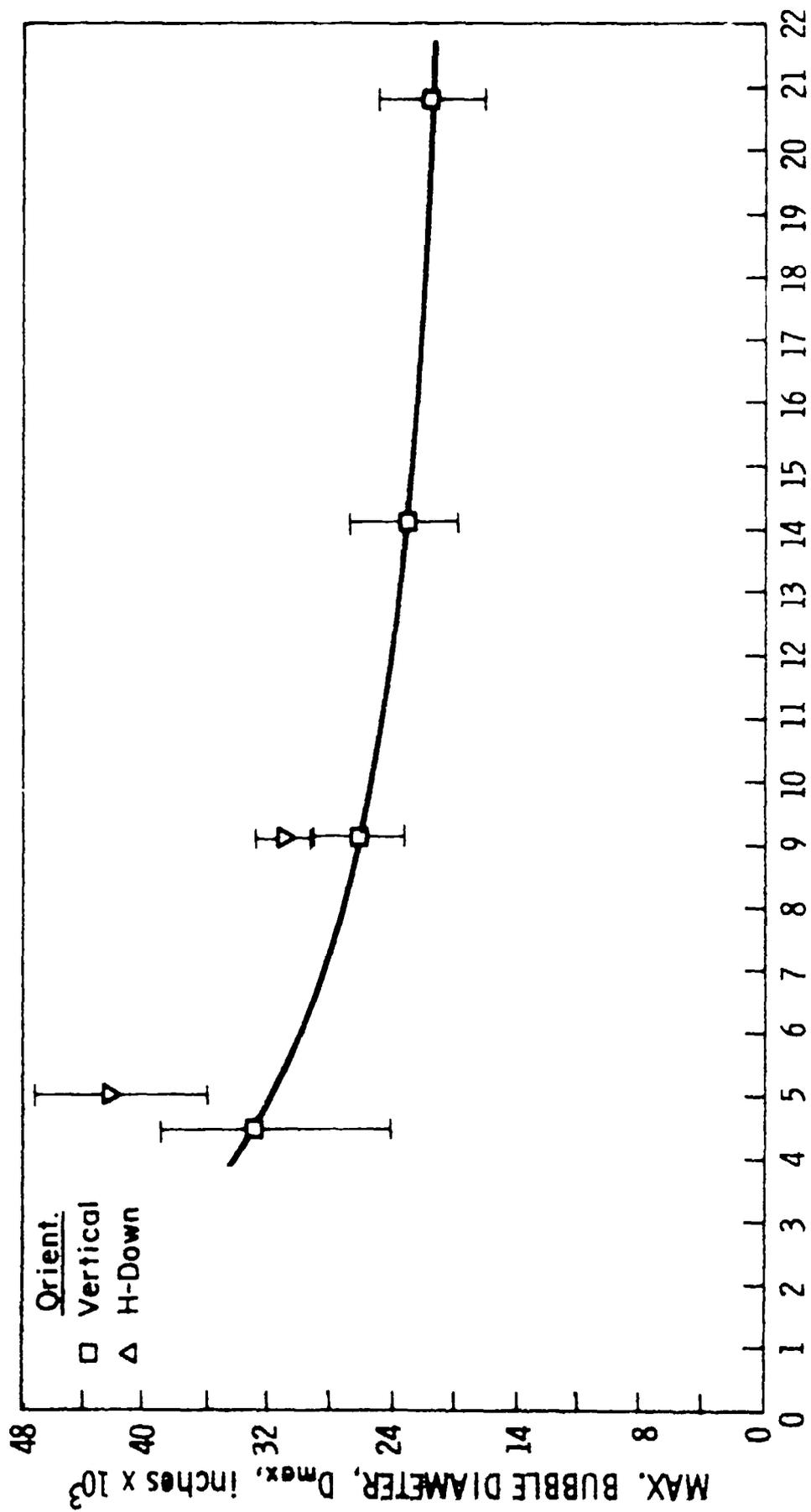
Fig. 85. Maximum bubble diameter, LN_2, vertical and horizontal-down, $a/q=1$
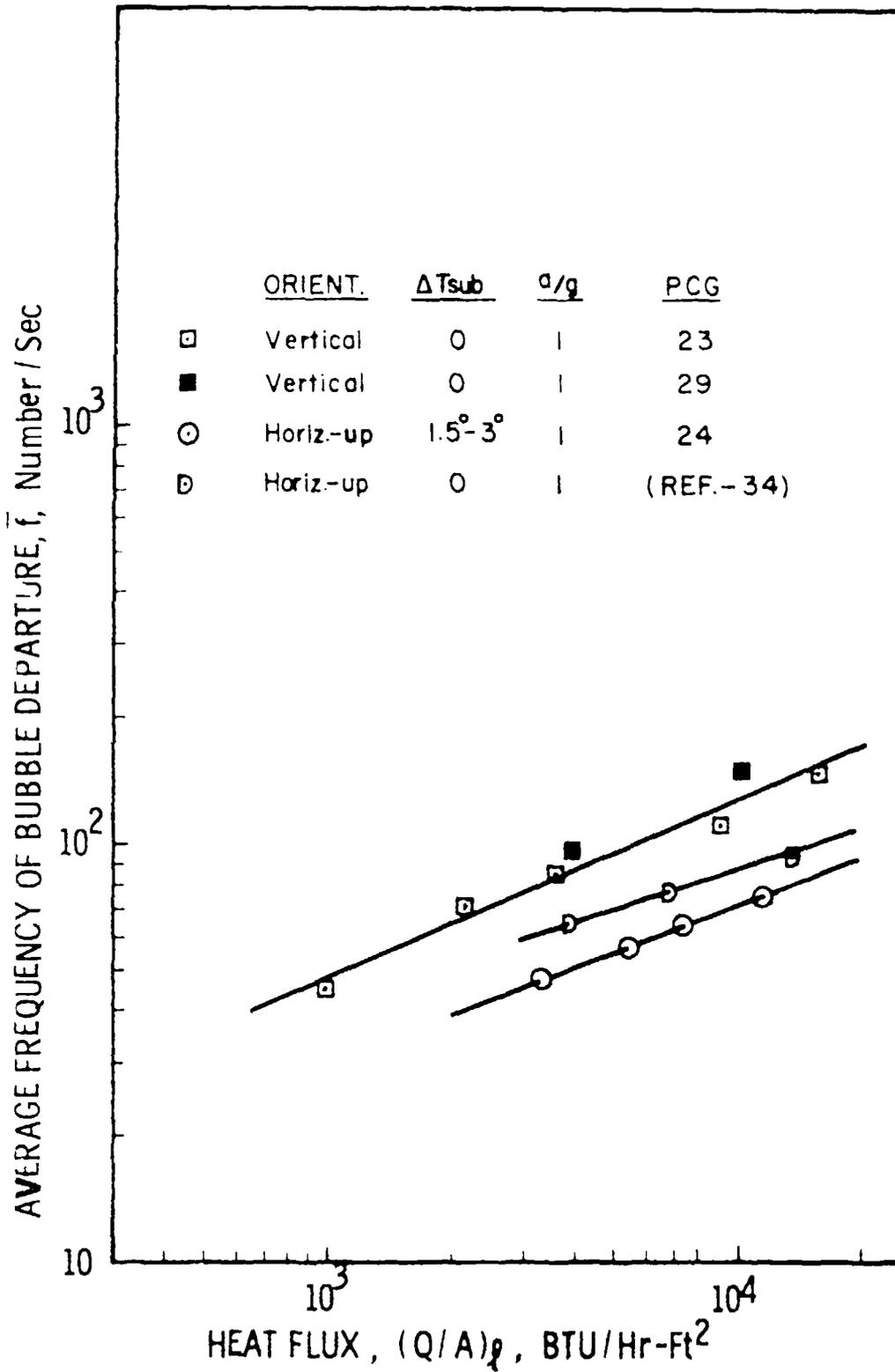
Fig. 86. Average frequency of bubble departure, F113,
vertical and horizontal-up, a/g=1
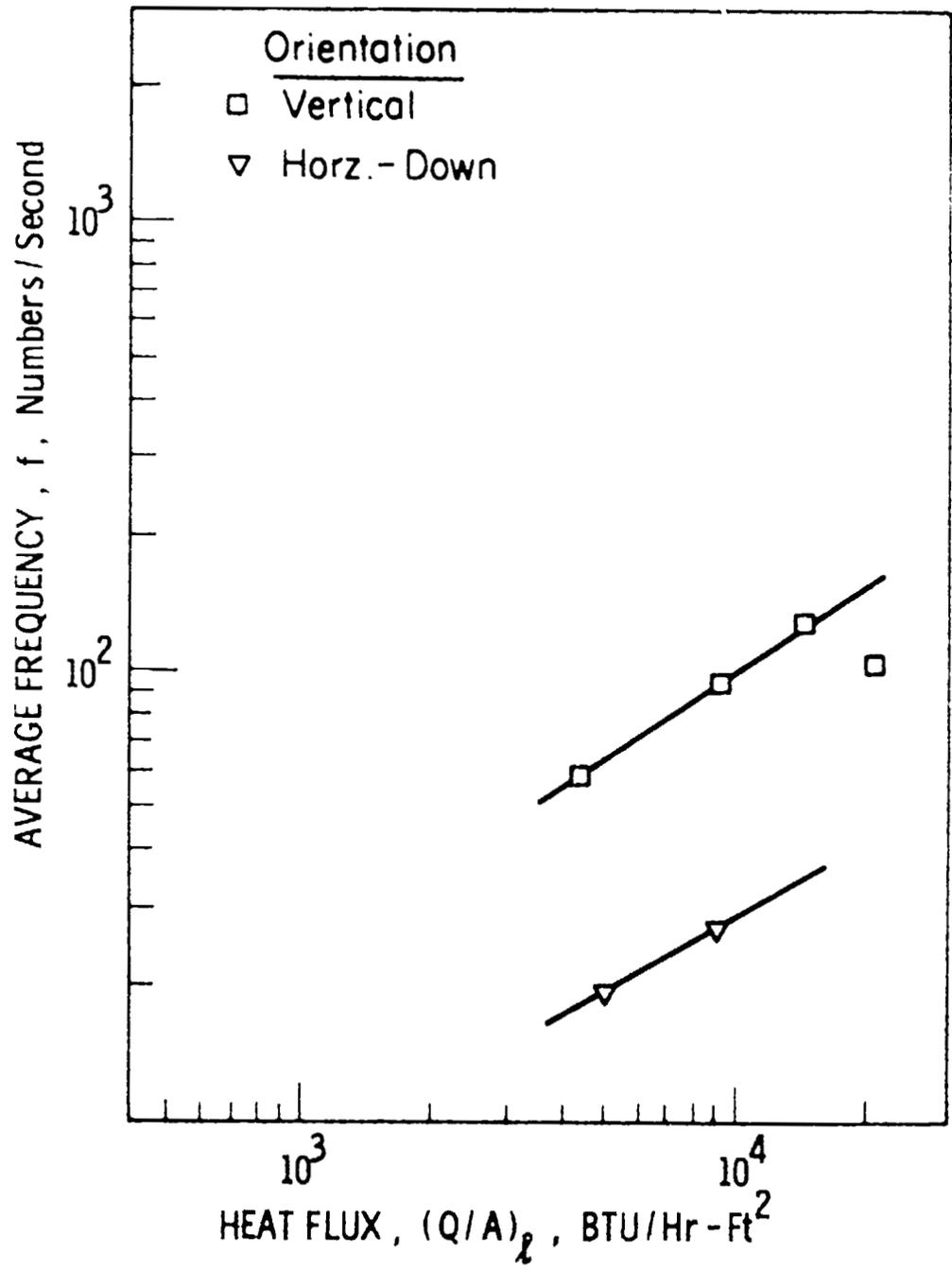
Fig. 87. Average frequency of bubble departure, LN_2, vertical and horizontal-down, $a/g=1$
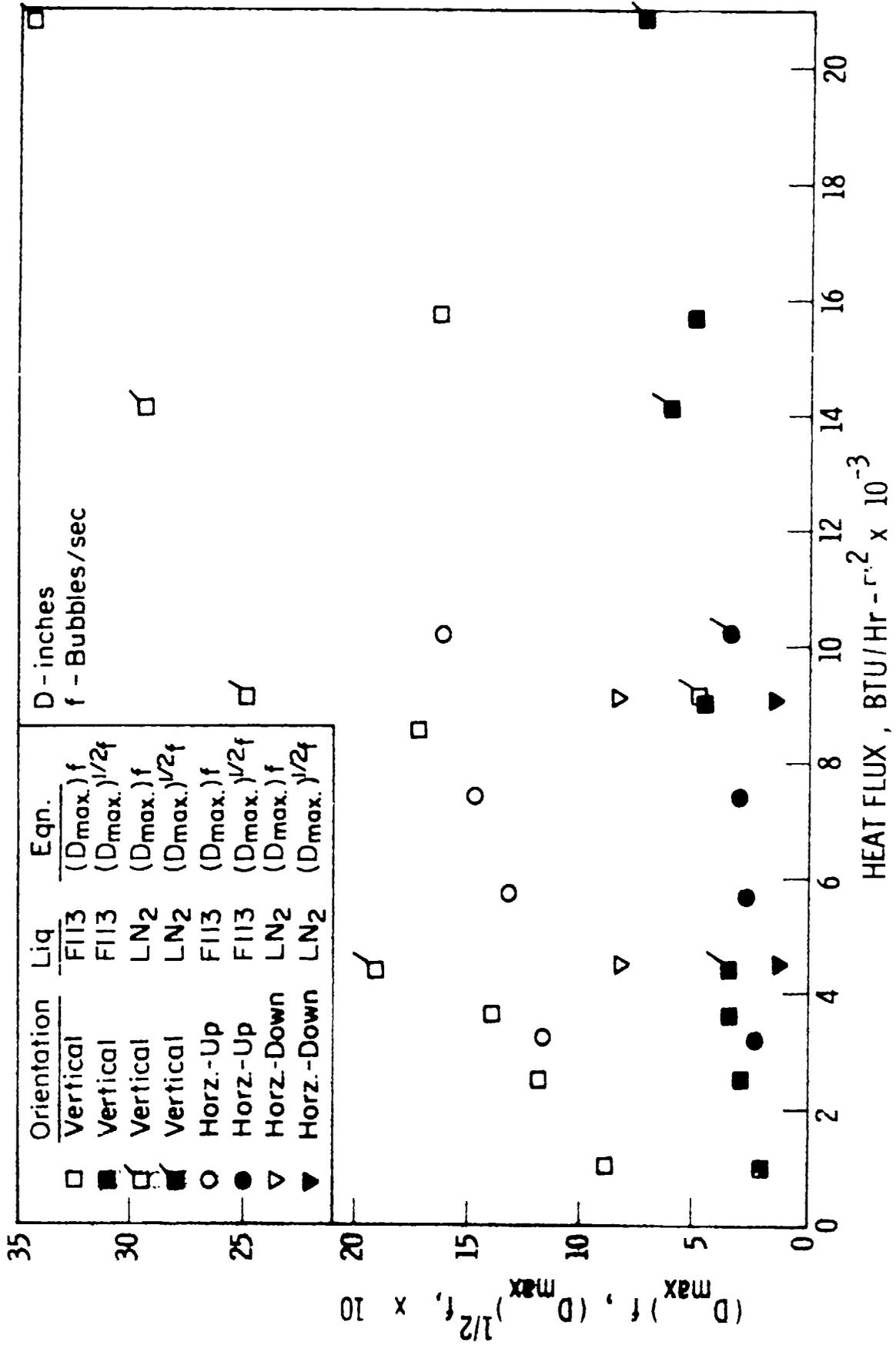
Fig. 88. Variation of $(D_{max})f$ and $(D_{max})^{1/2}f$, $a/g=1$.
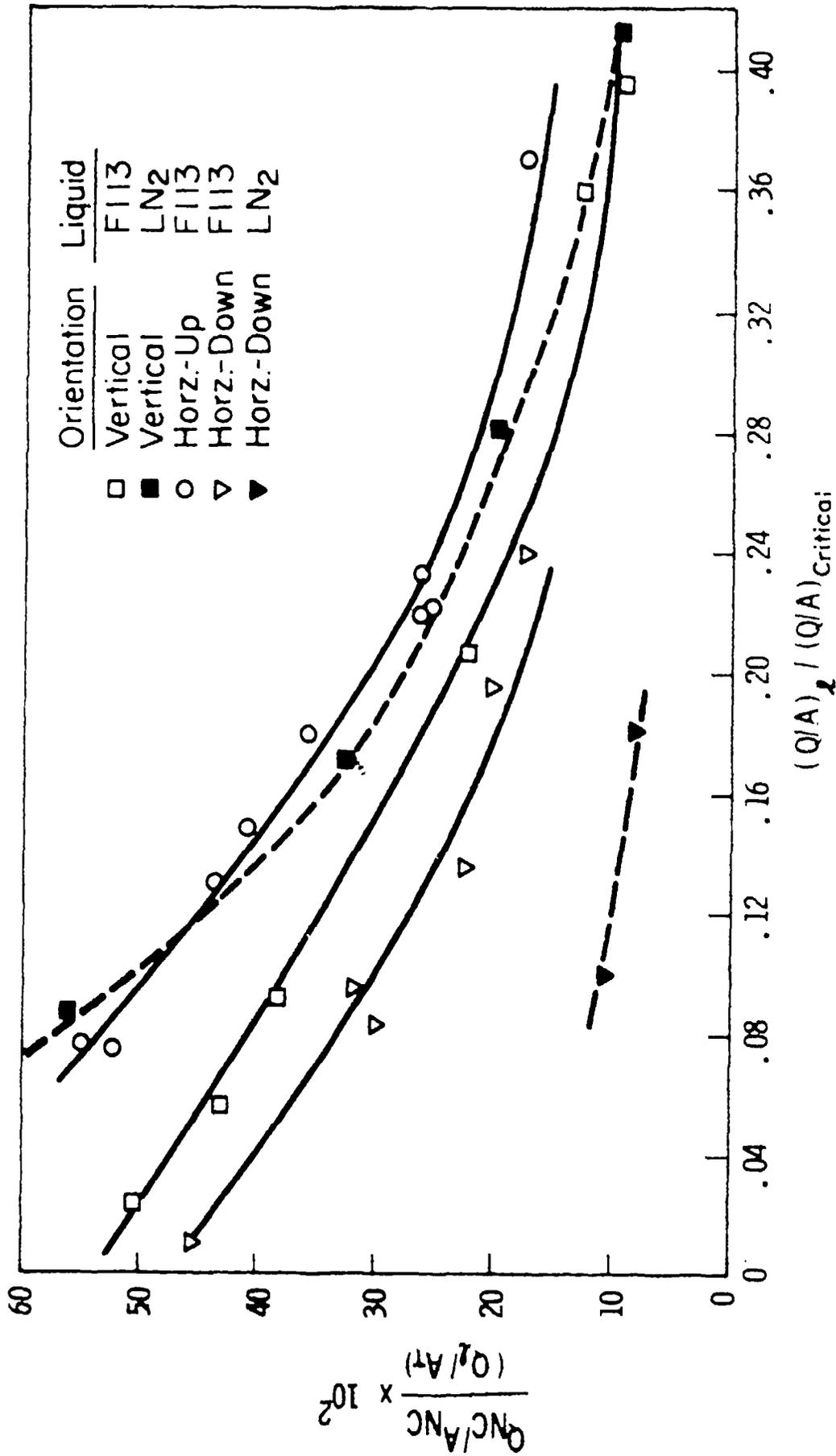
Fig. 99. Natural convection heat flux fraction with nucleate boiling, $a/q=1$
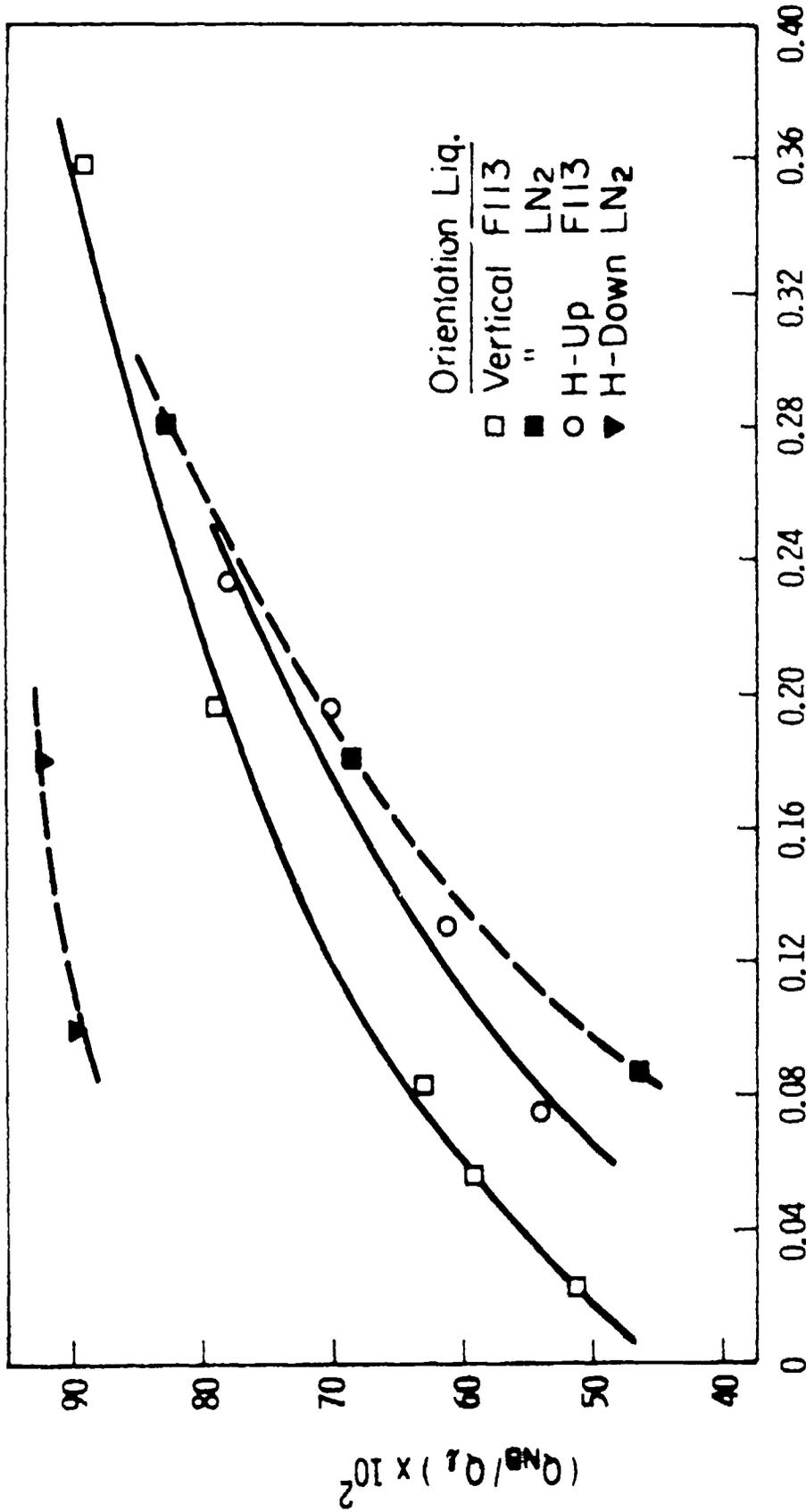
Fig. 90. Nucleate boiling heat flux percent
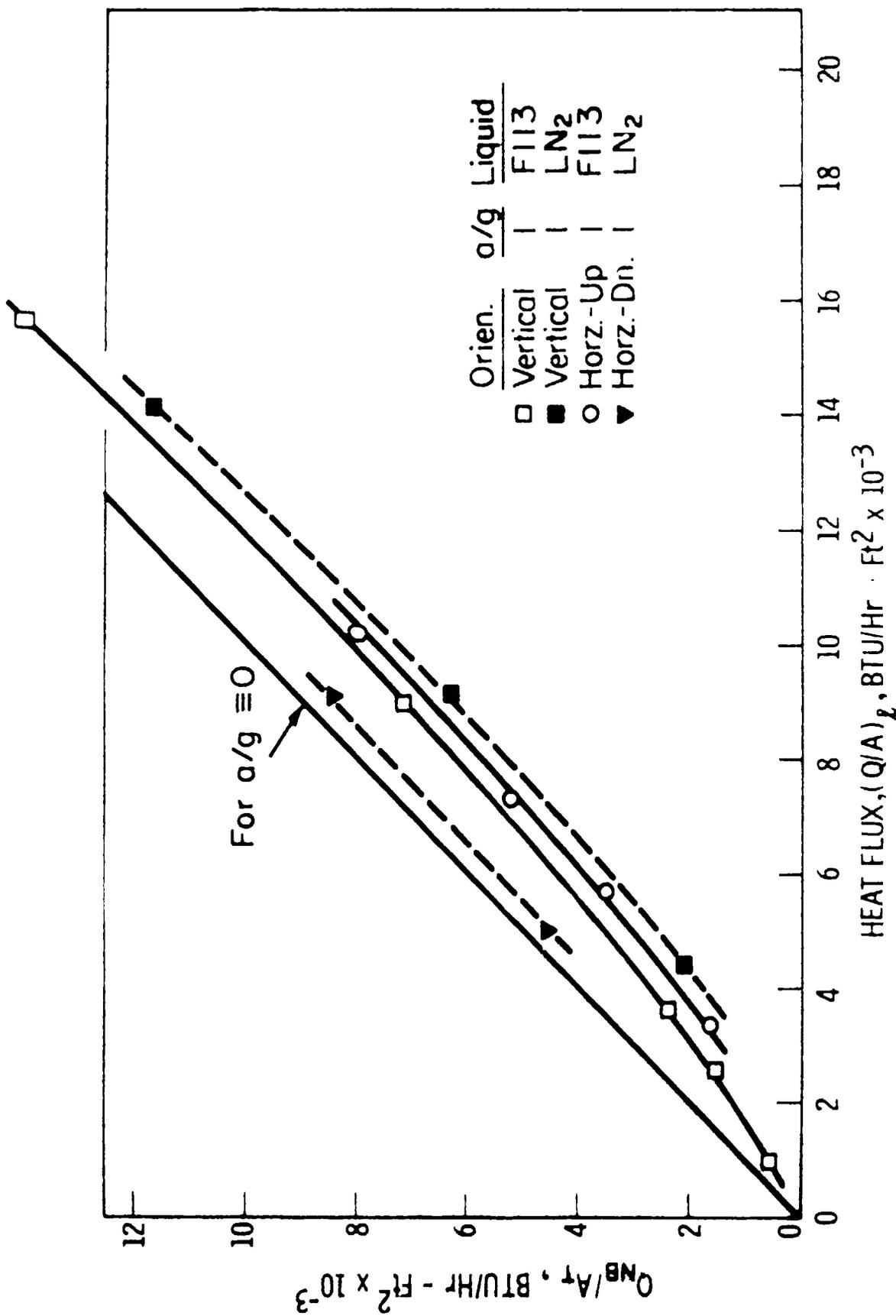
Fig. 91. Nucleate boiling heat flux
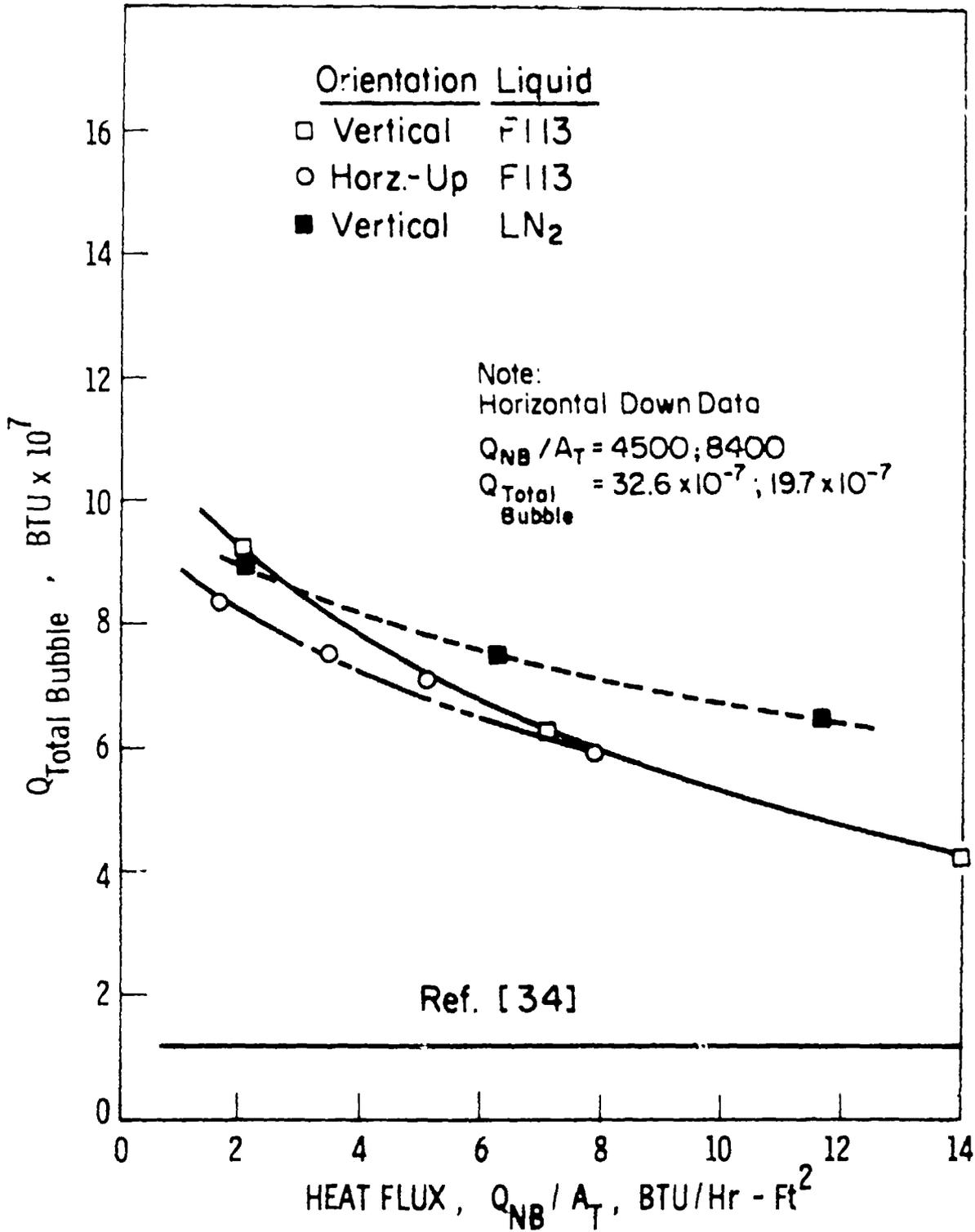
Fig. 92. Total bubble heat transfer
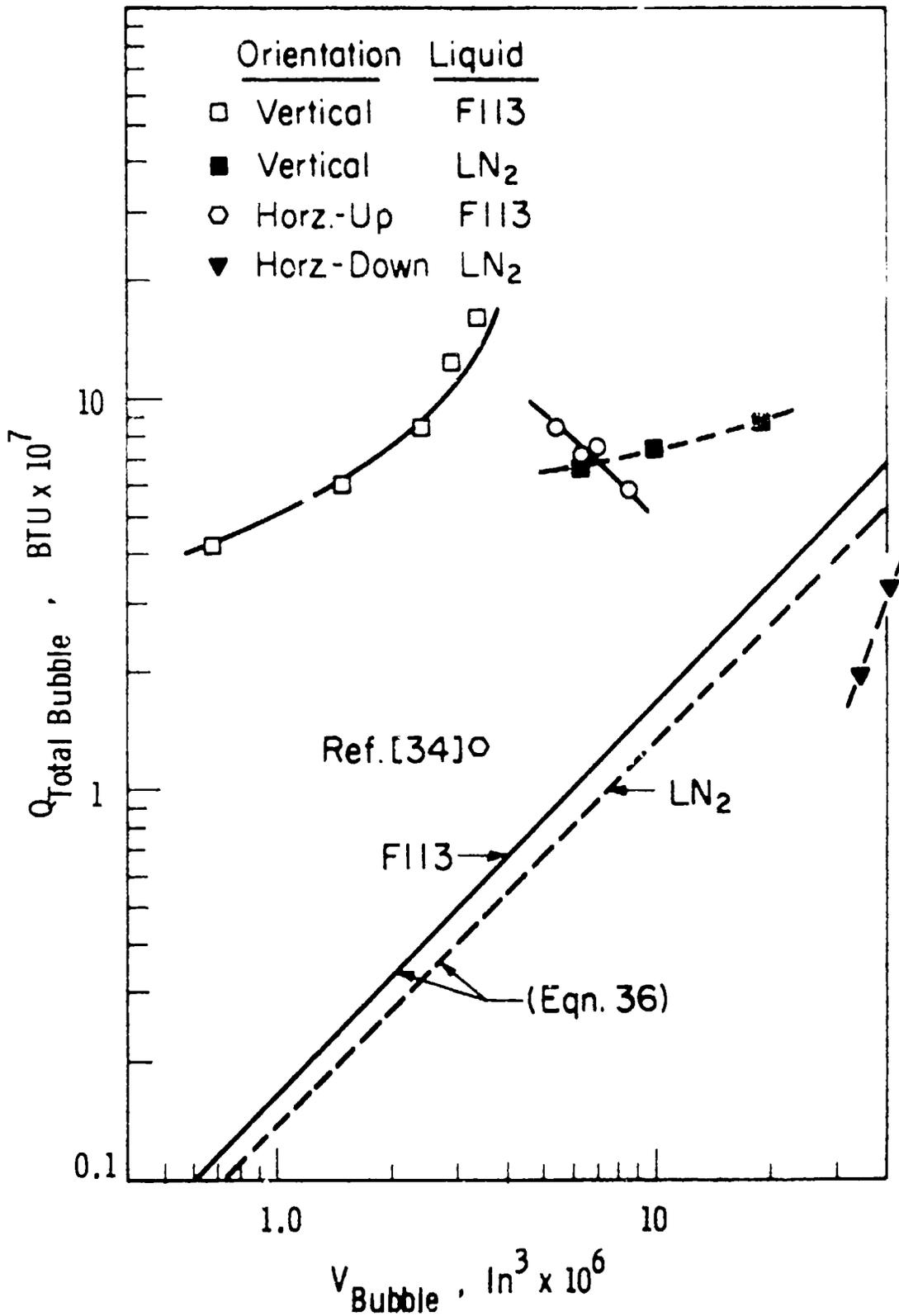
Fig. 93. Evaluation of latent heat transport model
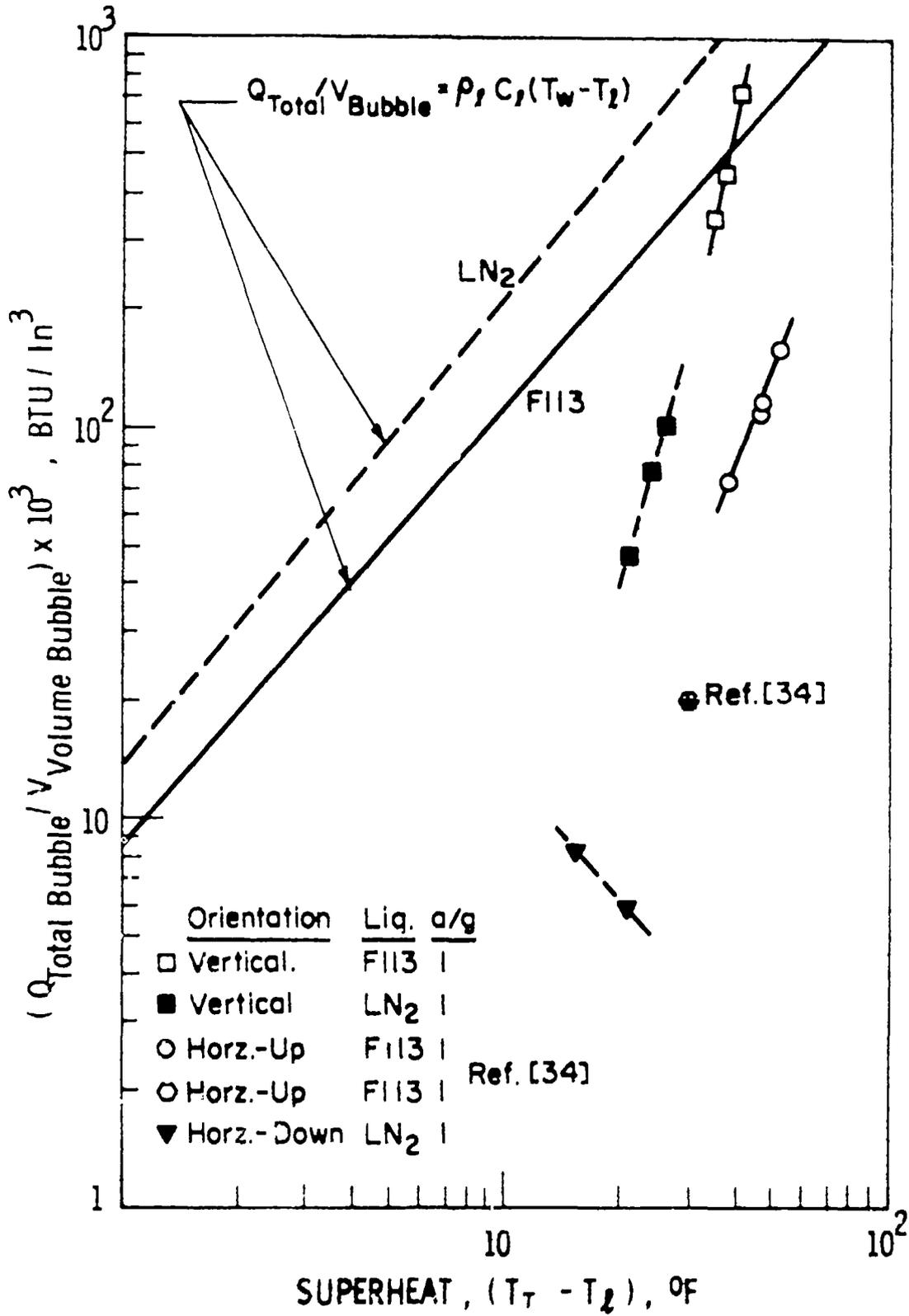
Fig. 94. Evaluation of vapor-liquid exchange model

APPENDIX A

ONSET OF CONVECTION

With the transient process being used here, a step increase in heat generation in the thin film deposited on the glass surface is used in order to achieve a step increase in heat flux to the liquid. The quantity measured is the heat generation in the film, which is distributed to both the liquid and the solid. The fraction going to the liquid can be computed if it is possible to calculate the fraction going to the solid side. A solution to this problem is available provided that the glass plate can be considered as a semi-infinite solid during the time period of interest. To assess this, use is made of the expression for the penetration depth of temperature with an imposed heat flux [57]

$$\delta = (6\alpha t)^{1/2} \tag{39}$$

Substituting the properties of pyrex into Eq. (39), it will take approximately 6.0 seconds for the far side of a 3/16 inch thick piece of pyrex to start rising in temperature. The maximum time periods being considered in our experiments are approximately 2.5 seconds, so the pyrex plate can be considered as a semi-infinite solid during this period.

The problem whose solution is now desired is that of two semi-infinite solids with a step increase in a plane heat source at the boundary of these two solids. The pyrex substrate is one solid, and the liquid being heated represents the other solid, up to the point where convection or boiling begin. The heat capacity of the thin film can be neglected. The solution is presented in Ref. [58], and reproduced below:

-189-

$$T_\ell(x,t) - T_i = \frac{2(Q/A)_T(a_s a_\ell t)^{1/2}}{k_\ell a_s^{1/2} + k_s a_\ell^{1/2}} \, i\,erfc\,\frac{x}{2(a_\ell t)^{1/2}} \tag{40}$$

$$T_s(x,t) - T_i = \frac{2(Q/A)_T(a_s a_\ell t)^{1/2}}{k_\ell a_s^{1/2} + k_s a_\ell^{1/2}} \, i\,erfc\,\frac{x}{2(a_s t)^{1/2}} \tag{41}$$

For a plane heat source of constant strength Q/A, it can be shown, with Eqs. (40) and (41), that the ratio of the heat flux to each region is constant and given by:

$$\frac{Q_\ell}{Q_s} = \frac{k_\ell}{k_s}\left(\frac{a_s}{a_\ell}\right)^{1/2} \tag{42}$$

The fraction of the total input which goes into the liquid is then given by

$$\frac{(Q/A)_\ell}{(Q/A)_T} = \frac{1}{1 + Q_s/Q_\ell} \tag{43}$$

The temperature distribution in the liquid $T_\ell(x,t)$ is of interest in establishing the conditions for incipient boiling under the transient process. The interface temperature, T_T, corresponding to $X=0$ in Eqs. (40) and (41), is

$$T_T - T_i = \frac{2(Q/A)_T(a_s a_\ell)^{1/2}}{\pi^{1/2}(k_\ell a_s^{1/2} + k_s a_\ell^{1/2})} t^{1/2} \tag{44}$$

Equation (44) can also be rewritten as

$$\frac{T_T - T_i}{(Q/A)_\ell} = \frac{2}{\pi^{1/2}} \frac{1}{k_\ell}(a_\ell t)^{1/2} \tag{45}$$

Substituting the properties of liquids and pyrex at the corresponding temperatures into Eq. (43), the fraction of the total energy input transferred to the liquids are:

To F113

$$\left[\frac{(Q/A)_\ell}{(Q/A)_T}\right]_{F113} = 0.166 \tag{46}$$

To LN_2

$$\left[\frac{(Q/A)_\ell}{(Q/A)_T}\right]_{LN_2} = 0.491 \tag{47}$$

Substituting properties into Eq. (45) and rearranging will give the temperature rise of the gold film:

In F113

$$\left[\frac{T_T - T_i}{(Q/A)_\ell}\right]_{F113} = 0.0223\, t^{1/2} \tag{48}$$

In LN_2

$$\left[\frac{T_T - T_i}{(Q/A)_\ell}\right]_{LN_2} = 0.00686\, t^{1/2} \tag{49}$$

The next process which occurs in a gravitational field prior to the inception of boiling is the onset of natural convection. Onset of natural convection has been characterized as an instability problem, and has been reasonably well described by Vest and Lawson [59] for the case of a horizontal wire.

Rayleigh [60] showed that the stability of a horizontal layer of fluid heated from below is governed by the numerical value of the dimensionless parameter

$$R_a = \frac{g\gamma\beta\delta^4}{\alpha\nu} \tag{50}$$

It has been shown by Jeffreys [61], Low [62], Pellew and Southwell [63] that the critical Rayleigh number is about 1700 for a fluid between two solid boundaries. Low [62], Pellew and Southwell [63] calculated the critical Rayleigh number for rigid lower and free upper boundaries, and for constant wall temperature. They found that the critical Rayleigh number, for such a fluid layer with constant underside wall temperature is about 1100. Sparrow et al [64] showed that the critical Ra=800 for fluid layers heated from below with constant imposed heat flux. From Eq. (50), it is then possible to compute the thickness which becomes unstable. δ can be expressed as a function of time using the approximate solution of the conduction problem in a semi-infinite solid with an imposed constant heat flux, expressed in terms of a "penetration depth" given by Eq. (39). The approximate solution also gives

$$T_T(t) - T_i = \left(\frac{4}{\pi}\right)^{1/2} \frac{(Q/A)_\ell}{k_\ell} \left(a t\right)^{1/2} \tag{51}$$

The temperature gradient within the penetration depth, assuming it to be linear, is given by

$$\beta = \frac{T_T(t) - T_i}{\delta} = \left[\frac{2}{3\pi}\right]^{1/2} \frac{(Q/A)_\ell}{k_\ell} \tag{52}$$

Substituting Eqs. (39) and (52) into Eq. (50), and taking the critical Ra number as 800, one obtains

$$\left[\frac{(Q/A)_\ell \, \gamma g a}{k \nu}\right]^{1/2} \tau_i = 7 \tag{53}$$

where τ_i is the time at which the instability sets in as manifested by the onset of natural convection.

Substituting the properties for LN_2 into Eq. (53), this reduces to:

$$\left[(Q/A)_\ell \right]^{\frac{1}{2}}_{LN_2} \tau_1 = 13.1 \tag{54}$$

For F113 it reduces to

$$\left[(Q/A)_\ell \right]^{\frac{1}{2}}_{F113} \tau_1 = 18 \tag{55}$$

Table 5 gives the summary of the results similar to Eq. (54) obtained for LN_2 and F113 using the three different critical Rayleigh numbers.

TABLE 4

The Critical Rayleigh Number and Time

Delay for Onset of Convection

Liquid	Type of Boundary Condition	Critical R_a	$[(Q/A)]^{1/2} \tau_1$
LN_2	Solid-solid (constant wall temp)	1700	19.08
F113	Solid-solid (constant wall temp)	1700	37.5
LN_2	Solid-free (constant wall temp)	1100	15.35
F113	Solid-free (constant wall temp)	1100	24.4
LN_2	Solid-free (constant heat flux)	800	13.09
F113	Solid-free (constant heat flux)	800	18

The above development applies to the onset of natural convection on a horizontal heated surface facing upward. The onset of natural convection on a vertical heated surface is treated somewhat differently.

As first pointed out by Siegel [68], the initial behavior of the temperature and velocity field for a semi-infinite vertical flat plate are the same as for the doubly infinite vertical plate. The temperature field could be obtained by solving an unsteady one dimensional heat-conduction problem. The transition to convection begins only when some effect from the leading edge has propagated up the plate to the particular point in question. Before this leading edge effect has propagated to a particular point the region effectively does not know that the plate has a leading edge. Goldstein and Briggs [65] obtained an equation for predicting the penetration distances of disturbances due to the influence of the leading edge for a vertical semi-infinite flat plate, for boundary conditions of a step change in surface heat flux, based on the velocity and temperature fields along a doubly infinite flat plate. The maximum value of the penetration distance, X_p, obtained at any time for arbitrary Prandtl number was

$$X_P = \frac{.0058\gamma(Q/A)_{\ell}(\alpha t)^{1/2} t^2}{k} \tag{56}$$

Substituting the height of the test surface for X_p and liquid properties, the following relations are obtained:

For F113

$$\left(Q/A\right)_{F113}^{2/5} \tau_1 = 21.3 \tag{57}$$

For LN_2

$$\left(Q/A\right)_{LN_2}^{2/5} \tau_1 = 16.1 \tag{58}$$

τ_1 values in Eqs. (57) and (58) give the time required for the leading edge effect to reach the upper edge of the vertical test surface, which represents in turn the completion of the onset of free convection.

APPENDIX B

ERROR ANALYSIS

In the following section the errors associated with the determination of test surface temperature, area, and heat flux are discussed. To obtain the percent of uncertainty in the quantities calculated the procedure described by Kline and McClintoc [66] is used. The uncertainty associated with computation of the result R, which is obtained by combining certain numbers of variables V_1, V_2, V_3...V_n, is given by

$$\frac{W_R}{R} = \left[\left(\frac{\partial R}{\partial V_1} \frac{W_1}{R} \right)^2 + \left(\frac{\partial R}{\partial V_2} \frac{W_2}{R} \right)^2 + \cdots \left(\frac{\partial R}{\partial V_n} \frac{W_n}{R} \right)^2 \right]^{1/2} \qquad (59)$$

where W_R is the uncertainty in the result R and W_1, W_2, W_3...W_n are the uncertainties associated with each independent variable.

A. TEST SURFACE TEMPERATURE

To calculate the uncertainty associated with the determination of test surface temperature, the uncertainties associated with R_T, R_c, T_c, dT/dR must be determined, as is noted in Eq. (59).

1) Test Surface Resistances

To measure the test surface resistance the set up shown in Fig. (13) is used. R_T is given by

$$R_T = \frac{E_T}{E_s} R_s \qquad (60)$$

The uncertainty associated with R_T is given by

$$\frac{W_{R_T}}{R_T} = \left[\left(\frac{W_{E_T}}{E_T} \right)^2 + \left(\frac{W_{E_s}}{E_s} \right)^2 + \left(\frac{W_{R_s}}{R_s} \right)^2 \right]^{1/2} \qquad (61)$$

-196-

For calibration runs, E_T and E_S are measured with a K-3 potentiometer. R_s is the .50729 Ω standard resistance. The uncertainties associated with those are $W_{E_T}/E_T = .015\%$, $W_{E_S}/E_T = .015\%$ and $W_{R_S}/R_s = .025\%$. Combining all these we obtain the uncertainty in computing R_c to be

$$\frac{W_{R_c}}{R} = \left(2.25 + 2.25 + 6.25\right)^{1/2} \times 10^{-4} = .033\% \qquad (62)$$

For regular runs, E_T and E_S are obtained from Sanborn recordings. The uncertainties due to non-linearity of $\pm.25$ division in the recorder amplifier are $W_{E_T} = 12.5 \times 10^{-4}$ volt and $W_{E_S} = 6.25 \times 10^{-6}$ volt at corresponding sensitivities of .005 volts/div. and 50 mv/div., respectively. The uncertainty associated with the .01 Ω standard resistance is $\pm.04\%$. For a typical case $E_T = 10.8275$ volt and $E_S = 20.815$ mv related to percent uncertainties were, $W_{E_S}/E_S = .03\%$ and $W_{E_T}/E_T = .0116\%$. Substituting these values in Eq. (62) gives

$$\frac{W_{R_T}}{R_T} = \left[(1.16)^2 + 4^2 + 3^2\right]^{1/2} \times 10^{-4} = .051\% \qquad (63)$$

2, Calibration Temperature T_c

To obtain calibration temperature the E.M.F. generated by a Cu-constantan thermocouple was measured by the K-3 potentiometer. The uncertainty associated with the K-3 potentiometer is $\mp 0.15\% + 0.5 \mu v$

$$For \quad E_c = 1970 \mu v \qquad W_{E_c} = 1.728 \mu v \qquad (64)$$

and using Leeds and Northrup standards, the percent uncertainty in calibration temperature, T_c, was found to be $W_{T_c}/T_c = .008\%$ for Freon 113. Following similar procedures and using NSD standards, the uncertainty in T_c for LN$_2$ was found to be $\pm.036\%$. of 139°R which is less than $\pm.05°R$.

3) Calibration Curve Slope dR/dT

In determination of calibration curves for the test surfaces at F113 saturation temperature levels, a Mueller Bridge and platinum resistance thermometer were used. The uncertainties in the Mueller Bridge readings were $\pm.02\%$. The uncertainties in the platinum resistance thermometer arises from two sources: i) the error in the variation of R_o which is $\pm.02°C$, ii) uncertainty coming from the assumption of linear variation between tabulated values which is $\pm.001°C$. The first error was always included in calculations. Therefore, during the calibration of a test surface, surface resistances were measured with an uncertainty of $W_{RW}/RW=\pm.0002$ and liquid temperatures were determined with an uncertainty of $\pm.01°C$. Thus the two ends of the calibration curve have the following values

$$T_1 = 117.5 \mp .0018°F \qquad T_2 = 65.25 \mp .0018°F$$
$$R_1 = 5.084 \mp .001 \qquad R_2 = 4.949 \mp .00099 \qquad (65)$$

For the worst case the uncertainty in the slope dT/dR is $\pm1.46\%$.

For calibration of the test surfaces in LN_2, the set up shown in Fig. (1) of Ref. [41] is used, along with copper-constantan thermocouples. Test surface resistance is obtained with an uncertainty of $\pm.033\%$ and liquid temperature is determined with an uncertainty of $\pm.036\%$.

Following the same procedure used for F113, calibration curves of the test surfaces in LN_2 are determined with an uncertainty of $\pm2.6\%$ in their slopes.

Test surface wall temperatures are calculated from Eq. (11)

$$T_T = T_c + m \left(R_T - R_c \right) \qquad (11)$$

The uncertainty associated with T_T is obtained from the following equation

$$W_{T_T} = \left\{ \left(W_{T_C} \right)^2 + \left(W_m \right)^2 + \left[W_{(R_w - R_c)} \right]^2 \right\}^{1/2} \qquad (66)$$

combining all these, gives the uncertainty in computing wall temperature of the test surface in F113 to be $\pm 1.33°F$. Following the same procedures and using corresponding uncertainties, the test surface temperatures in boiling with LN_2 are determined $\pm 1.68°R$ uncertainty.

B. AREA MEASUREMENTS

Uncertainties associated with the determination of the portion of the test surface area photographed arises from 1) uncertainty in measurements of the actual distance between dimension lines, 2) uncertainty in measuring actual test surface area, 3) uncertainties in measuring linear distances on the analyzer screen, 4) uncertainty in tracing the area from the analyzer screen, 5) uncertainties in determining enlarged areas by means of a planimeter.

The spacing between the dimensioning wires and the test surface dimensions are measured by a .001" traveling microscope. Therefore, uncertainty associated with .1 spacing and test surface area are $\pm .1\%$ and .14% respectively. Linear dimensions and the areas measured by hairlines on the analyzer screen have an uncertainty of $\pm .5\%$ and $\pm .7\%$ respectively. Tracing enlarged areas from the analyzer screen introduces an uncertainty of $\pm .5\%$. Finally determining traced areas by using a planimeter introduces an uncertainty of $\pm .6\%$. Therefore, the uncertainty in determination of the areas is

$$\frac{W_A}{A} = \mp \left[(14)^2 + (70)^2 + (50)^2 + (60)^2 \right]^{1/2} \times 10^4 = \mp 1.06\% \qquad (67)$$

C. HEAT FLUX

The uncertainties in determination of heat flux arise form a) the uncertainty associated with the determination of total heat flux from the relation

$$\left(Q/A\right)_{total} = \frac{E_T I}{A} = \frac{E_T}{A} \frac{-E_s}{R_s} \tag{68}$$

and b) the uncertainty associated with heat loss from the test section.

a) The uncertainties associated with the determination of the total heat flux is given by

$$\frac{W_{(Q/A)}}{(Q/A)} = \left[\left(\frac{W_{E_T}}{E_T}\right)^2 + \left(\frac{W_{E_s}}{E_s}\right)^2 + \left(\frac{W_{R_s}}{R_s}\right)^2 + \left(\frac{W_A}{A}\right)^2\right]^{1/2} \tag{69}$$

where

$$\frac{W_{E_T}}{E_T} = \mp.042\% \; ; \; \frac{W_{E_s}}{E_s} = \mp.0368\% \; ; \; \frac{W_{R_s}}{R_s} = \mp.04\% \; ; \; \frac{W_A}{A} = \mp 1.06\% \tag{70}$$

Substituting these values in Eq. (69) will give

$$\frac{W_{(Q/A)}}{(Q/A)} = \mp 1\% \tag{71}$$

b) Uncertainties associated with the heat loss from the test section is directly related to the uncertainties associated with the determination of $(T_T - T_\ell)$

$$W_{(T_r - T_\ell)} = \left[\left(W_{T_r}\right)^2 + \left(W_{T_\ell}\right)^2\right]^{1/2} \tag{72}$$

where $W_{T_T} = 1.337$, $W_{T_\ell} = .061$ as found before. Substituting in Eq. (72) gives $W_{(T_T - T)} = 1.338°F$ which in turn gives $\pm 2.1\%$ uncertainty in heat loss.

APPENDIX C

PHOTOGRAPHIC SAMPLES

In this section typical samples of photographic and thermal data are presented along with the results obtained from the analysis of these data.

Figures 95 and 96 illustrate typical photographic and thermal recordings obtained from transient boiling on a vertical surface in F113 at a/g=1 and a/g=0, respectively. These figures demonstrate the inception and spreading of boiling on a vertical surface at standard and zero gravity. The corresponding variation of the test surface temperatures are also plotted in these figures.

Figures 97 and 98 are typical photographic samples of steady state nucleate boiling for a vertical surface in F113 at a/g=1 and a/g=0, respectively, and were obtained consecutively by starting the camera well before the test package was released. The pictures were all taken at a framing rate of 2200 pictures per second. Figure 97 shows the sequence at a/g=1 beginning 0.13 seconds prior to release, and covers the time period of 0.02 seconds. All photographs obtained in this interval are reproduced in Fig. 97. Figure 98 shows the sequence at a/g=0, beginning 0.15 seconds after release of the test package. The samples reproduced in the upper row are for each tenth frame obtained in the time interval of 0.15 seconds to 0.20 seconds after release of the test package, while the samples in the lower row are for each tenth frame obtained in the time interval of 0.25 to 0.30 seconds after release.

The high speed pictures of boiling clearly show that bubbles continue to grow and depart from the active site during the early part of

the 0-G. However, during the later part of 0-G they remain stationary on the surface and grow without departing. Figures 99-101 illustrate this phenomenon. In Figs. 99 and 100, data for the same site is given, but with different time scales. Figure 99 shows the growth of a bubble at about .02 seconds after the init.ation of 0-G. The diameter of the bubble was about 0.001 inches when first observed. It then grew to a diameter of about .03 inches in .04 sec., then departed from the surface. After about .15 seconds elapsed in 0-G, another bubble appeared at the same site but did not depart from the surface, but rather continued to grow until it coalesced with other bubbles. Thi   oble appeared at the site .146 seconds after the release of the test   , with a diameter of .0013 inches and grew to a diameter of .084 inches until it coalesced with other bubbles growing at neighboring sites at about .34 sec. after test package release. Figure 100 shows the sequential growth of these two bubbles on a common time scale. The time scale of Fig. 100 is 50 times larger than that of Fig. 99.

The departure of the bubble in the early stages of G-G is believed to be caused by the inertial effects of the liquid motion set up during 1-G boiling. After a certain time in 0-G the liquid motion dies out due to viscous effects and the bubbles remain on the surface.

Figure 101 shows the bubble growth at 0-G for various heat fluxes after the liquid motion has died out.

Fig. 95. Typical transient boiling heat transfer and test surface temperature, F-113, vertical, $a/g=1$

-204-
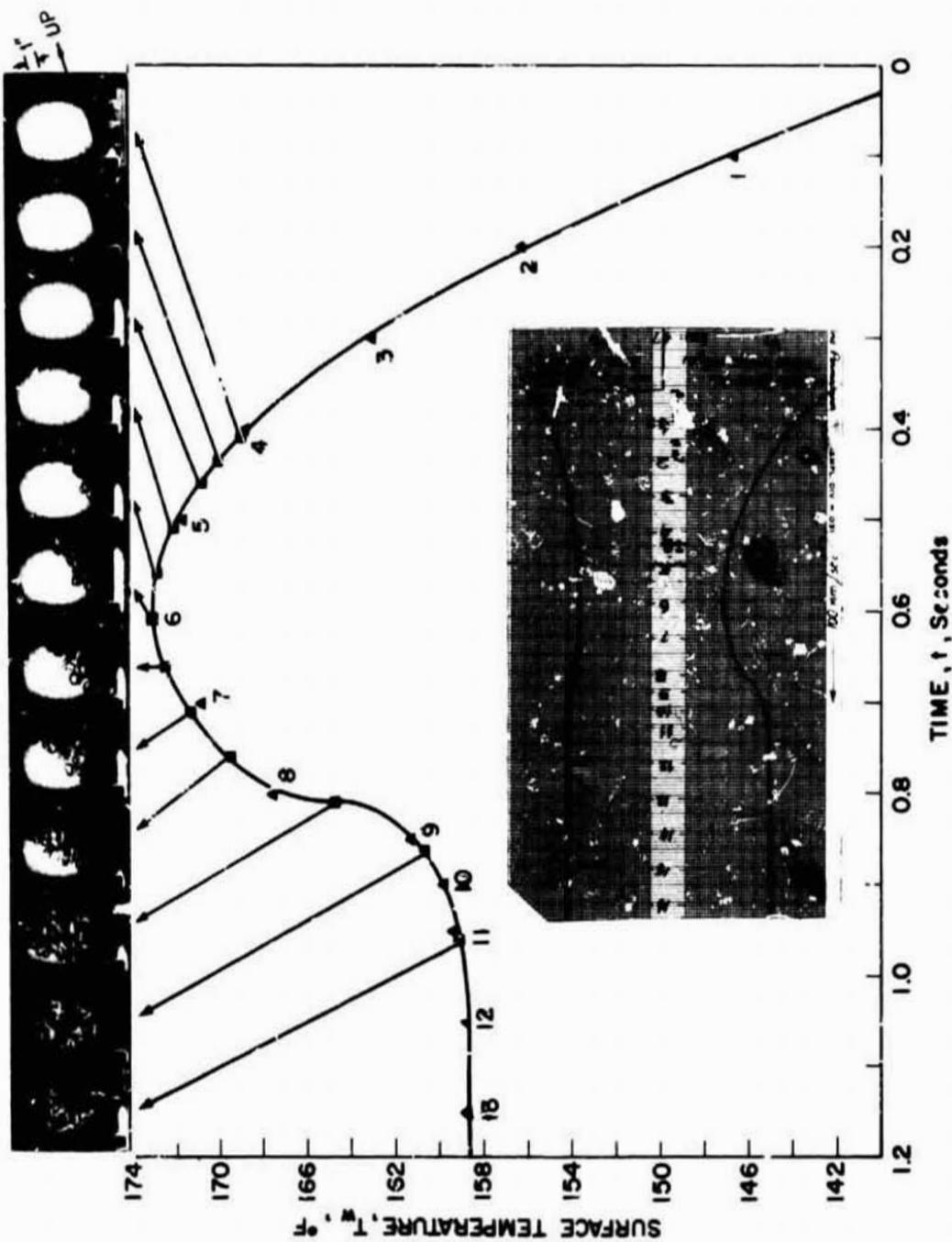
Fig. 96. Typical transient boiling heat transfer and test
surface temperature, Fl13, vertical, a/g=0
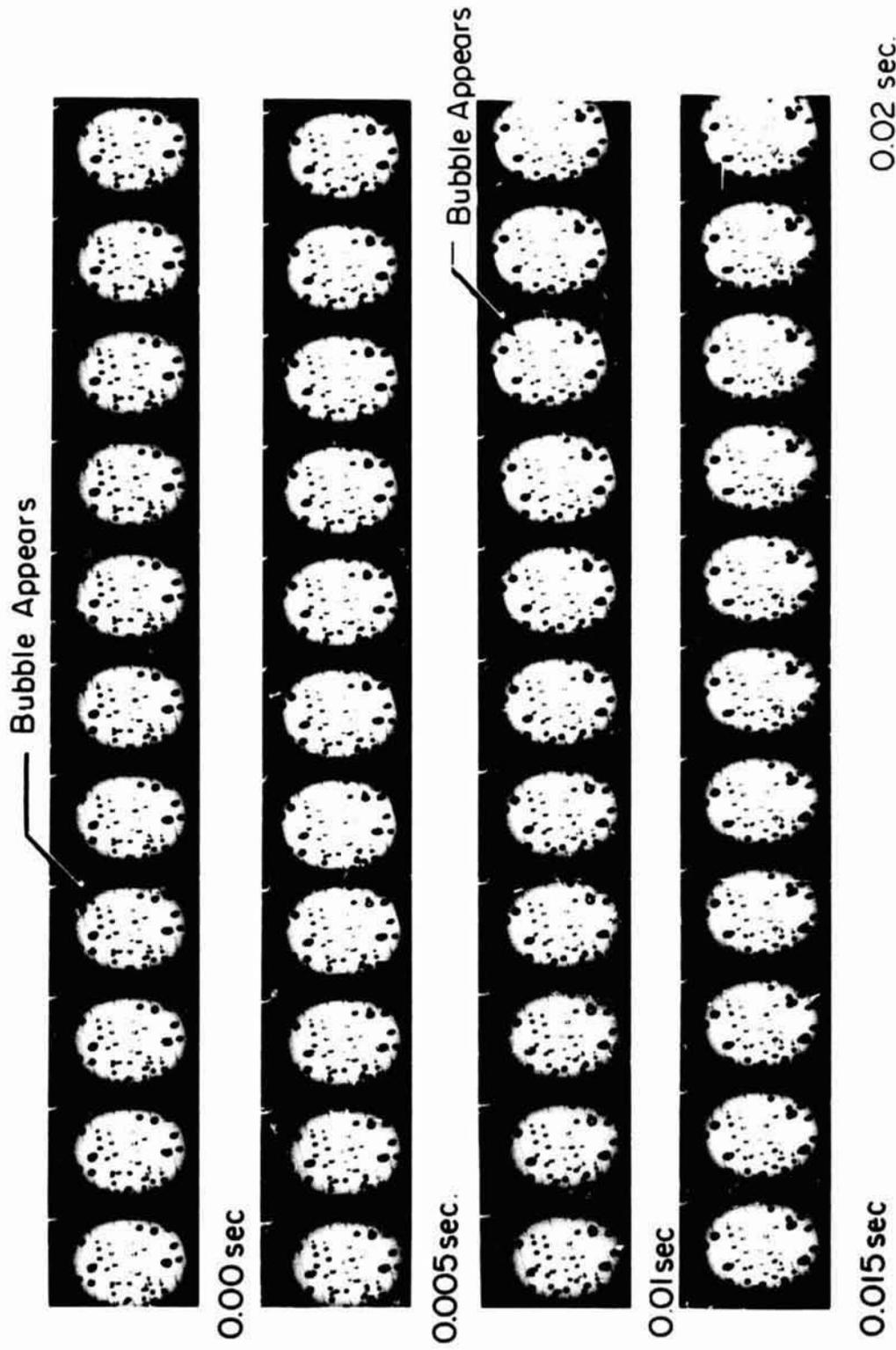
Fig. 97. Typical steady state nucleate boiling, F113, vertical, a/g=1, run 44, Q/A=4200 Btu/hr
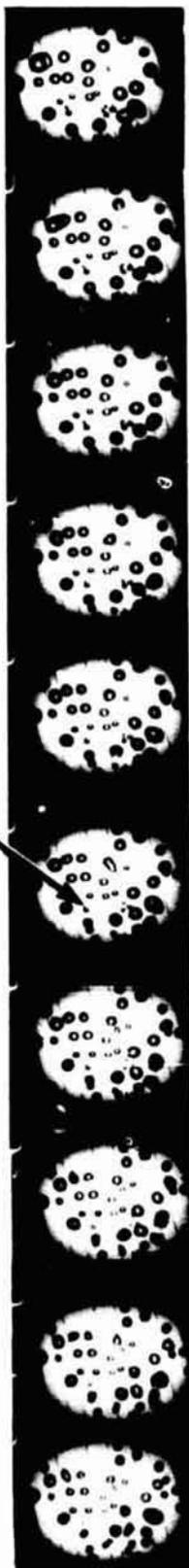
Fig. 98. Typical steady state nucleate boiling, F11^z, vertical, a/g=0, run 44, Q/A=4200
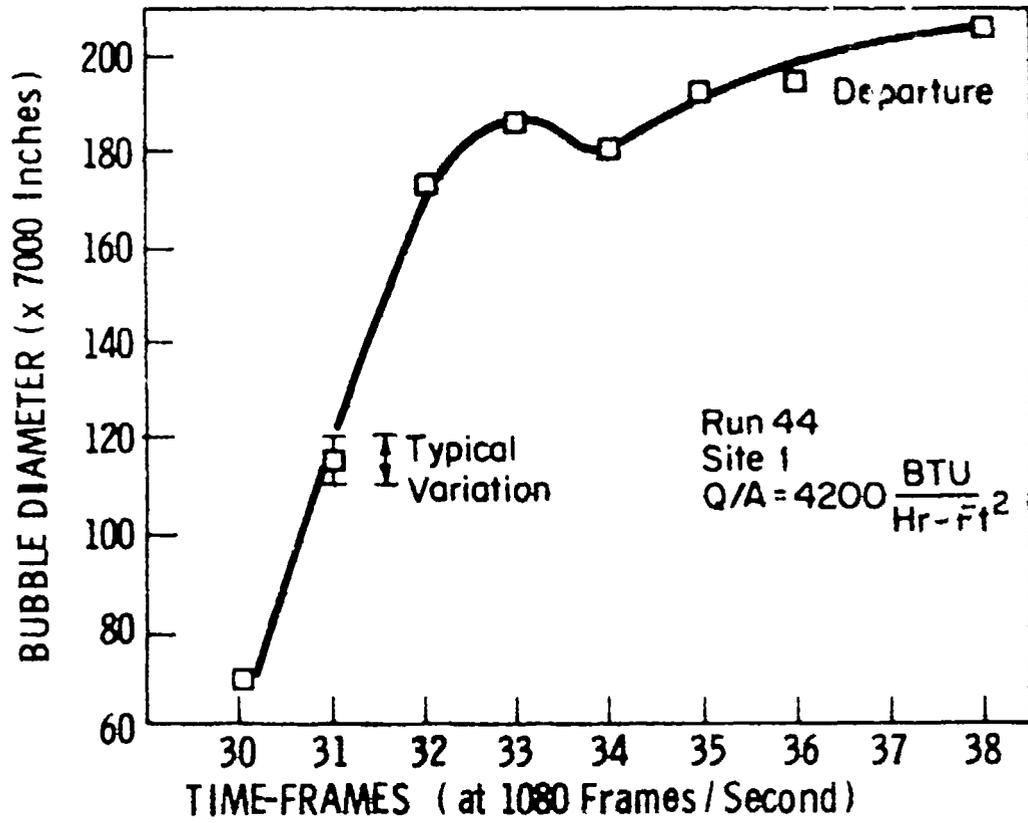
Fig. 99. Typical bubble growth, F113, vertical,
a/q=1, run 44, site 1
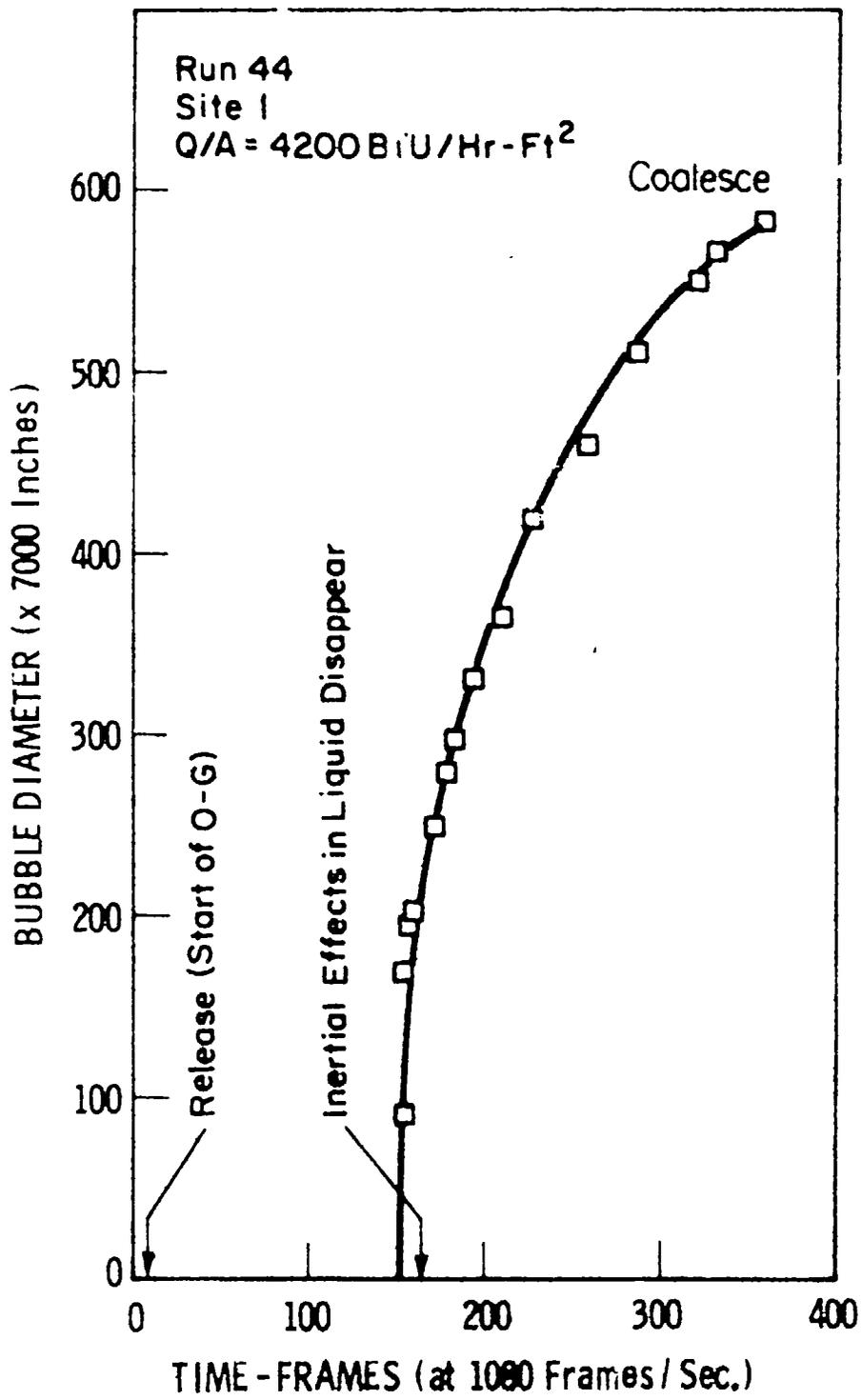
Fig. 100. Typical bubble growth, F113, vertical,
a/g ≈ 0, run 44, site 1
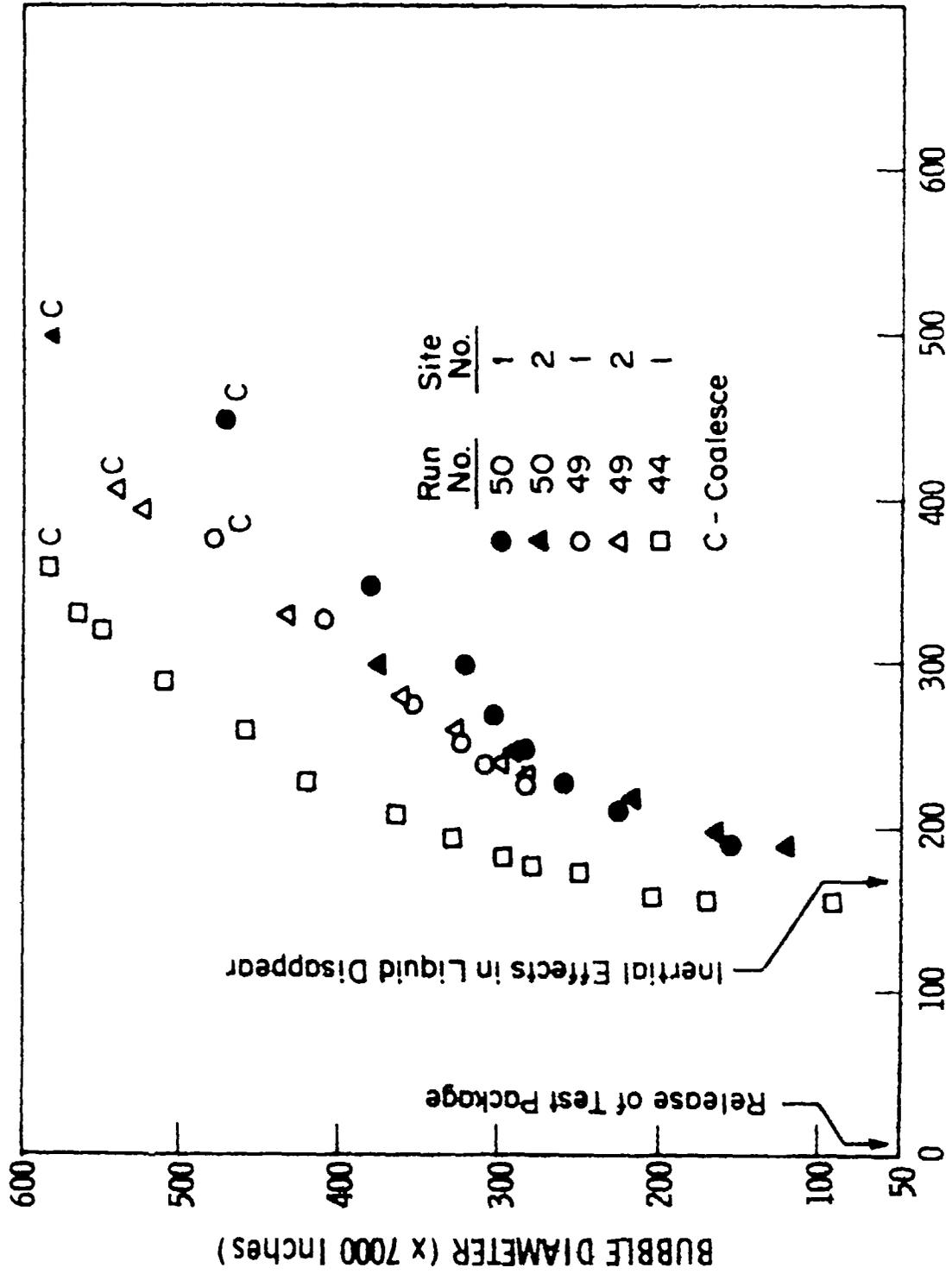
Fig. 101. Typical bubble growth for various heat fluxes, $a/q \simeq 0$

APPENDIX D

CALIBRATION RESULTS OF THIN GOLD FILMS

In this section calibration curves of various pyrex test surfaces coated with thin gold films are presented to show the type of shifting occuring in the resistivity of gold films with time and the effect of tempering on shifting.

Figures 102-105 are the calibration curves of the test surfaces PCG-15, 16, 19 and 20. Figures 106 and 107 are the calibration curves of PCG-21. Figures 108-110 are the calibration curves of PCG 22-24. Figures 111 and 112 are the calibration curves of PCG 29. Figures 102, 104-108 and 112 are the results of calibrations at LN_2 temperature level. Figures 109-111 are obtained at F113 temperature level. Figure 103 covers the complete temperature range.

Test numbers on the calibration curves indicate the sequence of each data point determined during calibration. Each data point represents mean of four measurements with currents between 5-30 ma . which corresponds to test surface heat fluxes, depending on the resistivity of the test surface of between .01 to 1.0 Btu/hr-ft^2. Calibration dates are also given on the figures.

The results presented in Figs. 102-112 clearly show that the slope dR/dT always remains constant indicating that once the complete calibration of a test surface had been made it was deemed sufficient to make only a single point calibration prior to and following each test run.

All calibration curves presented in Figs. 102-112 except Fig. 105 are obtained after the test surfaces are baked for about 15-18 minutes

-210-

at approximately 275°C. Figure 106 is obtained before tempering. Comparison of these two shows the effect of tempering on thin gold films. In this case the resistivity of the test surface PCG-21 at 138°R was dropped sharply from 1.055 to .88 Ω/SQ.

Test surfaces PCG 15, 16, 19 and 20 were kept in nitrogen with 3% H_2 at one atmosphere during the baking, and surfaces 21-24 and 29 were tempered in atmospheric air. No effect of oxidation during tempering is noticed.
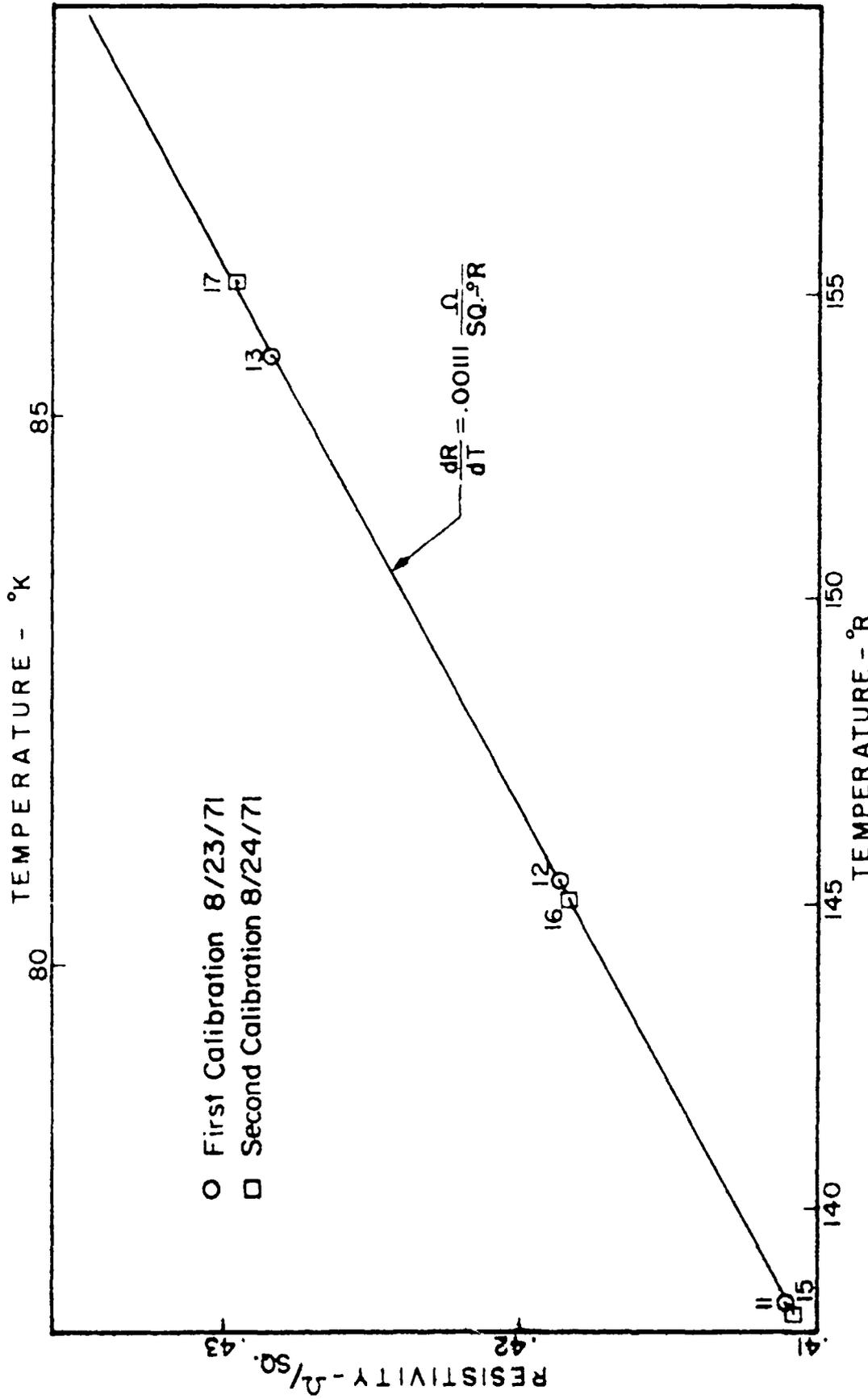
Fig. 102. Calibration, PCG 15, LN₂
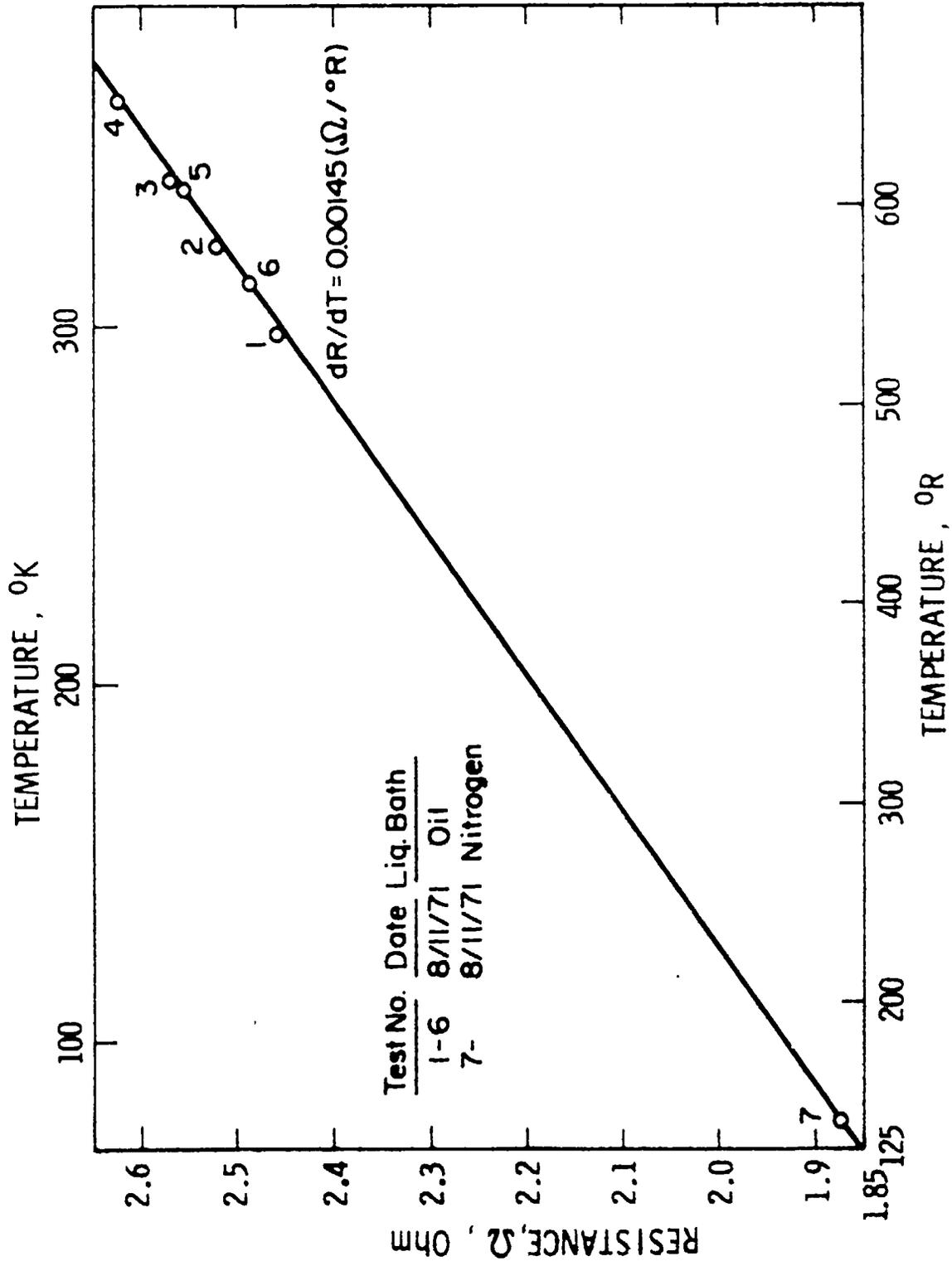
Fig. 103. Calibration, PCG 16, F113 and LN₂

Test No.	Date	Liq. Bath
1-6	8/11/71	Oil
7-	8/11/71	Nitrogen

dR/dT = 0.00145 (Ω/°R)

TEMPERATURE, °K

TEMPERATURE, °R
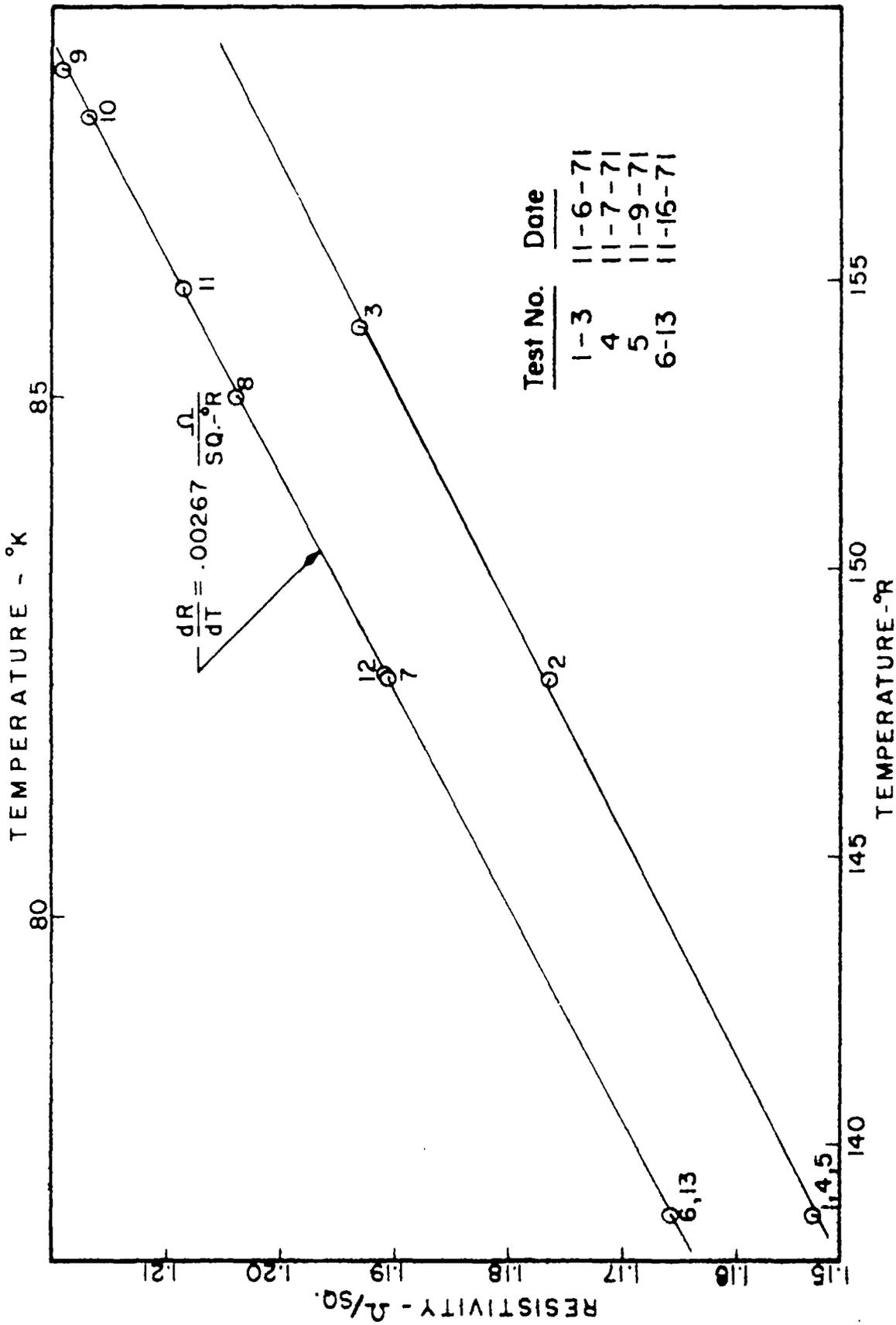
RESISTANCE, Ω, ohm

Fig. 104. Calibration, PCG 19, LN_2

$$\frac{dR}{dT} = .00267 \frac{\Omega}{SQ.-{}^\circ R}$$

Test No.	Date
1-3	11-6-71
4	11-7-71
5	11-9-71
6-13	11-16-71
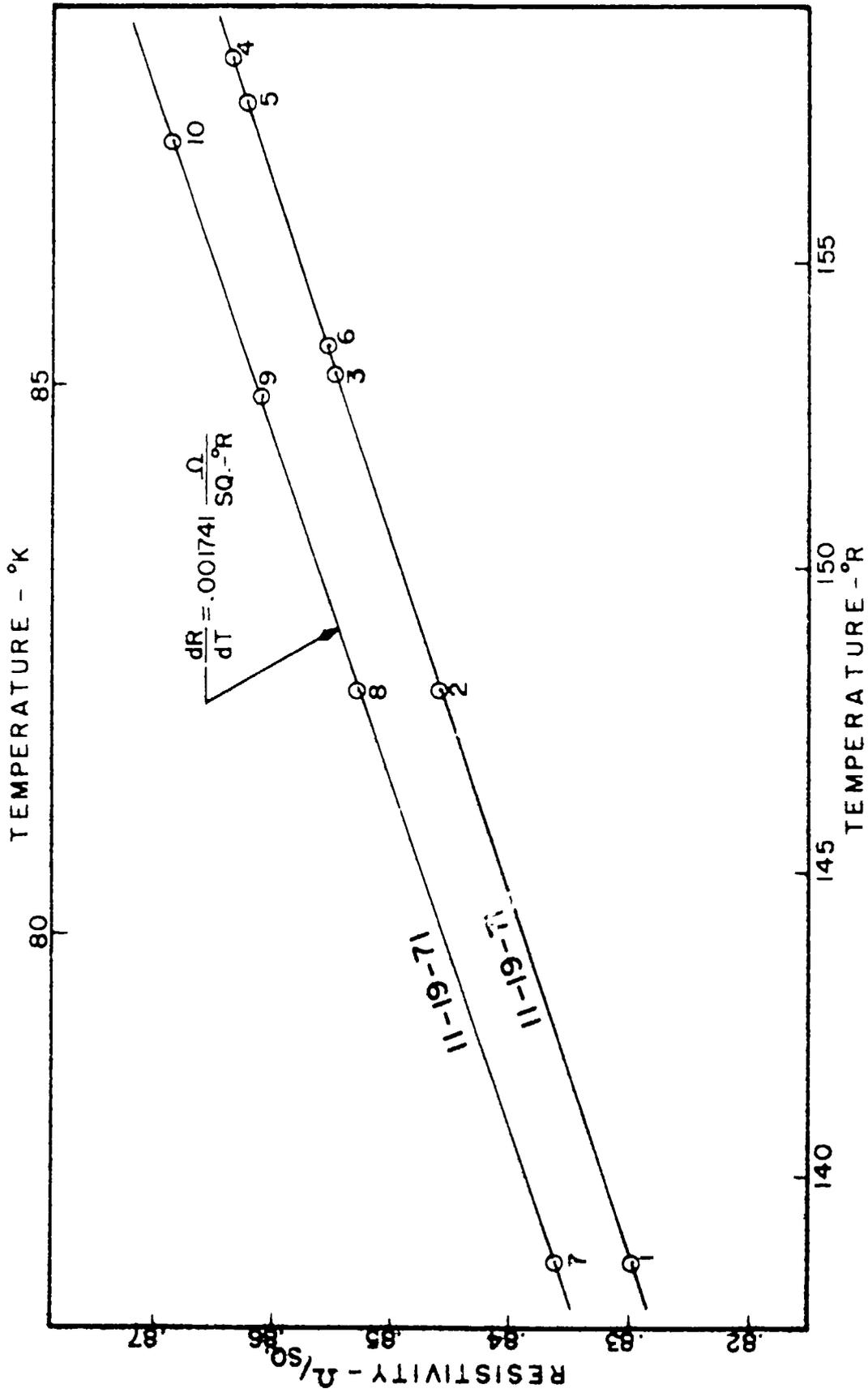
Fig. 105. Calibration, PCG 20, LN₂
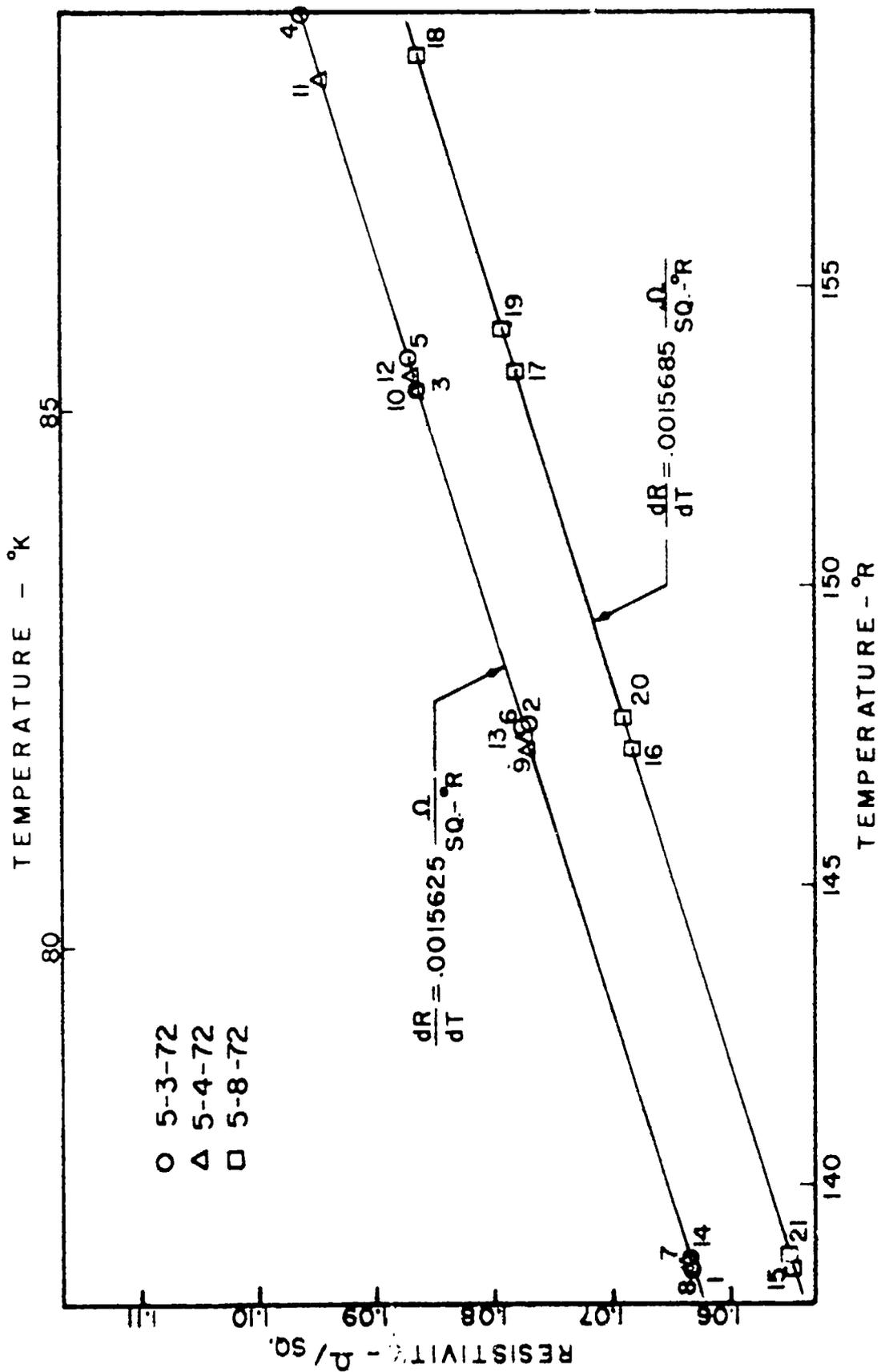
Fig. 106. Calibration, PCG 21, LN_2, prior to tempering
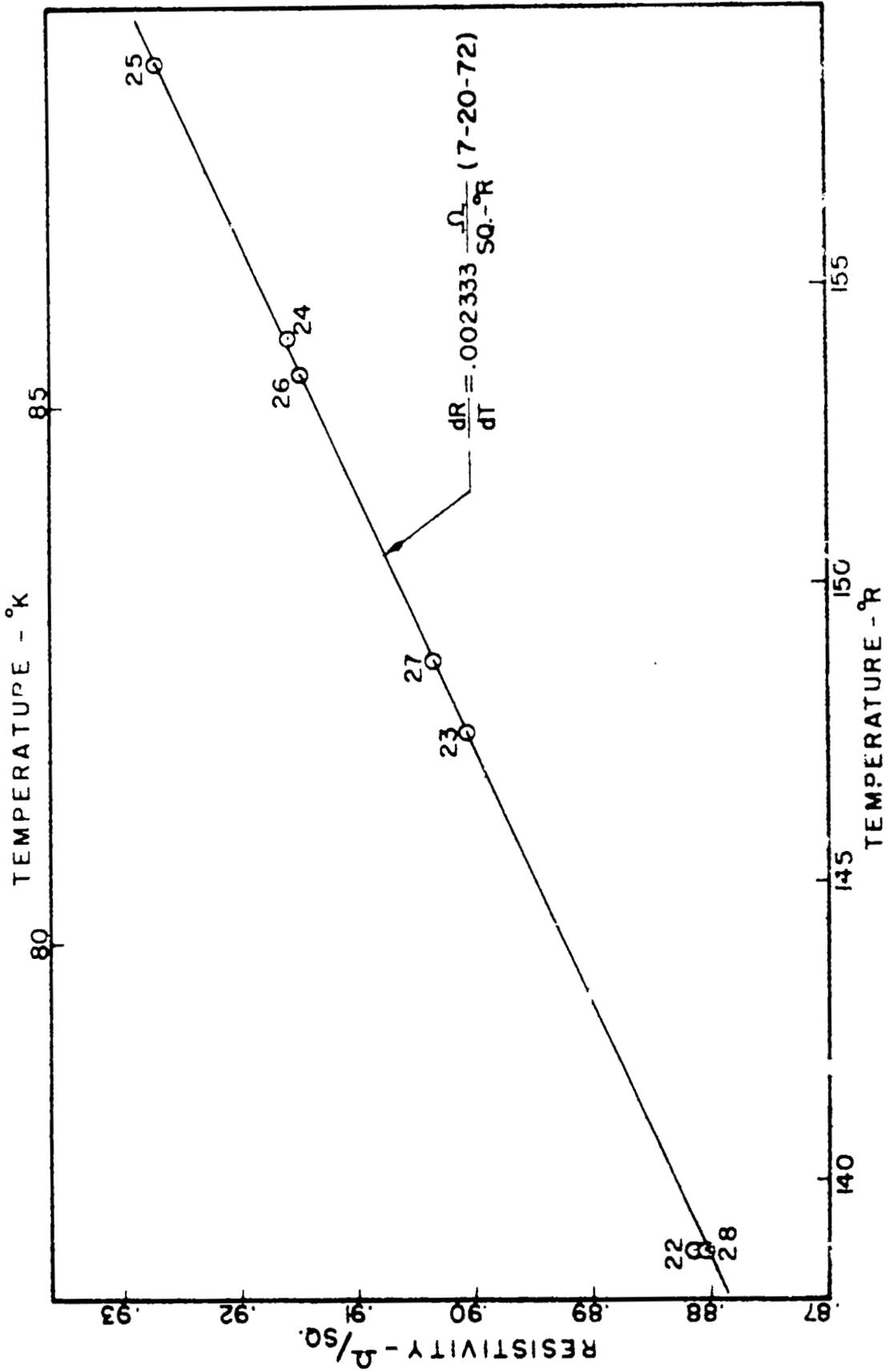
Fig. 107. Calibration, PCG 21, LN$_2$, after tempering
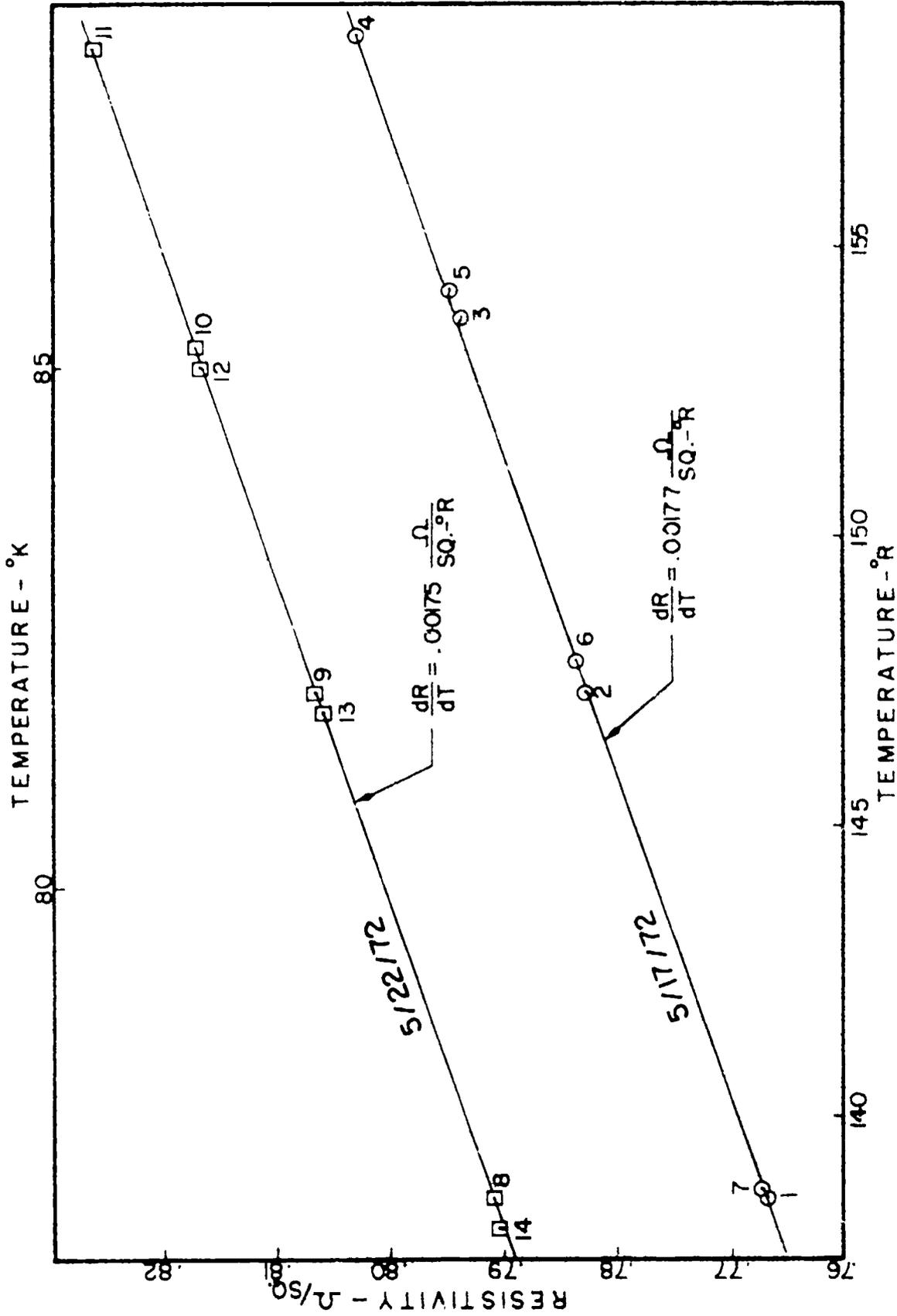
Fig. 108. Calibration, PCG 22, LN_2
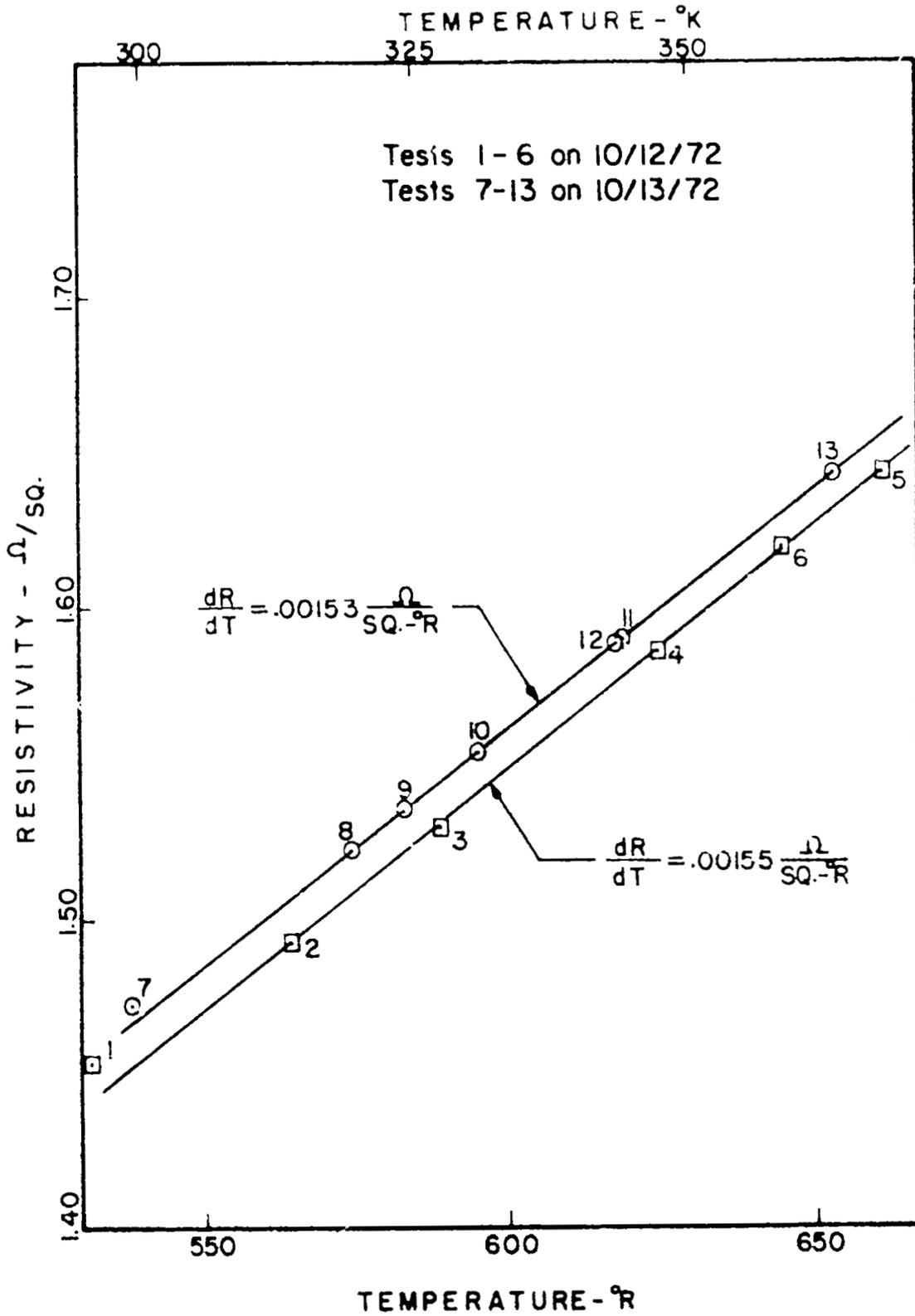
Fig. 109. Calibration, PCG 23, F113
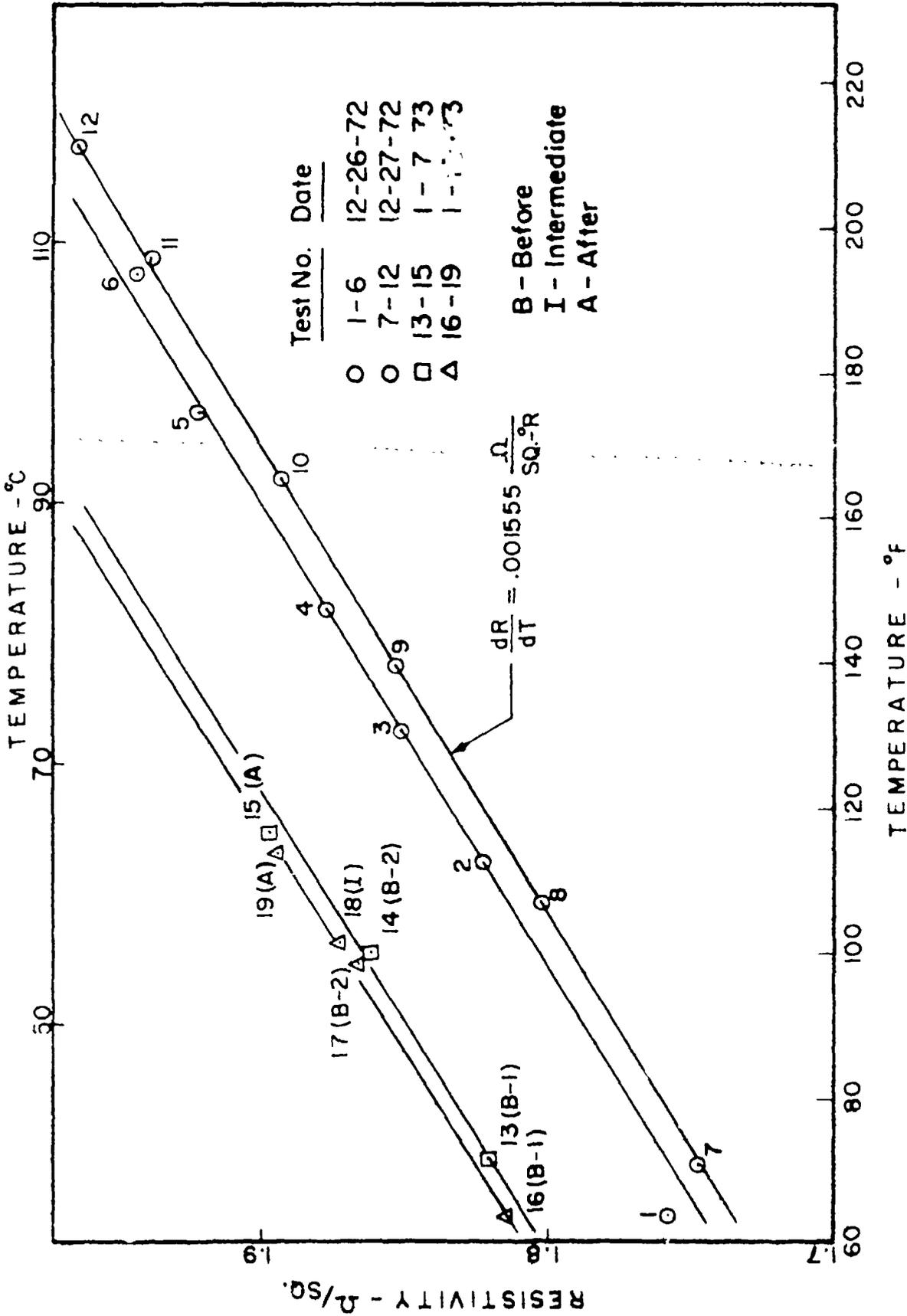
Fig. 110. Calibration, PCG 24, F113
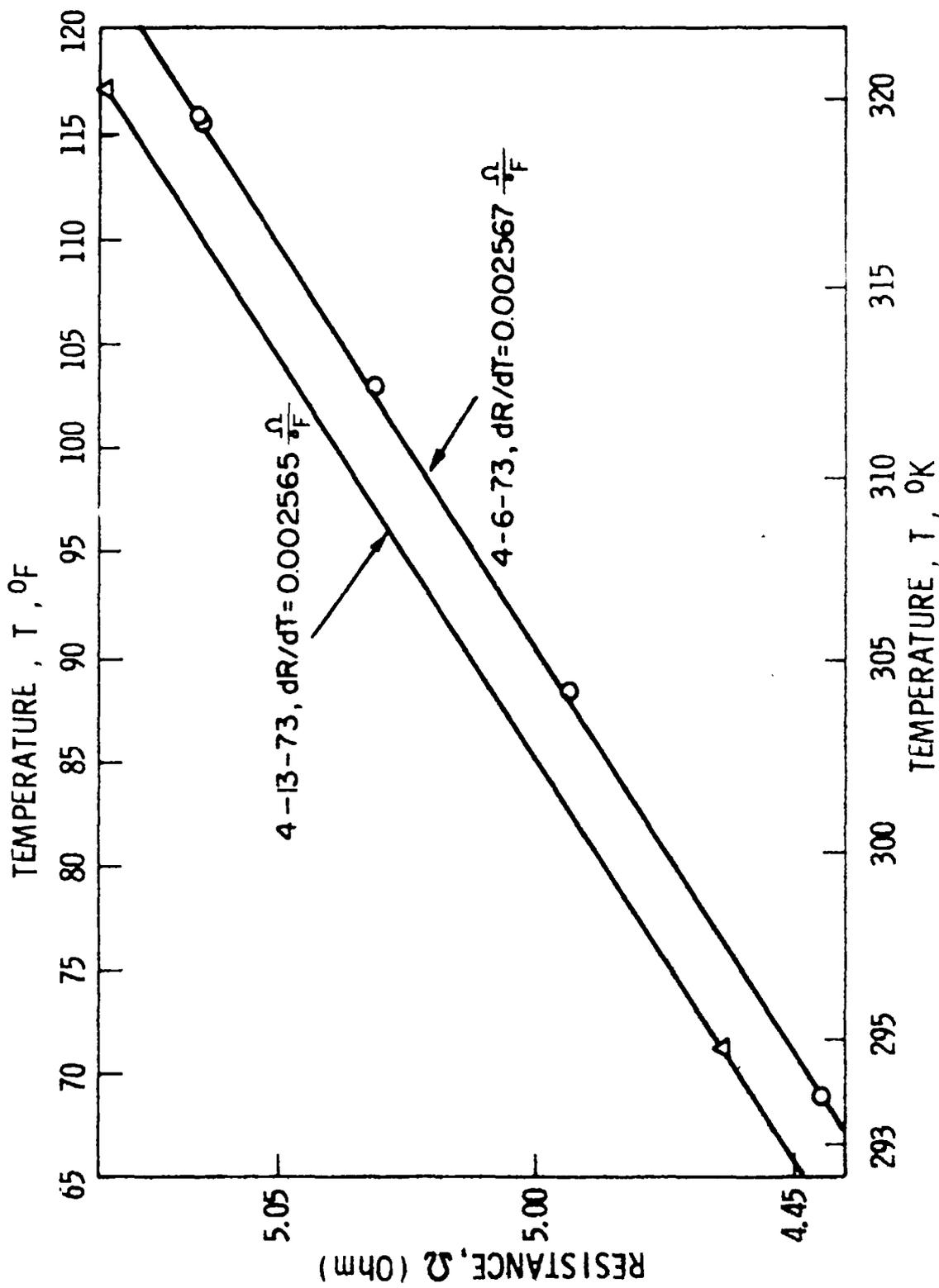
Fig. 111. Calibration, PCG 29, F113
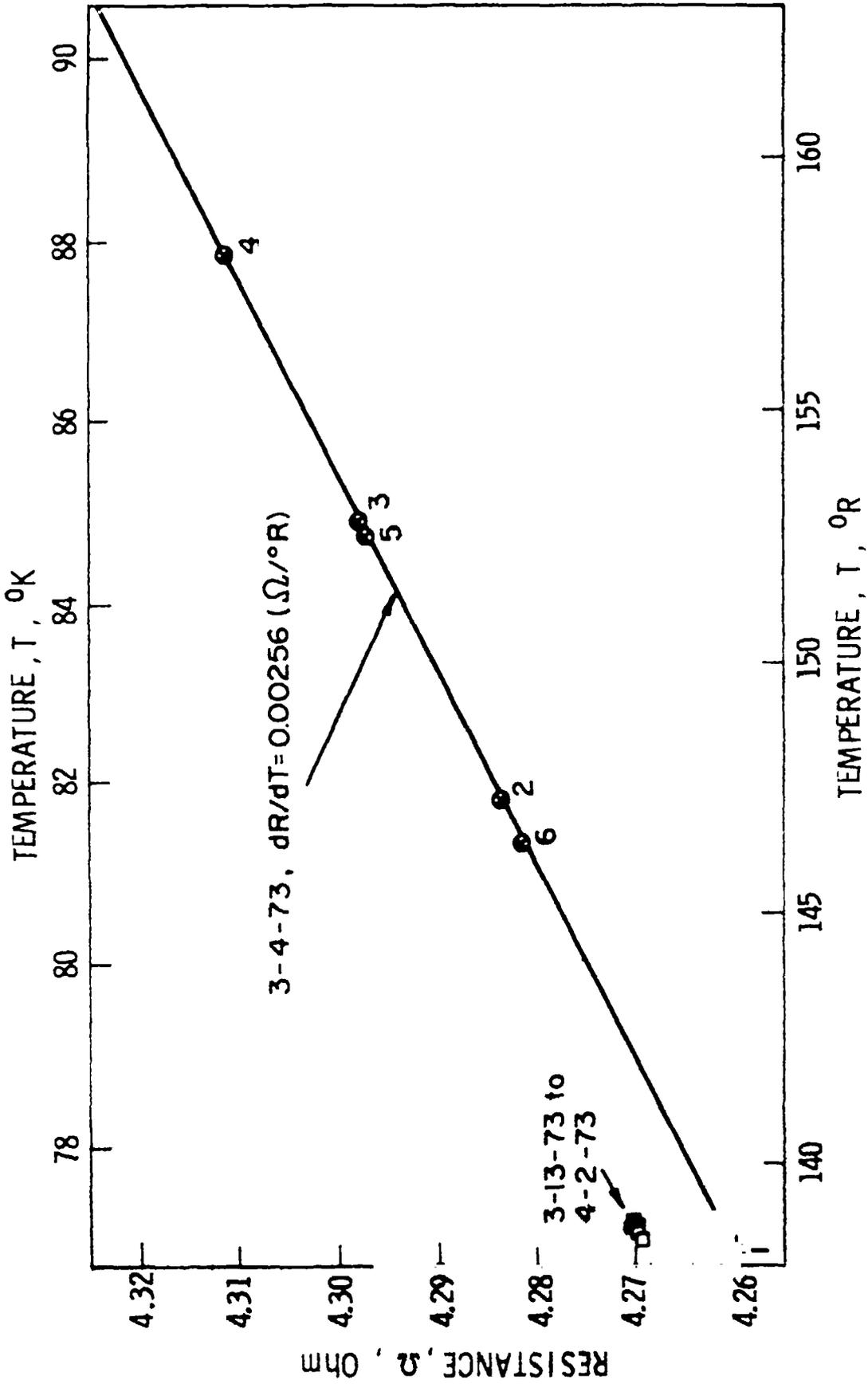
Fig. 112. Calibration, PCG 29, LN$_2$

The graph shows RESISTANCE, Ω, ohm (vertical axis, 4.26 to 4.32) versus TEMPERATURE, T, $^\circ$K (top axis, 78 to 90) and TEMPERATURE, T, $^\circ$R (bottom axis, 140 to 160).

3-4-73, dR/dT=0.00256 (Ω/$^\circ$R)

3-13-73 to
4-2-73

APPENDIX E

TEST SURFACE TEMPERATURE

The test surface temperature as measured is a mean value, and is determined from the total resistance of the surface. The surface resistance at any time is equal to the sum of the resistance of boiling part (R_B) and the resistance of the nonboiling part (R_{NB}) of the surface.
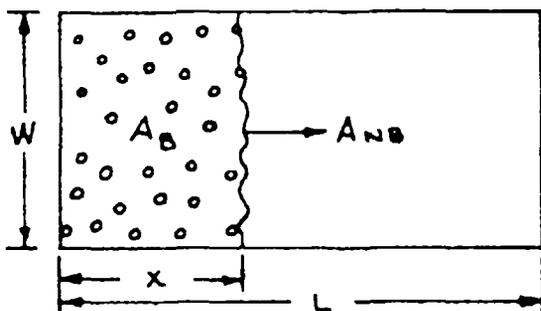
Assuming that boiling spreads linearly across the surface as shown above, the total surface resistance can be approximated as

$$R_T = R_B + R_{NB} \qquad (73)$$

For a given width and surface thickness, the resistance can be written as a function of the length of the surface as

$$R_T \cong \rho_B \, X(t) + \rho_{NB} \left[L - X(t) \right] \qquad (74)$$

Since the average surface temperature is a linear function of total resistance

$$T = \text{Constant } R_c \tag{75}$$

Equation (27) can also be written as

$$R_T = \text{Constant } T \tag{76}$$

where the constants in Eqs. (75) and (76) are different. Equation (76) may be written as follows

$$R_T = \text{Constant} \left\{ T_B X(t) + T_{NB}(t) \quad L - X(t) \right\} \tag{77}$$

Since T_B is not a function of time, differentiating and equating the Eq. (77) to zero will give the condition for maximum surface temperature.

$$\left[T_{NB}(t) - T_B \right] \frac{dX(t)}{dt} = \left[L - X(t) \right] \frac{dT_{NB}(t)}{dt} \tag{78}$$

Multiplying both sides of Eq. (78) by dt and separating the variables

$$\frac{d T_{NB}(t)}{T_{NB}(t) - T_B} = \frac{dX(t)}{L - X(t)} \tag{79}$$

Integrating Eq. (79) will give

$$\left[T_{NB}(t) - T_B \right] \left[L - X(t) \right] = \text{Constant} \tag{80}$$

where $X(t) \neq L$ and $T_{NB}(t) \neq T_B$

Multiplying both sides of Eq. (82) by the width of the test surface will result following relation

$$\left[T_{NB}(t) - T_B \right] \left[A_T - A_B \right] = \text{Constant} \tag{81}$$

Equation (81) is an approximate relation and the constant in the equation need not be evaluated. This relation can only be used to support

qualitatively, the experimental results obtained in present investigation which showed that surface temperature continued to increase even after inception of first site, until a certain percent of the test surface area is covered by the active nucleating sites. Equation (81) is a hyperbolic function, which indicates that as $A_T - A_B$ decreases $T_{NB} - T_B$ increases.

APPENDIX F

INDEX OF TESTS CONDUCTED

Run No.	Liquid	Orient.	Heat Flux	Transient	Steady State	Photographic	Thermal	a/g=1	a/g=0	PCG No.
39	F113	Vert		X		X	X	X		23
40	"	"			Y	Y	Y	Y	Y	"
1	"	"		X		X	X		X	"
2	"	"			X	X	X	X	X	"
3	"	"			X	X	X	X	X	"
4	"	"			X	X	X	X	X	"
5	"	"		X		X	X		X	"
6	"	"		X		X	X		X	"
7	"	"		X		X	X	X		"
8	"	"		X		X	X	X		"
9	"	"			X	X	X	X	X	"
50	"	"			X	X	X	X	X	"
1	"	"		X		X	X		X	"
2	"	"		X		X	X	X		"
3	"	"			X		X	X		"
4	"	H-Up			X	X	X	X	X	"
5	"	"		X			X		X	"
6	"	"			X		X	X	X	"
7	"	"		X		X	X		X	"
8	"	"			X	X	X	X		"
9	"	"			X	X	X	X		"
60	"	"			X	X	X	X		"
70	"	"			X	X	X	X	X	24
1	"	"			X	Y	X	X	X	"
2										"
3	"	"			X	X	X	X	X	"

Run No.	Liquid	Orient.	Heat Flux	Transient	Steady State	Photographic	Thermal	a/g=1	a/g=0	PCG No.
74	F113	H-Up			X	X	X	X	X	24
5	"	"			X		X	X		"
6	"	"		X		X	X		X	"
7	"	"		X		X	X	X		"
8	"	"		X			X	X		"
9	"	"		X		X	X		X	"
80	"	"		X		X	X	X		"
1	"	"		X		X	X		X	"
2										
3										
4										
5	"	"			X	X	X	X	X	"
6	"	"			X	X	X	X		"
7	"	"			X			X		"
8	"	"			X			X		"
9	"	"		X		X	X	X		"
90	"	"		X		X	X		X	"
1	"	"		X		X	X	X		"
2	"	"		X		X	X		X	"
3	"	"		X		X	X	X		"
4	"	"		X		X	X		X	"
5	"	H-Down			X		X	X	X	"
6	"	"			X		X	X	X	"
7	"	"			X		X	X	X	"
8	"	"			X		X	X	X	"
9	"	"		X			X	X		"
100	"	"		X			X		X	"
1	"	"		X		X	X	X		"
2	"	"		X		X	X		X	"
3	"	"		X		X	X	X		"

Run No.	Liquid	Orient.	Heat Flux	Transient	Steady State	Photographic	Thermal	a/g=1	a/g=0	PCG No.
104	F113	H-Down		X		X	X		X	28
5	LN$_2$	Vert		X		X	X	X		"
6	"	"		X		X	X	X		"
7	"	"		X		X	X	X		"
8	"	"		X		X	X	X		29
9A	"	"		X			X	X		"
9B	"	"		X		X	X	X		"
10A										"
10B	"	"		X		X	X	X		"
11	"	"		X		X	X	X		"
12	"	"		X		X	X	X		"
13	"	"		X			X	X		"
14	"	"			X	X	X	X	X	"
15	"	"		X		X	X	X		"
16	"	"			X	X	X	X		"
17	"	"		X		X	X		X	"
18	"	"			X	X	X	X	X	"
19A	"	"		X		X	X	X		"
19B	"	"		X		X	X		X	"
19C	"	"		X			X		X	"
19D	"	"		X			X		X	"
20	"	"			X	X	X	X	X	"
21	"	"			X	X	X	X	X	"
22	"	"		X		X	X	X		"
23	"	"		X		X	X		X	"
24	"	"		X		X	X		X	"
25										
26	"	H-Up		X		X	X	X		"
27										"

Run No.	Liquid	Orient.	Heat Flux	Transient	Steady State	Photographic	Thermal	a/g=1	a/g=0	PCG No.
128A	LN$_2$	H-Up		X			X	X		29
28B	"	"		X		X	X	X		"
29	"	"		X		X	X	X		"
30	"	"		X		X	X	X		"
31A	"	"		X			X	X		"
31B	"	"		X		X	X	X		"
32	"	"		X		X	X		X	"
33	"	"		X		X	X		X	"
34A	"	"		X			X	X		"
34B	"	"		X			X	X		"
35	"	"		X			X		X	"
36A		H-Down		X		X	X	X		"
36B	"	"		X			X	X		"
37A	"	"		X		X	X	X		"
38	"	"		X			X	X		"
39	"	"		X		X	X	X		"
40	"	"		X					X	"
41	"	"		X					X	"
42	"	"			X		X	X	X	"
43	"	"			X		X	X	X	"
44	"	"		X		X	X		X	"
45A	"	"		X		X	X	X		"
45B	"	"		X		X	X	X		"
46										
47	F113	"		X		X	X	X		"
48	"	"		X		X	X		X	"
49	"	"			X	X	X	X	X	"
50	"	"		X			X	X		"
51	"	"		X			X		X	"
52	"	"			X	X	X	X	X	"

Run No.	Liquid	Orient.	Heat Flux	Transient	Steady State	Photographic	Thermal	a/g=1	a/g=0	PCG No.
153	F113	H-Down			X		X	X	X	29
54	"	Vert			X		X	X	X	"
55	"	"			X		X	X	X	"
56	"	"		X				X		"
57	"	"		X				X		"
58	"	"		X					X	"
59	"	"		X				X		"
60	"	"		X					X	"

REFERENCES

1. Cole, R., "Investigation of Transient Pool Boiling Due to Sudden Large Power Surge," NACA TN 3885, 1956.

2. Rosenthal, M.W., R.L. Miller, "An Experimental Study of Transient Boiling," ORNL-2294 Oak Ridge Nat. Lab., 1957.

3. Copper, M.G., A.J.P. Lloyd, "Transient and Local Heat Flux in Nucleate Boiling," Int'l. Heat Transfer Conference, 3rd Chicago Proceedings, Vol. 3, 1966.

4. Garg, S.C., T.D. Patten, "Temperature and Pressure Transients Near the Heating Surface During Nucleate Pool Boiling of Saturated Water," Int'l. heat Transfer Conference 3rd Chicago-Proceedings, Vol. 3, 1966.

5. Hall, W.B., W.C. Harrison, "Transient Boiling of Water at Atmospheric Pressure," Int'l. Heat Transfer Conference, 3rd Chicago-Proceedings, Vol. 3, 1965.

6. Johnson, H.A., V.E. Schrock, F.B. Selph, J.H. Lienhard, Z.R. Rosztoczy, "Transient Pool Boiling of Water at Atmospheric Pressure," Int'l. Developments in Heat Transfer, Heat Transfer Conf., Boulder, Colorado, 1961, ASME, 1963.

7. McCurdy, H., "On the Delay Time for Bubble Formation in Water Moderated Reactors," Nuclear Structural Engineering, Vol. 1, no. 3, 1965.

8. Lurie, H., H.A. Johnson, "Transient Pool Boiling of Water on a Vertical Surface with a Step in Heat Generation," ASME Paper 61-WA-164, 1961.

9. Klosterhaus, E., "A Study of Nucleate Boiling in Liquid Nitrogen and Liquid Hydrogen at Normal and Zero Gravity," ME 600 project, The University of Michigan, Department of Mechanical Engineering, 1970.

10. Carpenter, L., "A Study of Nucleate Boiling with Thin Films in Liquid Nitrogen at Normal Gravity," ME 490 project, The University of Michigan, Department of Mechanical Engineering, 1971.

11. Graham, R.W, "Experimental Observations of Transient Boiling of Subcooled Water and Alcohol on a Horizontal Surface, NASA TN D-2507, 1965.

12. Kawamura, H., F. Tachibana, M. Akiyamo, "Heat Transfer and DNB Heat Flux in Transient Boiling," 4th Int'l. Heat Transfer Conference, Versailles, 1970.

13. Sakurai, A., K. Mizukami, M. Shiotsu, Kyoto "Experimental Studies on Transient Boiling Heat Transfer and Burnout," 4th Int'l. Heat Transfer Conference, Versailles, 1970.

14. Zuber, N., "Recent Trends in Boiling Heat Transfer Research," Applied Mechanics Reviews, Vol. 17, No. 9, 1964.

15. Rohsenow, W.H., "Heat Transfer with Boiling," ASHRE Semi-annual meeting, 1966.

16. Westwater, J.W., T.D. Drew and J.W. Hoops, Jr., "Advances in Chemical Engineering," 1. Academic Press Inc., 1956.

17. Kotake, S., "Effects of Reduced Gravity on Nucleate Boiling," Int'l. Jour.of Heat and Mass Transfer, Vol. 12, No. 54, 1969.

18. Sherley, J.E., "Nucleate Boiling Heat Transfer Data for Liquid Hydrogen at Standard and Zero Gravity," Advances in Cryogenic Engineering, Vol. 8, Plenum Press, 1963.

19. Merte, H. Jr., J.A. Clark, "Boiling Heat Transfer with Cryogenic Fluids at Standard, Fractional and Near Zero Gravity," Trans. ASME, Jour.of Heat Transfer, Vol. 86, No. 3, 1964.

20. Schwartz, S.H., "Saturated Pool Boiling of Water in Reduced Gravity Environment," Ph.D. Thesis, The University of Southern California, Los Angeles, Calif., 1966.

21. Lewis, E.W., J.A. Clark, H. Merte, Jr., "Boiling of Liquid Nitrogen in Reduced Gravity Fields with Subcooling," NASA 8-20278, 07461-70, Dept. of Mech. Eng., Univ. of Michigan, Tech. Report 2, 1967.

22. Usiskin, C., R. Siegel, "A Photographic Study of Boiling in the Absence of Gravity," Trans. ASME, Jour. of Heat Transfer, Vol. 81, No. 3, 1959.

23. Usiskin, C., R. Siegel, "An Experimental Study of Boiling in Reduced and Zero Gravity Fields," Trans. ASME, Jour. of Heat Transfer, Vol. 83, No. 3, 1961.

24. Littles, J.W., "Nucleate Pool Boiling of Saturated Freon 113 in a Reduced Gravity Environment," Ph.D. Thesis, The University of Texas at Austin, Aug. 1969.

25. Merte, H. Jr., E. Oker, J.W. Littles, "Boiling Heat Transfer to LN_2 and LH_2 Influence of Surface Orientation and Reduced Body Forces," Proceedings 13th Int'l. Congress of Refrigeration, Commission 1, Paper 1.62, Washington, DC 1971.

26. Papell, S.S., O.C. Faber, "Zero and Reduced Gravity Simulation on a Magnetic Colloid Pool Boiling System," NASA TN D-3288, 1966.

27. Clodfelter, R.G., "Low Gravity Pool Boiling Heat Transfer," Air Force Aero Propulsion Lab., Wright-Patterson Air Force Base, Ohio, Tech. Documentary Report No. APL-TDR-64-19,1964.

28. Siegel, R., E.G. Keshock, "Nucleate and Film Boiling in Reduced Gravity from Horizontal and Vertical Wires," NASA Tech. Report R-216, 1965.

29. Merte, H., Jr., "Incipient and Steady Boiling of Liquid Nitrogen and Liquid Hydrogen Under Reduced Gravity," Technical Report No. 7, Heat Transfer Lab., Department of Mechanical Engineering, The University of Michigan, 1970.

30. Marcus, B.D., D. Dropkin, "The Effect of Surface Configuration on Nucleate Boiling Heat Transfer," Int'l. Jour. of Heat Mass Transfer, Vol. 6, No. 9, 1963.

31. Githinji, P.M., R.H. Sabersky, "Some Effects of Orientation of the Heating Surface in Nucleate Boiling," Trans. ASME, Journal of Heat Transfer, Vol. 85, No. 4, 1963.

32. Hospeti, N.B., R.B. Mesler, "Vaporization at the Base of Bubbles of Different Shape During Nucleate Boiling of Different Shape During Nucleate Boiling of Water," AIChE Journal, Vol. 15, No. 2, 1969.

33. Rohsenow, W.H., J.A. Clark, "A Study of the Mechanism of Boiling Heat Transfer," Trans. ASME, Vol. 73, No. 5, 1951.

34. Judd, R.L., H. Merte, Jr., "Evaluation of Nuclear Boiling Heat Flux Predictions at Varying Levels of Subcooling and Acceleration," Int'l. Jour. of Heat Mass Transfer, Vol. 15, No. 5, 1972.

35. Westwater, J.W., "Boiling Heat Transfer," Amer. Scientist, Vol. 47, No. 9, 1959.

36. Rallis, C.J., H.H. Jawurek, "Latent Heat Transport in Saturated Nucleate Boiling," Int'l. Jour. of Heat Mass Transfer, Vol. 7, No. 10, 1964.

37. Forster, H.K., R. Grief, "Heat Transfer to a Boiling Liquid-Mechanism and Correlations," Trans. ASME, Jour. of Heat Transfer, Vol. 81, No. 1, 1959.

38. Moeller, C.E., "Gold Film Resistance Thermometers for Surface Temperature Measurements," Paper R7-29.

39. Belser, R.B., W.H. Hickline, "Temperature Coefficients of Resistance of Metallic Films in the Temperature Range of 85° to 600°C," Jour. of Applied Physics, Vol. 30, No. 3, 1959.

40. Belser, R.B., "Electrical Resistance of Thin Metal Films Before and After Artificial Aging by Heating," Jour. of Applied Physics, Vol. 28, No. 1, 1957.

41. Coeling, K.J., H. Merte, Jr., "Incipient and Nucleate Boiling of Liquid Hydrogen," Trans. ASME, Jour. of Eng. for Industry, Vol. 98, 1968.

42. Hsu, Y.Y., R.W. Graham, "Analytical and Experimental Studies of the Thermal Boundary Layer and Ebullition Cycle in Nucleate Boiling," NASA TN D-594, 1961.

43. Hsu, Y.Y., "On the Size Range of Active Nucliation Cavities on a Heating Surface," Paper No. 61-WA-177, ASME Winter Annual Meeting, New York, 1961.

44. Sweeney, D.W., C.M. Vest, "Measurements of Three Dimensional Temperature Fields Above Heated Surface by Holographic Interferometry," Internal Report, University of Michigan, Mech. Eng. Dept., 1973.

45. Westwater, J.W., D.B. Kirby, "Bubble and Vapor Behavior on a Heated Horizontal Plate During Pool Boiling Near Burnout," Chemical Engineering Progress Symposium Series, Vol. 61, No. 57, 1965.

46. Beckman, W.A., H. Merte, Jr., "A Photograpnic Study of Boiling in an Accelerating System," Trans. ASME, Jour. of Heat Transfer, Vol. 87, No. 3, 1965.

47. Gaertner, R.F., "Photographic Study of Nucleate Pool Boiling on a Horizontal Surface," Trans.ASME, Jour.of Heat Transfer, Vol. 87, No. 1, 1965.

48. Fritz, N., "The Vaporization Process According to Cinematographic Pictures of Vapor Bubbles," Z. Physik, Vol. 37, 1936.

49. Bashforth, F., C. Adams, "An Attempt to Test the Theories of Capillary Action," Cambridge University Press, 1883.

50. Staniszewski, B.E., "Nucleate Boiling Bubble Growth and Departure," MIT Technical Report No. 16, Cambridge, Mass., 1959.

51. Jakob, M., "Heat Transfer," Vol. 1, John Wiley & Sons, New York, 1949.

52. Zuber, N., "Nucleate Boiling. The Region of Isolated Bubbles and the Similarity with Natural Convection," Int'l. Jour. Heat Mass Transfer, Vol. 6, No. 1, 1963.

53. McFadden, P.W., P. Grassmann. "The Relation Between Bubble Frequency and Diameter During Nucleate Pool Boiling," Int'l. Jour. Heat Mass Transfer, Vol. 5, No. 2, 1962.

54. Westwater, J.W., A.S. Perkins, "Measurements of Bubbles Formed in Boiling Methanol," AIChE Journal, Vol. 2, 1956.

55. Merte, H. Jr., J.A. Clark, "Pool Boiling in an Accelerating System," Trans. ASME, Jour. of Heat Transfer, Vol. 83, No. 3, 1961.

56. Han, C.Y., P. Griffith, "The Mechanism of Heat Transfer in Nucleate Pool Boiling," Int'l. Jour. of Heat Mass Transfer, Vol. 8, No. 6, 1965.

57. Arpaci, V.S., "Conduction Heat Transfer," Addison-Wesley Pub. Co., Inc., Reading, Mass., 1966.

58. Carslaw, H.S., J.C. Jaeger, "Conduction of Heat in Solids," Oxford Press, 2nd Edition, 1959.

59. Vest, C.M., M.L. Lawson, "Onset of Convection Near a Suddenly Heated Horizontal Wire," Int'l. Jour. Heat Mass Transfer, Vol. 15, No. 6, 1972.

60. Rayleigh, Lord, "On Convective Currents in a Horizontal Layer of Fluid when the Higher Temperature is on the Underside," Phil. Mag., Vol. 32, 1916; also Scientific Papers, Vol. 6, Cambridge, England, 1920.

61. Jeffreys, H., "Some Cases of Instability in Fluid Motion," Proc. Roy. Soc., Vol. A118, 1928.

62. Low, A.R., "On the Criterion for Stability of a Layer of Viscous Fluid Heated from Below," Proc. Roy. Soc., Vol. A125, 1929.

63. Pellew, A., R.V. Southwell, "On Maintained Convective Motion in a Fluid Heated from Below," Proc. Roy. Soc., Vol. A176, 1940.

64. Sparrow, E.M., R.J. Goldstein, V.K. Jonsson, "Thermal Instability in a Horizontal Fluid Layer," Jour. of Fluid Mech., Vol. 18, No. 4, 1964.

65. Goldstein, R.J., D.G. Briggs, "Transient Free Convection About Vertical Plates and Circular Cylinders," Trans. ASME, Jour. of Heat Transfer, Vol. 86, No. 4, 1964.

66. Kline, S.J., F.A. McClintock, "The Descriptions of Uncertainties in Single Sample Experiments," Mechanical Engineering, Vol. 75, 1953.

67. Zuber, N., M. Tribus, J.W. Westwater, "The Hydrodynamics Crisis in Pool Boiling of Saturated and Subcooled Liquids," Proceedings of the International Conference on Developments in Heat Transfer, ASME, New York, 1962.

68. Siegel, R., "Transient Free Convection from a Vertical Plate," Trans. ASME, Vol. 80, No. 2, 1958.